technische universität
dortmund
Fakultät Physik – Experimentelle Physik 5

Long-term observations of the TeV blazar 1ES 1959+650

Temporal and spectral behavior in the multi-wavelength context

Dissertation

zur Erlangung des akademischen Grades eines
Doktors der Naturwissenschaften
(Dr. rer. nat.)

vorgelegt von

Dipl.-Phys. Michael Backes

Dezember 2011

Contents

Chapter 1
Introduction

Astroparticle physics bridges the research fields of astrophysics and particle physics, studying the highest energetic phenomena in the Universe. The central question of this research field is the origin of ultra high energetic charged particles, dubbed cosmic rays, stemming from astrophysical objects and arriving at Earth isotropically. Due to deflection in intergalactic magnetic fields, these particles cannot be traced back to their origins by their arrival directions. Hence, their sources can only be identified indirectly through electrically neutral particles as neutrinos and high energetic photons, stemming from the same sources. Blazars, a subclass of Active Galactic Nuclei with highly relativistic plasma outflows pointing towards the Earth, are for several reasons good candidates for being the origin of cosmic rays. In this context, the spectral and temporal long-term behavior of the blazar 1ES 1959+650 is studied throughout this thesis. Having shown strong hints of hadronic emission processes in the past, this blazar is a primary candidate for a source of cosmic rays and thus it was monitored with the MAGIC telescope since 2004. The temporal variability for different wavelength bands, which should be connected in the case of non-hadronic emission processes is examined in this thesis. Furthermore, the time-integrated spectral energy distribution is compiled from radio to very high energy gamma-rays and modeled for hadronic and leptonic emission scenarios to unveil the character of the emitting particles.
Additionally, the idea of long-term monitoring of blazars at very high energy gamma-rays is pursued further. The characterization of the mirrors for setting-up the FACT telescope for blazar monitoring and the coordination of DWARF, a worldwide network of Cherenkov telescopes are presented.
The contents of this thesis is structured as follows.

Chapter 2 gives a short overview of astroparticle physics, introducing the three messenger particles of cosmic radiation, their acceleration and emission processes and their inter-connections. Having introduced Active Galactic Nuclei as possible sources for cosmic rays, their properties are outlined in the second part of that chapter, focusing on the subclass of blazars and possible emission models of their non-thermal radiation.

Chapter 3 briefly reviews the nearly forty instruments used throughout this thesis for the compilation of the multi-wavelength data from radio to high energy gamma-rays.

Chapter 4 even enlarges the covered energy range to very high energy gamma-rays. The working principle of imaging atmospheric Cherenkov telescopes is illustrated and the HEGRA and MAGIC telescopes, from which data have been retrieved, are introduced. Additionally, general limitations of the latest generation telescopes are discussed. Two methods to improve both the quality and the computing performance of multivariate classification algorithms, developed in the peripherals of this thesis and used for the analysis of Cherenkov telescope data, are outlined here.

Chapter 5 is devoted to the FACT telescope. This is a completely refurbished former HEGRA telescope and the very first Cherenkov telescope whose camera is entirely based on semi-conductor devices for photon detection, called G-APDs. In the course of this thesis the mirror facets for FACT have been reworked and characterized, measuring the focal lengths and the spot sizes of each facet. Furthermore, the thickness of the protective quartz coating has been estimated from the measured spectral reflectivity.

Chapter 6 outlines the ways, in which long-term gamma-ray monitoring of known, bright blazars can deepen our knowledge about these sources. The blazar monitoring program of MAGIC is introduced and results on two of the tree sources monitored by MAGIC are briefly summarized.

Chapter 7 highlights the third source of the MAGIC monitoring program, 1ES 1959+650. The observational history of this blazar is reviewed, and both the spectral and the temporal behavior is presented. Together with the new results from the monitoring observations with MAGIC and recent observations with Fermi–LAT, this enables for the first time the compilation of the complete spectral energy distribution of this blazar. The presented measurements of the non-thermal emission from this blazar span over 20 orders of magnitude in energy with essentially no gaps. Although not being simultaneously recorded, the compilation of these data allows to study the underlying emission processes and particle populations.

Chapter 8 ties in with the results stemming from the MAGIC monitoring campaign as it reports on the efforts to set-up a global network of Cherenkov telescopes for the monitoring of bright blazars, DWARF. For this FACT, mentioned previously, will serve as a first cornerstone but here also the possibilities for further international collaborations are outlined and the feasibility of a worldwide network of Cherenkov telescopes is addressed.

Chapter 9 concludes the finding of this thesis and gives an outlook on further research possibilities based upon.

Chapter 2
Brief Introduction to Astroparticle Physics

The research field of astroparticle physics was founded a century ago in 1911 by Viktor Hess [Hes11, Hes12][1]. Being influenced by many surrounding research areas such as cosmology, magnetohydrodynamics[2], stellar and galaxy evolution and formation, it draws a bow from the smallest known phenomena in particle physics, which can be described by relativistic quantum mechanics, to the largest astronomical structures like active galaxies hosting supermassive black holes[3], being described by the laws of general relativity. In astrophysical sources, particles are accelerated to extremely high energies of up to 10^{21} eV. These particles are then propagated through the Universe, interacting with molecular clouds, intergalactic magnetic fields and cosmological imprints like the cosmic microwave background[4] or cosmologically redshifted starlight. Subsequently, they are detected with space-born or ground-based instruments, shedding light on their production and acceleration processes within their sources and thus on the astrophysical sources themselves. Figure 2.1 illustrates the described research field as well as the differences between the three types of messenger particles:

- charged particles, i.e. mainly protons (p) but also heavy nuclei,
- neutrinos (ν), and
- photons (γ)

which are all utilized in astroparticle physics in contrast to classical astronomy which makes use of the visible light. The following sections give a brief introduction to astroparticle physics. For more detailed descriptions the reader is referred to review articles such as [Bec08, KS11, HH09, LS11], to textbooks like [Aha04, DM09, Gai90, Gru00, Gru05, Lon10, Méz10, Per10, Sta10], to lecture notes like [Alf11, Kol10] and to references therein and in this text.

[1] For a detailed description of the historical development of the field of astroparticle physics see [Cir08].
[2] **M**agneto**h**ydro**d**ynamics, MHD
[3] **S**uper**m**assive **B**lack **H**ole, SMBH
[4] **C**osmic **M**icrowave **B**ackground, CMB

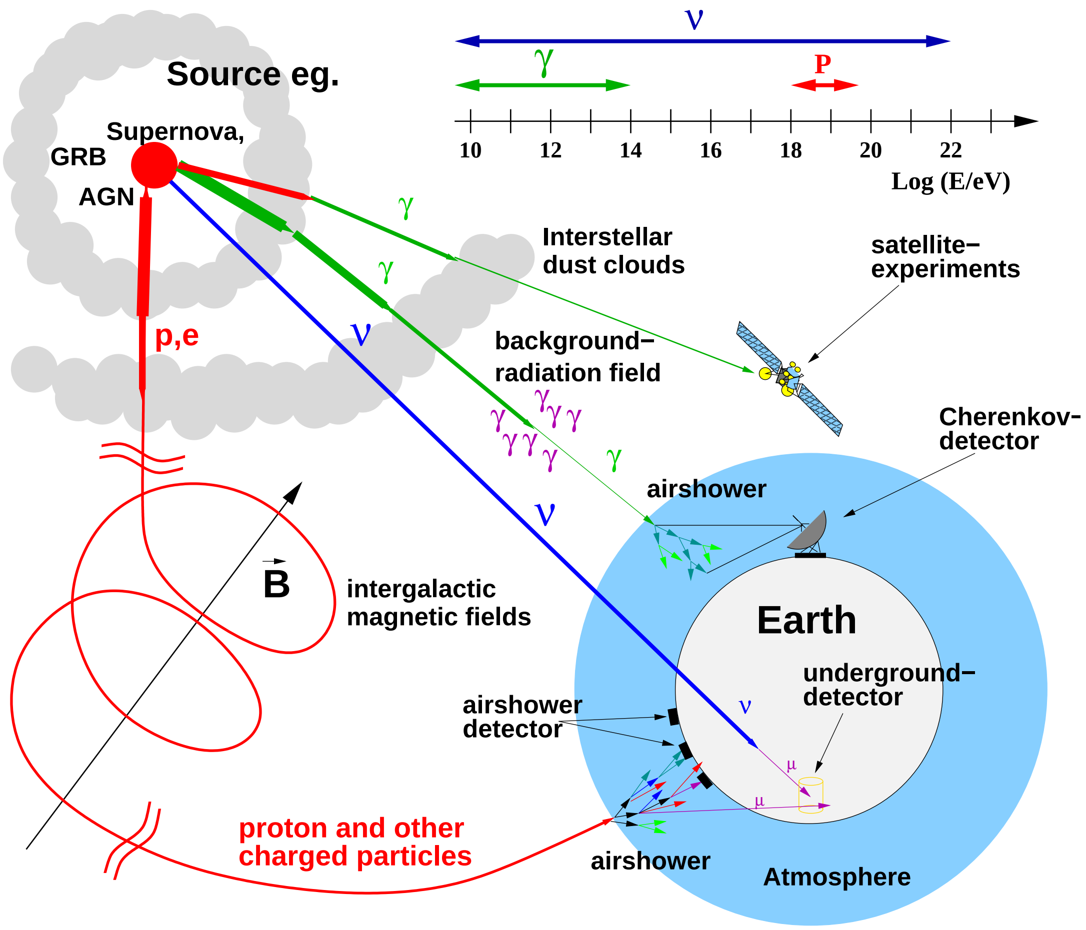

Figure 2.1: Overview of astroparticle physics: Sources of cosmic radiation, particle propagation to Earth, absorption mechanisms and detection methods [Dre09] after [Wag04].

2.1 Charged Cosmic Rays

2.1.1 Composition of Cosmic Rays

When speaking about cosmic rays[5], usually it is referred to the charged component of particle flux reaching the Earth. Above ~ 1 GeV it is mainly comprised by protons ($\sim 85\%$) and α-particles ($\sim 12\%$), with small contributions of leptons ($\sim 2\%$) and heavier elements up to iron ($\sim 1\%$) [Sta10]. A direct measurement of the charge distribution and thus the composition of cosmic rays, measured in the energy range of 10 GeV to 100 TeV per nucleon with the CREAM[6] experiment, is depicted in Figure 2.2.
At higher energies the composition of cosmic rays has to be inferred from indirect measurements with ground based detectors. It is still under debate, whether the highest energetic cosmic rays (above 10^{19} GeV) are comprised by heavy nucleons, i.e. iron, as measured by

[5] **C**osmic **R**ay, CR
[6] **C**osmic **R**ay **E**nergy **A**nd **M**ass, CREAM, see http://cosmicray.umd.edu/cream

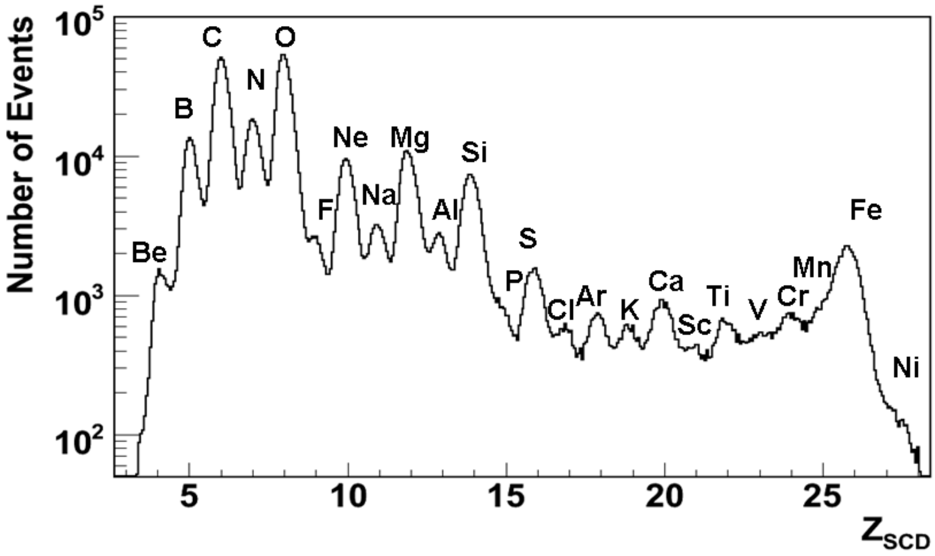

Figure 2.2: The charge distribution of cosmic rays starting with Beryllium, measured with the balloon experiment CREAM. The number of events is depicted depending on the nuclear charge Z. From: [Bla08], see also [P+07a].

the Pierre Auger Observatory[7] [The11c], or by protons, as measured by HiRes[8] [A+10a] and the Telescope Array[9] [T+10b], see Figure 2.3.

2.1.2 Energy Spectrum of Cosmic Rays

As cosmic rays are comprised by charged particles, they are deflected by intergalactic magnetic fields. Thus, they are hitting the Earth's atmosphere isotropically and cannot be traced back to their sources. Hence, the main research goal besides the composition of cosmic rays, as outlined in subsection 2.1.1, is their energy spectrum. From its spectral shape, conclusions concerning the source populations might be drawn indirectly, but final conclusions might only be drawn from astronomical measurements of neutrinos (see section 2.2) or (high-energy) photons (see section 2.3). A compilation of recent measurements of the cosmic ray energy spectrum, i.e. the particle flux $F = dN/dE$ plotted vs. energy E, is depicted in Figure 2.4. One can see that the spectrum of the cosmic rays can be described by a combination of power-laws for three ranges of energy [WBM98, V+99b]:

$$F(E) \propto \begin{cases} E^{-2.67}, & E < 10^{15.4}\,\text{eV} \\ E^{-3.10}, & 10^{15.4}\,\text{eV} < E < 10^{18.5}\,\text{eV} \\ E^{-2.75}, & 10^{18.5}\,\text{eV} < E \end{cases} . \tag{2.1}$$

The energy ranges around $10^{15.4}$ eV and $10^{18.5}$ eV whereas the spectral indices of the power-laws change are called *knee* and *ankle*, respectively, as indicated in Figure 2.4. For details

[7] **P**ierre **A**uger **O**bservatory, PAO, see http://www.auger.org
[8] **Hi**gh **Res**olution Fly's Eye Detector, HiRes [Tho04], see http://www.cosmic-ray.org
[9] **T**elescope **A**rray, TA [Tt09], see http://telescopearray.org

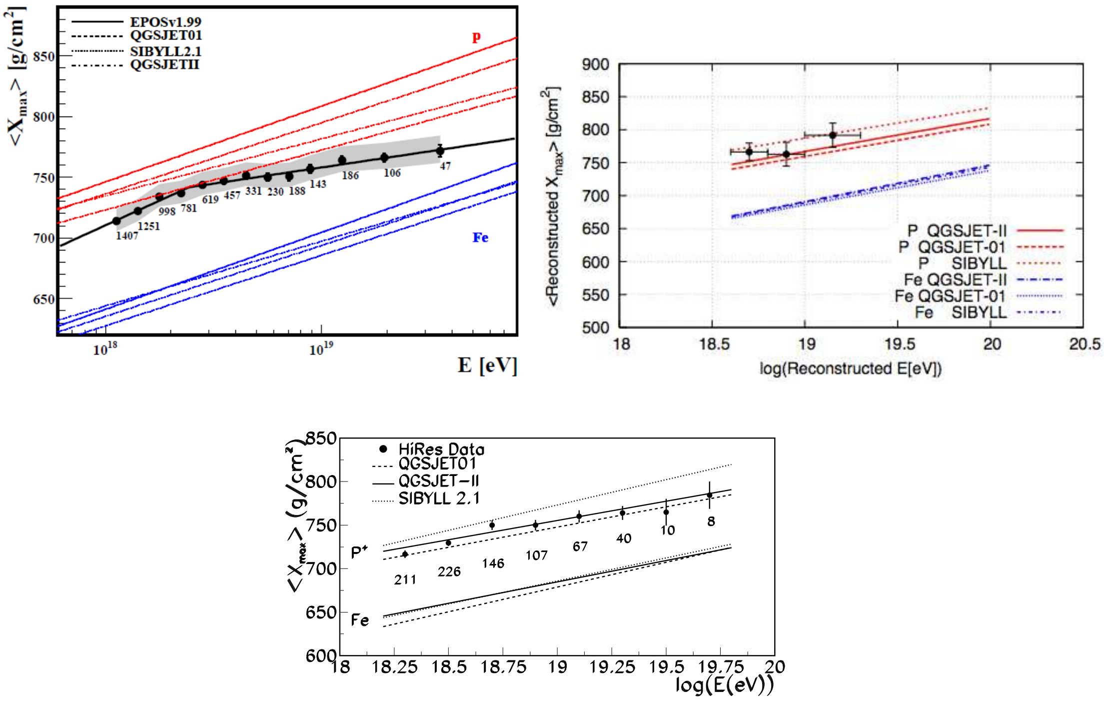

Figure 2.3: The composition of UHE cosmic rays as measured by the PAO (top left) [The11c], the TA (top right) [T+10b], and HiRes (bottom) [A+10a]. Depicted is the energy dependent mean of the shower maxima for measured events (dots) and Monte Carlo predictions for pure proton and pure iron samples (lines) computed with different interaction models as described in the inlays.

on the highest energetic part of the spectrum see subsection 2.1.4. The basic power-law behavior of the cosmic ray energy spectrum can be explained by the diffuse shock acceleration process, formulated by E. Fermi in 1949 [Fer49]. Within that framework, test particles are accelerated via several (collisionless) interactions with shock waves in magnetized plasmas. This naturally leads to a power-law spectrum of the accelerated particles, as one can easily deduce, c.f. [Gai90].

2.1.3 Sources of Cosmic Rays up to $\sim 10^{18}$ eV

As the shock acceleration mechanism gives a natural explanation for the power-law behavior of the energy spectrum of cosmic rays but not for the changes in spectral slope at the *knee* and the *ankle*, it is a common approach to explain these by different source populations. One example for this is depicted in Figure 2.5. Therefore it is assumed that the cosmic ray luminosity of a given source type is smaller than its electromagnetic luminosity. In Figure 2.5 one can see that the sum of cosmic ray luminosities of *supernova*

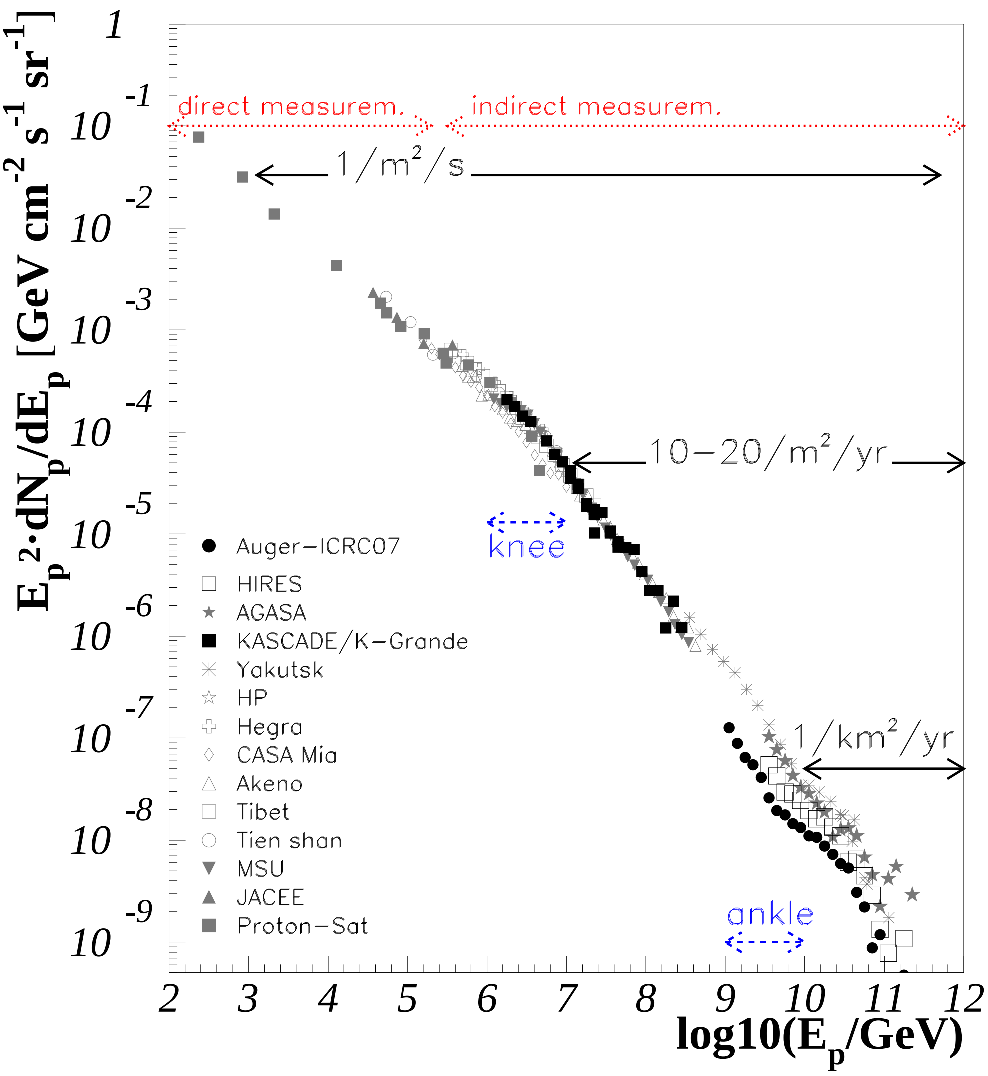

Figure 2.4: The cosmic ray energy spectrum measured by different experiments as stated in the inlay, weighted by E^2. Indicated are also the *knee* and *ankle* regions, as well as the approximate particle flux per time and area [Bec08].

remnants[10], *X-ray binaries*[11], and *pulsars*, or rather *pulsar wind nebulae*[12], naturally add up to a total luminosity matching that of the cosmic rays pretty well.
One of many other alternative explanations for the spectral break at the *knee* may be *wind supernovae*, having Wolf-Rayet stars as progenitors and being capable to accelerate par-

[10]**S**uper**n**ova **R**emnant, SNR
[11]**X**-**R**ay **B**inary, XRB
[12]**P**ulsar **W**ind **N**ebula, PWN

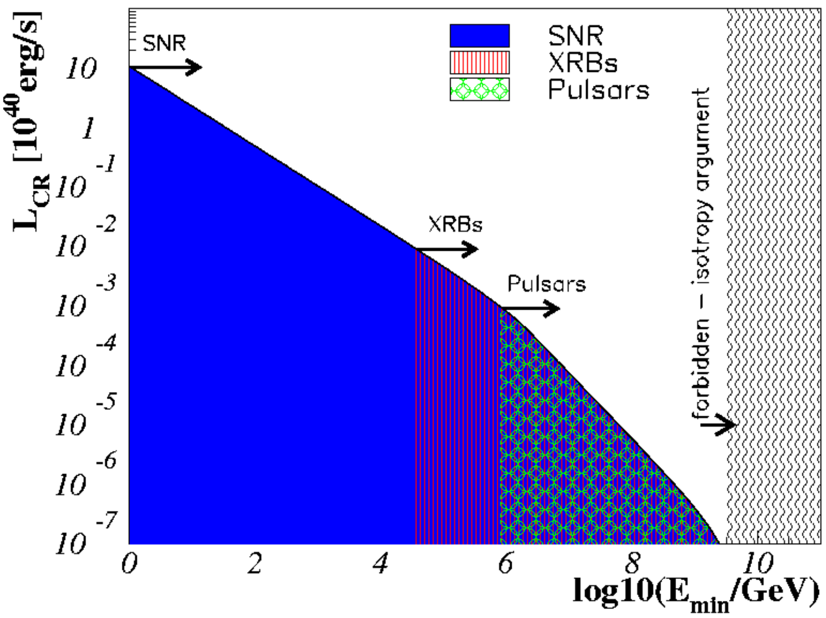

Figure 2.5: Integral cosmic ray energy spectrum as expected from the electromagnetic luminosities of galactic source types. The luminosity is plotted against the minimal energy E_{min}. The upper line (black) depicts the equivalent luminosity of cosmic rays with $E > E_{\mathrm{min}}$ The blue area shows the (electromagnetic) luminosity of supernova remnants. Similarly the red striped area (above $10^{4.5}$ GeV) shows additionally the luminosity of X-ray binaries and the green hatched area the luminosity of pulsars [Bec08].

ticles to much higher energies than conventional supernovae. Thus they would contribute to the cosmic ray spectrum also beyond energies of the *knee* [Rej98].

2.1.4 Sources of Cosmic Rays above $\sim 10^{18}$ eV

Extragalactic Origin

Cosmic rays exhibiting energies beyond the *ankle*, for several reasons are believed to be of extra-galactic origin: For instance, the charged particles can only be kept inside a galaxy if their *gyro-radius* r_g is smaller than the size of the galaxy:

$$r_g \leq \left(\frac{pc}{Ze}\right) \cdot \frac{\sin\phi}{Bc}, \tag{2.2}$$

where p is the momentum of the particle, Z the nuclear charge and ϕ the angle between the particles' trajectory and the magnetic field B. The expression pc/Ze is called *rigidity*. Assuming a galactic magnetic field of $B = 3\,\mu$G and $\phi = 90°$, for relativistic protons with

an energy of 10^{18} eV, r_g equals the thickness of the galactic plane ($\sim 300\,\mathrm{pc}$[13]). For further details, see [Gai90].
If cosmic rays with energies beyond the *ankle* were of galactic origin, there would be an anisotropy in their arrival directions pointing towards the galactic plane, which is not evident in experimental data.

Cosmic Ray Absorption in the Cosmic Microwave Background

For energies even far beyond the *ankle* there is a natural limit. Above a threshold energy of $5 \cdot 10^{19}$ eV the cosmic ray spectrum is diluted by photo-hadronic interactions with the CMB photon field, producing unstable delta-resonances and therefore, converting high energetic protons to lower energetic ones:

$$p + \gamma_{CMB} \rightarrow \Delta^+ \begin{array}{l} \nearrow \quad p + \pi^0 \\ \\ \searrow \quad n + \pi^+ \end{array} \tag{2.3}$$

This process was independently predicted by K. Greisen [Gre66], and G. T. Zatsepin and V. A. Kuzmin [ZK66] in 1966. Thus, this suppression of particles with energies $\gtrsim 5 \cdot 10^{19}$ eV is usually referred to as *GZK-cutoff*[14]. Experimentally, this effect was for a long time a matter of debate, as one can also see in Figure 2.4. The HiRes experiment reported hints of confirmation of that prediction [The05], whereas the AGASA[15] experiment had reported having observed so-called *trans-Greisen events*, i.e. events with energies beyond the GZK cutoff energy [Y+95]. Later, HiRes detected a suppression of the highest energetic events leading to a deviation from a power-law with a significance of $5\,\sigma$ [A+08a]. This was subsequently confirmed by observations of the Pierre Auger Observatory [Y+08a], showing a deviation from a power-law with a significance of $6\,\sigma$ [A+08d] and later of more than $20\,\sigma$ [A+10f]. Recent results, comprised by a 60% enlarged exposure compared to the previous publication are shown in Figure 2.6 [The11b].
This provides an update on the highest energetic part of Equation 2.1:

$$F(E) \propto \left\{ \begin{array}{cc} E^{-3.27\pm0.02}, & E < 10^{18.61\pm0.01}\,\mathrm{eV} \\ E^{-2.68\pm0.01}, & 10^{18.61\pm0.01}\,\mathrm{eV} < E < 10^{19.41\pm0.02}\,\mathrm{eV} \\ E^{-4.2\pm0.1}, & 10^{19.41\pm0.02}\,\mathrm{eV} < E \end{array} \right. , \tag{2.4}$$

whereas an exponential cut-off at $10^{19.63\pm0.02}$ eV is slightly favored above the power-law description stated above.

Active Galaxies as Source Candidates

Starting from diffuse shock acceleration, as mentioned earlier in this section, the energy gain of the particles depends on the size of the acceleration region L on the one hand and the strength of the magnetic field B on the other hand, according to

$$E_{\max} \propto ZLB, \tag{2.5}$$

[13] Parsec, $1\,\mathrm{pc} \approx 3.24$ lightyears
[14] **G**reisen-**Z**atsepin-**K**uzmin, GZK
[15] **A**keno **G**iant **A**ir **S**hower **A**rray, AGASA, see http://www-akeno.icrr.u-tokyo.ac.jp/AGASA

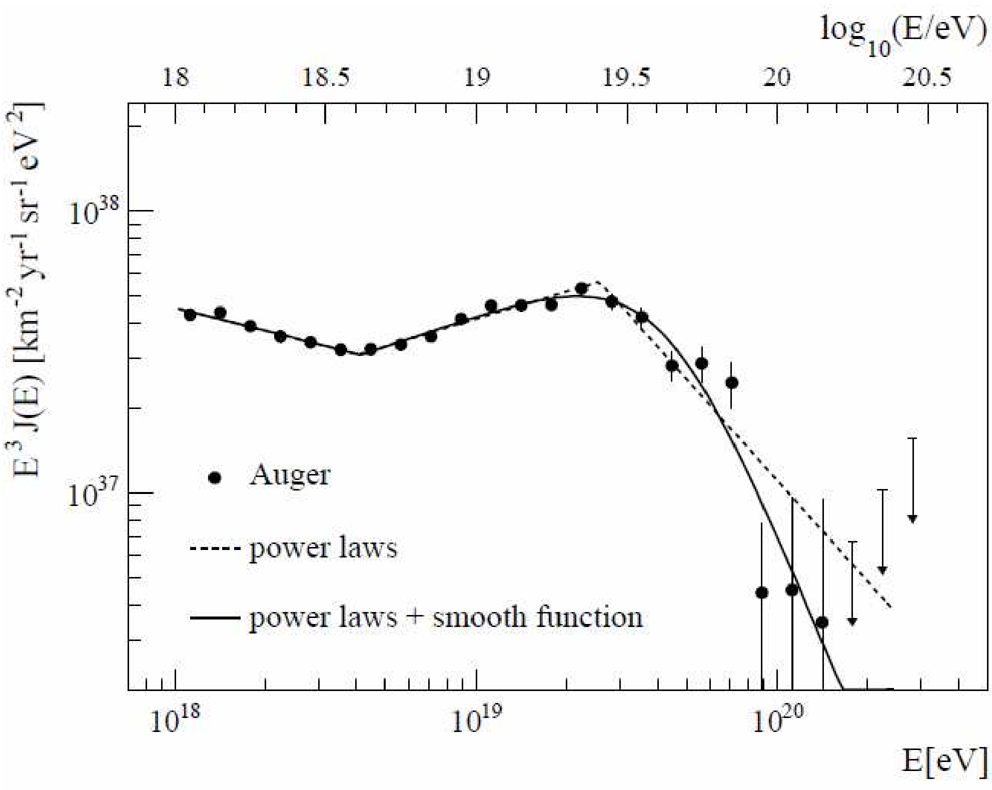

Figure 2.6: The highest energetic part of the cosmic ray energy spectrum as measured by the Pierre Auger Observatory drawn together with broken power-law fits according to Equation 2.4 as well as a smooth exponential cut-off [The11b].

where Z is the atomic number. Therefore, when searching for astronomical objects being the accelerators of the highest energetic cosmic rays, one may easily identify them in the so-called *Hillas plot*, c.f. Figure 2.7.

As one can see from Figure 2.7, the most promising candidates for acceleration of the highest energetic cosmic rays are neutron stars, gamma-ray bursts and the different acceleration regions of active galaxies, in particular the nuclei and the hot-spots which are moving along the radio jets. Although there are several attempts to explain the high energy end of the cosmic ray energy spectrum, through e.g. gamma-ray bursts[16] [Der02, Vie95, Wax95], or Cen A, the nearest radio galaxy [Bd11] as main contributing sources, active galaxies in general are believed the most favorable sources of the highest energetic cosmic ray particles [B+09f, DR10, Der11].

Additionally, the arrival directions of the first 27 events with energies beyond 56 EeV observed with the Pierre Auger Observatory were excluded to be isotropical at 99% confidence level. Furthermore, they showed a correlation of $69^{+11}_{-13}\%$ with nearby objects [A+07a, A+08c] from the 12^{th} edition of the catalog of active galactic nuclei by Véron-Cetty and Véron [VV06]. However, these mainly resemble the matter distribution along the supergalactic plane. In contrary, the most significant correlation that was found

[16] **G**amma-**R**ay **B**urst, GRB

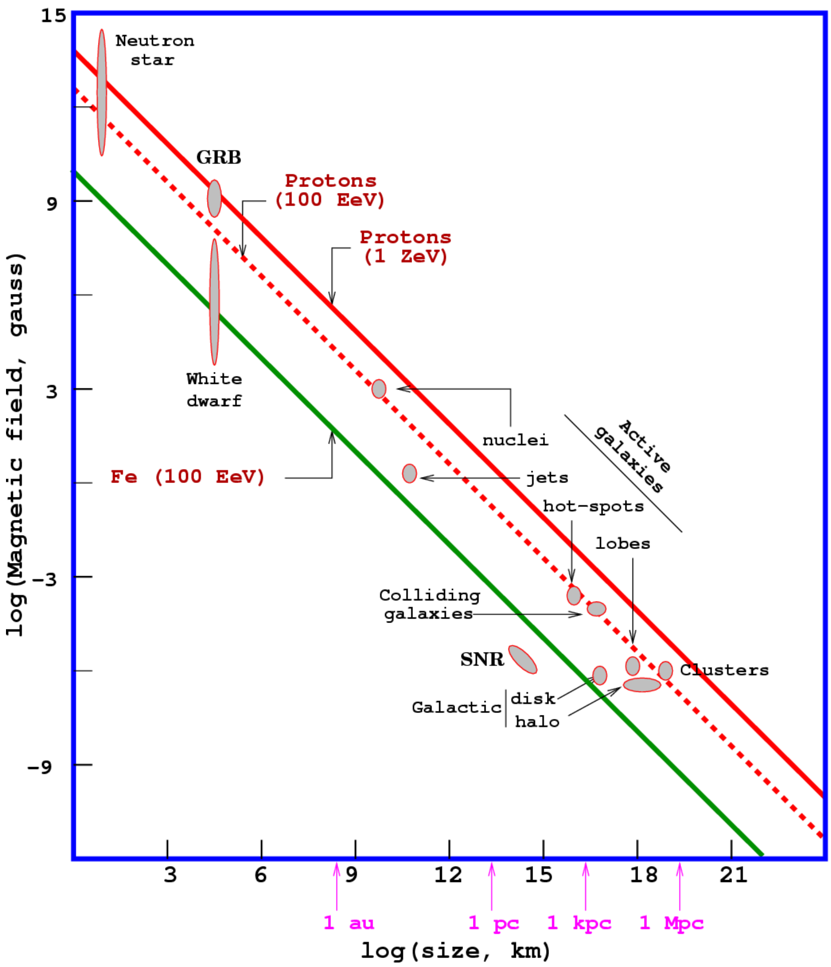

Figure 2.7: The "Hillas plot": Depicted is the magnetic field strength (B) vs. the size (L) of different astrophysical objects. Additionally, lines are drawn according to Equation 2.5 for maximum energies of 100 EeV (red, dashed) and 1 ZeV (red, solid) for protons ($Z = 1$) and of 100 EeV for iron ($Z = 26$, green, solid) [Kap07, Arg00].

by the HiRes experiment still had a chance probability of 24% [A+08b]. Meanwhile, the dataset of the Pierre Auger Observatory enlarged to 69 events and the observed correlation dropped to 38^{+7}_{-6}%, compared to 21% expected for isotropic cosmic rays [A+10g].
Being such promising sources of the highest energetic cosmic rays and thus maybe a key to resolving a century old mystery, the nature of *Active Galactic Nuclei*[17] will be presented in section 2.4.

[17] **A**ctive **G**alactic **N**ucleus, AGN

2.2 Astrophysical Neutrinos

In contrast to cosmic rays, neutrinos (ν) are neither deflected by intergalactic magnetic fields, as they are not electrically charged, nor are they absorbed, neither in optically thick sources nor on their way to earth due to their extremely small cross section. This is sketched in Figure 2.1. Thus, carrying information of the innermost region of their sources and also keeping their directional information, neutrinos are optimal messenger particles from astronomical sources. For supernovae it is even assumed that up to 99% of the energy is carried away by neutrinos [UB07]. But their small cross section also makes them hard to detect. To overcome this difficulty one needs to instrument huge effective detector volumes. The current generation instruments for such are of the cubic kilometer scale: IceCube[18] whose building-up in the antarctic ice has recently been finished in 2011 with an instrumented detector volume of $1\,\mathrm{km}^3$ and KM3NeT[19] which is going to be build-up in the Mediterranean Sea with a possibly even larger volume. Anyhow, the most recent results on the diffuse neutrino spectrum [A+11b] as well as on the search for neutrinos from GRBs [A+11a], and for single astrophysical neutrino sources as well as source classes of stacked samples of possible neutrino sources [A+11d] show no hint of an excess of astrophysical neutrinos over the (huge) background of neutrinos produces by cosmic rays hitting the Earth's atmosphere. Thus, the only astrophysical neutrinos (obviously besides those from the sun) detected up to now have been observed from the Supernova 1987A with SuperKamiokande[20] [Sup98] and SNO[21] [SNO02], which lead to the experimental detection of neutrino oscillations.

As neutrinos are electrically neutral and cannot be accelerated by the mechanisms discussed before in the context of cosmic rays (see subsection 2.1.2), neutrinos at very high energies can only be produced via decay or (weak) interaction processes. One of the main processes contributing in the production of high energetic neutrinos has already been given in Equation 2.3, although in this context the cosmic rays are interacting with source internal photons instead of those of the cosmic microwave background as outlined before [22]. As the arising pions are unstable and the neutrons are believed to leave the source and decay on their way to earth the following decay chains evolve:

$$p + \gamma \rightarrow \Delta^+ \begin{array}{l} \nearrow \; p + \pi^0 \qquad\qquad \rightarrow p + \gamma + \gamma \\ \searrow \; n + \pi^+ \quad \rightarrow p + e^- + \bar{\nu}_e + \nu_\mu + \mu^+ \quad \rightarrow n + e^- + \bar{\nu}_e + \nu_\mu + e^+ + \bar{\nu}_\mu + \nu_e . \end{array} \tag{2.6}$$

Additionally to the photo-hadronic process above, also the following hadronic process contributes to the high energy neutrino production:

$$p + p \begin{array}{l} \nearrow \; p + p + \pi^0 \qquad \rightarrow p + p + \gamma + \gamma \\ \searrow \; p + n + \pi^+ \quad \rightarrow p + n + \nu_\mu + \mu^+ \quad \rightarrow p + n + \nu_\mu + e^+ + \bar{\nu}_\mu + \nu_e . \end{array} \tag{2.7}$$

The given scenario is only an approximation, neglecting e.g. higher resonances and multi-pion production, but gives a good handle on qualitative results. For quantitative results

[18] IceCube, see http://www.icecube.wisc.edu
[19] **km**^{3} **N**eutrino **T**elescope, KM3NeT, see http://www.km3net.org
[20] **Super Kamioka n**ucleon **d**ecay **e**xperiment, SuperKamiokande, see http://www-sk.icrr.u-tokyo.ac.jp/sk/index-e.html
[21] **S**udbury **N**eutrino **O**bservatory, SNO, see http://www.sno.phy.queensu.ca
[22] Those interactions lead to the so-called cosmogenic neutrinos [BZ69].

on photo-hadronic interactions one should rather rely on a full Monte Carlo simulation like SOPHIA [M+00] or a more sophisticated parametrization like [KA08] or [H+10]. Anyway, it is obvious that a detection of astrophysical neutrinos from a single source or a stacked source class would directly imply the origin of the charged cosmic rays.

2.3 Photons from Outer Space

Being electrically neutral, photons are not affected by intergalactic magnetic fields and thus have been used for astronomical observations for thousands of years. Ever since the invention of the first (astronomical) telescope by Galileo Galilei revolutionized optical astronomy more than 400 years ago, inventions of new telescopes and especially telescopes operating in previously unexplored wavelength ranges have revolutionized our understanding of the Universe.
As sources of photon radiation are often compact and thus optically thick like e.g. the sun, photons are dominantly emitted from the surface of these objects as depicted in Figure 2.1. The most obvious case of photon emission is thermal radiation, i.e. blackbody radiation, being described by Planck's formula and thus connecting photon fluxes to a surface temperature, which is e.g. about 5,770 K for the sun [B+06b] and 2.725 ± 0.002 K for the cosmic microwave background [B+06b]. Herefrom it is already clear that astronomy can be conducted at any wavelength of electromagnetic radiation, ranging from radio waves up to very high energy[23] gamma-rays. But not all kinds of this radiation is evenly suited for being detected by ground-based telescopes, as illustrated in Figure 2.8. There, the spectral penetration depth is depicted for different wavelength. Although not displayed within that figure, the detection of the highest energetic gamma-rays is indirectly possible with ground based telescopes which will be explained in chapter 4.
Furthermore, there are also non-thermal processes to produce electromagnetic radiation. These are of special relevance for the production of VHE gamma-rays but as shown in subsection 2.4.2 can span over the entire electromagnetic spectrum. These processes may be of leptonic or hadronic nature, which will shortly be outlined in the following subsections. An illustrative introduction to these processes is given in [Wee03] whereas extensive overviews can be found in [RL85, Bra07, DM09].

2.3.1 Leptonic Processes: Connecting Low and High Energy Photons

Synchrotron radiation

The most important process for the production of non-thermal photons is synchrotron radiation. Relativistic charged particles gyrating in magnetic fields and thus being accelerated emit synchrotron radiation. As the energy loss by synchrotron radiation is rigidity and therefore mass dependent, synchrotron emission is generally dominated by a leptonic origin, i.e. emitting by electrons (and positrons). However, there are also scenarios in which the synchrotron emission of hadrons and their by-products, heavy leptons and mesons (mainly charged pions and kaons) play a major role due to significantly stronger magnetic fields [MP01]. In any case, synchrotron emission of a relativistic particle is

[23] **V**ery **H**igh **E**nergy, VHE. For the definition of the energy ranges used throughout this thesis see Appendix A.

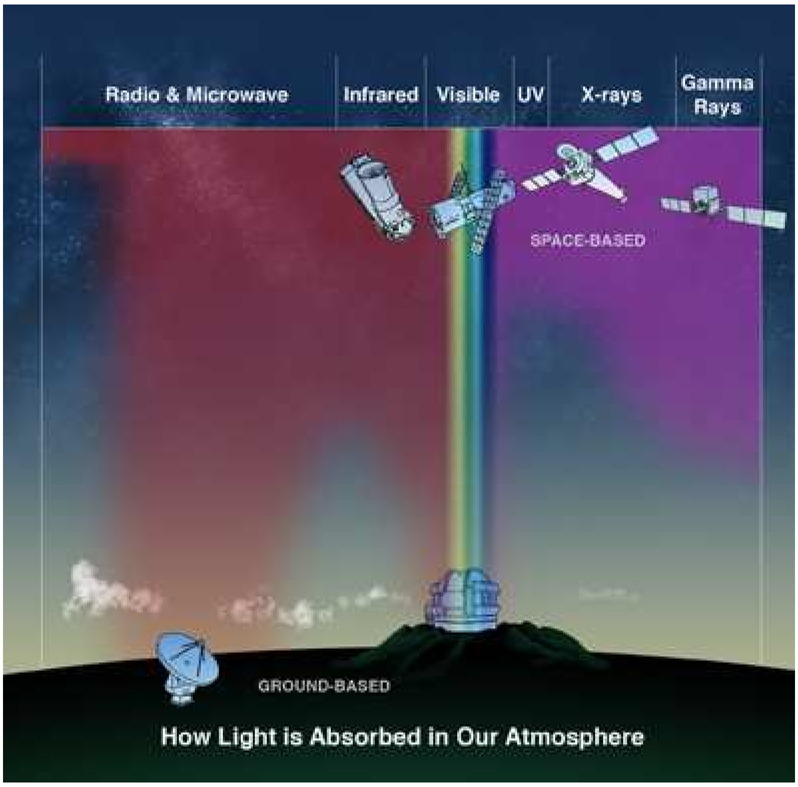

Figure 2.8: Illustration of the spectral penetration depth of electromagnetic radiation into the Earth's atmosphere. Only for radio and optical frequencies a detection from ground is possible. As examples for satellites operating in the infrared, optical, X-ray, and gamma-ray regime, IRAS [2.8.1], Hubble [2.8.2], Chandra [2.8.3] and Fermi [2.8.4] are depicted [NCS11].

[2.8.1] **I**nfrared **A**stronomical **S**atellite, IRAS, see http://lambda.gsfc.nasa.gov/product/iras

[2.8.2] **H**ubble **S**pace **T**elescope, HST, see http://hubble.nasa.gov

[2.8.3] **C**handra **X**-ray **O**bservatory, CXO, see http://chandra.harvard.edu

[2.8.4] **F**ermi **G**amma-ray **S**pace **T**elescope, FGST, see http://fermi.gsfc.nasa.gov

strongly beamed into the particle's direction of motion, opening an angle of γ^{-1}, with γ being the Lorenz factor,

$$\gamma = \sqrt{1 - \frac{v^2}{c^2}}, \tag{2.8}$$

where v is the particle's velocity and c the speed of light. Additionally, the time scale of radiation gets shortened by γ^{-3}, the emission frequency gets shifted by γ^3 and the total emitted power is boosted by γ^2. Notably, not only monoenergetic primary particles but also a power-law energy distribution of the primary particle population (as given by Fermi acceleration, see subsection 2.1.2) lead to a power-law spectrum in the synchrotron emission spectrum.

Synchrotron self absorption

In case of optically thick sources, where the mean free path for photons in photon-electron interactions is smaller than the actual source size, the synchrotron photons get re-absorbed by their emitting electron population, which is called synchrotron self absorption [Ree67]. Regarding AGN, this is of special interest concerning the low frequency end of the spectral energy distributions, where in models featuring only one emission zone, the radio emission is generally (self) absorbed.

(Inverse) Compton scattering

Compton scattering is the interaction of free electrons with photons with a non-negligible momentum transfer. In general, this process is thought to transfer momentum from a high energy photon to the electron. However, the process of inverse Compton scattering, transferring momentum from the electron to the photon, is of interest here. In general, this process takes place in the so-called *Thompson regime*, i.e. following to the Thompson cross section

$$\sigma_t = \frac{8\pi}{3}\left(\frac{q^2}{mc^2}\right)^2 . \tag{2.9}$$

For extremely high photon energies, i.e. $hv \gtrsim m_e c^2 \approx 511\,\mathrm{keV}$, the Compton process enters the *Klein-Nishina regime*, where not the classical (Thompson) approximation, but the (first order) quantum electrodynamical expression of the photon electron cross section applies, which strongly suppresses this interaction [KN29]. An obvious but important feature of the inverse Compton process is that the resulting (high energy) radiation density is strongly depending on the initial photon density and thus establishing a strong correlation between the low energy regime and the high energy regime.

Pair production

Another quantum electrodynamical process is the photon induced pair production. Here two photons react to form an electron positron pair. The threshold energy for this process can be derived as

$$E_{\gamma,thr} = \frac{m_e^2 c^4}{h\nu}, \tag{2.10}$$

with $h\nu$ being the energy of the target photon and m_e the electron rest mass. In general this process is also important source internally (see e.g. [B^+11h]), but for blazars, which are of special interest here (see subsection 2.4.1), this process is subordinate. But regarding the cosmological distances of AGN and the intergalactic radiation field this process, dubbed extragalactic absorption, plays a major role.

Extragalactic absorption

In Figure 2.1 not only the extinction of photons by dust clouds but also the absorption due to $\gamma\gamma$- pair production is depicted. The extragalactic background light[24], whose

[24] **E**xtragalactic **B**ackground **L**ight, EBL

main components are in the IR to UV energy ranges, interacts with high energy photons preferably in the TeV energy range

$$\gamma_{\mathrm{TeV}} + \gamma_{\mathrm{IR}} \rightarrow e^{+} + e^{-}. \tag{2.11}$$

Thus, the VHE photon flux from cosmological distances (cosmological redshift $z > 0.03$) is noticeably attenuated, the higher the redshift and the energy, the stronger the attenuation. Having measured an VHE spectrum of a source with known redshift, the source intrinsic spectrum can be inferred by modeling of the EBL and de-absorbing the measured spectrum, with models like e.g. [K+04a, FRV08, G+09, KD10, D+11b] and an sexperimental limit on the density of the EBL can be inferred [A+06b, MR07, A+08h].
For sources of VHE gamma-ray radiation whose redshift is unknown, the knowledge of this process can be used to constrain the redshift of the source [P+10].

2.3.2 Hadronic Processes: Connecting Photons, Protons, and Neutrinos

An alternative process for the production of high energetic photons is the decay of neutral pions. As stated in Equation 2.6 neutral pions decay into two photons, both having energies in the TeV range. In this scenario, the gamma-ray flux is no longer necessarily correlated to the X-ray flux as it is the case in leptonic models, which directly shows a way of detecting such processes. Moreover, this process would link the VHE gamma-ray flux to a proportional flux of high-energetic neutrinos, as the branching ratio of the processes given in Equation 2.6 and Equation 2.7 is 2/3 for the neutral pions against 1/3 for the charged pions[25]. Thus, the detection of a flux of high energetic neutrinos is another way of identifying this process which would in turn be a smoking gun for the sources of the highest energetic cosmic rays.

2.4 Active Galactic Nuclei

Modern surveys show that more or less every galaxy – like our own – hosts a central *black hole*[26][27] (see [Sch06b]) with masses of $\sim 10^6 - 10^9$ solar masses. In active galaxies there is an additional strong accretion flow onto the supermassive black hole, leading to the fact that non-thermal emission of the innermost region of the galaxy, called nucleus, outshines the whole rest of the galaxy by several orders of magnitude. The nucleus is comprised by the central black hole, surrounded by an accretion disk and a dust torus, as well as two highly collimated relativistic plasma outflows perpendicular to the accretion disk, called jets. The torus supplies the accretion disk with matter. It also obscures the central region of the nucleus, depending on the viewing angle (c.f. Figure 2.9). Due to the process of accretion, particles in the accretion disc are accelerated to relativistic velocities and strongly emit non-thermal synchrotron radiation, which are the seed photons in external Compton models, to be discussed later-on in subsection 2.4.2. For further reading on accretion disks in AGN the reader is referred to e.g. [Bla07] and the contained references.

[25] More sophisticated calculations alter this branching ratio by up to 20% [H+10].
[26] **B**lack **H**ole, BH
[27] In fact, near the center of the Milkyway there is even a second black hole with a mass of ~1,000 solar masses orbiting around the Milkyway's central black hole that is a 2,600 times more massive [B+06b].

According to [BZ77] the jets in AGN are formed by magnetic fields extracting the spin energy of a rotating black hole. Although this formalism was initially derived for force-free magnetospheres, recent general relativistic MHD simulations show its applicability also under these circumstances [Cam07]. Recent extensive overviews on MHD theory and jet production can be found in [Pun08, Bes10]. Despite the not finally settled theoretical question of jet production in the ergosphere of black holes, it is obvious from observations that these jets are highly magnetically collimated and can reach lengths of millions of light years[28]. Charged particles move along the jets at relativistic (and apparently super-luminal) speed within so-called plasmoids from which strong non-thermal radio and X-ray emission are observed. So, it is inferred that these plasmoids are regions of strong shock acceleration. For a recent overview on relativistic jets, see [Ghi11].
The first AGN was detected in 1963 [Sch63], dubbed Quasi Stellar Object[29]; but only in 1992 a general model of AGN was developed, unifying several formerly distinct source classes under a cylindrically symmetric model, attributing the differences to the viewing angle of the observer w.r.t. the cylinder axis [PU92, UP95, Urr04], as illustrated in Figure 2.9.
Further classification attributes of this unified model of AGN are the strength of the radio emission, which seems to be correlated to the shape of the host galaxy (spiral or elliptic) and the optical luminosity. In Figure 2.12 a detailed classification diagram is shown. In the following, only the subclass of blazars shall be of further interest.
For a slightly outdated but extensive general overview on AGN the reader is referred to [Kro99], for a more recent overview of effects being related to jets from AGN there will soon be a new book [BHK11].

2.4.1 Blazars

By far, most of the known extragalactic emitters of VHE gamma-rays are Active Galactic Nuclei and among those, the largest subclass is comprised by blazars. According to the unification scheme for AGN, blazars are characterized by relativistic plasma outflows (jets) pointing towards the observer [PU92]. Thus, it is plausible that already for geometric reasons, observations of blazars probe deepest into the jets of AGN and, by this, carry most of the information about their central engine. Recent observations with high-resolution VLBI[30] support this assumption, pinning down the emission region of outbursts in blazars as BL Lac and M 87 to the innermost region of the AGN [M$^+$08a, A$^+$09e], though similar observations of the blazar OJ 287 suggest an emission region located > 14 pc away from the central supermassive black hole [A$^+$11j]. Blazars show non-thermal continuum emission ranging from radio to VHE gamma-rays, covering an energy range of 20 orders of magnitude. The spectral energy distribution[31] of this emission typically shows a two hump structure with one hump ranging from radio to X-rays and the second one peaking in the GeV to TeV range. According to the overall shape of the SED, blazars are phenomenologically classified into flat spectrum radio quasars[32], low-frequency peaked

[28] For comparison: The diameter and height of the galactic plane of the Milky Way measure about 100,000 light years and 16,000 light years, respectively [B$^+$06b].
[29] **Q**uasi **S**tellar **O**bject, QSO
[30] **V**ery **L**ong **B**aseline **I**nterferrometry, VLBI
[31] **S**pectral **E**nergy **D**istribution, SED
[32] **F**lat **S**pectrum **R**adio **Q**uasar, FSRQ

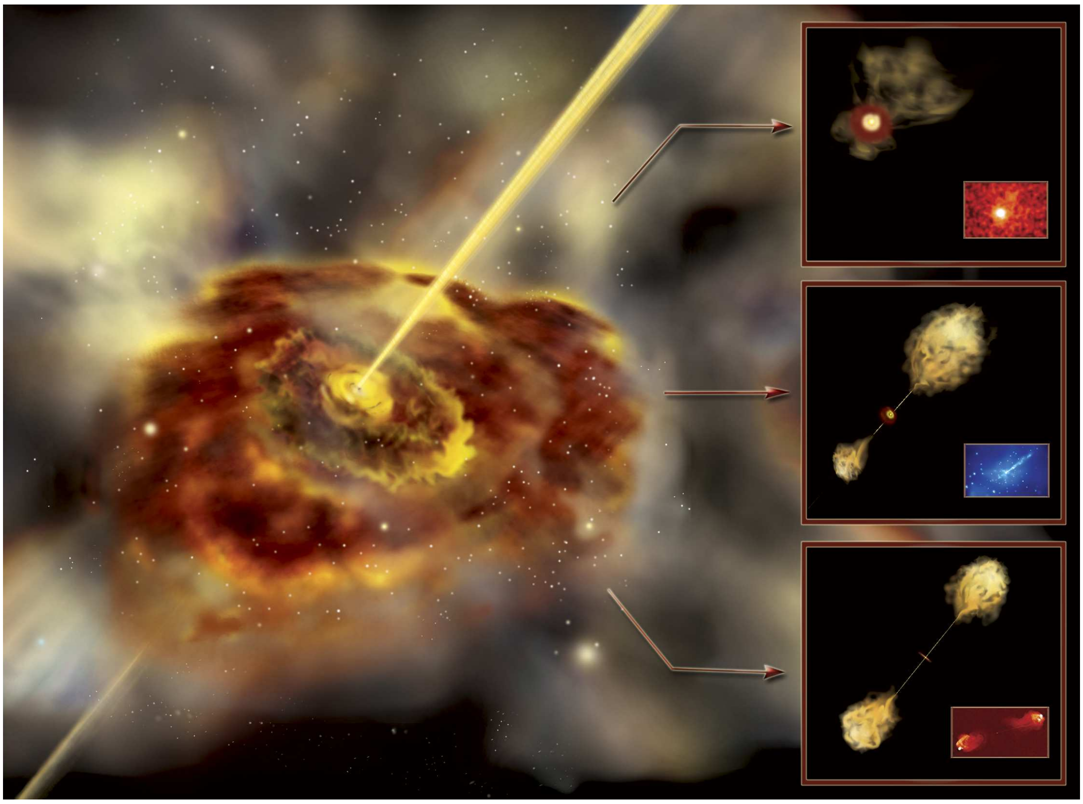

Figure 2.9: *Left:* An artist's impression of the morphology of AGN, showing torus, accretion disk and two jets. *Right bottom:* A schematic sketch perpendicular to the jet axis is depicted. In the inlay an accordant radio observation, in which the jets and the so-called radio-lobes at their ends are clearly seen. *Right middle:* A sketch of the AGN observed under an acute angle. The inlay shows an accordant optical observation with an extremely bright core and the jet pointing past the observer. Note that the host galaxy is not visible. *Right top:* A sketch of an observation along the jet axis. The accordant observation in the inlay is made in X-rays or gamma-rays. [ESS07].

BL Lac objects[33] and high-frequency peaked BL Lac objects[34]. The first ones show strong optical emission lines, whereas the class of BL Lac objects exhibits none or only very weak optical line emission. Furthermore a trend is observed that the higher the peak frequency of the lower energetic hump in the SED, ν_{peak}, the lower the overall luminosity, with $\nu_{\text{peak}}^{\text{FSRQs}} \leq \nu_{\text{peak}}^{\text{LBLs}} \leq \nu_{\text{peak}}^{\text{HBLs}}$. This is called the *blazar sequence* [F+98]. The emission of blazars is typically highly variable in all wavebands. This may be caused e.g. by the inhomogeneous medium that the jets are passing through [B+10a], the inhomogeneity of the accreted material, or even by changes in the direction of matter movement along the jets. The latter would lead to strong flux variations caused by differential Doppler-boosting [Rie05b]. The strongest flux variations as well as the shortest variability time

[33] **L**ow-frequency peaked **B**L **L**ac object, LBL
[34] **H**igh-frequency peaked **B**L **L**ac object, HBL

scales are observed at the highest energies with timescales for flux doubling ranging down to minutes as observed for Mkn 501 with MAGIC[35] [A+07f] and for PKS 2155-304 with H.E.S.S.[36] [A+07c]. Albeit, the variability timescales in other wavelength may last up to years [S+88] or even longer [Hud11, HB08].

2.4.2 Emission Models

The continuous emission spectra of blazars are subject of recent debates, just as the nature of the underlying acceleration mechanism. Although theoretical models, generally can explain quite well the shape of the observed blazar SEDs, the question whether leptons or protons are causing the electromagnetic emission in blazars is far from being settled.
In leptonic models, the low energy hump of the SEDs is caused by synchrotron radiation (see section 2.3.1) of a population of highly relativistic electrons. The same electron population may interact afterwards either with those synchrotron photons (Synchrotron Self Compton[37], see also subsection 2.3.1) [BK79, TMG98a] or an external photon field (External Compton[38]) [DS93] via inverse Compton scattering (see section 2.3.1), accounting for the high energy emission. These models describe most of the observed data very well (c.f. Figure 2.10 and see [A+11e, A+11g, Z+11]) and can reasonably explain even the shortest variability timescales. But for the Flat Spectrum Radio Quasar 3C 279 it has recently been shown that single zone leptonic models, even under the assumption of external photon fields, are not suited to explain the SED [BRM09].
Hadronic emission models are generally more complicated as they also feature leptonic emission processes for secondary leptons, which in this scenario are also dominantly contributing to the low energy hump via synchrotron emission. The high energy bump, in turn, is caused by either proton synchrotron emission (Proton Synchrotron Blazar [MP01], Synchrotron Mirror Model [Boe05]), or by the decay of neutral pions, stemming from interactions of protons with internal or external photons fields or among themselves [Man93] (see also Figure 2.7 and subsection 2.3.2). These scenarios are not only able to explain the SED shapes reasonably well, but are also capable of naturally explaining "orphan flares". These are enhancements of the high energy flux that are not accompanied by a simultaneous enhancement in the low energy emission and have been observed for the blazars 1ES 1959+650 [K+04b] in 2002, Mkn 421 [B+05b] in 2004, and recently also for Mkn 501 [NST11]. In leptonic models, these observations can only be explained by using extreme source parameters [L+09b] or several emission zones [KT06], as in general a correlated behavior of the low and high energy emission is expected. Anyway, both of those loopholes are theoretically disfavored as the former one requires fine-tuning of parameters and the latter one effectively doubles the number of free parameters in the model.
Another feature of hadronic emission models is the prediction of high energy neutrino emission [Man95, HH05, RBP05, D+11a]. Hence, the detection of either neutrinos from a blazar or a SED only being explained by hadronic models, would be smoking guns for the source of cosmic rays.

[35] **M**ajor **A**tmospheric **G**amma **I**maging **C**herenkov telescopes, MAGIC, see subsection 4.3.1 and `http://magic.mppmu.mpg.de`
[36] **H**igh **E**nergy **S**tereoscopic **S**ystem, H.E.S.S., see `http://www.mpi-hd.mpg.de/hfm/HESS`
[37] **S**ynchrotron **S**elf **C**ompton, SSC
[38] **E**xternal **C**ompton, EC

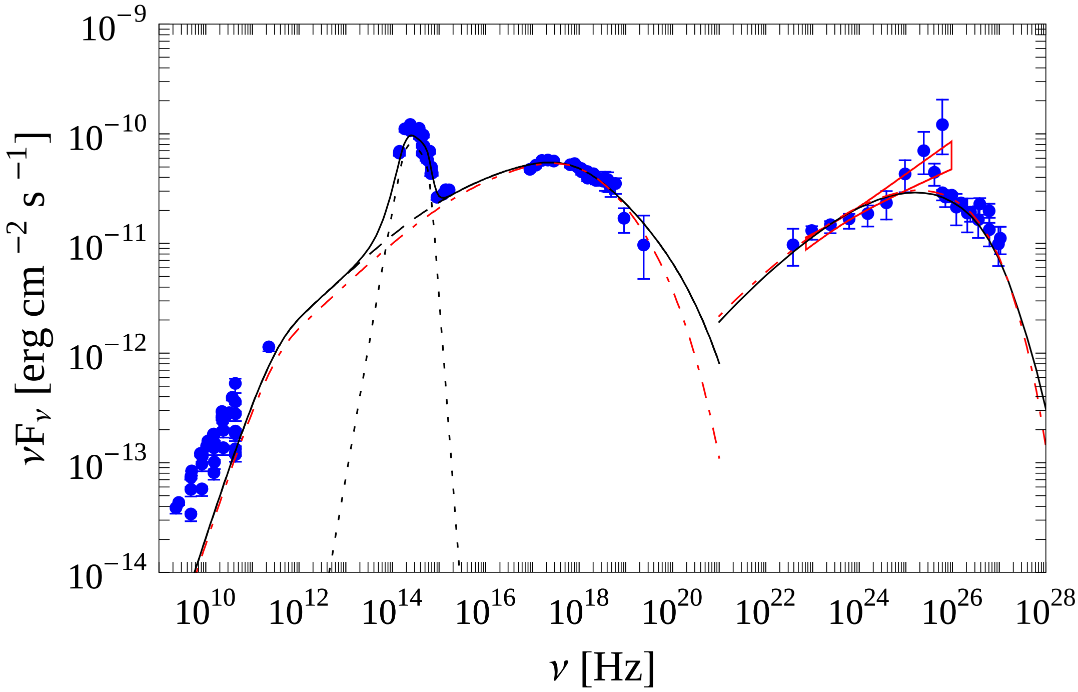

Figure 2.10: The spectral energy distribution of Mkn 501 with unsurpassed spectral coverage as measured during an extensive multi-wavelength campaign between March 15 2009 and August 1 2009 (blue points). Additionally, two SSC models with variability timescales of 4 days (black curve) and 0.35 days (red dashed curve) are shown, which explain the data extremely well. For further details see [A+11f].

2.4.3 Binary Black Holes in AGN

Uninfluenced by the question for the predominant acceleration mechanisms, also the question of the central engine of AGN is under debate. In the recent bottom-up scenarios of galaxy formation, the big elliptical galaxies, which host most of the luminous, radio-loud AGN, are built up by the merging of smaller spirals (see [Sch06b]). This was also supported by computer simulations [M+07]. Additionally, it is believed that every galaxy hosts a supermassive black hole, as mentioned before. By this, it is a natural expectation that especially the big elliptical galaxies contain more than one central black hole. This, in turn, leads directly to a model of binary black holes[39] [BBR80], as it was shown that systems of more than one black hole are unstable except for binary systems [SVA74]. One might add that recent findings suggest that for a fraction of moderate-luminosity X-ray selected AGN up to a redshift of $z = 2.2$, processes such as disk instabilities or tidal disruptions play a larger role in AGN fuelling than merging. Although for high-luminosity AGN (as focused on here) major mergers seem to be the main fueling mechanism [A+11m].
Although widely separated binary black hole systems [K+03, H+06, F+11a] and recently also relatively narrow ones [R+09c, BL09, LB09, TDDH11, EBHL11] have been observed,

[39] **B**inary **B**lack **H**ole, BBH

it is still quite ambiguous whether BBHs enter the separation where gravitational wave emission becomes important and finally coalesce within a Hubble time. On the other hand, the activity of AGN seems to be intimately connected to galaxy merging [R+11b, E+11] and there are even models connecting the activity state of AGN (like Seyfert or quasar type activity) to the separation of the internal BBH system [Lob06], giving rise to the assumption that especially in blazars, the separation of eventual binary systems is so small that one will not be able to resolve them in the near future. Although, their detection is not quite impossible, but indirect. Due to the interaction of the secondary BH with either the accretion disc or the jet via tidal forces, a quasi periodic behavior should be observed in the emission of the sources, e.g. [Rie08]. In fact, there are several observational evidences of such behavior (for an overview, see [Kom06]): Helical trajectories along the jets, as they have been observed in high-resolution radio images, could be explained as orbital modulation in the framework of BBHs, leading to quasi periodic variability as calculated in [Rie07] and observed for the blazar 3C 279 [L+09c]. In Figure 2.11 a sketch of such a trajectory on top of an artist's impression of a helical jet is depicted. The best studied object, probably harboring a BBH, is OJ 287, where optical outbursts with a periodicity of 12 years are observed [S+88] and even the period shortening due to gravitational wave emission is tested [V+08]. A similar periodicity of 10 years has recently been found in optical data of Mrk 501 [Y+08b]. This is especially interesting in the context of BBHs as based on an observed periodicity of 23 days in gamma-rays by the Telescope Array [H+98] and HEGRA [Kra99, K+01], the BBH interpretation of the source [RM00, RM01] predicted an optical periodicity of 6-14 years. Analyses of not only HEGRA and Telescope Array gamma-ray data but also RXTE–ASM X-ray data fortified the findings of a 23 day periodicity [Oso06]. Recent studies confirm these results on MAGIC, VERITAS and Whipple gamma-ray and SWIFT and RXTE X-ray data, additionally claiming 36 and 72 day periods in the RXTE lightcurve [R+09b]. Furthermore, periodicities in the optical and X-ray emission of several other, partially also gamma-ray emitting blazars (like PKS 2155-304) have been reported, e.g. [L+09a, Fan00]. Nevertheless, it should be noted that there are also other explanations for this short-term periodicity, as e.g. instabilities in the accretion disk [F+08a] and that for a redshift $z < 1$ simulations expect only 5–10 BBH systems with sub-parsec scale separation [VMD09].

Another interesting aspect of such BBH systems is that those would be possible sources of gravitational waves as predicted from general relativity. Such gravitational waves would be detectable with the planed space interferometer LISA[40] [D+03]. But in order to reach the sensitivity needed and due to the low signal to noise ratio it will be necessary to simulate signal templates in advance [McK06], which is in general possible [B+06a] but needs to make assumptions about the masses and distances of the BBH systems. These in turn could be inferred from observations of periodic electromagnetic signals.

Altogether, two conclusions arise from the presented scenario:

Monitoring of Blazars with a variety of instruments operating over the whole electromagnetic spectrum, so called multi-wavelength[41] observations, are mandatory to shed light on the internal structure and emission processes of AGN and maybe even solve the question regarding the origin of cosmic rays. In chapter 3 the variety of instruments used in the framework of this thesis will be introduced and in section 7.3 the results of this synopsis

[40]**L**aser **I**nterferometer **S**pace **A**ntenna, LISA

[41]**M**ulti-**W**ave**l**ength, MWL

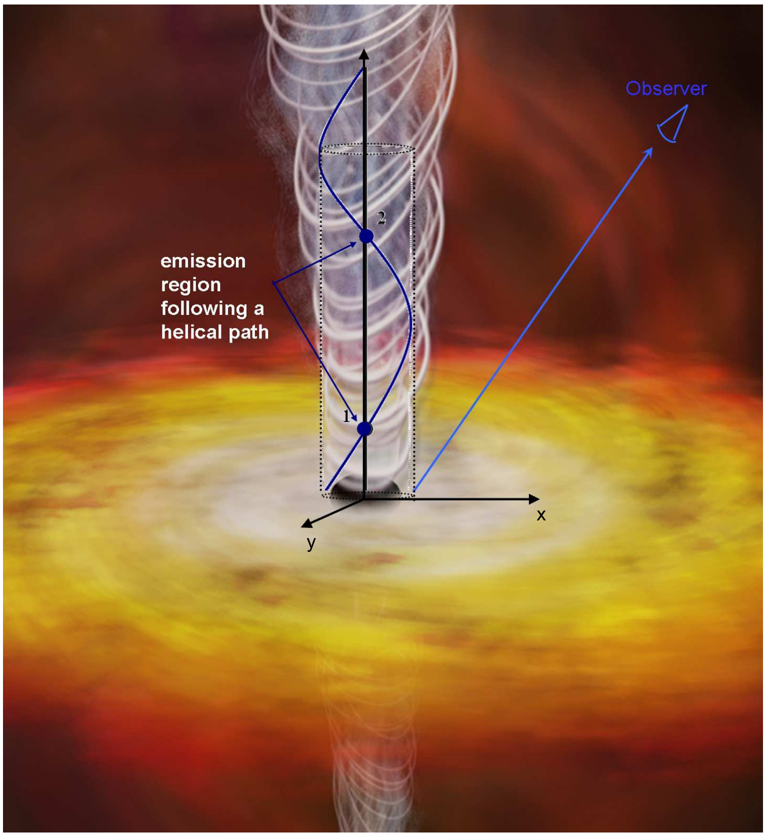

Figure 2.11: Sketch of the helical motion of the jet in an AGN caused by a binary black hole system [RM01], underlaid with an artist's impression [NCW07].

will be presented.

Gamma-ray observations of the duration of weeks are much better suited to find periodic behavior of the sources than optical observations for decades. Therefore, gamma-ray monitoring observations are required on a long-term basis. In section 6.1 the results of such observations with the MAGIC telescope will be presented, in chapter 5 a new Cherenkov telescope dedicated to monitoring observations of blazars will be introduced, which has partly been built up in the course of this thesis, and in chapter 8 a global network of Cherenkov telescopes which is being set up will be presented.

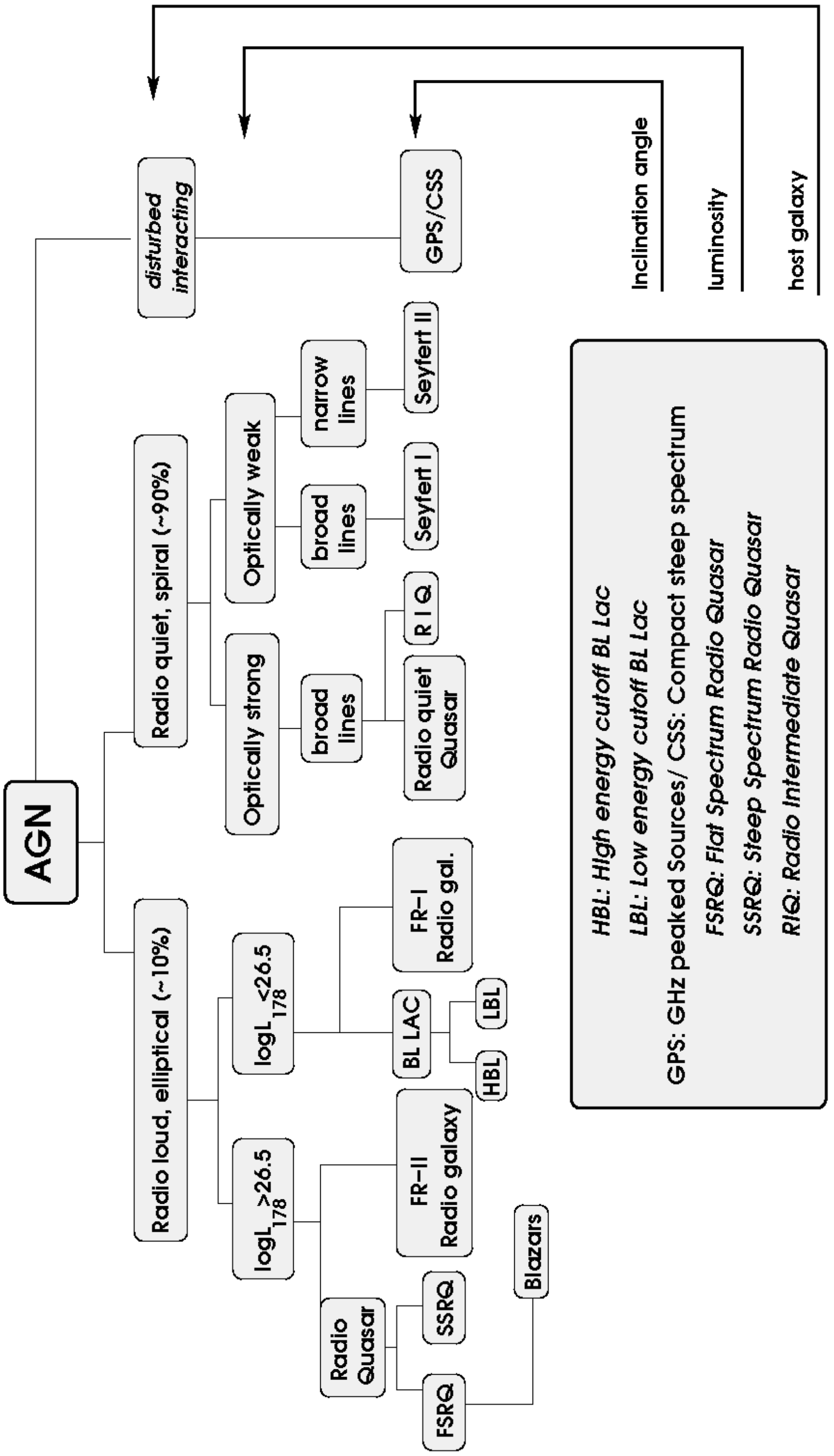

Figure 2.12: AGN classification diagram: Classification is based on 1. the radio luminosity (mainly corresponding to the type of the host galaxy), 2. the optical luminosity and 3. the inclination angle [Bec08], after [Gro06].

Chapter 3
Instruments for Multi-Wavelength Astronomy

It has been shown in chapter 2 that AGN are possible sources of the highest energetic cosmic rays as well as of gravitational waves. In either context, but especially in shedding light on the particle acceleration and radiation production mechanism the great importance of multi-wavelength observations has been stressed. In this chapter, a brief overview of the various instruments used in this study is presented. Introducing forty instruments, this overview is strictly limited in its level of detail, suitably for more information the reader is referred to the instruments' official websites and references given in the text. As the main work within this thesis deals with very high energy gamma-ray astronomy, Cherenkov telescopes, used to detect these highest energetic photons, are described in more detail in the subsequent chapter 4.
The instruments are presented in rising order of the frequency/energy range they operate in. An illustrative overview is given in Figure 3.1.

3.1 Radio and Microwave

3.1.1 Single-Dish Instruments

GBT 91 m The 91 m Green Bank Telescope[1] was a 300 ft (∼91 m) radio telescope at the Green Bank Observatory before it collapsed on November 15, 1988. Conducting the Northern Sky Survey, source catalogs at 4.85 GHz (6 cm) [BWE91] and 1.4 GHz (20 cm) [WB92, WB95] have been composed.

UMRAO The 26 m radio telescope of the University of Michigan Radio Astronomy Observatory[2] [Mur00] has build-in receivers for observations of the frequencies of 4.8, 8.0, and 14.5 GHz. It can operate in a completely automated way, not requiring personal attendance at the telescope and then reaches around 90% efficiency in observation time.

[1] 91 m **G**reen **B**ank **T**elescope, GBT 91 m, see http://www.gb.nrao.edu/fgdocs/300ft/300ft.html
[2] **U**niversity of **M**ichigan **R**adio **A**stronomy **O**bservatory, UMRAO, see http://www.astro.lsa.umich.edu/obs/radiotel

Most of this time is dedicated to monitoring the total flux and linear polarization from 200 AGN [A+03b].

Effelsberg 100 m The Effelsberg 100 m Radio Telescope[3] is used in the F-GAMMA program[4] [F+07, A+08j] for AGN monitoring and observes at the wavelengths of 110, 60, 36, 28, 20, 13, 9, and 7 mm.

RATAN–600 The RATAN–600 radio telescope[5] [KP79] is a stationary radio telescope with a diameter of 576 m, operating in the frequency range of 610 MHz–30 GHz (1–50 cm) with an angular resolution of 2 arcsec. Since 1997, there has been a radio broad band monitoring campaign on 550 AGN [K+99b, K+02].

OVRO Since 2007 the 40 m radio telescope at the Owens Valley Radio Observatory[6] conducts a monitoring campaign of about 1500 AGN at 15 GHz (20 mm) [R+11d].

Metsähovi At the Metsähovi Radio Observatory[7] the 14 m radio telescope is used to monitor blazars at the frequency of 37 GHz [N+07a].

IRAM The IRAM[8] 30 m telescope participates in the F-GAMMA program, monitoring AGN at the wavelengths of 3, 2, 1, and 0.9 mm.

3.1.2 Interferometers

By using several spaced apart telescopes to observe the same source, the angular resolution can vastly be improved as outlined in e.g. [Bra03].

WSRT The Westerbork Synthesis Radio Telescope[9] is a interferometric system of 14 telescopes of 25 m diameter each, arranged on a linear 2.7 km baseline, which performed the Westerbork Northern Sky Survey[10] [R+97] at 92 cm wavelength.

UTRAO The University of Texas Radio Astronomy Observatory[11] was a five element interferometer operating at 335, 365, and 380 MHz, conducted the 365 MHz Texas survey from 1974–1983 [D+96].

[3] see http://www.mpifr.de/radioteleskop
[4] **F**ermi-**G**ST **AGN** **M**ulti-frequency **M**onitoring **A**lliance, F-GAMMA, see http://www.mpifr-bonn.mpg.de/div/vlbi/fgamma
[5] RATAN, *rus.:* Academy of Science Radio Telescope, see http://www.sao.ru/ratan
[6] **O**wens **V**alley **R**adio **O**bservatory, OVRO, see http://www.astro.caltech.edu/ovroblazars
[7] see http://www.metsahovi.fi
[8] **I**nstitut de **Ra**dioastronomie **M**illimétrique, IRAM, see http://iram-institute.org/EN/content-page-55-7-55-0-0-0.html
[9] **W**esterbork **S**ynthesis **R**adio **T**elescope, WSRT, see http://www.astron.nl/radio-observatory/astronomers/wsrt-astronomers
[10] **We**sterbork **N**orthern **S**ky **S**urvey, WENSS
[11] **U**niversity of **T**exas **R**adio **A**stronomy **O**bservatory, UTRAO

VLA The Very Large Array[12] [T+80, NTE83] is an array of 27 telescopes with diameters of 25 m, each in a Y-shaped arrangement. The exact form of the array can be altered to give priority either to sensitivity or to angular resolution. The observed frequency bands rage from 1.34–1.73, 4.5–5.0, 14.4–15.4, and 22–24 GHz.

VLBA The Very Long Baseline Array[13] [N+94] is an interferometric radio telescope system made of ten radio telescopes situated in the USA. Each single telescope has a diameter of 25 m and together they span a maximum baseline of 8,000 km from Hawaii to the U.S. Virgin Islands. With the superb angular resolution it is mainly used to resolve the inner structure of AGN close to the core. The MOJAVE[14] program [L+09e], succeeding the VLBA 2 cm survey[15] is monitoring the brightest northern AGN at 15 GHz (2 cm) since 1994.

3.1.3 Satellites

Planck The Planck satellite[16] [A+11i] uses the LFI[17] [M+11] and the HFI[18] [A+11h] to measure the anisotropy of the cosmic microwave background. Anyway these instruments can also be used to study foreground sources. The LFI operates at 30, 44, and 70 GHz, whereas the HFI measures at frequencies of 100, 143, 217, 353, 545, and 857 GHz.

3.2 Infrared

Spitzer–IRS The InfraRed Spectrograph[19] [H+04b] aboard the Spitzer Space Telescope[20] [W+04] is an infrared spectrometer with four sub-detectors, operating in the wavelength ranges of 5,200–14,500 nm (Short-Low Module), 9,900–19,600 nm (Short-High Module), 14,000–38,000 nm (Long-Low Module), and 18,700–37,200 nm (Long-High Module). The Spitzer Space Telescope started its operation in August 2003.

2MASS Strictly speaking, 2MASS is not an instrument, but the 2 Micron All Sky Survey[21] [S+06]. It has been performed in the near-infrared J- (1,250 nm), H- (1,650 nm), and K_S-band (2,160 nm) with two automated 1.3 m telescopes at the Fred Lawrence Whipple Observatory, Arizona (USA), and the Cerro Tololo Inter-American Observatory, Chile, between 1997 and 2001.

---

[12] **V**ery **L**arge **A**rray, VLA, see http://www.vla.nrao.edu
[13] **V**ery **L**ong **B**aseline **A**rray, VLBA, see http://www.vlba.nrao.edu
[14] **M**onitoring **O**f **J**ets in **A**ctive galactic nuclei with **V**LBA **E**xperiments, Mojave, see http://www.physics.purdue.edu/astro/MOJAVE
[15] see http://www.cv.nrao.edu/2cmsurvey
[16] see http://www.esa.int/SPECIALS/Planck
[17] **L**ow **F**requency **I**nstrument, LFI
[18] **H**igh **F**requency **I**nstrument, HFI
[19] **I**nfra**R**ed **S**pectrograph, IRS, see http://irsa.ipac.caltech.edu/data/SPITZER/docs/irs
[20] **S**pitzer **S**pace **T**elescope, SST, “Spitzer” in honor of Lyman Spitzer, Jr., see http://www.spitzer.caltech.edu
[21] 2 **M**icron **A**ll **S**ky **S**urvey, 2MASS, see http://www.ipac.caltech.edu/2mass

NOT The 2.5 m Nordic Optical Telescope[22] on the Canary Island of La Palma, equipped with the NOTCam[23] is capable of conducting near infrared observations in the J-, H-, and K_S-band centered at 1,250 nm, 1,626 nm, and 2,140 nm, respectively.

3.3 Optical

3.3.1 Satellite-Born

Hubble–WFPC2 The Wide Field Planetary Camera 2[24] [H+95b, H+95a] aboard the Hubble Space Telescope[25] has been in operation from December 1993 until May 2009 and had build-in optics to correct for the spherical aberration caused by the primary mirror. It could be operated with several optical filters[26] in the wavelength range of 115–1,100 nm. The used F702W filter (595–820 nm) is similar to the Cousins R-band.

INTEGRAL–OMC The Optical Monitoring Camera[27] [M+03] aboard the INTEGRAL satellite[28] [W+03, J+03] observes with a Johnson V-filter centered at 550 nm.

3.3.2 Ground-Based

KVA Within the Tuorla blazar monitoring program several blazar are monitored in the optical R-band (centered at 650 nm) with the 1.03 m telescope at the Tuorla Observatory and the robotic 0.35 m telescope KVA on La Palma[29].

Goddard Robotic Telescope The Goddard Robotic Telescope[30] [S+09a] is a 14” optical telescope at the Goddard Geophysical and Astronomical Observatory which is used for the follow-up of Swift and Fermi GRBs as well as observations of Fermi–LAT AGN.

New Mexico Skies New Mexico Skies[31] is a privately operated observatory offering several optical telescopes in six domes located at 2,225 m a.s.l. within the Lincoln National Forest.

Tenagra-II The automated 0.81 m Tenagra-II telescope[32] is operated privately in South Arizona and is offering observation time to academic institutions.

---

[22] **N**ordic **O**ptical **T**elescope, NOT, see http://www.not.iac.es
[23] see http://www.not.iac.es/instruments/notcam
[24] **W**ide **F**ield **P**lanetary **C**amera **2**, WFPC2, see http://www.stsci.edu/hst/wfpc2
[25] **H**ubble **S**pace **T**elescope, HST, see http://www.nasa.gov/mission_pages/hubble
[26] see http://www.stsci.edu/hst/wfpc2/documents/filters.pdf
[27] **O**ptical **M**onitoring **C**amera, OMC, see http://sci.esa.int/science-e/www/object/index.cfm?fobjectid=31175&fbodylongid=722
[28] **Inte**rnational **G**amma-**Ra**y **A**strophysics **L**aboratory, INTEGRAL, see http://sci.esa.int/science-e/www/area/index.cfm?fareaid=21
[29] see http://users.utu.fi/~kani/1m
[30] **G**oddard **R**obotic **T**elescope, GRT
[31] **N**ew **M**exico **S**kies, NMS, see http://www.newmexicoskies.com
[32] see http://tenagraobservatories.com

Perugia Automatic Imaging Telescope The Perugia Automatic Imaging Telescope[33] is a 0.4 m robotic telescope that has been used since 1994 for optical variability monitoring of blazars.

Palomar60 The 60-inch (1.5 m) telescope at the Palomar Observatory[34] [C+06] is mainly used for photometric follow-up observations of Super Novae but also observed AGN in g-band (centered at 524 nm).

3.4 Ultraviolet

Swift–UVOT The Ultraviolet/Optical Telescope[35] aboard the Swift satellite[36] [G+04a] operates in the 160–800 nm range. For a technical description see [R+05b], for information about the band passes and photometric calibration see [P+08].

GALEX The Galaxy Evolution Explorer[37] [M+05] started its operation in 2003 and was the first instrument to conduct e.g. an extragalactic ultraviolet all-sky survey. It measures in two bands, near ultraviolet[38] and far ultraviolet[39], being centered at 227.1 nm and 152.8 nm, respectively.

3.5 X-Rays

Recently, cross-calibration measurements have been conducted with Chandra–ACIS, Suzaku–XIS, Swift–XRT, and XMM-Newton–EPIC (MOS and pn) for the soft-band (2–8 keV), and Suzaku–HXD-PIN, RXTE–PCA, and INTEGRAL–IBIS-ISGRI, and for the hard-band (15–50 keV). These revealed differences as large as 20% and 9% for the soft-band flux and power-law index, respectively, and 46% for the hard-band flux [T+11].

Swift–XRT The X-Ray Telescope[40] aboard the Swift satellite[41] [G+04a] observes in the energy range of 0.2–10 keV with an energy resolution of 140 eV at 5.9 keV. Details can be found in [B+05d].

XMM-Newton–EPIC (MOS) The European Photon Imaging Camera[42] [V+96] aboard the XMM-Newton satellite[43] [J+01] is comprised by three cameras of which one is made

[33] **A**utomatic **I**maging **T**elescope, AIT, see http://astro.fisica.unipg.it/osserv.htm
[34] see http://www.astro.caltech.edu/palomar/60inch.html
[35] **U**ltra**v**iolet/**O**ptical **T**elescope, UVOT
[36] see http://swift.gsfc.nasa.gov
[37] **Gal**axy **E**volution **Ex**plorer, GALEX, see http://www.galex.caltech.edu
[38] **N**ear **U**ltra**v**iolet, NUV
[39] **F**ar **U**ltra**v**iolet, FUV
[40] **X**-**R**ay **T**elescope, XRT, see http://swift.gsfc.nasa.gov/docs/swift/about_swift/xrt_desc.html
[41] see http://swift.gsfc.nasa.gov/docs/swift/swiftsc.html
[42] **E**uropean **P**hoton **I**maging **C**amera, EPIC, see http://xmm.esac.esa.int/external/xmm_user_support/documentation/technical/EPIC
[43] **X**-ray **M**ulti-Mirror **M**ission-**Newton**, XMM-Newton, see http://xmm.esac.esa.int

of pn-CCDs[44] [S+01] and two are made of metal oxide semi-conductor[45]-CCDs [T+01]. It has been operating since December 1999 in the energy range of 0.15–15 keV.

***Beppo*SAX** The *Beppo*SAX[46] [Sca93] X-ray satellite was in operation from April 1996 until April 2002. It was equipped with three narrow field instruments for different energy ranges: LECS[47] [P+97] (0.1–10 keV), MECS[48] [B+97] (1.3–10 keV), and PDS[49] [F+97] (13–300 keV), allowing spectral studies over more than three decades in energy.

RXTE–ASM The All-Sky Monitor[50] [L+96] aboard the Rossi X-ray Timing Explorer[51] has been monitoring the whole sky in the energy range of 2–10 keV since December 1995.

INTEGRAL–JEM-X The Joint European X-Ray Monitor[52] [B+04e] aboard the INTEGRAL satellite provides images in the 3–35 keV energy band with a spectral resolution of 1.3 keV at 10 keV.

RXTE–PCA The Proportional Counter Array[53] [J+06] aboard the Rossi X-ray Timing Explorer has been in operation since December 1995 in the energy range of 2–60 keV with an energy resolution $< 18\%$ at 6 keV.

Swift–BAT The Burst Alert Telescope[54] [B+05a] aboard the Swift satellite[55] [G+04a] is mainly used for the immediate detection of GRBs in the energy range of 15–150 keV but with long time integration it is also capable of determining the spectral properties of faint sources in the hard X-rays[56].

RXTE–HEXTE The High Energy X-ray Timing Experiment[57] [R+98] aboard the Rossi X-ray Timing Explorer has been in operation since December 1995 in the energy range of 15–250 keV with an energy resolution 15% at 60 keV.

---

[44] **C**harge **C**oupled **D**evice, CCD
[45] **M**etal **O**xide **S**emi-conductor, MOS
[46] **S**atellite per **A**stronomia **X**, *ital.:* X-Ray Astronomy Satellite, SAX, "Beppo" in honor of Giuseppe "Beppo" Occhialini, see http://www.asdc.asi.it/bepposax
[47] **L**ow **E**nergy **C**oncentrator **S**pectrometer, LECS
[48] **M**edium **E**nergy **C**oncentrator **S**pectrometer, MECS
[49] **P**hoswich **D**etector **S**ystem, PDS
[50] **A**ll-**S**ky **M**onitor, ASM, see http://xte.mit.edu
[51] **R**ossi **X**-ray **T**iming **E**xplorer, RXTE, "Rossi" in honor of Bruno B. Rossi, see http://heasarc.gsfc.nasa.gov/docs/xte
[52] **J**oint **E**uropean X-Ray **M**onitor, JEM-X, see http://sci.esa.int/science-e/www/object/index.cfm?fobjectid=31175&fbodylongid=721
[53] **P**roportional **C**ounter **A**rray, PCA, see http://heasarc.gsfc.nasa.gov/docs/xte/PCA.html
[54] **B**urst **A**lert **T**elescope, BAT, see http://swift.gsfc.nasa.gov/docs/swift/about_swift/bat_desc.html
[55] see http://swift.gsfc.nasa.gov/docs/swift/swiftsc.html
[56] see e.g. http://heasarc.gsfc.nasa.gov/docs/swift/results/bs58mon
[57] **H**igh **E**nergy **X**-ray **T**iming **E**xperiment, HEXTE, see http://heasarc.gsfc.nasa.gov/docs/xte/HEXTE.html

3.6 Gamma-Rays

As shown in Figure 2.8 gamma-rays are absorbed high up in the Earth's atmosphere. Thus, observations only become possible by the use of satellite-borne experiments. This in turns leads to the main limitation of these instruments, as the limited size and payload of the rockets and satellites restricts the (effective) detector area, resulting in an intrinsic upper bound to the energy range of about 100 GeV for the strongest sources, c.f. Figure 2.10. For the detection of even higher energetic gamma-rays, Cherenkov telescopes can be utilized, which is describe in chapter 4.

INTEGRAL–IBIS-ISGRI The INTEGRAL Soft Gamma-Ray Imager[58] [L+03] aboard the INTEGRAL satellite is the top layer of the Imager on-Board the INTEGRAL Satellite[59]. This in turn is an imaging gamma-ray telescope utilizing the coded-mask technique. It is comprised by 16384 pixels made of CdTe and operates in the energy range from 15 keV to 10 MeV with a spectral resolution of 8–10% in the energy range from 100 keV to 1 MeV.

CGRO–COMPTEL The Imaging Compton Telescope[60] [S+93b] aboard the Compton Gamma-Ray Observatory[61] has been in scientific orbit from April 1991 until June 2000. It operated in the energy range of 0.8–30 MeV with an energy resolution better than 8.8%. Though the COMPTEL source catalogue was published a decade ago [S+00], recent publications on limits to the MeV photon flux of Active Galactic Nuclei [S+08b] and on the reanalysis of the original COMPTEL data [Z+10] may have strong scientific impact, especially as the MeV energy range is still widely unexplored.

AGILE–GRID The GRID[62] [P+03a] aboard the AGILE satellite[63] [T+08b] has been in scientific operation since April 2007. Based on a silicon tracker, its energy range is 30 Mev–50 GeV.

Fermi–LAT The Large Area Telescope[64] [A+09k] aboard the Fermi Gamma-ray Space Telescope[65] is gamma-ray detector based on pair conversion. It operates in the energy range of 20 MeV–300 GeV though the upper end of the energy range is mostly limited by the number of detected photons. Scientific operation started in August 2008.
Recent theoretical modeling of the emission of the Crab Nebula suggest slight differences in the energy scale of the ground based Cherenkov telescopes and the test-beam calibrated Fermi–LAT of 3% for MAGIC and 4.2% for the Hegra CT system [MHZ10].

[58] **I**NTEGRAL **S**oft **G**amma-**R**ay **I**mager, ISGRI, see http://sci.esa.int/science-e/www/object/index.cfm?fobjectid=31175&fbodylongid=720
[59] **I**mager on-**B**oard the **I**NTEGRAL **S**atellite, IBIS, see http://projects.iasf-roma.inaf.it/ibis
[60] Imaging **Compt**on **Tel**escope, COMPTEL, see http://heasarc.gsfc.nasa.gov/docs/cgro/cgro/comptel.html
[61] **C**ompton **G**amma-**R**ay **O**bservatory, CGRO, see http://heasarc.gsfc.nasa.gov/docs/cgro
[62] **G**amma-**R**ay **I**maging **D**etector, GRID
[63] **A**strorivelatore **G**amma a **I**mmagini **Le**ggero, *ital.:* Light Imager for Gamma-ray Astrophysics, AGILE, see http://agile.rm.iasf.cnr.it
[64] **L**arge **A**rea **T**elescope, LAT, "Fermi" in honor of Enrico Fermi, see http://www-glast.stanford.edu
[65] **F**ermi **G**amma-ray **S**pace **T**elescope, FGST or Fermi, see http://fermi.gsfc.nasa.gov

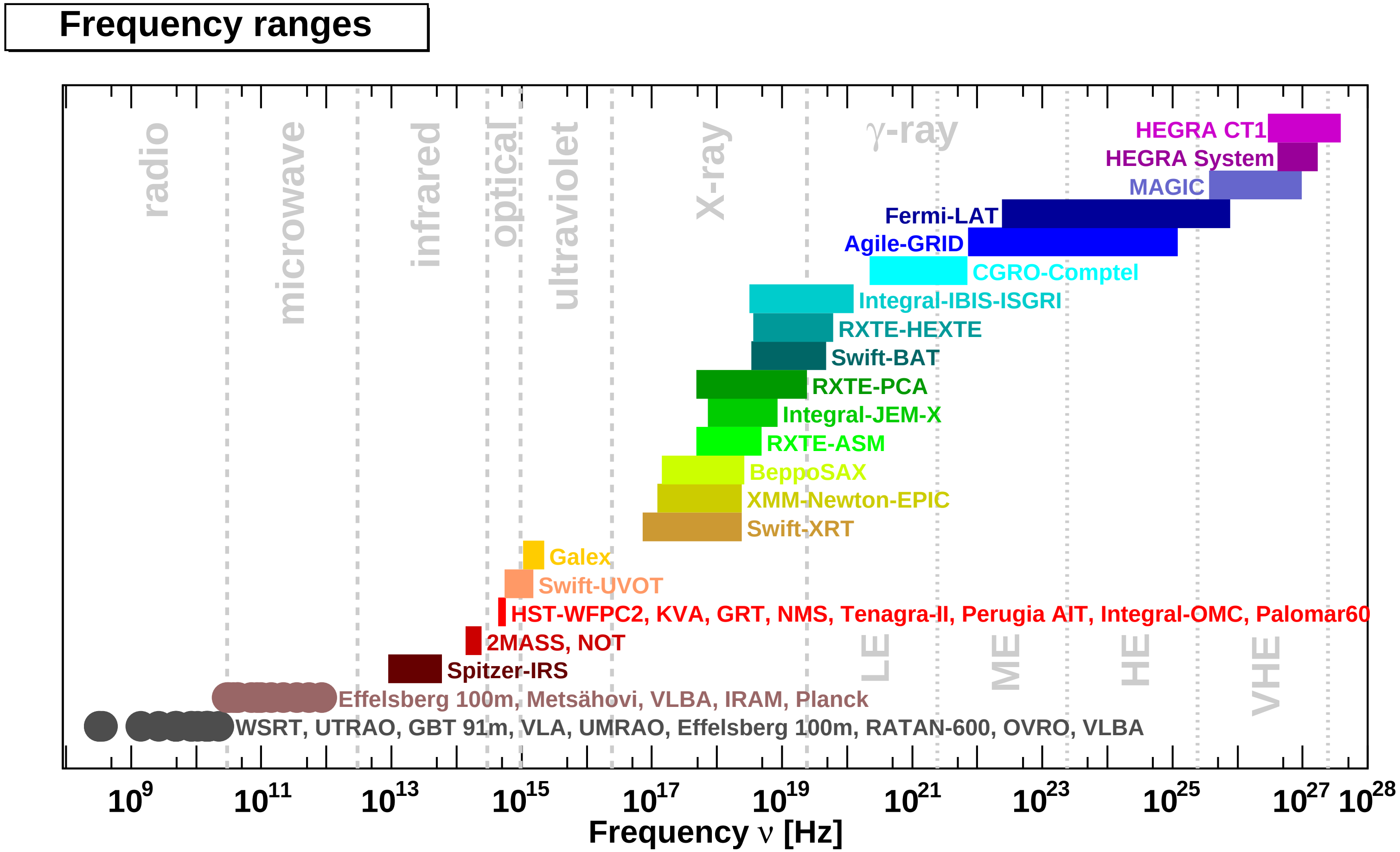

Figure 3.1: Frequency ranges of the different instruments used in this study.

Chapter 4
Cherenkov Telescopes

As mentioned in section 2.3, the detection of the VHE gamma-rays is not possible by satellites, but conducted with imaging atmospheric Cherenkov telescopes[1]. A comprehensive overview on the detection technique of IACTs is given in [Wee03, Boj02] and the technique as well as recent results are reviewed in [HH09, A^+08f, Hin09, CLN08]. Accordingly, only a short introduction is presented in section 4.1. After that, an overview of the latest generation Cherenkov telescopes is given in section 4.3 before in subsection 4.2.1 to subsection 4.3.1 short introductions to the IACTs used within this thesis are given. A detailed overview of the performance characteristics of those IACTs is given in Table 4.2. Lastly, in section 4.4 the problem of distinguishing gamma-ray induced signals from the huge hadronic background is outlined and the algorithms developed in the context of this thesis are introduced.

4.1 Imaging Atmospheric Cherenkov Technique

The main constraints of satellite-born experiments are the very restricted possible payload and instrument size. These intrinsically limit their effective area and thus their sensitivity at very high energies as the detectable photon flux is rapidly decreasing with energy, c.f. Figure 2.10. To overcome this, Cherenkov telescopes are utilized which make use of the atmosphere as part of the detector and thus allow for huge detector volumes.
High energetic photons impinging on the Earth's atmosphere induce so-called electromagnetic air-showers via (leptonic) pair production and subsequent bremsstrahlung of the electrons and positrons. As the energy transferred to the leptons is so high, they move at velocities larger than the speed of light in the atmosphere and as a result produce Cherenkov radiation [Che34]. The emitted spectrum depends on wavelength as $1/\lambda^2$, but due to absorption in the atmosphere at 2,000 m a.s.l. it has the form depicted in Figure 4.1.

This light is focused by the mirrors of IACTs and imaged on a photon detector plane. The signals are recorded most effectively by very fast data acquisition systems[2] like FADCs[3],

[1] **I**maging **A**tmospheric **C**herenkov **T**elescope, IACT
[2] **D**ata **AQ**uisition, DAQ
[3] **F**lash **A**nalog to **D**igital **C**onverter, FADC

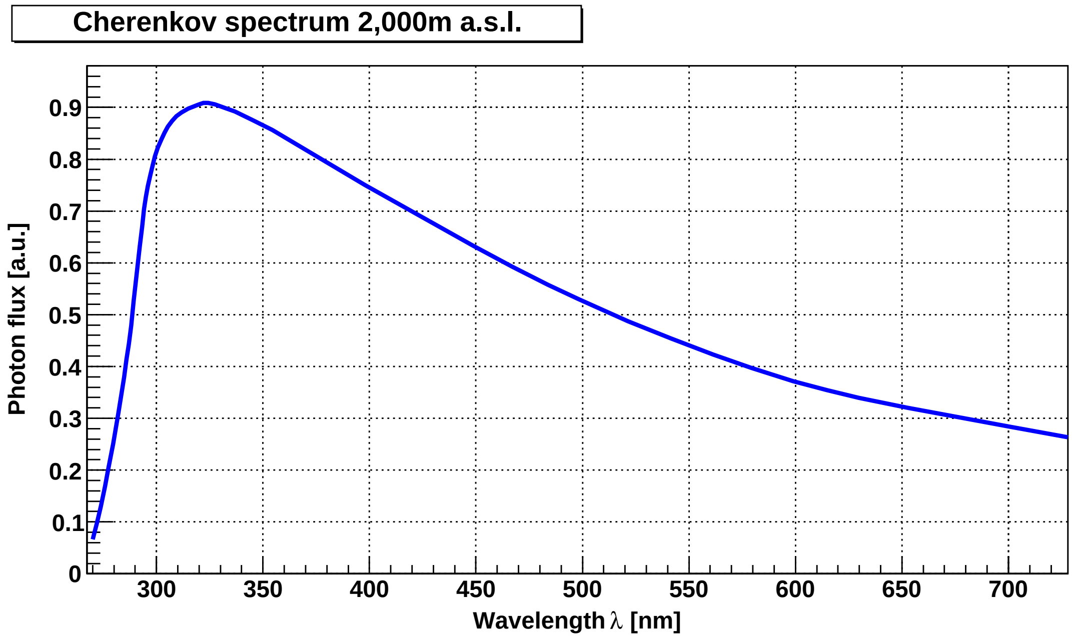

Figure 4.1: Spectrum of Cherenkov radiation from air showers in 2,000 m a.s.l.

sampling the temporal evolution of the around 5 ns short air showers. In Figure 4.2 the working principle of IACTs is illustrated.
As not only gamma-rays but also charged cosmic rays (c.f. section 2.1) induce air showers, the detection of sources of VHE gamma-rays is highly non-trivial. In general, the shapes of hadronic and gamma induced showers differ e.g. in width, light density, temporal evolution and orientation. This is also reflected in the images recorded from air showers utilizing Cherenkov telescopes [Hil85]. These differences are due to the production of massive mesons in hadronic interactions, leading to a much larger transverse momentum compared to electromagnetic air showers. In Figure 4.3 simulations of a proton induced air shower, an iron induced one, and a gamma induced one with an energy of the primary particle of 1 TeV are depicted to illustrate the differences.

4.2 Historical Instruments

4.2.1 HEGRA CT 1

The first HEGRA[4] Cherenkov telescope, CT 1, was operated between 1992 and 2002 at the Observatorio del Roque de los Muchachos on the Canary Island of La Palma, Spain. In 1995 the former camera with only 37 pixels was exchanged for one with 127 pixels and in 1998 the DAQ system was upgraded and the former 5 m^2 round glass mirrors were exchanged with hexagonal all-aluminum mirrors with in total 10 m^2 mirror area. Further details, especially on the upgrade in 1998 can be found in [C+00, K+98].

[4] **H**igh **E**nergy **G**amma **R**ay **A**stronomy, HEGRA, see http://www.mpi-hd.mpg.de/hfm/HEGRA/HEGRA.html

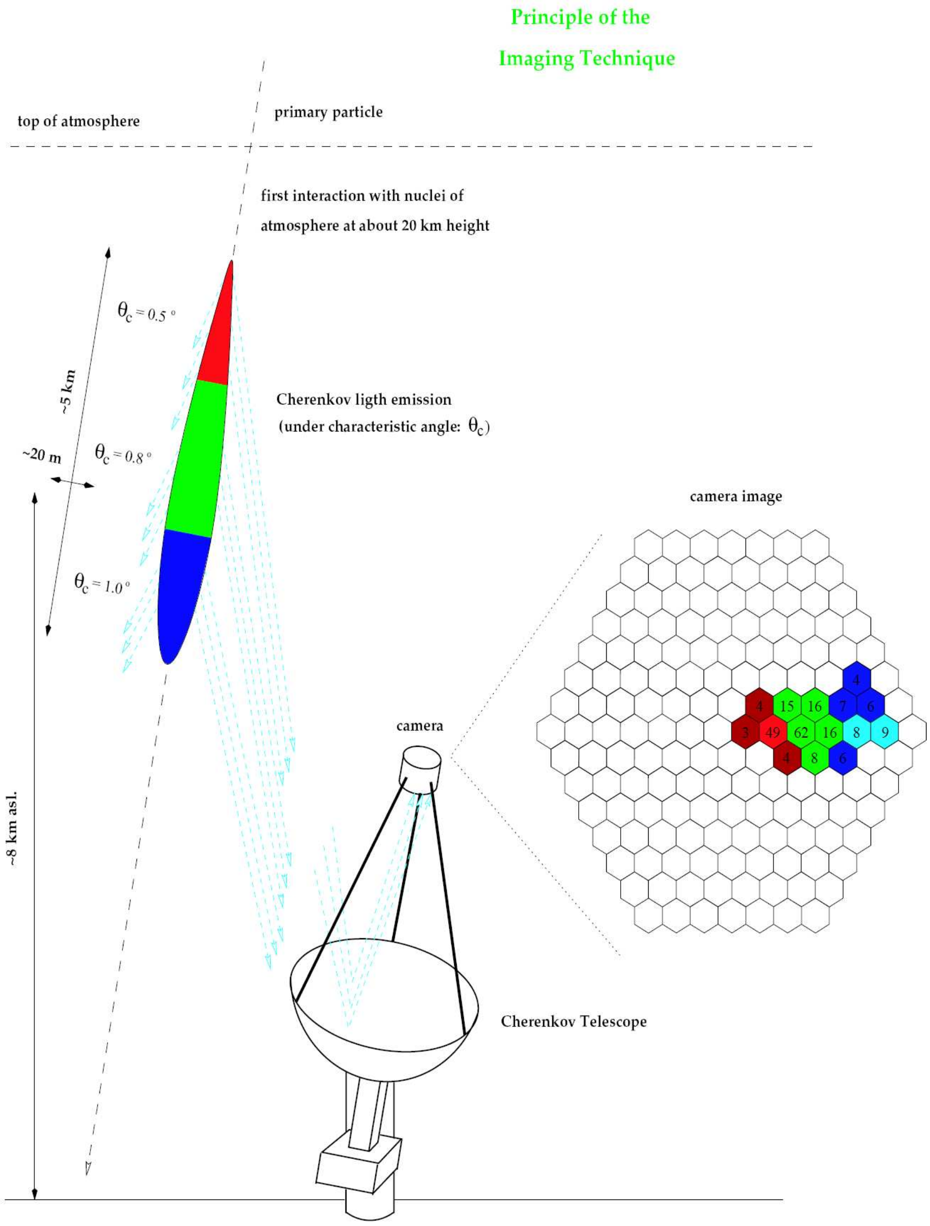

Figure 4.2: Working principle of an IACT: An air shower is developing in the atmosphere and emits Cherenkov light. The time evolution of the air shower is depicted in color code from red to blue. By the co-axial alignment of the telescope to the air shower main axis the form and temporal evolution of the shower is imaged onto the camera. The numbers depicted are examples for a gamma induced air shower with a primary energy of about 1 TeV [Mun06].

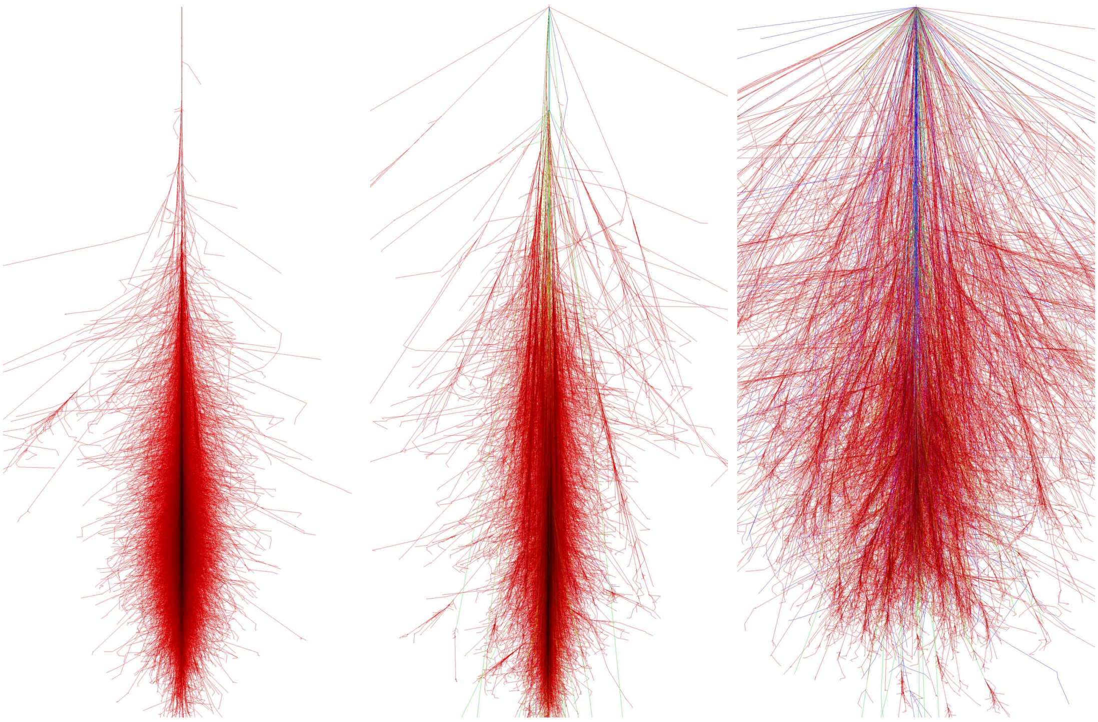

Figure 4.3: Side view onto simulated air showers with an energy of 1 TeV each, of the primary particle for perpendicular incidence, i.e. zenith angle = 0°, and the first interaction in taking place in a height of 30 km. *Left:* a gamma induced air shower, *Middle:* a proton induced one, *Right:* an air shower caused by a primary iron core (^{56}Fe) [Sch07a].

4.2.2 HEGRA CT System

The HEGRA Cherenkov telescope system was a stereoscopic system of five identical Cherenkov telescopes (CT 2 – CT 6) in operation between September 1995 and September 2002. One of those, namely CT 3, is depicted in Figure 4.5. The HEGRA array has also been situated at the Roque de los Muchachos on the La Palma at about 2,200 m. a.s.l. Four of the telescopes have been arranged in a square shape with sides lengths of 100 m and one, CT 3, stood at the center of the square. Containing a mirror area of five times 8.5 m^2 and cameras consisting of 271 pixels with a field of view of 0.25 °, each, the energy threshold of the system was about 0.5 TeV. For more information see e.g. [D$^+$97, DHH97, K$^+$99a, P$^+$03b].

4.3 Latest Generation Instruments and General Limitations

Since the first ground-based detection of very high energy gamma-rays from outer space in 1989 [W$^+$89], the field of gamma-ray astronomy with IACTs has made a significant progress, increasing the number of detected VHE gamma-ray sources from 14 in 2004 to

Figure 4.4: The HEGRA telescope CT 1 after the upgrade with hexagonal aluminum mirrors in 1998 [K+98].

presently more than 120 of both galactic and extragalactic origin[5]. This progress is owed to the IACTs of the latest generation, namely CANGAROO-III[6], H.E.S.S.[7], MAGIC[8], and VERITAS[9]. They are depicted in Figure 4.6, and general characteristics are given in Table 4.1. The MAGIC telescopes are introduced in subsection 4.3.1. The tremendous increase in source detections became possible by both, decreasing the energy threshold and increasing the overall instruments' sensitivity simultaneously. Hence, in the VHE regime IACTs are much more sensitive than gamma-ray satellites or water Cherenkov experiments, like e.g. Fermi–LAT and Milagro[10], respectively. But IACTs suffer from their extremely limited fields of view, compared to the former. Thus, instead of all-sky surveys IACTs are used for deep single source exposures, in general leading to a dependency on external triggers for the observation of already known sources. To overcome this bias the regular monitoring observations of the TeV-brightest AGN have been conducted with the MAGIC

[5] For a recent overview of detected sources see http://www.mppmu.mpg.de/~rwagner/sources or http://tevcat.uchicago.edu.

[6] **C**ollaboration of **A**ustralia and **N**ippon (Japan) for a **GA**mma **R**ay **O**bservatory in the **O**utback, CANGAROO, see http://icrhp9.icrr.u-tokyo.ac.jp

[7] **H**igh **E**nergetic **S**tereoscopic **S**ystem, H.E.S.S., see http://www.mpi-hd.mpg.de/hfm/HESS

[8] **M**ajor **A**tmospheric **G**amma-ray **I**maging **C**herenkov Telescopes, MAGIC, see http://magic.mpp.mpg.de

[9] **V**ery **E**nergetic **R**adiation **I**maging **T**elescope **A**rray **S**ystem, VERITAS, see http://veritas.sao.arizona.edu

[10] see http://umdgrb.umd.edu/cosmic/milagro

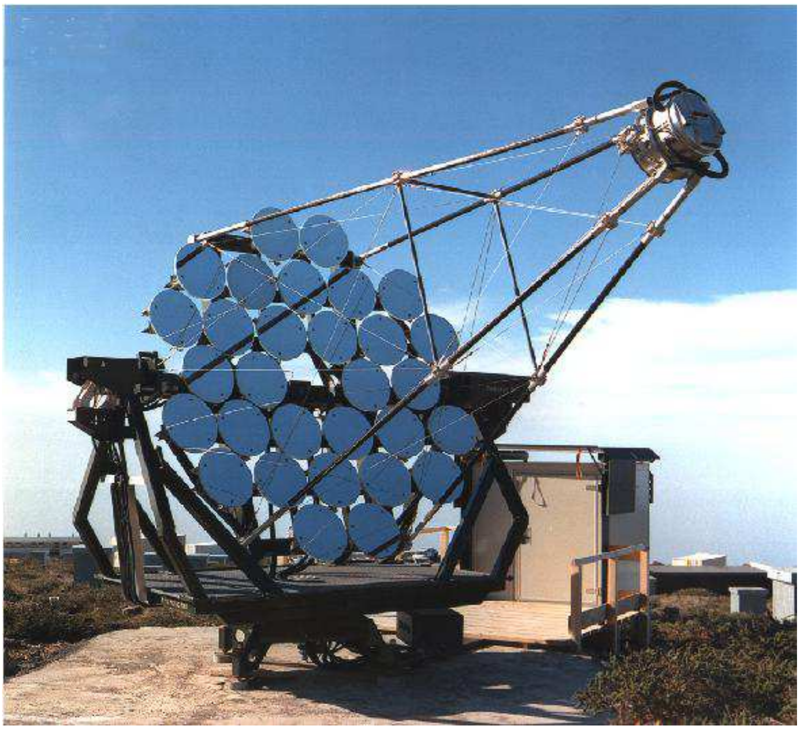

Figure 4.5: The HEGRA telescope CT 3 of the HEGRA Cherenkov telescope system [Ast07].

Instrument	Telescopes	Mirror Ø	Altitude	Site
CANGAROO–III	4	10 m	160 m	Woomera, Australia
H.E.S.S. (II)	4 (+1)	12 m (28 m)	1,800 m	Gamsberg Mountain, Namibia
MAGIC	2	17 m	2,200 m	La Palma, Spain
VERITAS	4	12 m	1,275 m	Amado (AZ), USA

Table 4.1: General information on the four major IACT systems.

telescope for several years (chapter 6) and even a worldwide network of IACTs for such monitoring observations is being set-up (chapter 8). The physical motivation as well as the results of the MAGIC monitoring campaign and the status of the DWARF network for VHE gamma-ray monitoring will be outlined in the given chapters.

4.3.1 MAGIC Telescope(s)

The MAGIC telescopes are the largest IACTs for VHE gamma-ray astronomy, featuring two times 236 m^2 mirror area. They are situated at 2,200 m a.s.l. at the Observatorio del Roque de los Muchachos of the European Northern Observatory on the Canary Island of La Palma. The first MAGIC telescope [A+08i] has been in scientific operation since 2004 [B+04a] and underwent a major upgrade in the beginning of 2007 when a 2 GSamples/s FADC data acquisition system was installed [G+08]. With this high temporal resolution, the influence of background photons could be significantly diminished and the separation of signal events from the hadronic background events could be improved [A+09h]. Both effects resulted in a sensitivity such that a source emitting a gamma-ray flux of 1.6% of that of the Crab Nebula with the same spectral behavior could be established with $5\,\sigma$ significance within 50 h of observation time. Thus, above 300 GeV, a flux of 30% of the Crab Nebula flux could be detected within 30 min [H+09b] (see Figure 4.8). Furthermore, MAGIC can be operated under moderate moonlight and twilight conditions (c.f. Figure 4.7) and despite the higher amount of background photons these data can be processed with the standard software pipeline [BWM03, M+09c] without any further modifications. For even brighter conditions, special image cleaning procedures have been developed [A+07g, B+09k, Hei10]. In 2009 the second telescope started scientific operation [T+10d], leading to a sensitivity improvement of a factor of two in the whole energy range from 50 GeV to several TeV, at the same time also improving the energy resolution [A+11k].

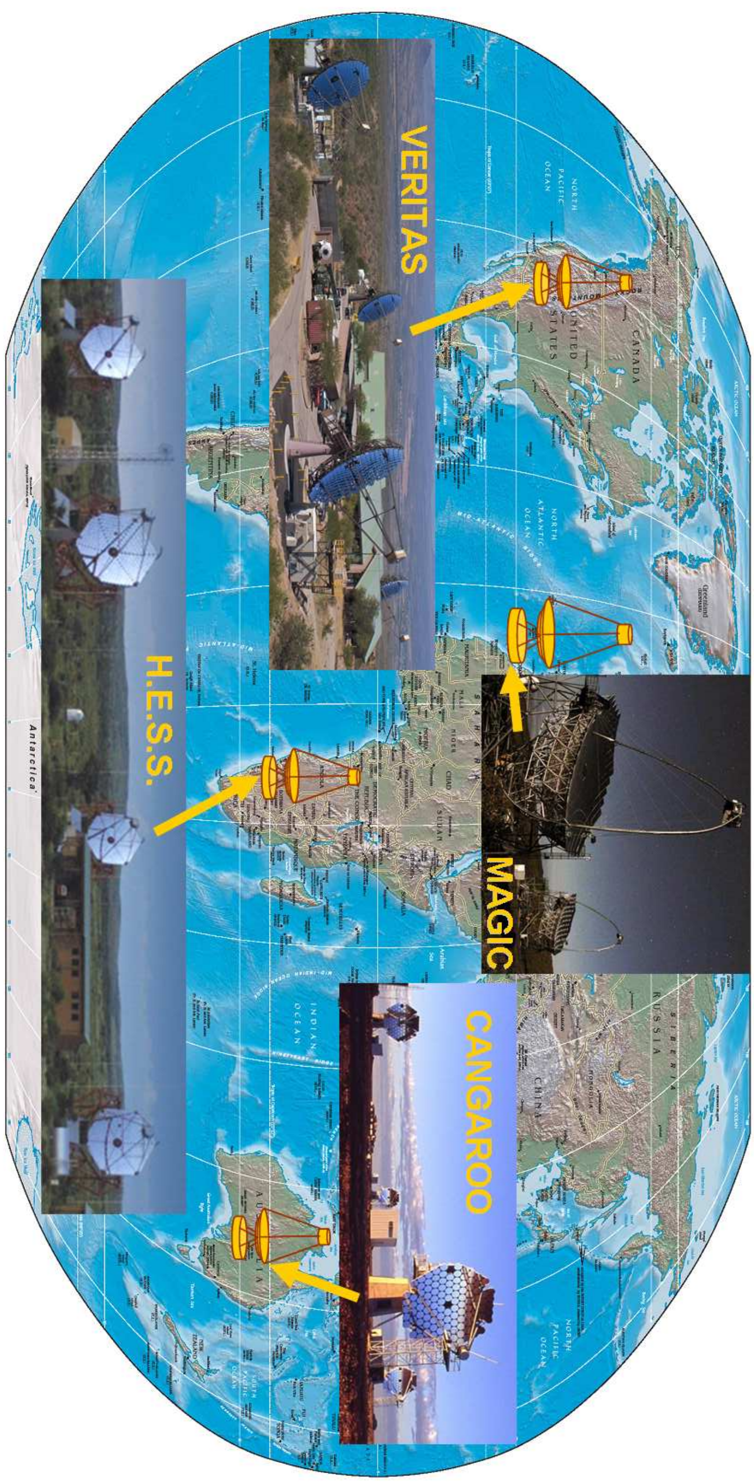

Figure 4.6: Pictures and sites of the recent major imaging atmospheric Cherenkov telescopes [HC07, Col07b, Col07a, CIA07].

Figure 4.7: The MAGIC telescopes observing during moonlight. MAGIC–II is at the left, MAGIC–I at the right.

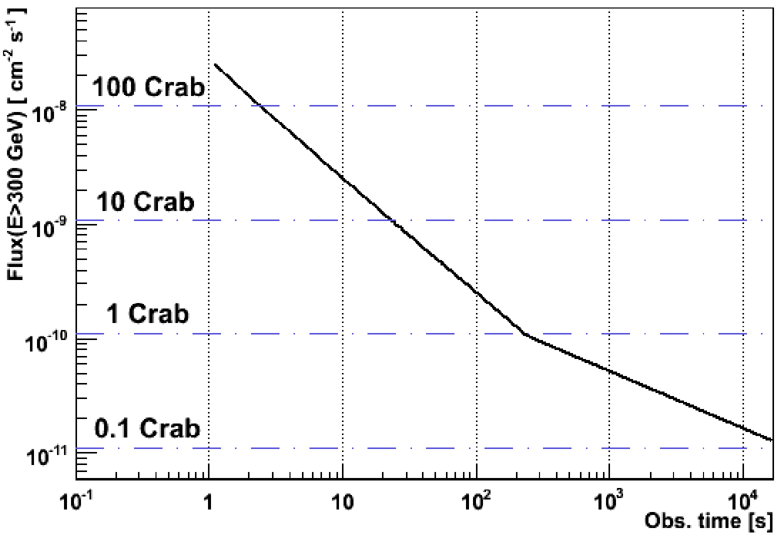

Figure 4.8: MAGIC-I sensitivity corresponding to a detection with $5\,\sigma$ significance according to [LM83] as a function of observation time [H+09b].

4.4 Improvements on Data Analysis

At the lowest detectable energies, the number of events is by far the largest (c.f. Figure 2.4). Yet especially for those, the differences between gamma-ray and hadronic air showers mentioned in section 4.1 are only subtle and as sucg their separation is difficult. To cope with that, not only one-dimensional cuts in the surface brightness [BW97] or in the (nearly equivalent) signal dependent ellipse area [Rie05a, R+05a] are currently being conducted, but multivariate methods [B+04c] are used. These statistical learning methods like random forest [Bre01, A+08g], boosted decision trees [OvE09], or artificial neural nets [D+09a] are capable of using non-linear multidimensional classification criteria and therefore can handle even the harsh signal to background ratios of about 1:1,000 for the strongest sources down to about 1:100,000 for the weakest sources. In the context of this thesis the optimization of the separation of signal and background events via statistical learning methods has been approached in a twofolded way.

New multivariate classification methods have been developed, focusing on the optimization of both, the separation power, and the computation time. The stratified sampling classifier Ada^{2}Boost [Sch07b] has been upgraded to use real value confidences instead of bi-nominal values for classification. In this manner, it is possible to exploit the advantages of ensemble classifiers as random forest or decision stump ensembles within the Ada^{2}Boost algorithm, resulting in a superior classification performance. Additionally, a re-sampling of the training set was introduced for very large data sets. Within this context the same separation power is achieved with a smaller amount of over all training examples and additionally, the amount of examples handled at a time is by far reduced. Both result in a significantly lower execution time compared to the original algorithm. A detailed discussion can be found in [Hel11] and [11].

Besides the question of performance of the separation algorithm, the question of the optimal classification threshold has been addressed. In Cherenkov astronomy one deals with highly imbalanced data, as outlined before, and additionally with unknown classification costs. In [10] it is shown that the assumption of a binomial classification probability, i.e. a single classification probability for all events independent of the event properties is justified. Following this assumption, the cut value for a real-value confidence classificator can be chosen ensuring that the mean squared error in the estimate of the number of gamma events in a mixed sample can be minimized.

Instrument:	CT 1	CT 1$^+$	CT 3-CT 6	MAGIC	Whipple 10 m	FACT
Mirror area [m^2]	5	10	8.5	236	75	9.5
Mirror diameter D [m]	~2.8	~3.9	3.9	17	10	3.9
Mirror reflectivity		83–85%	85–89%	80–90%	80–90%	85–93%
Focal length F [m]	4.9	4.9	4.92	16.97	7.3	4.89
F/D	~1.7	1.26	1.26	1.0	0.73	1.26
Field of view (FoV) [°]	3.2	3.2	4.3	3.5	2.6	4.5
# of pixels	127	127	271	396+180	379	1,440
FoV per pixel [°]	0.25	0.25	0.25	0.1; 0.2	0.12	0.11
Pixel diameter [mm]	21	21	21	30; 60		9.5
PMT diameter [mm]	19	19	19	25; 38	13	3.3 × 3.3
PMT quantum efficiency	14%	14%	14%	21%		35% (peak)
FADC [MHz]	QDC	QDC	120	300 / 2,000	QDC	2,000
Trigger rate [Hz]	1		5	250	100	~70
Trigger threshold$^\times$ [ph.e.]	2 P: 22		2 T 2 P: 8	4 NN c.p.: 9.5	3 NN: 30	t.b.d.
Energy threshold [TeV]	~1.5	~0.7	~0.5	~0.06	~0.3	t.b.d.
Sensitivity: Crab-σ in 1 h	1.9	3.7	2.3	18	5.6	t.b.d.

$^+$ CT 1$^+$ stands for CT 1 after the upgrade of the mirrors and the DAQ
$^\times$ Trigger conditions: x P=x pixels, x NN=x neighboring pixels, x NN c.p.=x double adjacent pixels, y T=y telescopes.

Table 4.2: Performance characteristics of selected IACTs [DHH97, D$^+$97, C$^+$00, K$^+$98, K$^+$07a].

Chapter 5
FACT – The First G-APD Cherenkov Telescope

As outlined in section 4.3 the recent achievements in VHE gamma-ray astronomy were mainly driven by technological developments enabling a giant leap in sensitivity as achieved by the most recent instruments. Now the field is standing at the crossroads, seeking another significant increase in sensitivity compared to the currently best instruments for the next generation instrumentation, CTA[1] [The10].
As the sensitivity of IACTs depends on the overall photon detection efficiency, i.e. on the conversion of Cherenkov photons reflected from the primary mirror into measurable photoelectrons, it is only natural to seek for better devices for photon detection. For all IACTs built up to now, photomultiplier tubes[2] have been the first choice. Recently, a new semiconductor device with excellent single photon response became available: the so-called Geiger-mode Avalanche Photodiode[3]. The First G-APD Cherenkov Telescope[4] is the first Cherenkov telescope employing a camera based entirely on G-APDs. An introduction to these new photo sensors is given in section 5.1 and the first prototype test for the camera is outlined in section 5.2. An overview of the newly developed G-APD camera, employing a highly integrated data acquisition system is given in section 5.3. The FACT telescope is based on the former HEGRA telescope CT 3, still situated at the Roque de los Muchachos Observatory on the Canary Island of La Palma at about 2,200 m a.s.l. as presented on several occasions [B+08b, B+08a, B+09b]. The telescope mount has received a complete technological upgrade, including a new drive system, described in section 5.4. Also the mirrors have been exchanged by completely refurbished ones. The characterization of the mirrors has been conducted in the course of this thesis and is outlined in section 5.5. Finally, the recent status of the telescope is summarized in section 5.6.

[1] **C**herenkov **T**elescope **A**rray, CTA, see http://www.cta-observatory.org
[2] **P**hoto**m**ultiplier **T**ube, PMT
[3] **G**eiger-mode **A**valanche **P**hoto**d**iode, G-APD
[4] **F**irst G-**A**PD **C**herenkov **T**elescope, FACT

5.1 Geiger-Mode Avalanche Photodiodes

PMTs have been the workhorse in detecting single or few photons ever since their invention. The main reasons for this are a photon detection efficiency[5] of 20–30% around 300–450 nm wavelength and their high intrinsic amplification ($\mathcal{O}(10^5 - 10^7)$). But due to their

- limited possibilities to increase their quantum efficiency[6] further,
- sensitivity to even weak magnetic fields,
- needs of stabilized HV power supplies,
- easy damage by high light levels,
- expensive production techniques

one would like to replace them by more advanced devices. With the invention of G-APDs[7], many of these drawbacks could be overcome by robust semiconductor devices, keeping the high intrinsic amplification and promising even higher PDEs than that of PMTs (for an overview, see [RL09]): G-APDs are operated at voltages around 70 V, much lower than for PMTs, and they are neither damaged by bright illumination during operation nor sensitive to magnetic fields. Altogether, this makes them promising candidates for replacing PMTs in the next generation of Astroparticle Physics instrumentations and especially in IACTs [T+08c, B+08d, W+09a]. For this purpose, several intrinsic properties of a given G-APD type, including the afterpulse behavior [K+09a], the angular acceptance and the dependence of the charge output on the illumination [K+09b] have been studied with a special focus on their possible application in IACTs. In addition, the first Cherenkov light from air-showers has been detected with an installation of an array of four G-APDs on the MAGIC telescope [B+07c]. Motivated by this, the idea of a two-step test for this new technology to be operated under Cherenkov telescope conditions was developed [B+09g]. In a first step a small test camera consisting of 144 G-APDs should be evaluated (section 5.2) and the second step a full-size camera operated on an existing Cherenkov telescope should be build (section 5.3).

5.2 36-Pixel Test Camera M0

In the first step of the test to study G-APDs as a possible replacement for photomultipliers in IACTs, a small test camera was built [W+09b]. This camera was made up of 144 G-APDs of the type Hamamatsu MPPC S10362-33-50-C [Ham09]. The signals of groups of four G-APDs were combined in an analog sum to make one pixel. Therefrom, the camera consisted of 36 pixels being arranged in a 6x6 lattice. The trigger decision was derived from a 3-fold coincidence from the innermost 16 pixels. Upon a trigger, all signals from the 36 pixels were digitized using the Domino Ring Sampling chip[8] DRS2 [Rit04].The latter is based on a capacitor array, allowing a high sampling rate of 2 GSamples/s and

[5] **P**hoton **D**etection **E**fficiency, PDE
[6] **Q**uantum **E**fficiency, QE
[7] sometimes also called **Si**licon **P**hoto **M**ultiplier, SiPM
[8] **D**omino **R**ing **S**ampling chip, DRS

being read out after a trigger by a fairly slow (40 MHz) ADC[9] system. A similar digitization system, also based on the DRS2, was previously used by the second MAGIC telescope [P+07b], which is upgraded with a system based on DRS4.

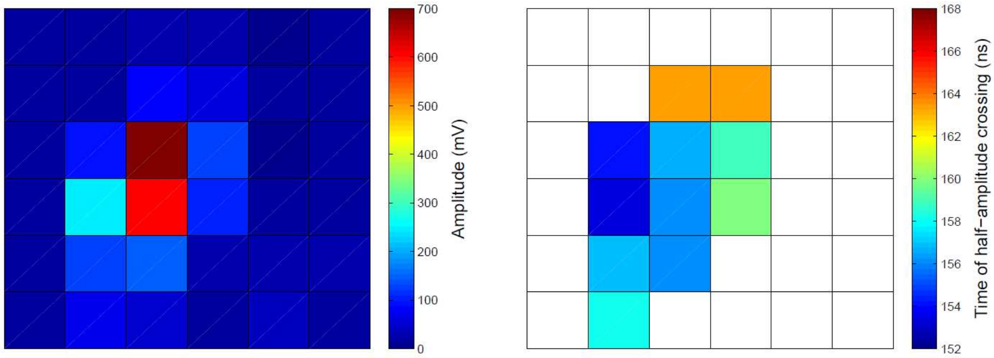

Figure 5.1: An air shower event detected with the Test Camera M0, for which the signal amplitudes (left) and the corresponding signal arrival times, defined by the time of half-amplitude crossing (right) are given.

This test set-up, combined with an 80 cm diameter focusing mirror, served to observe Cherenkov light from VHE air-showers (c.f. Figure 5.1) in the presence of the rather bright night-sky background[10] of Zurich. This test proved that it is possible to observe air-showers by a self-triggered camera built entirely of G-APDs [A+09i, A+11q]. In Figure 5.2 the dependency of the trigger rate on the single pixel threshold for the Test Camera M0 is depicted. The transition between the trigger rate being dominated by the NSB to being dominated by air showers can clearly be seen.

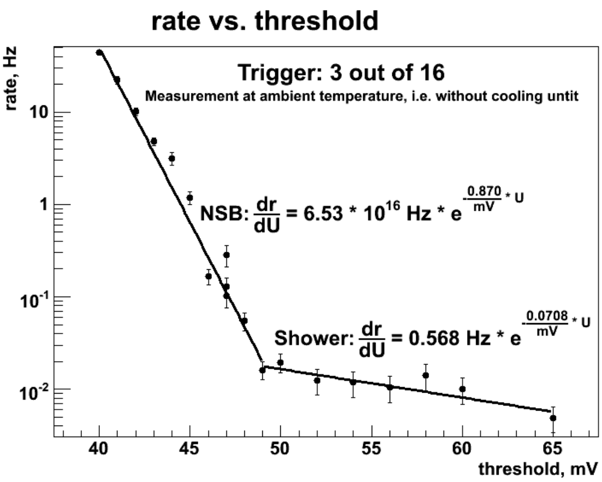

Figure 5.2: The dependency of the trigger rate on the single pixel threshold in a 3 out of 16 trigger configuration for the Test Camera M0.

[9] **A**nalog to **D**igital **C**onverter, ADC
[10] **N**ight-**s**ky **b**ackground, NSB

This, and similarly auspicious findings of another group [M+09b, MT10] convinced us to design the first real-size Cherenkov telescope equipped with a G-APD camera, FACT.

5.3 FACT Camera

The FACT camera consists of 1,440 G-APDs of the same type as already successfully operated in the test camera. Each G-APD represents a pixel and is equipped with a light guide and connected to a read-out channel. To account for the non-linear dependence of the G-APDs' gain on their temperature, a feedback system for readjusting the bias voltages is in use. It was developed based on an external temperature-stabilized LED pulser and was extensively tested [A+11n].
Taking into account the isotropic angular acceptance of the used G-APDs [K+09b], a new design for non-imaging light concentrators made of UV transparent plexiglas has been developed [B+09h] and produced by injection molding [H+11]. These light concentrators have an upright parabolic shape (in contrast to Winston cones with a tilted paraboloid shape), guiding the incident light with total reflections from a hexagonal entrance to a square exit window which matches the sensitive area of the G-APDs. This scheme allows an arrangement of the pixels in a hexagonal pattern. Therefor, it matches the requirements of a minimal angular dependence of light collection used for advanced analysis methods developed for Cherenkov astronomy, as e.g. introduced in [A+09h]. The use of solid material for the light guides allows higher input area/output area-ratios and avoids Fresnel reflections at transitions of materials of different refraction indices as at the camera front window. For this, the material of the light guides and the front window was chosen to match the refraction index of the protective epoxi layer on top of the G-APDs. To avoid plexiglas-air surfaces between the front window and between the cones, and the cones and the G-APDs, those are glued upon each other as described in [K+11b]. The light loss due to air bubbles introduced during this glueing processes account to less than 0.5% and can be neglected. In Figure 5.3 a conceptual sketch of the camera is depicted. Figure 5.4 shows a picture of the assembled camera during lab tests.
In contrast to a simple majority coincidence in the 36-pixel test camera, the trigger signal for FACT is generated by a signal over threshold logic for every analog sum of 9 adjacent pixels, arranged in non-overlapping patches. The data acquisition (DAQ) system is based on the DRS4 [Rit08], which is an improved successor of the DRS2, used in the test camera. This allows higher sampling rates (up to 5 GSamples/s) and a significantly reduced dead-time. Calibrating any cell of these capacitor arrays, reduces the RMS to 2 mV compared to the amplitude of a single photon signal of 10 mV [K+11a]. The trigger logic and the DAQ are housed in water cooled crates, located directly behind the sensor plane inside the camera (Figure 5.3). The data transfer down from the telescope is handled via optical link Ethernet connections. Details on the trigger and data acquisition electronics can be found in [A+11o, A+11p].

5.4 Drive System

The new telescope drive system is essentially a down-scaled version of the drive system implemented in the MAGIC telescopes [B+09j]. It is based on a programmable logic

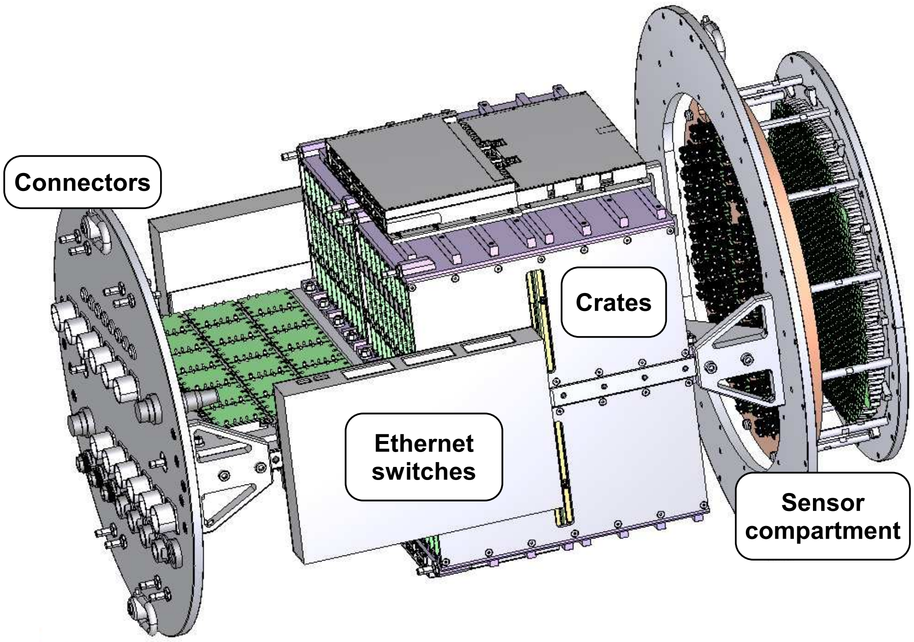

Figure 5.3: Conceptual drawing of the FACT camera. The length is 81.2 cm, the diameter amounts to 53.2 cm.

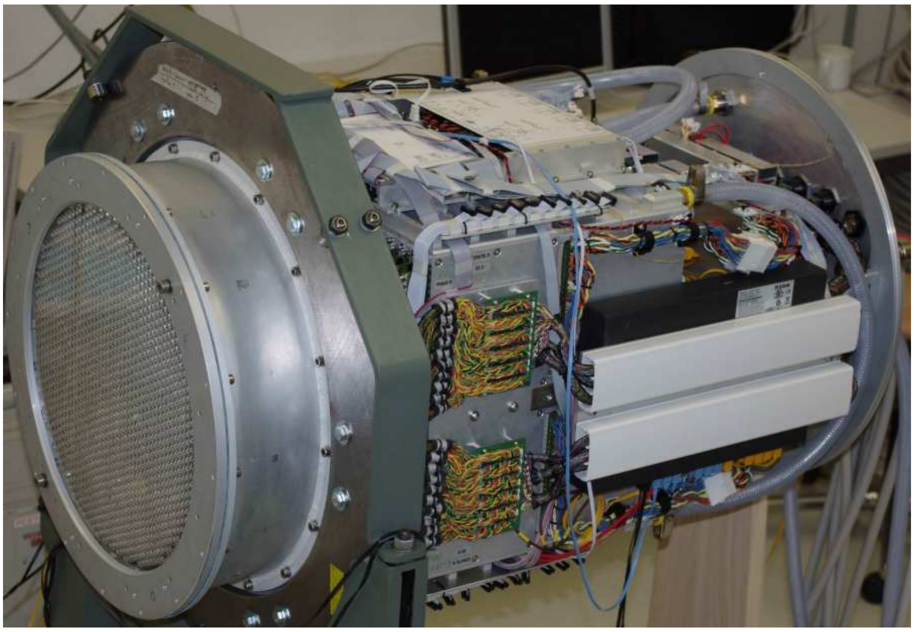

Figure 5.4: Picture of the assembled FACT camera during lap tests.

controller, accessible via Ethernet. New gear trains, fitting the new motors to the existing telescope system, have been designed and all drive components have already been assembled and successfully used, e.g. during the focusing of the mirrors.

5.5 Mirrors

The existing glass mirrors of HEGRA CT 3 have been exchanged with the mirrors originally built for an upgrade of HEGRA CT1 [C+00]. These mirrors are made entirely of aluminum with an honeycomb inlay between the front and the back plates, c.f. Figure 5.5. They are of hexagonal shape, covering an area of 0.317 m^2 each. Being comprised of 30 of such mirrors (c.f. Figure 5.19), the total reflective surface of FACT amounts to 9.51 m^2.

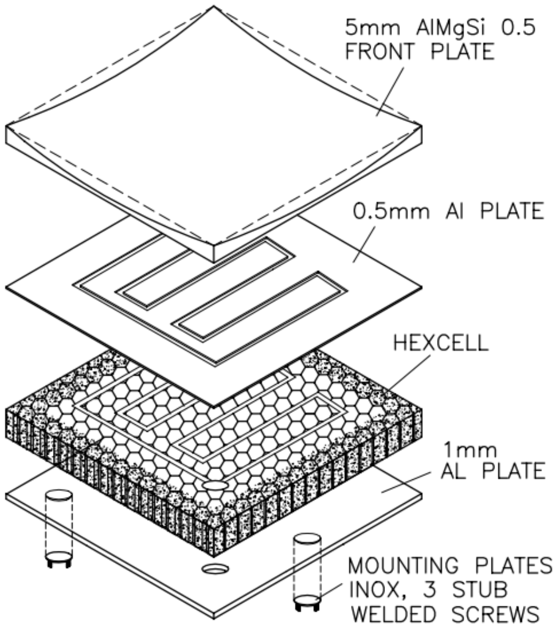

Figure 5.5: The inner structure of the FACT mirrors [C+00].

5.5.1 Re-Working and Spectral Reflectivities

The over twelve year old mirrors have been re-machined per diamond-milling by the company LT Ultra Precision Technology GmbH[11]. Subsequently, they have been coated with SiO_2 at the Fraunhofer Institute for Manufacturing Technology and Applied Materials Research[12]. Within a Methane atmosphere of a few mbar, silicon is deposited to the mirrors with a sputtering technique and afterwards oxidized. Thus, SiO_2 is build up with some admixture of Carbon from dissociation of Methane. The coating thickness has a major influence on the spectral reflectivity by thin layer interference and should be less than 120 nm, taking the spectral shape of the Cherenkov radiation into account (c.f. Figure 4.1). Measurements of the spectral reflectivity of MAGIC-II mirrors show, that homogeneity across single mirror facets is often not given [Sch09]. Instead, for the FACT mirrors, the specular reflectivity of all mirrors was measured to be constant within 4 %

[11] see http://www.lt-ultra.com

[12] Fraunhofer Institute for Manufacturing Technology and Applied Materials Research, *ger:* Fraunhofer-**I**nstitut für **F**ertigungstechnik und **A**ngewandte **M**aterialforschung, IFAM, see http://www.ifam.fraunhofer.de

over the surface of every single mirror. The mean measured spectral reflectivity of all mirrors is shown in Figure 5.6. The extrapolation for values below 360 nm wavelength is done with a fit of a polynomial function of sixth order to the data, c.f. Table 5.1.

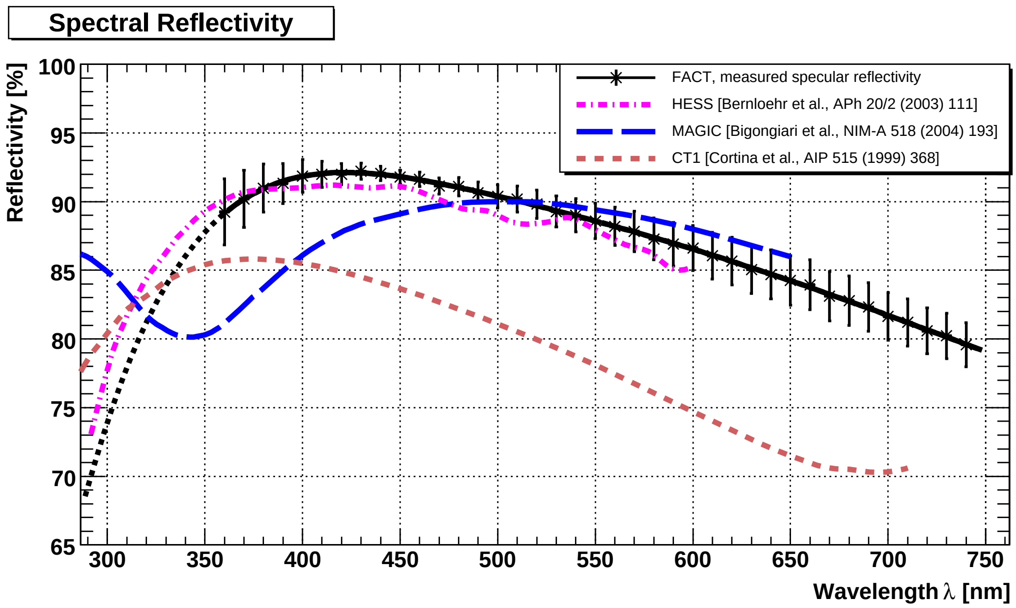

Figure 5.6: Mean measured reflectivity of the mirror facets for FACT. The standard deviations are given as error bars. The former reflectivity of the used mirrors (CT1) [C+00], as well as those for H.E.S.S. [B+03a] and MAGIC [B+04b] mirrors are given for comparison. The shape of the individual curves for CT1, MAGIC, and FACT is determined by the thickness of the SiO_2 coating via thin layer interference.

As already pointed out in [Rol09], the coating of the mirrors has been conducted in two charges effecting the coating thickness and thus the spectral reflectivity. The different charges form two classes of mean reflectivity as depicted in Figure 5.7. The parametrization of the sixth order polynomial fits is given in Table 5.1.

Parameter	Distribution 1	Distribution 2	Mean
p_0 $[10^3]$	-1.06465	-1.12449	-1.36456
p_1	11.70600	11.47170	14.57980
p_2 $[10^{-2}]$	-4.87834	-4.44898	-6.02623
p_3 $[10^{-5}]$	10.77200	9.08789	13.19940
p_4 $[10^{-7}]$	-1.33333	-1.03024	-1.61782
p_5 $[10^{-11}]$	8.76387	6.12355	10.51050
p_6 $[10^{-14}]$	-2.38826	-1.48743	-2.82706

Table 5.1: Parametrizations of the sixth order polynomial fits to the reflectivity distributions: $f(x) = p_0 + p_1 \cdot x + p_2 \cdot x^2 + p_3 \cdot x^3 + p_4 \cdot x^4 + p_5 \cdot x^5 + p_6 \cdot x^6$.

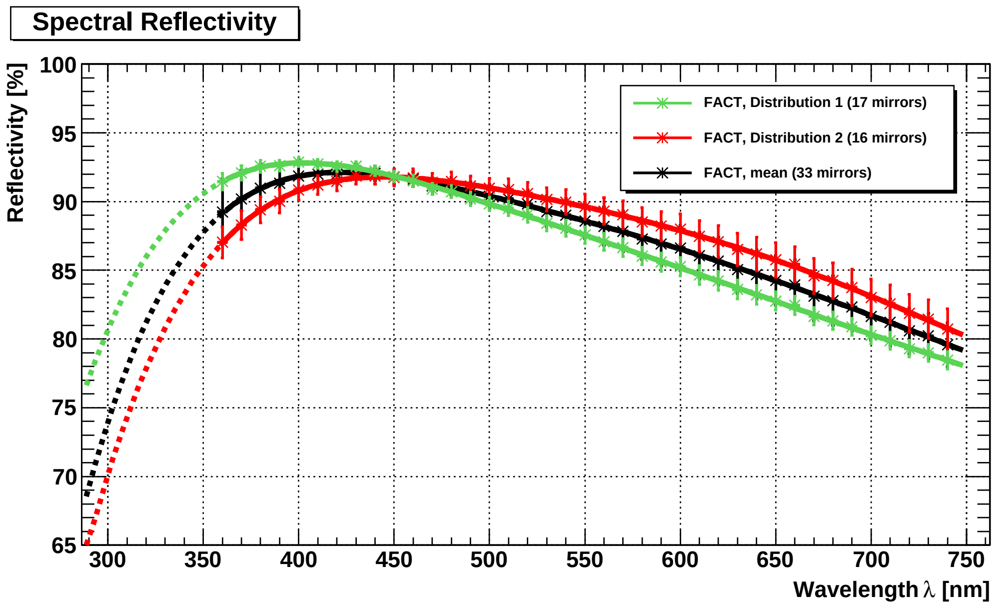

Figure 5.7: Mean measured reflectivity of the two classes of mirror facets for FACT. The standard deviations are given as error bars. The mean value reported in Figure 5.6 is shown as a reference. The shape of the individual curves is determined by the thickness of the SiO_2 coating via thin layer interference.

In order to determine the coating thickness, the reflectivity of a single mirror has been remeasured with a PerkinElmer LAMBDA 650 UV/Vis Spectrophotometer[13]. This offers a wider wavelength range of 190–900 nm compared to 360–740 nm of the former measurements; the wavelength accuracy is stated as ±0.15 nm in the manufacturer's technical specifications[14]. The measurements have been conducted in steps of 1 nm in the wavelength range of 200–800 nm. These results as well as the means for "distribution 1" from Figure 5.7 are shown in Figure 5.8. Clearly an inter-instrument offset can be seen, probably due to slightly different integration angles for the specular reflections. Applying a scaling factor of 1.0375 to the new measurements, the results for both measurements are in such good agreement, that they can both be described by the same sixth order polynomial between 270–750 nm.
From the interference minimum measured to occur for $\lambda_{\text{min}} = 272$ nm, the coating thickness d can be calculated using the first order approximation

$$d = \frac{\lambda_{\text{min}}}{2\sqrt{n^2 - \sin^2(\epsilon)}}, \tag{5.1}$$

where n is the refractive index of the SiO_2 coating and ϵ the incidence angle[15].

[13] see http://www.perkinelmer.com/Catalog/Product/ID/L650
[14] see http://www.perkinelmer.de/CMSResources/Images/44-74791SPC_LAMBDA650UVVis.pdf
[15] For a deduction see e.g. [Sch09].

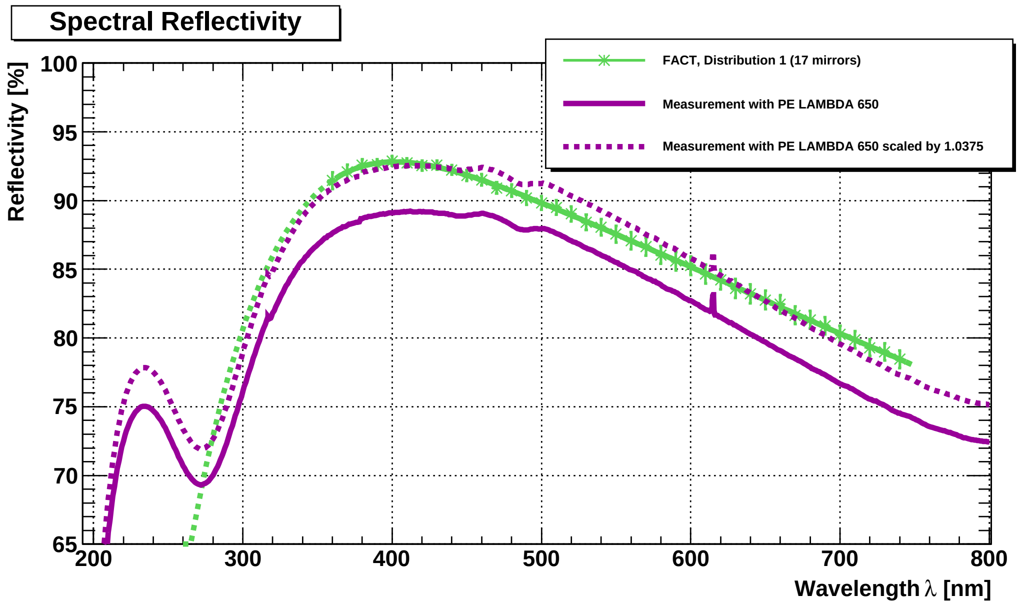

Figure 5.8: Measured reflectivity of a single mirror with the PE LAMBDA 650 UV/Vis Spectrophotometer along with the mean values for the "distribution 1" from Figure 5.7. Additionally, the spectrophotometer measurement scaled by a factor of 1.0375 is depicted.

Assuming an incidence angle of 30°, the refractive index of SiO_2 at 272 nm wavelength is reported as 1.58874 [GG99] and 1.58879 [B+09c] for crystalline silica and 1.49719 [MAL65] for fused silica[16]. Hence, the coating thickness d is estimated as 90.2 nm and 96.4 nm respectively.

5.5.2 Focal Lengths and Point Spread Functions

After the milling process described in subsection 5.5.1 some tension might persist inside the aluminum plate and cause distortion to the spherical symmetry of the mirror. By this, a non-spherical distortion would be introduced to the reflected image due to the effect of astigmatism: A unidirectional tensional force inside the aluminum plate would cause the mirror to have two different focal lengths, one for the direction parallel (sagittal focus) and one for the direction orthogonal to the direction of the force (tangential focus) as shown in Figure 5.9.
To check the influence of astigmatism to the planar focal length measurements presented in [Rol09], a new test setup was designed. To test for the astigmatism effect the whole mirror should be illuminated from twice the focal length measured before and the reflection in the same distance from the mirror should be evaluated. For this purpose a laser-LED was used, which was expanded by a concave lens with a focal length of 30 mm (Figure 5.10), so that the given laser spot of a diameter of $\lesssim 1$ mm was expanded to ≈ 60 cm in a distance of 9.8 m. An additional laser-LED of the same type together with an adjustable mirror stand (Figure 5.10) was used to set the optical axis and half-transparent paper with a mm

[16] The values have been retrieved via `http://refractiveindex.info`.

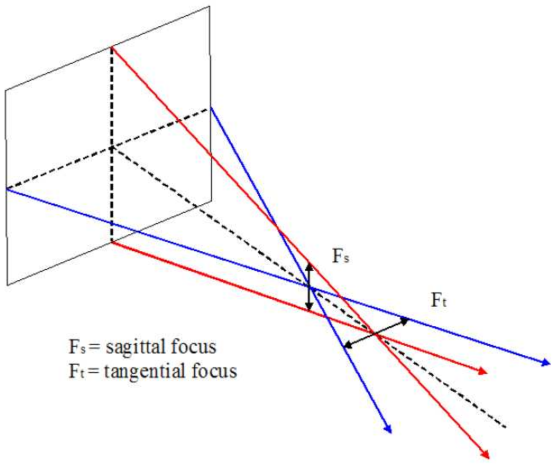

Figure 5.9: Sketch of astigmatism effects caused by unidirectional internal tension inside a mirror [Sch09].

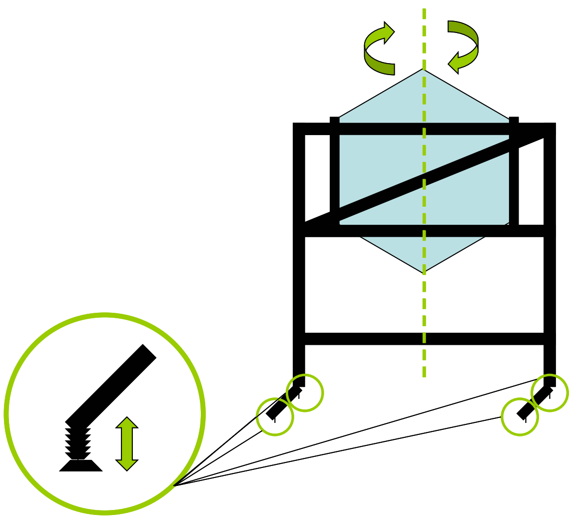

Figure 5.10: Laser-LED and concave lens (left) and mirror stand (right) for the focal lengths measurement.

grid was used as a screen. This screen was backside-illuminated by the reflection of the mirrors and pictures were taken of the front side. A sketch of this setup is depicted in Figure 5.11. An overview of the resulting images is shown in Figure 5.12.
From Figure 5.12 it is clearly visible that all but the mirrors 6, 13, 16, 19, 30, and 34 show significant effects of astigmatism. From some pictures like for the mirrors 11, 17, or 25 it is obvious that the conducted planar focal length measurement was – at best – capable of determining the sagittal or tangential focus. Additionally, lots of additional distortions can be seen in the pictures. Due to this, the test setup has been refined for being capable of measuring the global (pseudo) focal length of the whole mirror. Additionally,

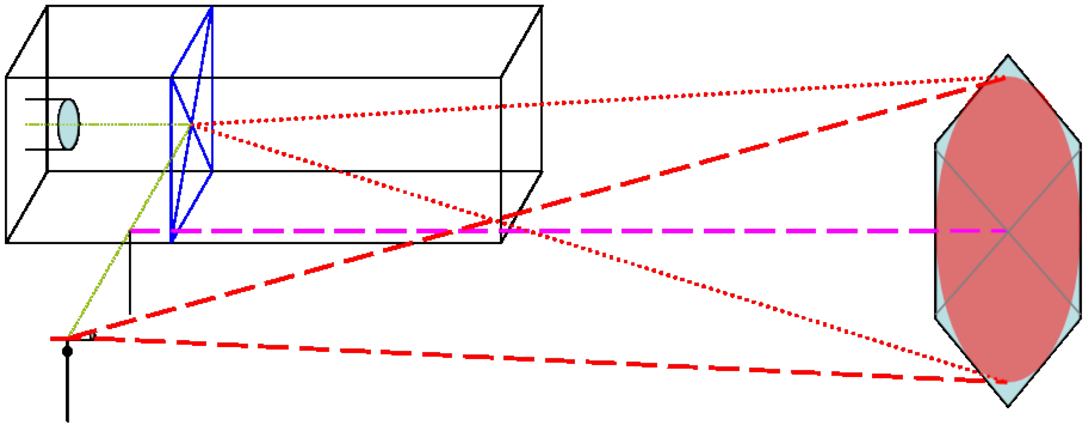

Figure 5.11: Set-up for the focal length measurement. The point like light source is depicted in the front, the light paths are illustrated by red lines, falling onto the hexagonal mirror and from there onto the screen (blue) which is protected from stray light by a light tight tube. In pink the laser beam defining the optical axis is depicted.

it provides information about the size and form of the image at the pseudo focal point, i.e. the PSF[17].
Here, the light source was exchanged for a (normal) red LED behind a 1 mm pinhole to avoid image distortion due to interference. Figure 5.13 illustrates the measurement procedure: At several distances from the mirror, starting from in front of the near focal point to behind the far focal point, three pictures of the reflected light source are taken with a commercial Sony α550 camera with an image resolution of $4,592 \times 3,056$ pixels equipped with a SIGMA MAKRO 105 mm F2.8 EX DG objective lens. The pictures taken near the pseudo focal point for all mirrors are shown in Figure 5.17 and Figure 5.18.
The distribution of the focal lengths as well as the individual focal length for each mirror facet are depicted in Figure 5.16. The distribution shows a very small spread of 8 mm around the mean focal length $\overline{f}$ of 4.890 m.
Additionally, pictures without light source are taken to produce difference images. To these difference images ellipses are fitted, containing 95 % of the remaining light. Afterwards the half-axis of these three ellipses per position are averaged and the area of the ellipses are assigned to the corresponding distance to the mirror, see Figure 5.14. By calculating the minimum of a parabolic fit of this area vs. distance dependence, both, the focal length and the minimal spot size of 95 % light content are obtained at once as exemplified in Figure 5.14. Other methods like searching for the focal distance where the excentricity of the ellipse equals 1, have also been tried, but the estimation of the ellipse area yielded by far the most robust results.
In Figure 5.15 the distribution of the spot sizes of the 30 mirrors used for FACT are depicted as well as the spot sizes of the individual mirror facets. The physical pixel size of FACT pixels is about 78 mm^2, thus the green lines in Figure 5.15 and Figure 5.14 correspond to one quarter of the pixel area, i.e. 19.54 mm^2. The mean of the distribution

[17] **P**oint **S**pread **F**unktion, PSF

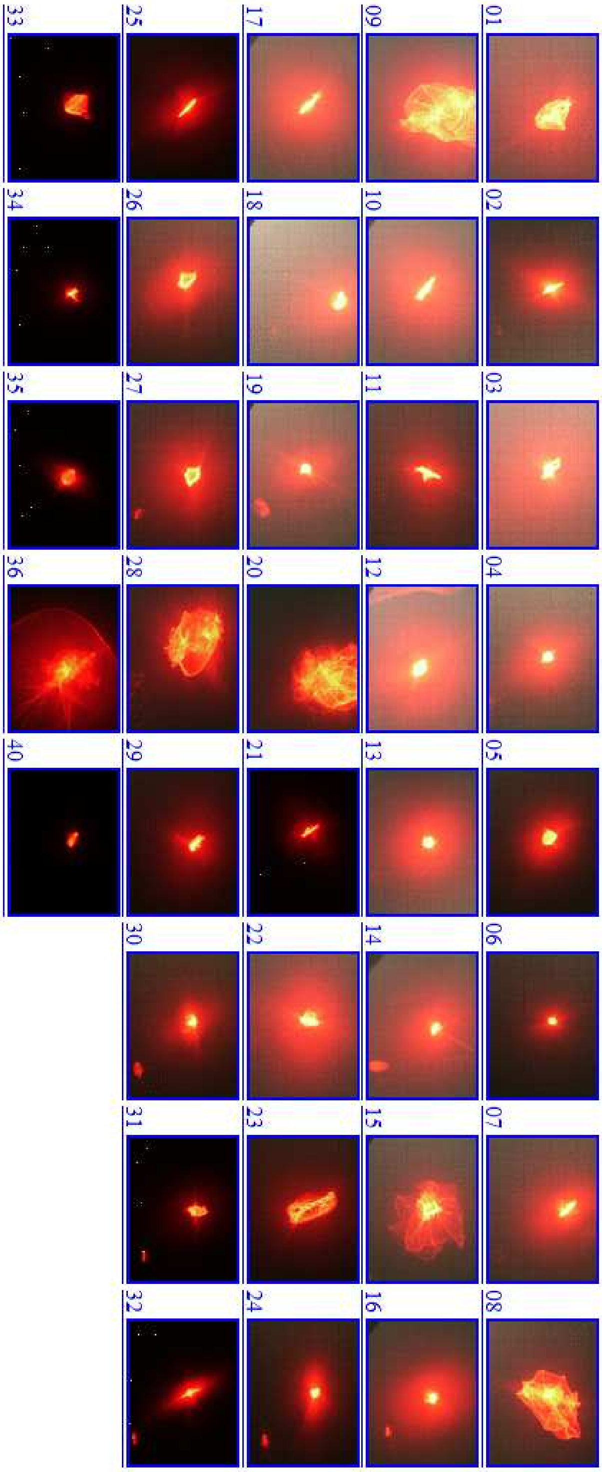

Figure 5.12: Images of a point-like light source at twice the planar focal distance.

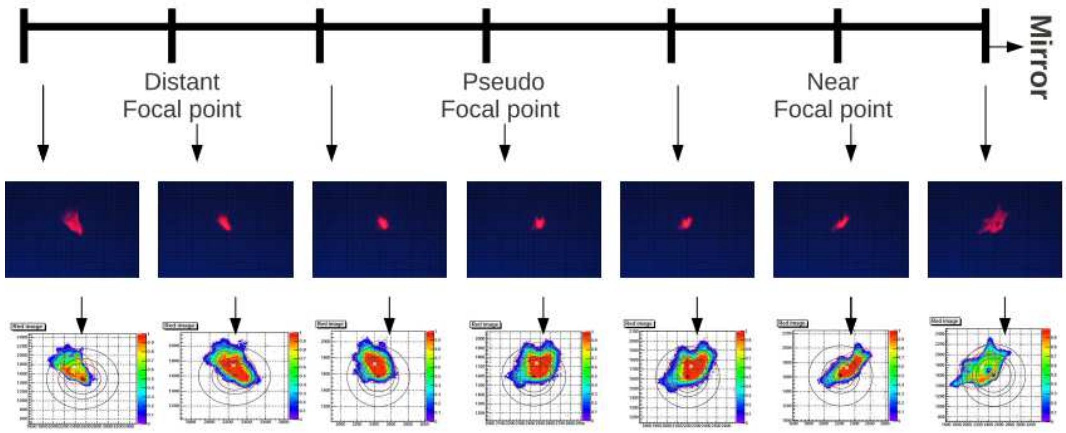

Figure 5.13: Focal length and PSF measurement procedure illustrating the astigmatism effect on the PSF depending on the distance to the mirror.

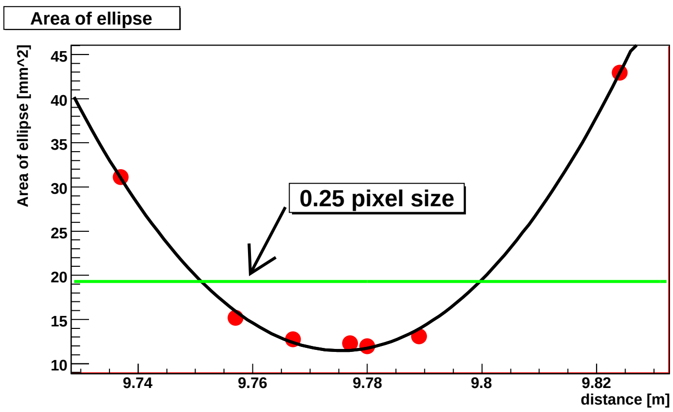

Figure 5.14: Area of the ellipse vs. twice the focal distance for one of the mirror facets.

of spot sizes is $(15.95 \pm 6.73)\,\mathrm{mm}^2$. Therefore, nearly all of the mirror facets focus 95 % of the reflected light in an area well below one quarter of a pixel size, which is an excellent value.

5.6 Status and Outlook

The construction and extensive lab testing of the camera [B+11e] as well as the assembly of the new telescope components have been carried out during the year 2011 [B+11g, B+11f]. The final assembly has been conducted in October 2011 and the commissioning has begun directly afterwards. A picture of the first data taking operations is shown in Figure 5.19 and first events induces by Cherenkov light of atmospheric particle showers have been

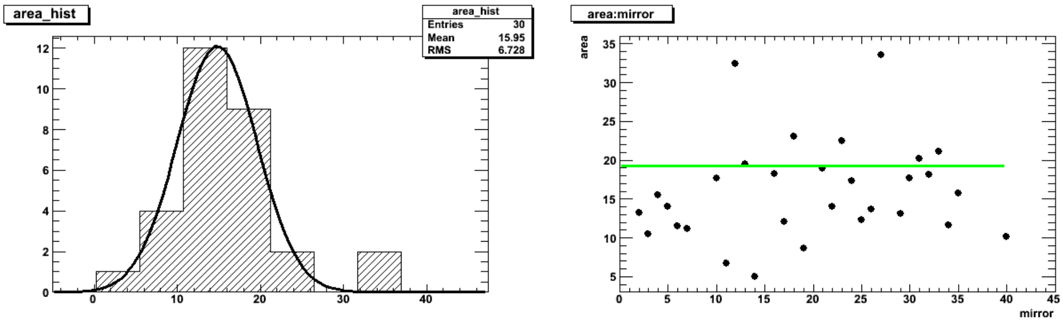

Figure 5.15: *Left:* Distribution of spot sizes of FACT mirrors. *Right:* Spot sizes of the individual mirrors.

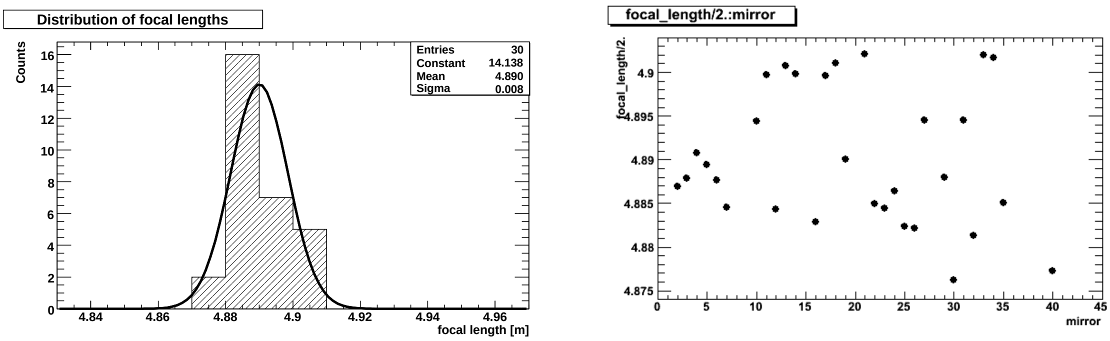

Figure 5.16: *Left:* Distribution of the focal lengths of the FACT mirrors. *Right:* Focal length of the individual mirrors.

recorded, see Figure 5.20[18]. For the analysis of the recorded data, the fully functional analysis software package MARS [B$^+$05c, BD08] is at hand and can be used with only a few changes for the analysis of FACT data. For the mandatory Monte Carlo simulations, CORSIKA [HK10] air-shower simulations and the newly developed detector simulation subroutines in MARS CheObs [BD09] are used. First simulations based on this software showed very promising results [B$^+$09i]. A successful test of the novel G-APD camera will be a first step to consider the new photosensors for the next generation of IACTs, including CTA. After the successful technological demonstration, FACT itself will be transferred to conduct a physics observation program. It will be the first telescope installed in order to build-up a world-wide network of Cherenkov telescopes [B$^+$08c, B$^+$07e] for monitoring bright blazars in the northern hemisphere [B$^+$09a], which will be discussed in detail in chapter 8.

[18] see http://fact.ethz.ch/first

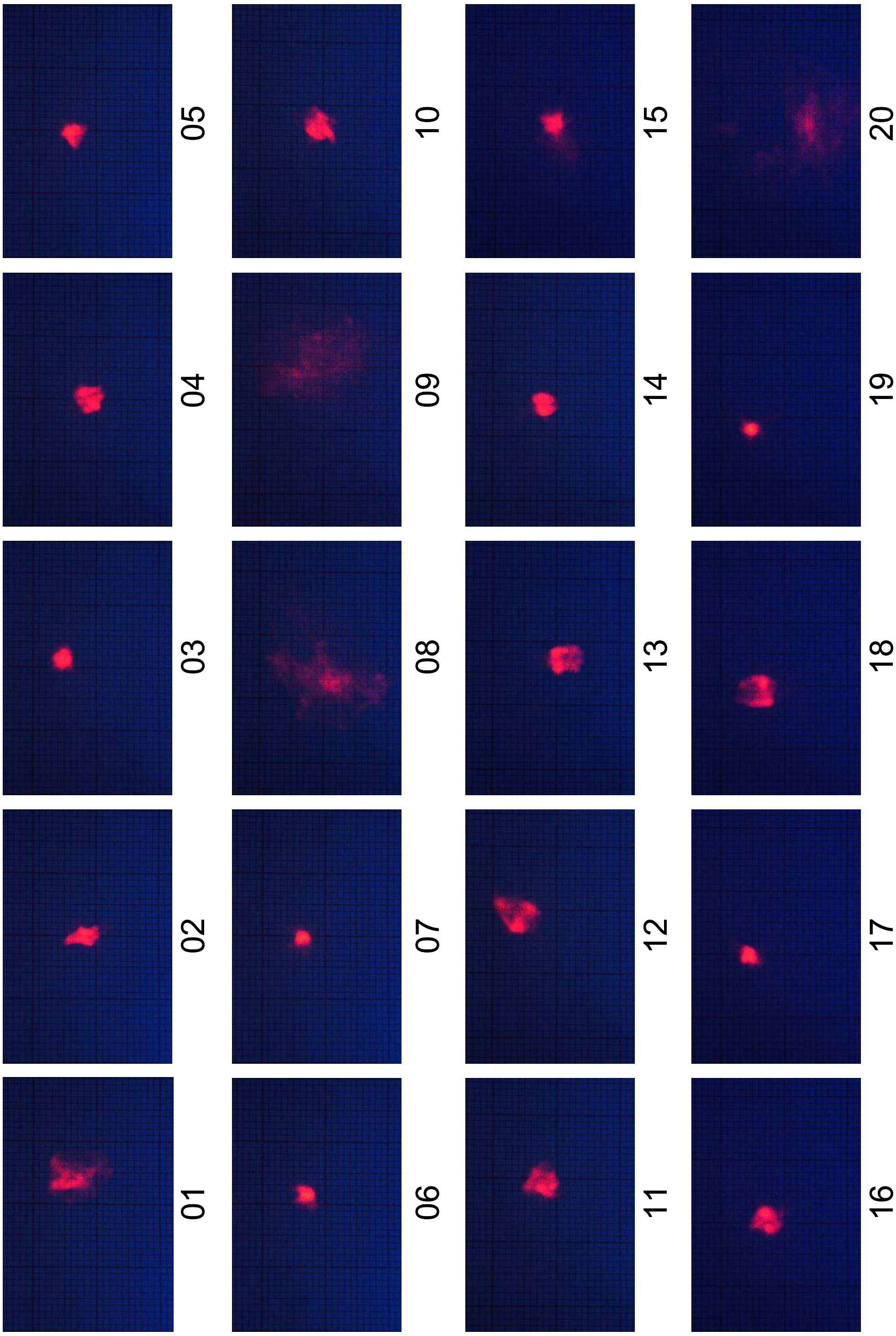

Figure 5.17: Images of a point-like light source near twice the (pseudo) focal distance. Note that those images are taken only near and not exactly at twice the pseudo focal distance and that for completeness also images for the defect mirrors 8, 9, and 20 are shown.

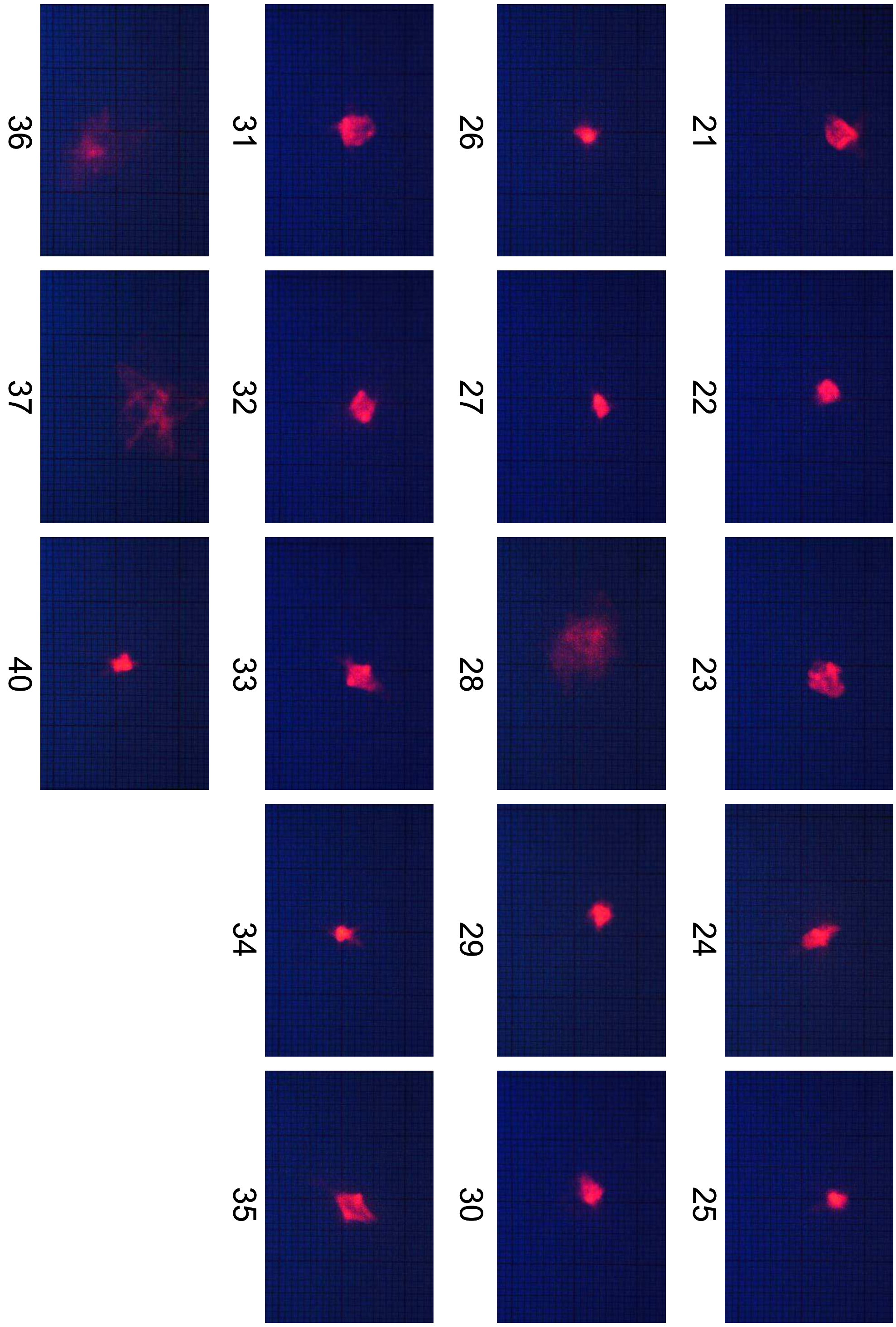

Figure 5.18: Images of a point-like light source near twice the (pseudo) focal distance. Note that those images are taken only near and not exactly at twice the pseudo focal distance and that for completeness also images for the defect mirrors 28, 36, and 37 are shown.

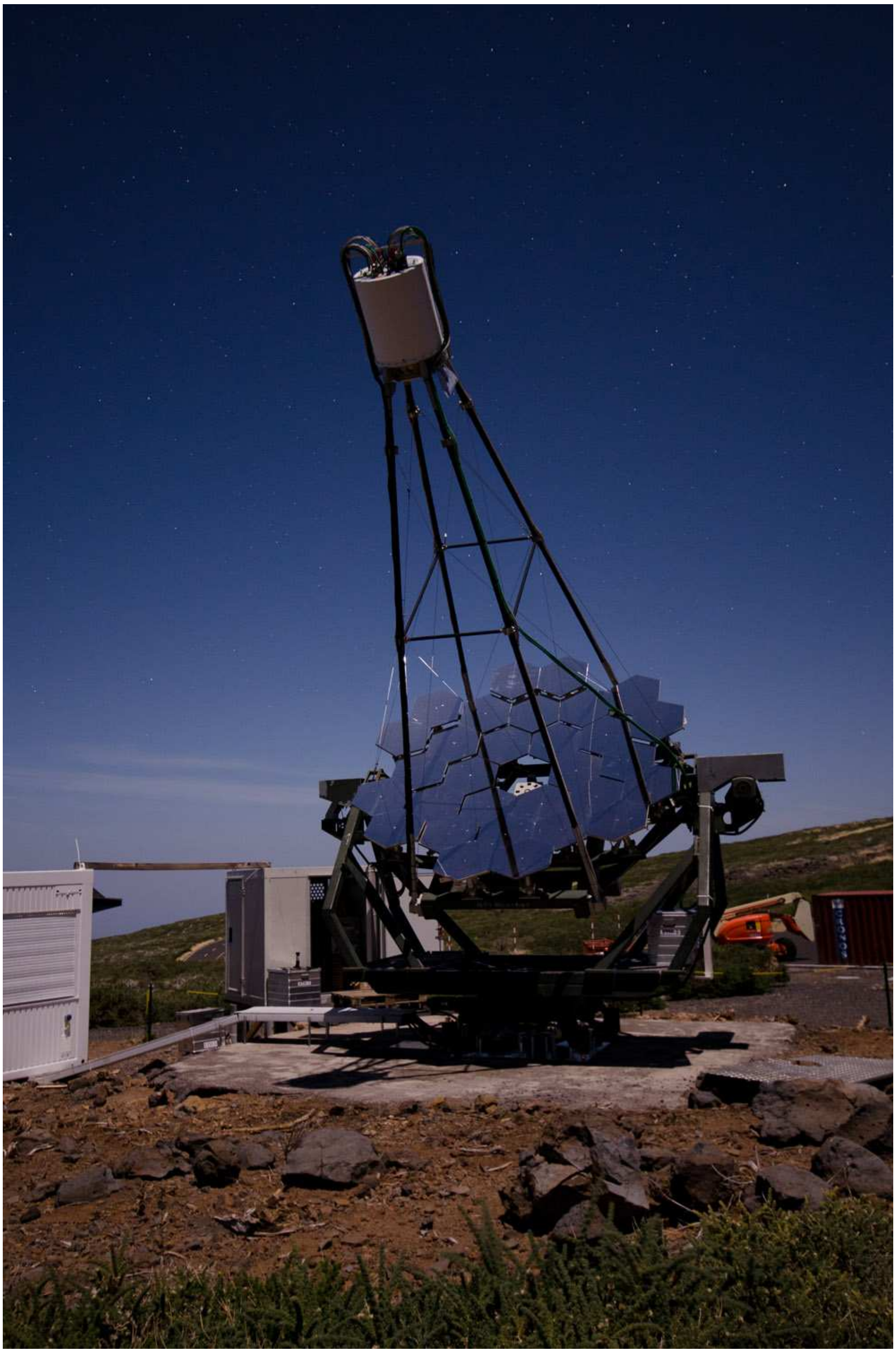

Figure 5.19: The FACT telescope conducting nightly observations during a full-moon night in the commissioning phase in October 2011. Picture courtesy of Thomas Krähenbühl.

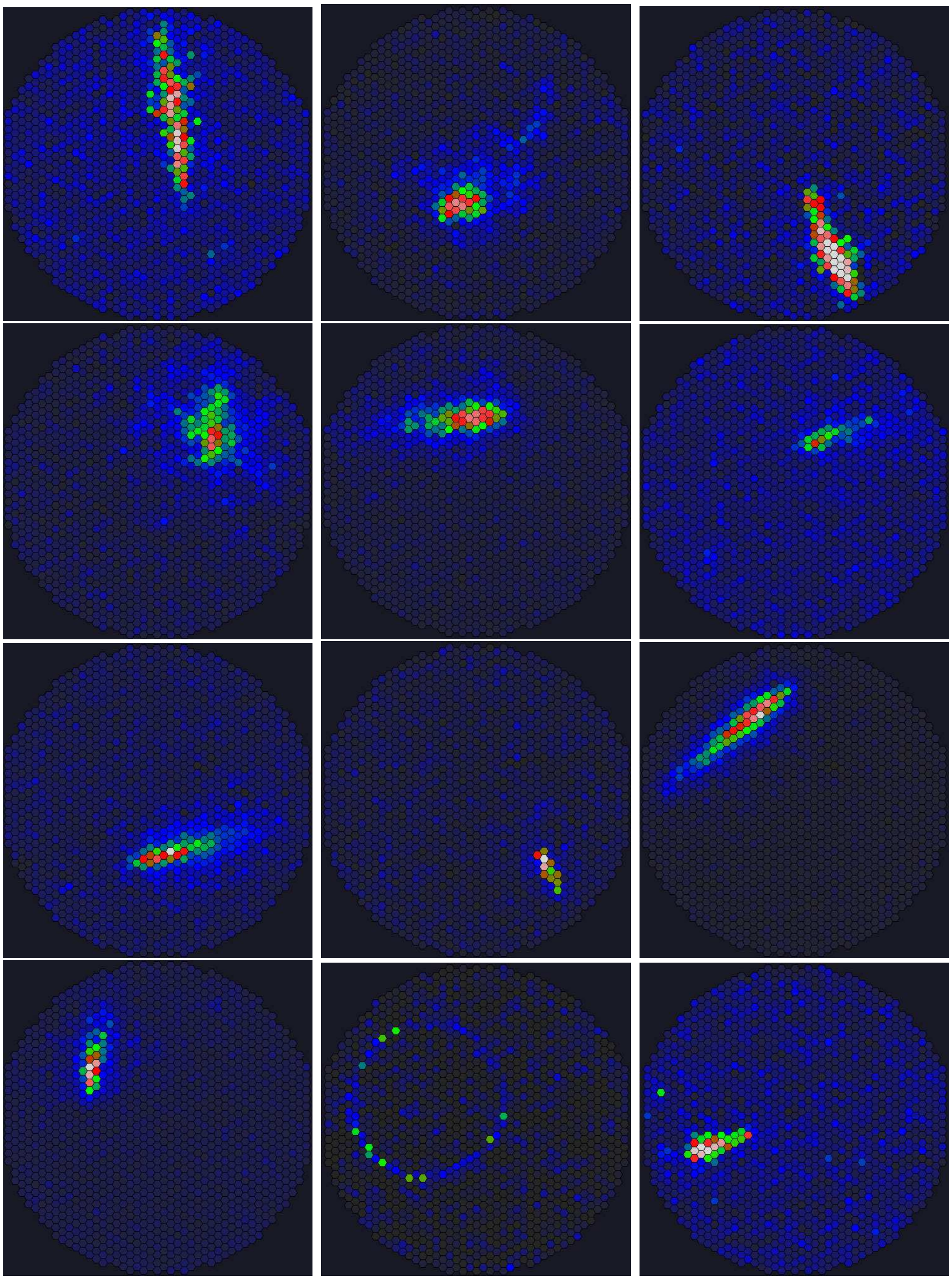

Figure 5.20: Some of the first air shower events recorded by the FACT telescope in the commissioning phase in October 2011.

Chapter 6
VHE Gamma-Ray Monitoring of Blazars

The variability of the very high energy emission from blazars seems to be connected to the feeding and propagation of relativistic jets stemming from supermassive black holes. The key to understanding their properties may be measuring well-sampled gamma-ray lightcurves, revealing the typical source behavior unbiased by prior knowledge from other wavebands. But observations and detections of Active Galactic Nuclei by Cherenkov telescopes are often triggered by information about high flux states in other wavelength bands, as outlined in chapter 4. To overcome these limitations, monitoring observations which are independent of the source state are mandatory. The goals of monitoring observations are to obtain an unbiased distribution of observed flux states shedding light on the duty cycle of AGN, to investigate potential spectral changes during periods of different source activity, and to correlate the results with multi-wavelength observations. Also clues on a potential periodic behavior of the sources might be drawn from a study of the obtained lightcurves. By testing predictions of theoretical models, like e.g. the correlation between the TeV flux level and the peak frequency predicted in SSC models, monitoring deepens our knowledge about the particle acceleration and photon emission processes in AGN.
To achieve this, single deep observations of different source states and monitoring observations providing information about the long-term behavior of the sources have to be combined. A wide multi-wavelength coverage is mandatory for both kinds of observations. Moreover, unbiased monitoring is obviously the only handle to the detection of *orphan flares*, being a strong indicator for acceleration sites of hadronic cosmic rays as pointed out in subsection 2.4.2. Robust estimations of the flaring state probabilities (as studied in [R+09a]) might open the opportunity of cross-correlating gamma-ray observations with those of the neutrino telescope IceCube and allow for an estimation of the statistical significance of such a correlation of blazar flares with possible extra-terrestrial neutrinos observed by IceCube [SBAe08]. Instead, conclusions on single neutrino events can only be drawn from cross-correlating complete data samples from both, the gamma-ray and the neutrino astronomy. Either way, such a cross-correlation would be the smoking gun of hadronic acceleration processes within the sources and would immediately settle this fundamental question of modern high energy astrophysics. In this sense also a database has been set

up, collecting all available VHE lightcurve data on the longest known VHE gamma-ray blazars [T+10c, TSKB07]. Another important aspect is the possibility to trigger Target of Opportunity[1] observations of either telescopes in other wavelength bands, or even other IACTs. Especially for that reason, the VERITAS collaboration has until recently operated the Whipple 10 m telescope [Pf09], and now started monitoring observations with VERITAS [B+11d]. Also the ARGO-YBJ experiment [Df11] conducts monitoring observations of TeV-bright blazars [B+11b]. In the course of this thesis, a worldwide network of Cherenkov telescopes conducting blazar monitoring has been proposed [B+09a] and initiated, see chapter 8.
In the following, the monitoring program with the MAGIC telescopes will be outlined and the according results on the blazars Mkn 421 and Mkn 501 will shortly be summarized in section 6.1. The blazar 1ES 1959+650 will extensively be discussed and findings on its temporal behavior and spectral properties will be presented in chapter 7. Afterwards, the DWARF network for long-term monitoring of the TeV-brightest blazars will be introduced in chapter 8.

6.1 AGN Monitoring with MAGIC

The VHE gamma-ray telescope MAGIC has conducted dedicated monitoring observations of nearby AGN since 2006. The observations have been scheduled in an unbiased way, not making use of e.g. information from other wavelengths. They have been evenly distributed over the according observation periods. Three well established, TeV-bright blazars were selected for this monitoring campaign: Mkn 421, Mkn 501, and 1ES 1959+650. The former being on average the two VHE brightest blazars, the latter one being especially interesting because of a huge flux increase in 2002. Simultaneously, even two neutrino events from the same direction have been observed by AMANDA[2], whereas this was not statistically significant [Bf05]. The observations for the brighter sources had a typical duration of 15-30 min, lasting at least 30 min for 1ES 1959+650. As MAGIC is capable to observe during moderate moon and twilight conditions, a sizable amount of the monitoring has been conducted in such conditions. In the following results of the monitoring of nearby AGN with the MAGIC telescope during the complete phase of mono-scopic observations are presented, i.e. from summer 2004 until summer 2009. Data taken under poor observation conditions have been rejected based e.g. on trigger rate, atmospheric transparency, and mean sky brightness measured as DC current of the photomultipliers. Most of the observations have been performed in wobble-mode, i.e. with simultaneous determination of the flux of background events [F+94]. All analysis steps have been verified on contemporary Crab Nebula data.

6.1.1 Results on Mkn 421

Mkn 421 was the first extragalactic object detected to emit VHE gamma-rays [P+92] and is on average the brightest AGN in the VHE regime. It has been observed by MAGIC

[1] **T**arget **o**f **O**pportunity, ToO
[2] **A**ntarctic **M**uon **A**nd **N**eutrino **D**etector **A**rray, AMANDA, see http://icecube.wisc.edu/science/amanda

since 2004 [A+07e], showing remarkable flaring activity in 2006 [A+09f] during a multi-wavelength campaign [A+10h] and in 2008 [D+09b], revealing a significant correlation of the VHE and X-ray emission [H+09b]. Altogether there have been 118 observations with MAGIC resulting in the lightcurve depicted in Figure 6.1.

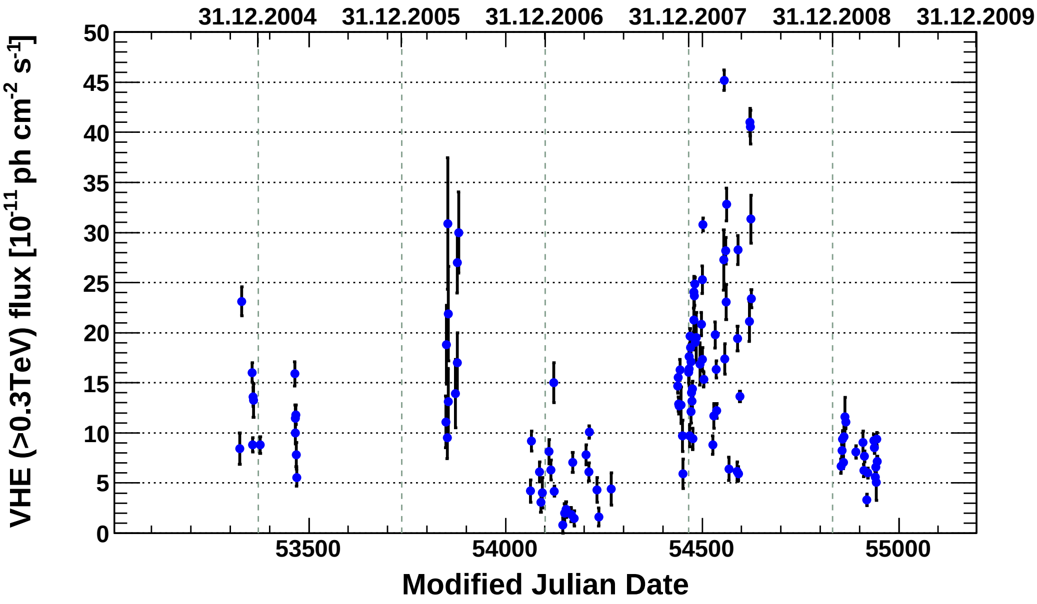

Figure 6.1: MAGIC lightcurve of Mkn 421 observed above 0.3 TeV from 2004 until 2009. Observations less significant than $1\,\sigma$ have been omitted.

6.1.2 Results on Mkn 501

Mkn 501 was detected as an emitter of VHE gamma-rays in 1995 [Q+96] and showed an extreme outburst in 1997 [P+98] when even a periodic behavior of the gamma-ray emission was observed by the Telescope Array [H+98] and HEGRA [Kra99,K+01]. MAGIC observed Mkn 501 in an extreme outburst in 2005, showing a strong correlation of the spectral shape on the observed flux [A+07f]. Since that time it has been observed with the MAGIC telescope, resulting in over 90 hrs of observations on 103 days, presented in Figure 6.2. Subsets of these data have already been published separately [A+07f, A+09j, A+11g, FMV+10].

6.2 Conclusion and Outlook

Results of the long-term monitoring campaign conducted over six years with the first MAGIC telescope were presented. Further studies on the flux state distribution, the spectral slope dependence on the flux and correlations with other wavelengths for Mkn 421 and Mkn 501 are ongoing and will be presented in [12]. Results of the MAGIC monitoring and multi-frequency observations of 1ES 1959+650 will be presented in chapter 7.

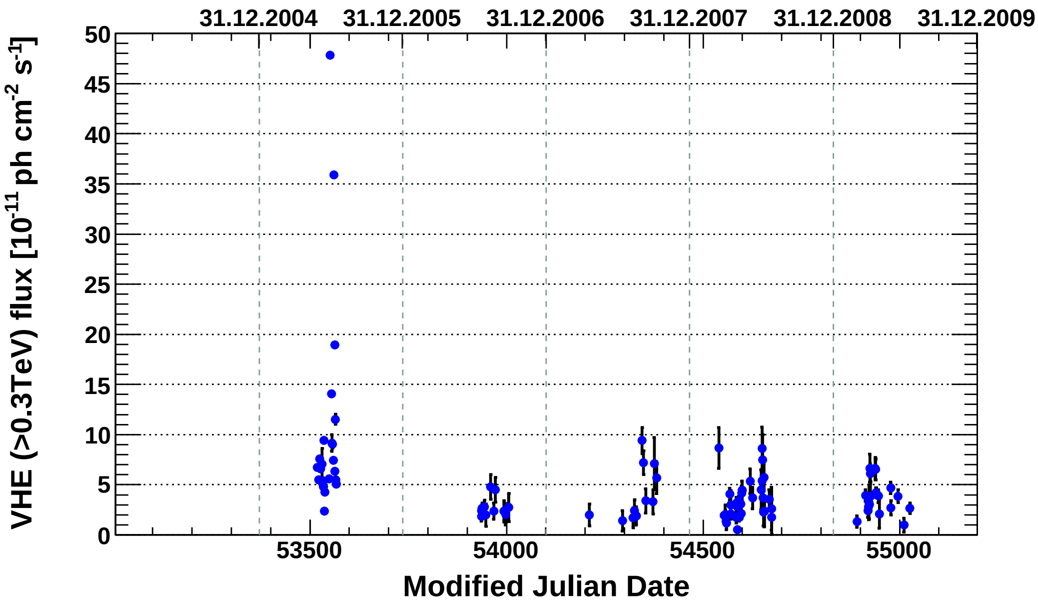

Figure 6.2: MAGIC lightcurve of Mkn 501 observed above 0.3 TeV from 2005 until 2009. Observations less significant than $1\,\sigma$ have been omitted.

Although there are ongoing monitoring programs of bright blazars with MAGIC [GB+08, B+07a, H+09b] and until recently with Whipple [S+08c], those observations – which occur especially in the case of MAGIC at most of about 30 min duration – are far from being complete and thus can complement the full-time IceCube or Fermi–LAT observations only in a very limited way. But as the latest generation Cherenkov telescopes, such as MAGIC, H.E.S.S., and VERITAS are overbooked with discovery observations at their sensitivity limit or deep multi-wavelength observations of known sources, it is obvious that these instruments cannot assign more precious observation time to time-consuming monitoring observations. This issue as well as using ground-based gamma-ray observatories with exposures limited by dark-time lead to the fact that a global network of several telescopes needs to be set-up to carry out full-time measurements – this is the starting point for the DWARF network, first proposed in [B+08c] and outlined in chapter 8.

Chapter 7
The Blazar 1ES 1959+650

7.1 Basic Properties of 1ES 1959+650

The blazar 1ES 1959+650[1] was first observed in X-rays within the Einstein Slew Survey [E+92] with the Imaging Proportional Counter[2] [GHF81] aboard the Einstein Observatory[3] [G+79]. It was subsequently identified as a BL Lacertae object by a combined X-ray/radio/optical technique [S+93a], supplying also optical spectroscopy measurements, revealing a flat and featureless spectrum with no emission lines (see also [M+96]) and only few absorption lines from which a redshift of $z = 0.047$ was derived [S+93a]. In a later analysis of the whole Einstein Slew Survey for BL Lacertae objects, optical spectroscopic measurements, taken with the 2.1 m telescope and the Goldcam spectrograph at Kitt Peak National Observatory, were presented (see Figure 7.1), yielding a higher signal to noise ratio and leading to a redshift estimate of $z = 0.048$ [P+96]. Also optical polarization of $(2.76{\pm}0.25)\%$ and $(2.92{\pm}0.41)\%$ with polarization angles of $147.1^\circ{\pm}2.1^\circ$ and $163.4^\circ{\pm}4.0^\circ$, respectively, have been observed [P+96], supporting the BL Lacertae classification and even showing variability in the polarization angle.

7.1.1 Host Galaxy

Optical high-resolution observations for 990 s with NOT (see section 3.2) in July 1996 revealed an unusual radial brightness profile, significantly deviating from a de Vaucouleurs profile [de 48] of an elliptical galaxy. The data was best described by a three component (core, disc, and bulge) model with position angles changing from 95° at a radius $r = 3''$ to 140° at $r = 15''$ and a diminishing excentricity from 0.2 to 0. Additionally, a dust lane was observed $\sim 1''$ north of the center in the E-W direction, roughly oriented along the major axis of the host galaxy [H+99b], see Figure 7.2. These findings have been confirmed by Hubble Space Telescope WFPC2 (see section 3.3.1) observations of a dust lane $0.8''$ north of the nucleus of 1ES 1959+650 [S+99, F+00].

[1] $RA = 19\,\mathrm{h}\ 59\,\mathrm{m}\ 59.8\,\mathrm{s}$, $Dec = +65\,\mathrm{d}\ 08\,\mathrm{m}\ 55\,\mathrm{s}$ in EquJ2000.0 coordinates

[2] **I**maging **P**roportional **C**ounter, IPC

[3] also **H**igh **E**nergy **A**stronomy **O**bservatory 2, HEAO 2, see http://heasarc.gsfc.nasa.gov/docs/einstein/heao2.html

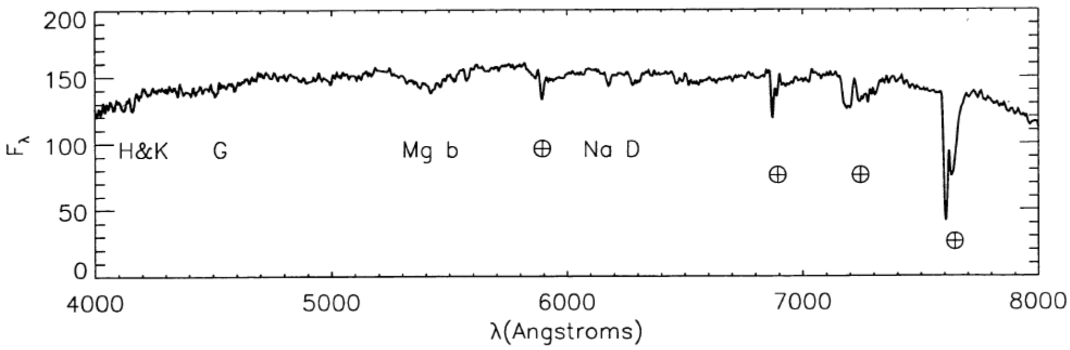

Figure 7.1: Optical Spectroscopy of 1ES 1959+650 showing a featureless spectrum with no emission lines [P+96].

7.1.2 Central Black Hole

The mass of the black hole in the center of 1ES 1959+650 amounts to about $10^{8.3}\,M_\odot$. An overview of the values stated in the literature is given in Table 7.1. There are three types of methods used to derive the mass M of the black hole either relating it to the variability time scale, to the velocity dispersion σ of the central area around the black hole, or to the host luminosity. Notably, the variability time scale used in [M+10] is seven hours from VHE gamma-ray observations [H+03a], as no optical micro-variability, i.e. short-term flux variations, has been observed from 1ES 1959+650, neither in 1994 [Cam04], nor in 2003 [X+02], or 2005 [Pog06].

Method	Reference	$\log_{10}\left(\frac{M}{M_\odot}\right)$	Reference
Time scale	[X+02]	≤ 8.6	[M+10]
Velocity dispersion	[MF01a]	8.12 ±0.13	[FKT02]
	[MF01b]	8.30	[WLZ02]
	[G+00]	8.22	[WLZ02]
	[B+03b]	8.15 ±0.17	[F+03]
	[T+02]	7.96 ±0.16	[W+05]
	[WU02]	8.1	[M+10]
Luminosity	[MD03]	8.3	[FKT02]
	[B+03b]	8.56	[F+03]
	[B+03b]	8.53	[FCT03]

Table 7.1: Overview of the values for the mass of the central black hole in 1ES 1959+650 derived by different methods.

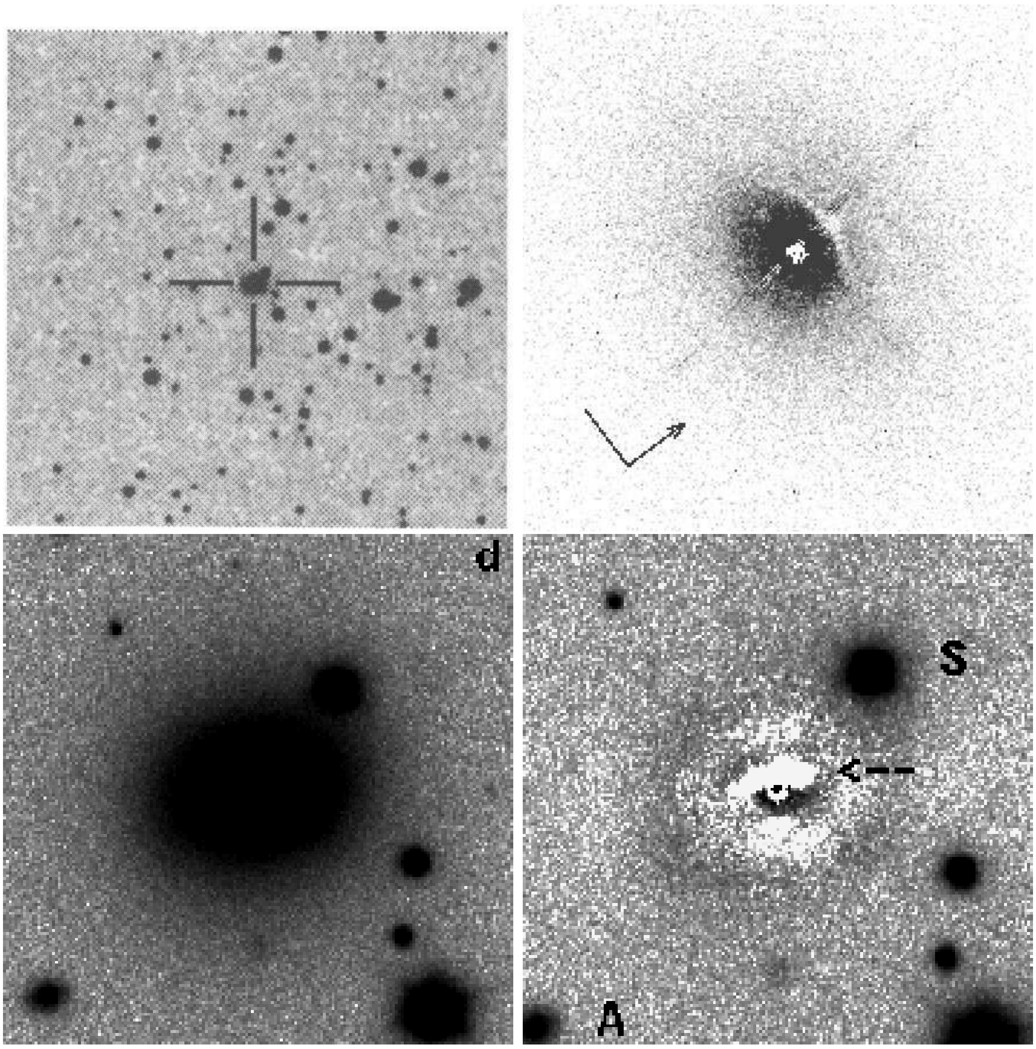

Figure 7.2: Optical images of 1ES 1959+650 by [P+96] (top left), Hubble Space Telescope [S+99] (top right), with the arrow pointing north, and NOT, before (bottom left) and after galaxy subtraction (bottom right), where in the latter the dust lane is indicated by an arrow [H+99b].

7.1.3 Radio Morphology

The radio morphology of 1ES 1959+650 has deeply been studied with VLA observations at 1.4 GHz [RGS03, G+04b] and with VLBA observations at 5 [RGS03, B+04d], 15.4 [PE04, PPE08, L+11a], 22.2 [PPE08, PPE10], and 43 GHz [PPE10], respectively.
Pictures of the VLA and 43 GHz VLBA observations are given in Figure 7.3. Basic source parameters derived from those observations are summarized in Table 7.2. The Doppler factor δ depends on the Lorenz factor γ (see Equation 2.8) and the viewing angle θ as

$$\delta = \frac{1}{\gamma\,(1 - \beta_\gamma \cos\theta)}. \tag{7.1}$$

There is no counter jet observed but an upper limit on the luminosity is given as $\leq 1/8$ of the luminosity of the visible jet [G+04b].

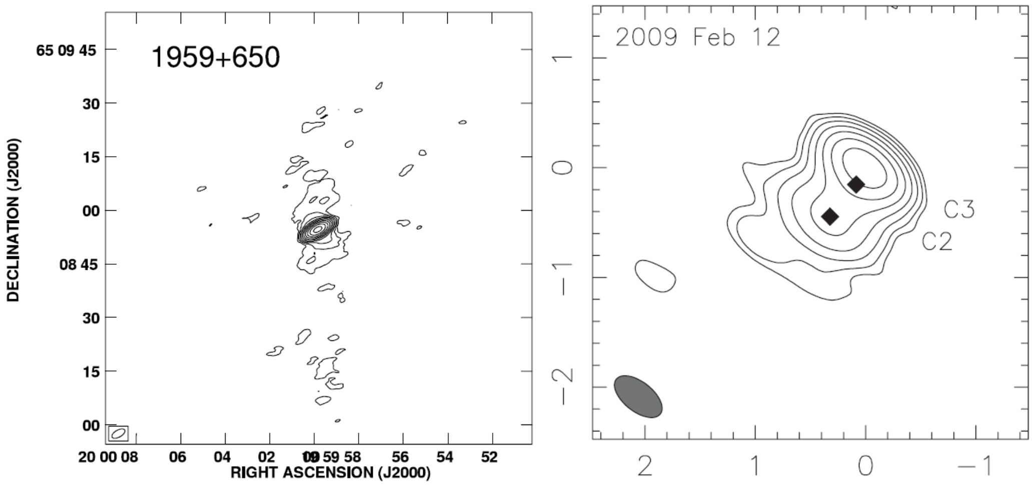

Figure 7.3: Radio Morphology of 1ES 1959+650. Depicted are VLA observations at 1.4 GHz [G+04b] (left) and 43 GHz VLBA observations [PPE10] (right). For the latter the scale on the axis is mas.

7.2 Temporal Behavior of 1ES 1959+650

7.2.1 Radio Observations

Apart from the morphological studies reported in section 7.1, monitoring observations of the 15 GHz radio flux have been conducted with UMRAO [K+04b, G+06b], within the MOJAVE program [L+11a], with OVRO [Pan11] and with the Effelsberg 100 m telescope within the F-GAMMA program [FA11]. These data are depicted in Figure 7.4. The large values reported in 2003 are accompanied with extremely large average relative errors of $(51{\pm}19)\%$ compared to average relative errors of $(3.1 \pm 0.4)\%$ and $(2.1 \pm 0.4)\%$ for Effelsberg 100 m and OVRO data, respectively. Thus, the UMRAO data will be excluded from further analysis. Additional data, especially for spectral studies presented in section 7.3, have been retrieved from RATAN-600 [A+10e], Metsähovi [LTN11], IRAM [FA11] and from NED[4] for GBT 91 m, WSRT, and UTRAO.

7.2.2 Optical Observations

Besides the searches for optical micro-variability reported in section 7.1, 1ES 1959+650 has been subject of several optical monitoring campaigns. The Abastumani Astrophysical Observatory started monitoring observations in May 1997 [Kap09, K+09c] (see Figure 7.5) but as a publication on those is pending, they may not be used for further analysis in the course of this thesis. The latter holds also true for optical data taken in the course of a

[4] **N**ASA/IPAC **E**xtragalactic **D**atabase, NED, see http://ned.ipac.caltech.edu

Reference	Apparent Speed [c]	PA [°]	EVPA [°]	Pol [%]
[RGS03]		-5 (VLA)		
		-5 (VLBA)		
[PE04] (c1)		158.1–159.9		
(c2)	0.1	134-140.5		
[B+04d] (core)			$\pm 36^a$	1.5
(jet)		≈ 0	$\pm 13^a$	4
[G+04b]		-5		
[PPE08] (c2)		124.0–126.7		
[PPE10] (core)			-59.4	3.9
(c2)	0.1±0.02		-32.6	4.0
[L+11b] (core)		139	149	2.3
[L+11a]			143–156	2.1–3.7

Reference	α [°]	$\theta_{\gamma=3}$ [°]	$\theta_{\gamma=5}$ [°]	$\theta_{\gamma=10}$ [°]	$\delta_{\gamma=5}$
[PE04]				0.8	
[G+04b]	16–26		16–26		1.7–3.3
[G+06a]		17 ± 5^b			3.4^b
[W+07]		6.9	11.1	9.7	5.2
[P+09b]	37.6		—		—
[L+11b]	37				

[a] Only PA−EVPA given in [B+04d].
[b] Assuming $\gamma \approx 1/\sin\theta \approx 3.4$.

Table 7.2: Radio morphology parameters. The apparent speed is given in units of the speed of light, PA denotes the position angle of the jet (component), EVPA is the electron vector position angle and gives the direction of the linear polarization, and Pol gives the intensity of polarized emission in percent. α is the jet opening angle, θ the angle to the line of sight, and δ the Doppler factor for a given Lorenz factor γ.

multi-wavelength campaign with the WIYN[5] 0.9 m telescope[6] in 2006 and 2007[7] [Fie07], see Figure 7.5.
The vast majority of the optical observations have been conducted in R-band. Most of those data have been taken in the context of the Tuorla blazar monitoring program [T+07a] with the 1.03 m telescope at the Tuorla Observatory, and the 35 cm telescope at the KVA Observatory[8]. The aim of this monitoring program is to study the connection between optical and VHE gamma-ray mission from blazars [L+09d]. Data from the Perugia AIT have been obtained from [T+08a]. The Goddard Robotic Telescope, New Mexico Skies, and

[5] University of **W**isconsin, **I**ndiana University, **Y**ale University, and **N**ational Optical Astronomy Observatory (NOAO), WIYN
[6] see `http://www.noao.edu/0.9m`
[7] see `http://www.astro.wisc.edu/~fields/pages/Project.html`
[8] see `http://users.utu.fi/~kani/1m`

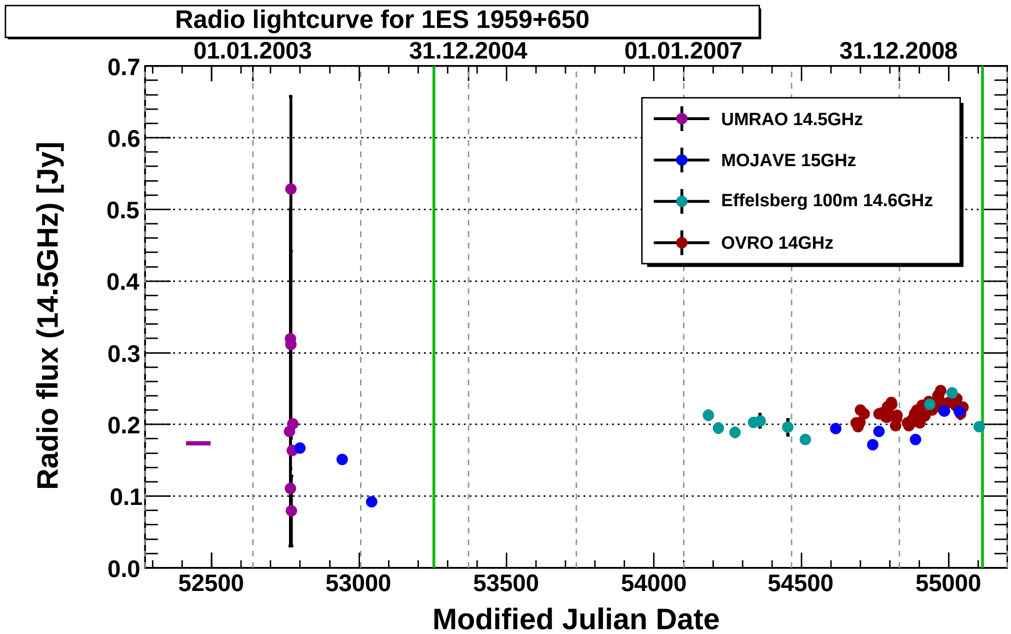

Figure 7.4: Radio lightcurve of 1ES 1959+650 in the frequency range of 14.5 GHz obtained from UMRAO [G+06b], MOJAVE, Effelsberg 100 m [FA11], and OVRO [Pan11]. The magenta horizontal line indicates the average flux that was observed in 2002 with UMRAO [K+04b]. The green vertical lines denote the observation window of the MAGIC monitoring campaign.

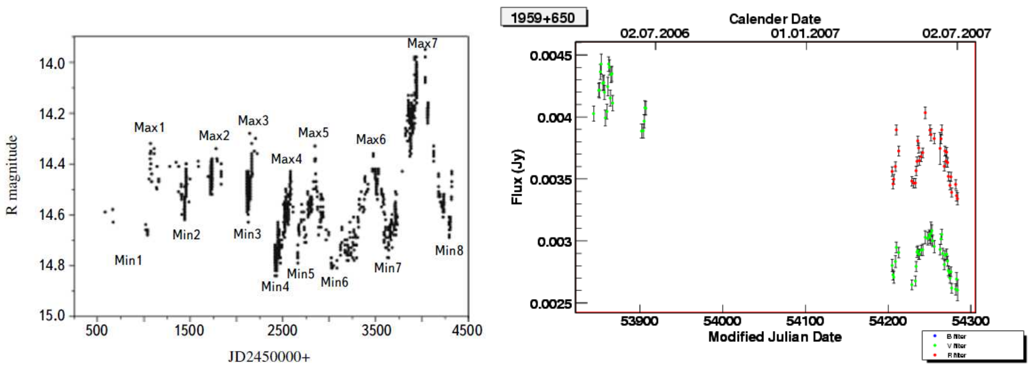

Figure 7.5: Optical lightcurves of 1ES 1959+650 by Abastumani [Kap09] (left) and WIYN [Fie11] (right).

Tenagra-II delivered data in R- and V-band [Pan11]. Swift–UVOT observations have been acquired from [T+08a], and INTEGRAL–OMC data are retrieved via HEAVENS[9] [W+10]. For all optical measurements the host galaxy flux has been subtracted, in R-band according to [N+07b] and in V-band following the $z = 0$ approximation from the model of [FSI95], stating $F_{\mathrm{V}} - F_{\mathrm{R}} = 0.61\,\mathrm{mJ}$. The resulting optical lightcurve is displayed in Figure 7.6.

[9] **H**igh-**E**nergy **A**strophysics **V**irtually **En**lightened **S**ky, HEAVENS, see http://www.isdc.unige.ch/heavens

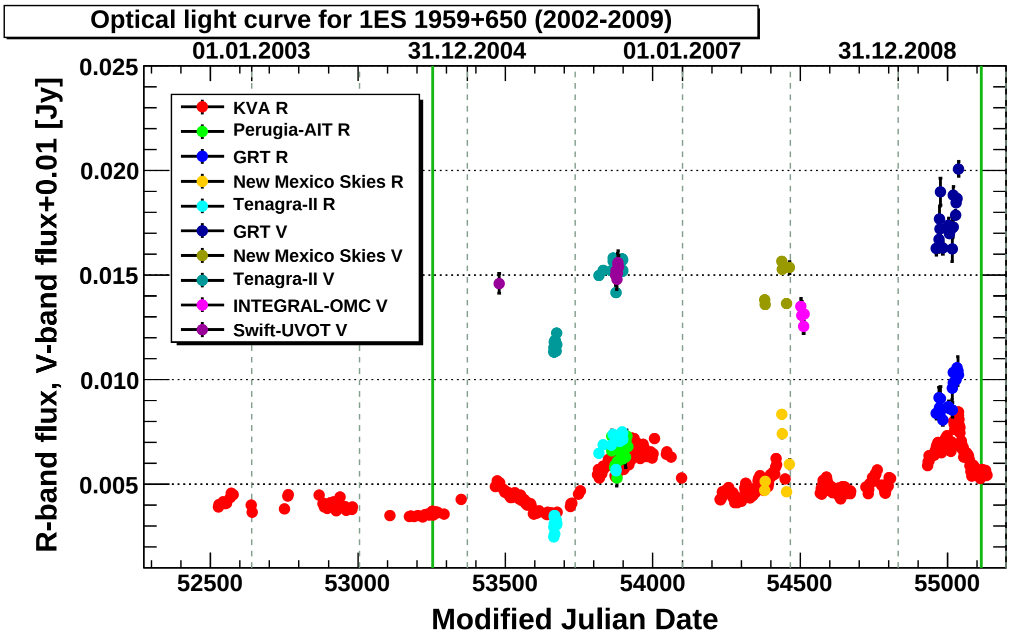

Figure 7.6: Optical lightcurve of 1ES 1959+650 compiled by the data mentioned in the text. The green vertical lines denote the observation window of the MAGIC monitoring campaign.

7.2.3 X-Ray Observations

After the detection with HEAO 2 [S+93a], 1ES 1959+650 was also observed with ROSAT[10] [Tru82] and listed in the ROSAT all-sky bright source catalog [V+99a], it was observed with RXTE–PCA from July till September 2000 and with the USA[11] [R+01] experiment aboard ARGOS[12] from October until November 2000 [G+02]. *Beppo*SAX observed 1ES 1959+650 in May 1997 [B+02] and in September 2001, and hence it was included in the spectral catalog of six years of observations [DSG05], reporting broken power-laws with spectral breaks around 1 keV. Additionally, it was included in the "*Beppo*SAX–WFC[13] [J+97] X-ray source catalogue" [V+07], which reports a mean unabsorbed flux between 2–10 keV of $(9.6\pm4.4)\cdot10^{-11}$ erg cm^{-2} s^{-1}, whilst the minimum and maximum values are reported as 4.6 and $25.0\cdot10^{-11}$ erg cm^{-2} s^{-1}, respectively, indicating strong variations. The pointed observations report according fluxes of 1.38, 8.3, and $10.60\cdot10^{-11}$ erg cm^{-2} s^{-1} [DSG05]. Fluxes (again between 2–10 keV) reported by Swift–XRT in April 2005 and additional data taken during a multi-wavelength campaign in 2006 are reported by [T+07b] and [T+08a]. Data obtained with XMM-Newton–EPIC in November 2002, January and February 2003 are reported in [P+05]. A comprehensive overview of *Beppo*SAX, XMM-Newton–EPIC and Swift–XRT pointed X-ray observations

[10] **Rö**ntgen**sat**ellit, ROSAT, *ger.:* X-ray Satellite, see http://www.dlr.de/dlr/en/desktopdefault.aspx/tabid-10424

[11] **U**nconventional **S**tellar **A**spect, USA

[12] **A**dvanced **R**esearch and **G**lobal **O**bservation **S**atellite, ARGOS

[13] **W**ide **F**ield **C**amera, WFC, two X-ray cameras aboard *Beppo*SAX with wide fields of view, perpendicular to the pointed observations.

is given in [M+08b], from which also the spectral data points depicted in Figure 7.19 are retrieved. The all-time lightcurve of X-ray fluxes between 2–10 keV can be seen in Figure 7.7. For this, 75 counts s^{-1} in RXTE–ASM correspond to the flux of the Crab Nebula in that energy range [G+02][14], which is measured as $1.7 \cdot 10^{-11}$ erg cm^{-2} s^{-1} [G+02]. Additionally, the daily RXTE–ASM observations have been averaged over 20 observations. Time integrated fluxes reported by *Beppo*SAX and Suzaku are given in Table 7.3.

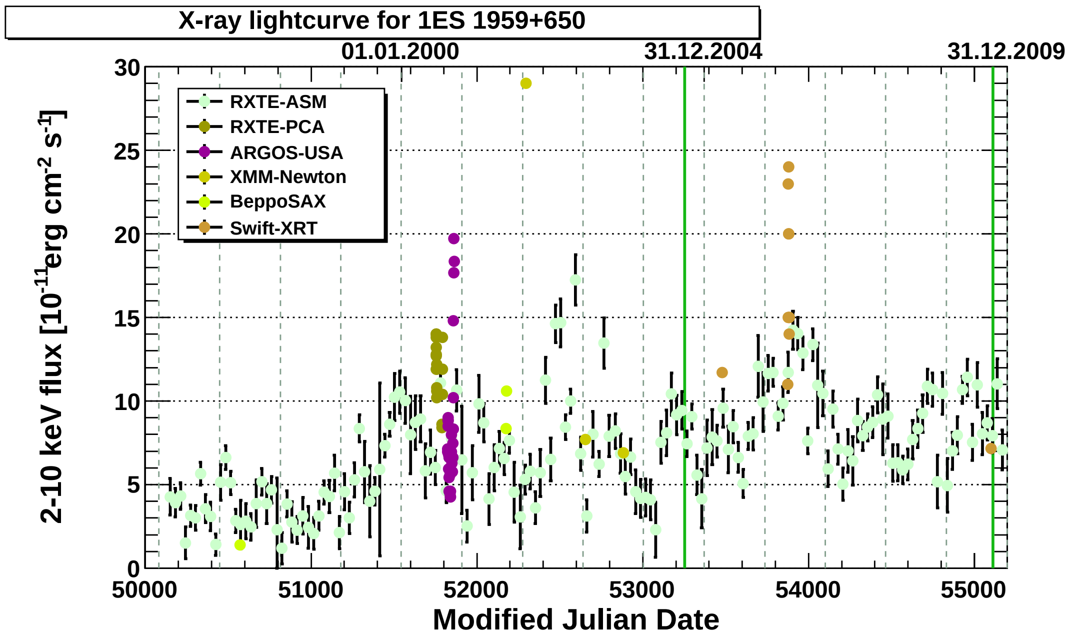

Figure 7.7: X-ray lightcurve of 1ES 1959+650 in the energy range of 2–10 keV compiled by the data mentioned in the text. The daily RXTE–ASM fluxes have been averaged over 20 observations, denoted by the horizontal bars. The green vertical lines denote the observation window of the MAGIC monitoring campaign.

Additional spectral information are acquired from time-integrated observations by RXTE–PCA, RXTE–HEXTE [RMR11] and Swift–BAT, see Figure 7.19. For the latter several time windows have been published: nine months[15] [T+08d], 22 months[16] [T+10e], and 58 months[17] [B+10b]. Observing in an all-sky survey mode, daily quick-look results have been provided by the ASM/RXTE team[18]. Swift–BAT transient monitor results between 15–50 keV are provided by the Swift–BAT team[19] and are shown in Figure 7.9. Additionally, regular monitoring of LAT Monitored Sources (see below) is done with Swift–XRT in the energy range of 0.3–10 keV within the Swift Monitoring Program[20], see Figure 7.8.

[14] The same number is given at http://xte.mit.edu/ASM_lc.html.
[15] see http://heasarc.gsfc.nasa.gov/docs/swift/results/bs9mon
[16] see http://heasarc.gsfc.nasa.gov/docs/swift/results/bs22mon
[17] see http://heasarc.gsfc.nasa.gov/docs/swift/results/bs58mon
[18] see http://xte.mit.edu/ASM_lc.html
[19] see http://heasarc.gsfc.nasa.gov/docs/swift/results/transients
[20] see http://www.swift.psu.edu/monitoring

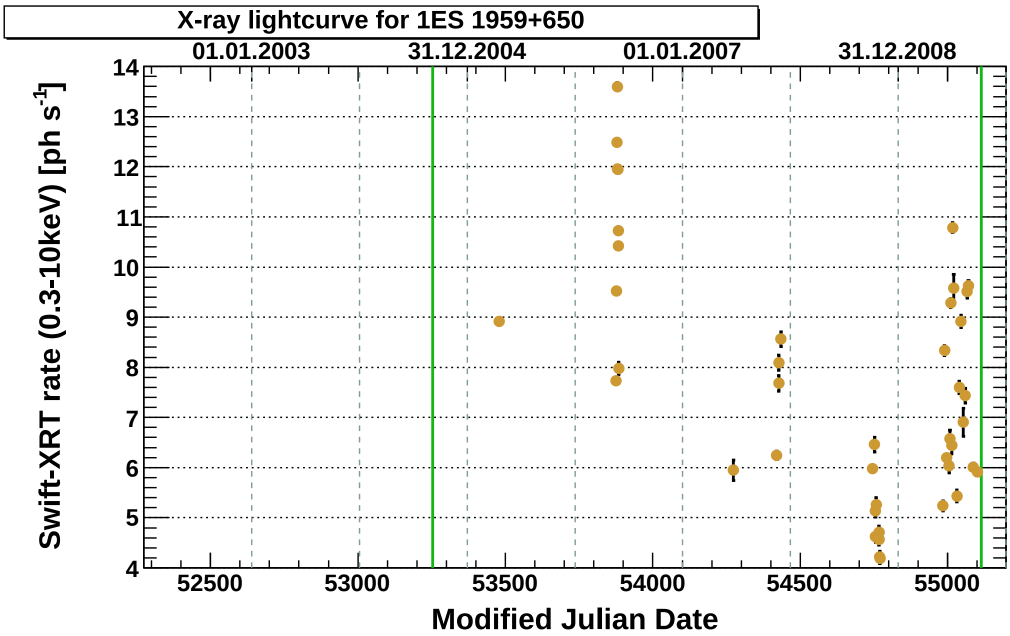

Figure 7.8: X-ray lightcurve of 1ES 1959+650 in the energy range of 0.3–10 keV obtained from Swift–XRT. The green vertical lines denote the observation window of the MAGIC monitoring campaign.

Instrument	Reference	Date	Date [MJD]	$F_{2-100\,\mathrm{keV}}$ $[10^{-11}\,\mathrm{erg\,cm^{-2}\,s^{-1}}]$
*Beppo*SAX–WFC	[V+07]	1996 - 4		
		until 2002 - 4		9.6±4.4
Suzaku	[T+08a]	2006 - 5 - 24±1	53879±1	20

Table 7.3: Time integrated X-ray fluxes between 2–10 keV reported by *Beppo*SAX–WFC [V+07] and Suzaku [T+08a] for the given time windows.

7.2.4 Gamma-Ray Observations

INTEGRAL–IBIS Although neither being listed in the second INTEGRAL AGN catalog [B+09e] nor in the INTEGRAL–IBIS 7-year catalog [KTR+10], an integral flux of 1.9±0.4 erg $\mathrm{cm^{-2}\,s^{-1}}$ between 20–200 keV has been reported in [BRS09]. Anyway, it was detected in November 2007 with a significance of 5.3 σ during two days [B+07d], triggering pointed Swift observations [B+07b] and resulting in a multi-wavelength SED modeling of this INTEGRAL high state of 1ES 1959+650 [B+10c].

CGRO–COMPTEL As neither a detection of 1ES 1959+650 was reported in the first COMPTEL catalog [S+00], nor upper limits have been published [S+08b] in the course of this thesis a reanalysis of COMPTEL data was triggered. This resulted in the first available upper limits for this source, based on all CGRO–COMPTEL data taken between

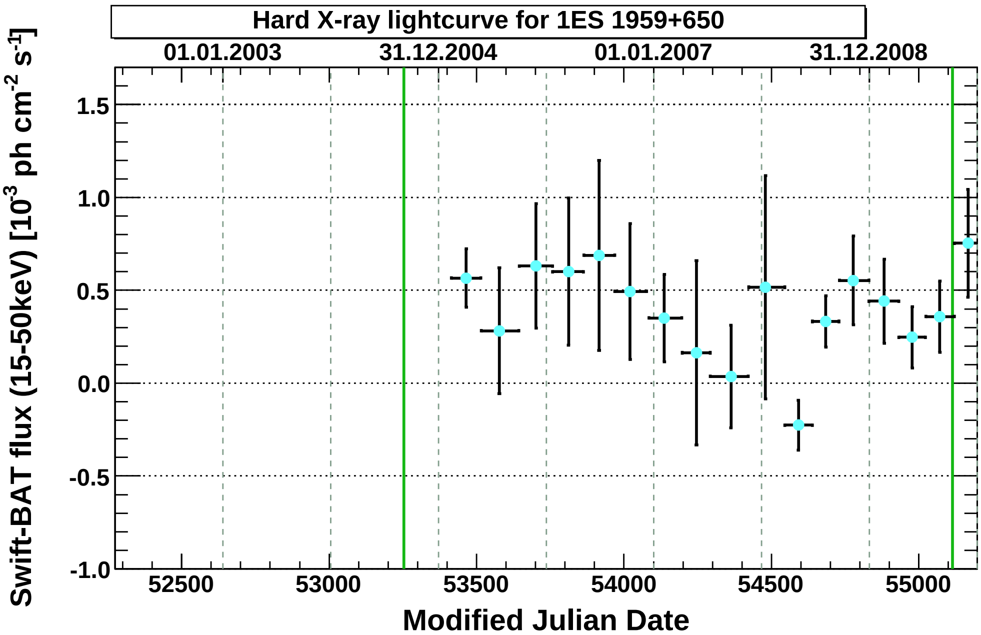

Figure 7.9: Hard X-ray lightcurve of 1ES 1959+650 in the energy range of 15–50 keV obtained from Swift–BAT. The daily fluxes have been averaged over 91 observations, denoted by the horizontal bars. The green vertical lines denote the observation window of the MAGIC monitoring campaign.

April 1991 and June 2000 [Col11c]. The values of $2\,\sigma$ upper limits under the assumption of an E^{-2} energy spectrum are given in Table 7.4.

ν [Hz]	νF_ν [erg/cm^2/s]	σ_ν^- [Hz]	σ_ν^+ [Hz]
3.985e+020	1.030e-010	1.744e+020	3.067e+020
1.248e+021	8.300e-011	5.428e+020	9.821e+020
3.985e+021	1.920e-010	1.755e+021	3.101e+021

Table 7.4: Spectral energy distribution upper limits based on all COMPTEL data [Col11c].

CGRO–EGRET 1ES 1959+650 was not detected with EGRET[21] aboard the CGRO neither in the third EGRET catalog [H+99a], nor in an revised version [CG08].

AGILE–GRID Neither being included in the first AGILE catalog [P+09a], nor in recent publications on TeV sources [R+11c], 1ES 1959+650 has been continuously observed by AGILE and a reanalysis of the data triggered in the course of this thesis led to the preliminary $2\,\sigma$ upper limit of $6.0 \cdot 10^{-8}\,\mathrm{cm^{-2}\,s^{-1}}$ for $E > 100\,\mathrm{MeV}$. [Lon11].

[21] **E**nergetic **G**amma **R**ay **E**xperiment **T**elescope, EGRET, see http://heasarc.gsfc.nasa.gov/docs/cgro/egret

Fermi–LAT 1ES 1959+650 was one of 42 BL Lacertae objects already detected with a significance of 10 σ after the first three months of observations with Fermi–LAT and thus included in the LBAS[22] [A+09c] and in the list of LAT Monitored Sources[23]. By this, daily and weekly flux averages above 100 MeV are available, but 1ES 1959+650 is such a weak source for Fermi–LAT that significant detections are very scarce on those timescales. In subsequent publications, a lightcurve of the first five months in monthly bining [A+09d], and a detailed energy spectrum based on the first six months of observations [A+10d] were presented. Later the first and second Fermi–LAT source catalogs were published, based on eleven months (1FGL) [A+10b] and two years (2FGL) [The11a] of data, respectively. These refined especially the energy spectrum as depicted in Figure 7.22. The most detailed lightcurve so far published comprises the first eleven months of data in weekly time bins with fluxes above 300 MeV [A+10c], see Figure 7.10.

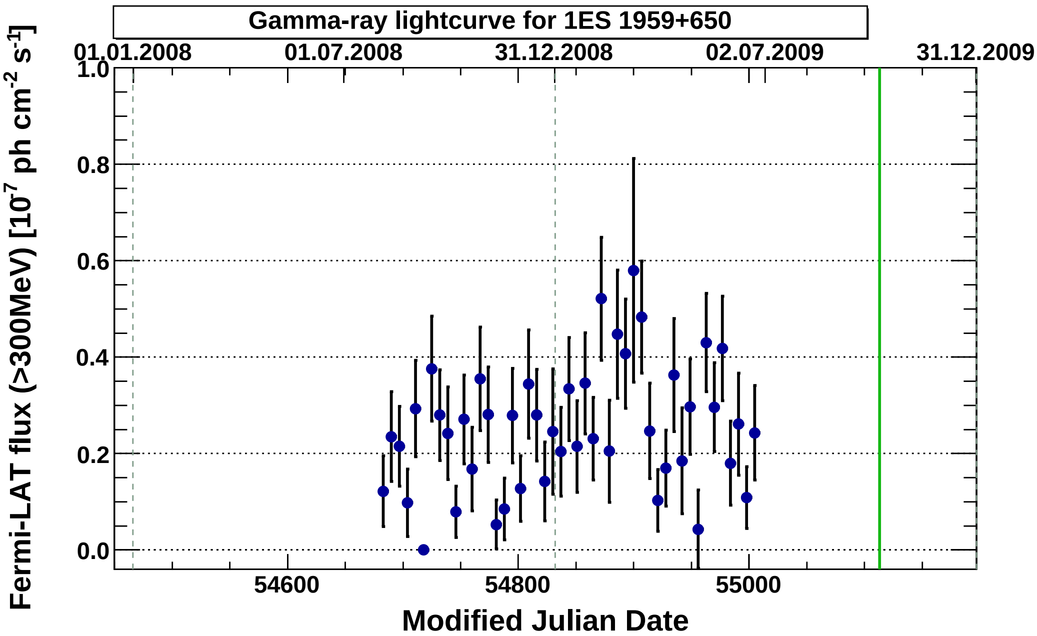

Figure 7.10: Gamma-ray lightcurve of 1ES 1959+650 in the energy range of >300 MeV obtained from Fermi–LAT [A+10c] in weekly time bins. The green vertical lines denote the observation window of the MAGIC monitoring campaign.

7.2.5 VHE Gamma-Ray Observations

After the upper limits had been reported by the Whipple [C+97,Buc99,H+04a] and CAT[24] collaborations [Khe02], the detection of 1ES 1959+650 was reported by the Utah Seven Telescope Array [Y+99] for data of 1997 at an overall significance level of 3.9 σ, with two subsets of the data passing the commonly applied 5 σ limit for source discoveries [Nis99], but without accounting for trials. The final undisputed detection was reported by the

[22] **L**AT **B**right **A**GN **S**ample, LBAS
[23] see http://fermi.gsfc.nasa.gov/ssc/data/policy/LAT_Monitored_Sources.html
[24] **C**herenkov **A**rray at **T**hémis, CAT

Whipple 10 m telescope in 2002 [Wo02,H+03a,H+03b], when the source underwent a strong flaring activity in VHE gamma-rays, also reported by the HEGRA system of Cherenkov telescopes [Hor03, A+03a], HEGRA CT1 [Kra03, TK03], and CAT [Khe02, DT03]. Later it was also detected by MAGIC (as outlined in detail below), by the GT-48 Cherenkov telescope of the Crimean Astrophysical Observatory in 2004 [Fid06] and recently by VERITAS [B+11d]. The flaring activity observed in 2002 triggered a multi-wavelength campaign, during which the first orphan flare was observed [K+04b], i.e. a gamma-ray flare without a simultaneously enhanced X-ray flux as expected from SSC models. Nevertheless, these and also subsequent multi-wavelength observations in 2003 [G+06b] and 2006 [H+08, T+08a] succeeded in explaining the observed spectral energy distribution by single-zone SSC models. An overview of the modeling so far is given in Table 7.11.

MAGIC Results

1ES 1959+650 was one of the first objects observed by MAGIC in 2004 [T+05, Tt06, Ton06], resulting in one of the very first MAGIC publications [A+06c]. Since then a regular monitoring has been conducted [GB+08, H+09b, S+09b, W+11a], resulting in ∼71 h of useful data, spread over 47 days with more than $1\,\sigma$ detections as shown in Figure 7.11. An overview of the observations through the different years is given in Table 7.5. For further details on the according analysis procedure and data selection criteria, the reader is referred to the references given in the table.
Also considering the previous publications [A+06c, T+08a], no significant flux variations have been observed for 1ES 1959+650 as discussed in subsection 7.2.8. For an overview and the discussion of the spectral properties see section 7.3.

Year	T_{obs} [h]	T_{eff} [h]	σ	$\sigma/\sqrt{\mathrm{h}}$	References	References for cross checks
2004	6.92	5.82	8.2	3.4	[Ton06, A+06c]	
2005	22.3	19.6	6.3	1.4	[Hay08]	[Sch06a, Zan06]
2006	17.4	14.3	10.4	2.8	[Hay08, T+08a]	[Bac08]
2007	18.79	12.77	10.6	3.0	[Uel09]	[Sat10]
2008	13.80	4.91	4.5	2.0	[Uel09]	[Sat10]
2009	22.03	13.86	9.7	2.6	[Uel12]	

Table 7.5: Spectral energy distribution upper limits based on all COMPTEL data.

7.2.6 Neutrino Observations

After the detection of a gamma-ray *orphan flare* in June 2002 [K+04b] two neutrinos have been observed from the direction of 1ES 1959+650 with the AMANDA-II neutrino telescope, one of them being coincident with the gamma-ray flare [Bf05, A+05a]. Although this coincidence has not been statistically significant, this conspicuous hint for hadronic acceleration processes within the source (c.f. subsection 2.4.2) triggered theoretical modeling [HH05, RBP05] as well as the search for time-clustered neutrino events from predefined source directions in IceCube [SBAe08]. Also a program for MAGIC follow-up ob-

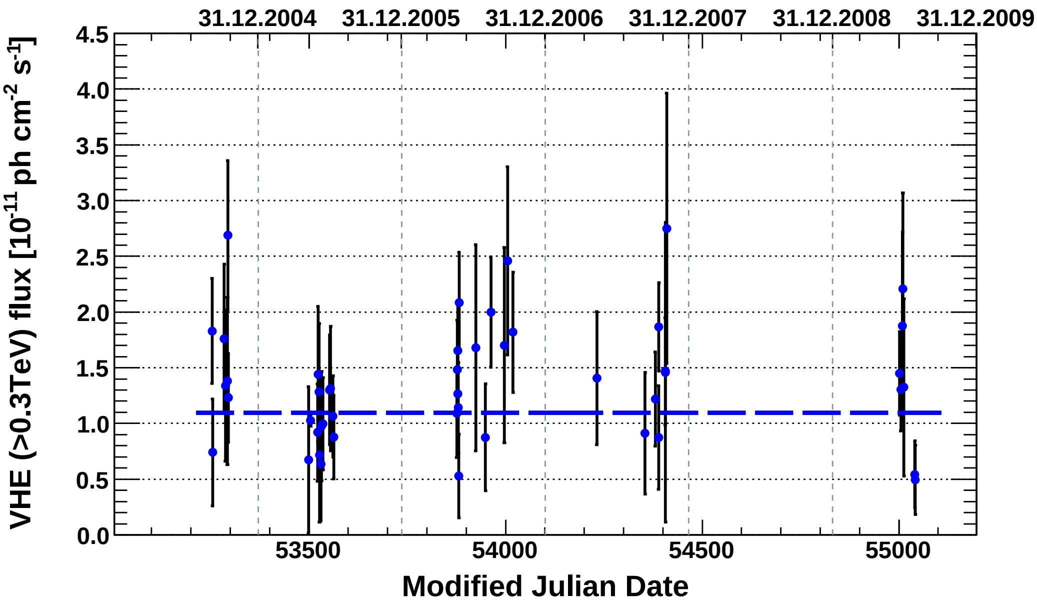

Figure 7.11: MAGIC lightcurve of 1ES 1959+650 observed above 0.3 TeV from 2004 until 2009. Observations less significant than 1 σ have been omitted.

servations in case of observed time-clustered neutrinos has been initiated [A+08e, A+07b]. Anyhow, none of the subsequent analyses neither of time-integrated data from AMANDA-II [Ack07, A+09b], IceCube (22 string configuration) [A+09a], or IceCube (40 string configuration) [A+11d], nor time-dependent analyses of IceCube (22 string configuration) [B+09d], or IceCube (40 string configuration) [A+11c] showed any significant excess, albeit this would be a crucial result.

7.2.7 Cosmic Ray Observations

In 2006 the HiRes collaboration reported on the cross-correlation of UHE cosmic rays with BL Lacertae objects. For 1ES 1959+650 they stated two events in excess of the expected background, which was only found in 0.8% of isotropic Monte Carlo sets [A+06a].

7.2.8 Fractional Variability F_{var}

To study the variability of a given data set, e.g. a time series, one has to distinguish between the intrinsic variability and the variations expected from measurement uncertainties. For this, in [V+03] the fractional variability amplitude F_{var} is derived. Diminishing the sample variance S^2 by the expected contribution from the measurement errors, the mean squared error

$$\overline{\sigma^2} = \frac{1}{N}\sum_{i=1}^{N}\sigma_i^2, \tag{7.2}$$

one gets the excess variance

$$\sigma_{\mathrm{XS}}^2 = S^2 - \overline{\sigma^2} \tag{7.3}$$

and by normalizing by $1/\overline{x}^2$ and extracting the root one gets the fractional variability amplitude

$$F_{\mathrm{var}} = \sqrt{\frac{S^2 - \overline{\sigma^2}}{\overline{x}^2}}. \tag{7.4}$$

The error on F_{var} is derived as

$$\sigma_{F_{\mathrm{var}}} = \sqrt{\left(\sqrt{\frac{1}{2N}}\frac{\overline{\sigma^2}}{\overline{x}^2 F_{\mathrm{var}}}\right)^2 + \left(\sqrt{\frac{\overline{\sigma^2}}{N}}\frac{1}{\overline{x}}\right)^2}. \tag{7.5}$$

In Figure 7.12 the values of the fractional variability according to Equation 7.4 are depicted for the lightcurves presented in subsection 7.2.2 to subsection 7.2.5 against the observation wavelength. For this calculation, only data points larger than 0 by more than $1\,\sigma$ have been considered. The according values are given in Table 7.6. One can clearly see that there is strong variability of up to 40% present in the optical and in X-ray lightcurves. Concerning the optical emission, the variations in R-band are significantly higher than those in V-band, for any single telescope measuring both, R- and V-bands and for all measurements of one band together. Except for the flare of 2003 discussed earlier, hardly any variability is seen in the radio emission. Due to the missing measurement uncertainties of any daily data presented in Figure 7.7, no fractional variability could be calculated for those lightcurves. The Swift–BAT lightcurve lacks highly significant observations, even in the used binning of 91 observations per bin and thus no variability could be detected. The Fermi–LAT lightcurve shows a medium level of variability, comparable with the overall R-band variability but lower than the variabilities in X-rays observed by RXTE–ASM on 20 days time-scale and by Swift–XRT on daily values.
Noteworthy, all MAGIC observations show no hint of variability. Except for 2004, where $F_{\mathrm{var}} = 0.07 \pm 0.56$, for all single years of data, i.e. 2005–2009, and for the lightcurve spanning all the six years, $F_{\mathrm{var}} = 0$ is obtained. This steady state in VHE gamma-rays of 1ES 1959+650 will be utilized in section 7.3 to obtain the most precise gamma-ray spectrum of that source up to now and to justify the modeling of a time-averaged spectral energy distribution.

7.2.9 Periodicities

Motivated by the theoretical implications of periodic signals in VHE gamma-ray lightcurves outlined in subsection 2.4.3 an initial study on this issue has been conducted. Based on the long-term VHE lightcurves of Mkn 421, Mkn 501 and 1ES 1959+650 compiled for [T+10c][25] the methods of [Pal09] and [Ree07] have been employed. As these yielded spurious periods of around 28 days, most probably being connected to periodic observational gaps due to

[25] see http://nuastro-zeuthen.desy.de/magic_experiment/projects/light_curve_archive/index_eng.html

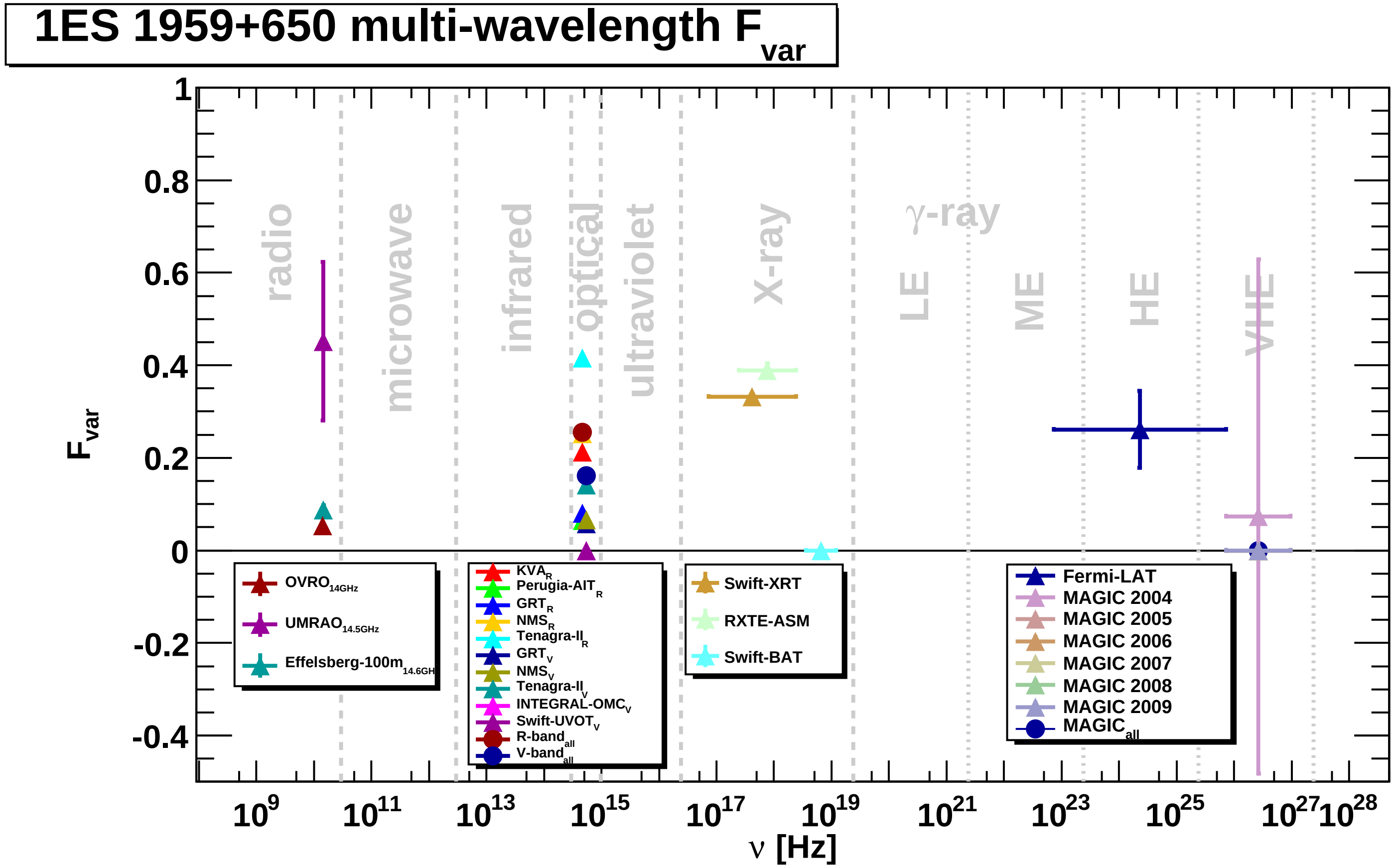

Figure 7.12: Fractional variability F_{var} against wavelength for 1ES 1959+650.

Instrument	Band	Binning [days]	F_{var}	$\sigma_{F_{\text{var}}}$	$\sigma_{F_{\text{var}}}/F_{\text{var}}$
OVRO	14 GHz	1	0.0528	0.0030	5.7%
UMRAO	14.5 GHz	1	0.4515	0.1712	37.9%
Effelsberg 100 m	14.6 GHz	1	0.0876	0.0105	12.0%
KVA	R-band	1	0.2130	0.0008	0.4%
Perugia–AIT	R-band	1	0.0651	0.0113	17.4%
GRT	R-band	1	0.0808	0.0097	12.0%
NMS	R-band	1	0.2529	0.0129	5.1%
Tenagra–II	R-band	1	0.4154	0.0019	0.5%
all R-band	R-band	1	0.2557	0.0009	0.4%
GRT	V-band	1	0.0578	0.0058	10.1%
NMS	V-band	1	0.0658	0.0045	6.8%
Tenagra-II	V-band	1	0.1420	0.0007	0.5%
INTEGRAL–OMC	V-band	1	0	—	—
Swift–UVOT	V-band	1	0	—	—
all V-band	V-band	1	0.1612	0.0024	1.5%
Swift–XRT	0.3–10 keV	1	0.3323	0.0022	0.7%
RXTE–ASM	2–10 keV	20	0.3891	0.0146	3.8%
Swift–BAT	15–50 keV	91	0		
Fermi–LAT	> 300 MeV	7	0.2610	0.0831	31.8%
MAGIC 2004	> 300 GeV	1	0.0735	0.5555	756.0%
MAGIC 2005	> 300 GeV	1	0	—	—
MAGIC 2006	> 300 GeV	1	0	—	—
MAGIC 2007	> 300 GeV	1	0	—	—
MAGIC 2008	> 300 GeV	1	0	—	—
MAGIC 2009	> 300 GeV	1	0	—	—
all MAGIC	> 300 GeV	1	0	—	—

Table 7.6: The fractional variability F_{var} for the different instruments and wavelengths.

full moon, an extensive overview of methods to search for signals in irregularly sampled datasets has been performed [6]. As we saw considerably scope to improve those methods, an unified approach, utilizing also robust regression methods has been developed [9]. This method bears a possibility to calculate a significance level also against the assumption of red noise in contrast to the usually assumed white noise. Anyhow, it is still not capable to cope with signals "leaking" into neighboring frequencies. More details on the forthcoming algorithms will be reported in [Thi12].

7.3 VHE Energy Spectrum of the Steady State of 1 ES 1959+650

7.3.1 VHE Energy Spectra

Very high energy gamma-ray spectra of the flaring state of 1ES 1959+650 in 2002 were reported by the HEGRA [K+04b], CAT [DT03] and Whipple collaborations [D+05]. Additionally, the HEGRA collaboration reported on an energy spectrum of any non-flaring state observations of that source from 2000–2002 [K+04b][26] and on a time averaged spectrum measured with HEGRA CT1 [Kra03, TK03, Ton06]. Those measurements, along with the spectra reported by MAGIC in 2004 and 2006 and with upper limits for the years 2000–2003 by Milagro are depicted in Figure 7.13. The huge differences in flux and spectral shape between the flaring state in 2002 and the non-flaring states are clearly visible. From 2004 through 2009 yearly energy spectra have been obtained with the MAGIC telescope. Table 7.8 gives an overview of all reported parameter values for power-law fits with and without exponential cut-off.

The data points of the energy spectra obtained with MAGIC are depicted in Figure 7.14. For any year, a power-law is fitted to the (colored) data points of the according main analysis. The parameters of the power-law fits $F(E) = p_0 \cdot (E/1\,\mathrm{TeV})^{p_1}$ are given in the inlays and also in Table 7.7. For 2008, only an integral upper limit above 300 GeV was reported in [Sat10]. This has been converted to a band of differential upper limits, assuming the given range of spectral slopes $\alpha = 2.1 \ldots 2.8$. One can see that for all years except 2007 the main and cross-check analyses are in good agreement. The disagreement of the values reported for KS2007 from those of MT2007 is still under investigation.

Year	$p_0 = F_{1\,\mathrm{TeV}}$ $[10^{-12}\,\mathrm{TeV}^{-1}\,\mathrm{cm}^{-2}\,\mathrm{s}^{-1}]$	$p_1 = \alpha$	E_{min} [TeV]	E_{max} [TeV]
2004	3.976 ± 0.575	-2.803 ± 0.1517	0.18	4.0
2005	1.578 ± 0.280	-2.597 ± 0.2457	0.15	3.0
2006	2.672 ± 0.356	-2.537 ± 0.1686	0.15	3.0
2007	2.498 ± 0.423	-2.496 ± 0.1894	0.20	3.0
2008	1.470 ± 1.034	-2.505 ± 0.7589	0.20	1.2
2009	2.141 ± 0.114	-2.582 ± 0.0963	0.18	4.0

Table 7.7: Parameters for uniform power-law fits $F(E) = F_{1\,\mathrm{TeV}} \cdot (E/1\,\mathrm{TeV})^{\alpha}$ to the VHE gamma-ray energy spectra of 1ES 1959+650.

[26] The slightly different spectral data reported in [Göt06] for the same observations are additionally listed in Appendix D, but will be neglected for further studies.

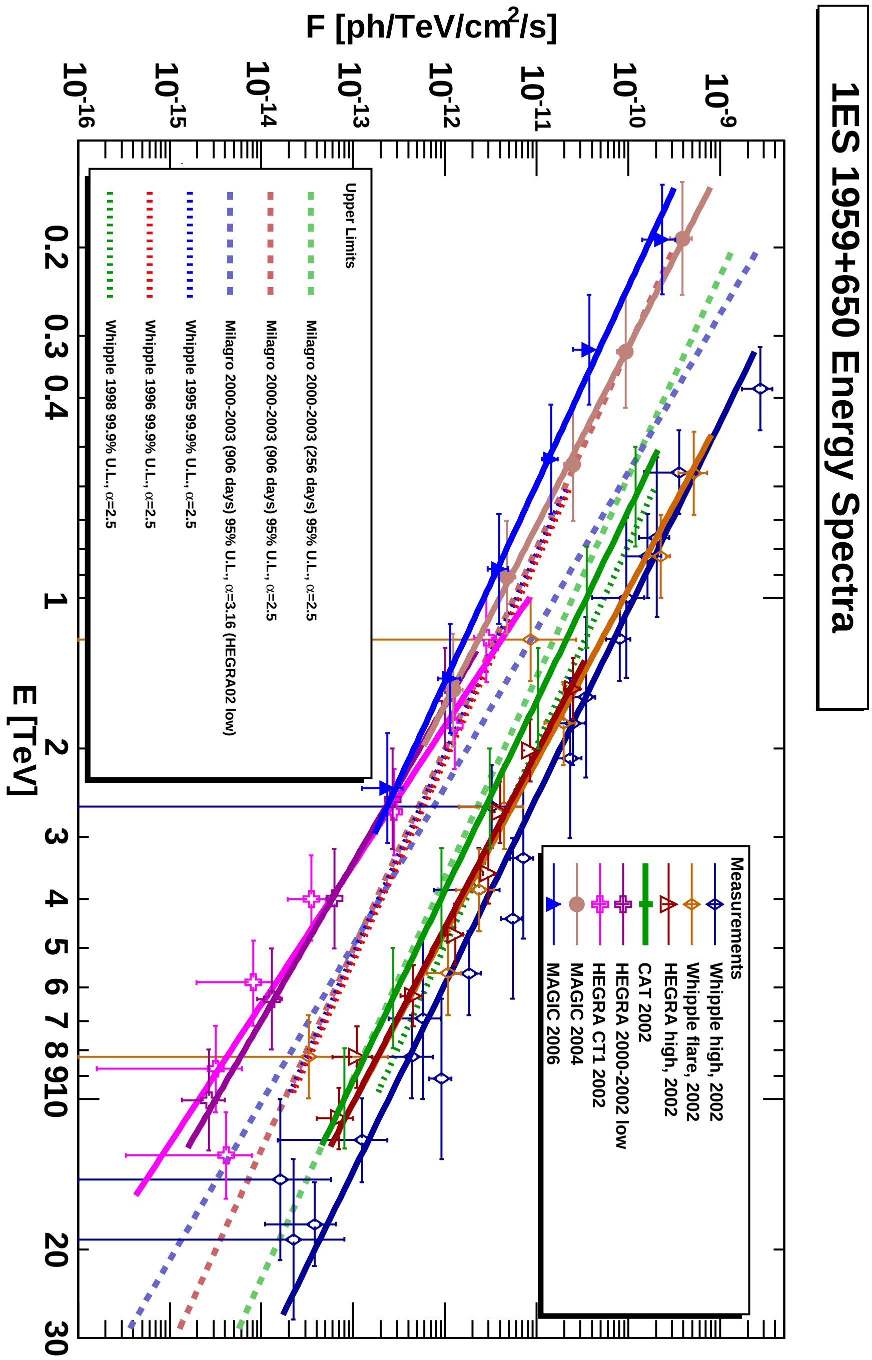

Figure 7.13: Energy spectra and upper limits on 1ES 1959+650. The references for the measurements are given in Table 7.8. The upper limits are reported in [H+04a] for the Whipple 10 m and in [Hay05, Wil05, Hay04] for Milagro.

Year	Reference	Instrument	$F_{1\,\mathrm{TeV}}$ $[10^{-12}\,\mathrm{TeV}^{-1}\,\mathrm{cm}^{-2}\,\mathrm{s}^{-1}]$	α	E_{cut} [TeV]	E_{min} [TeV]	E_{max} [TeV]
2009	[Uel12]	MAGIC	2.43 ± 0.37	-2.47 ± 0.15	—	0.18	4.0
	[Tes09]	MAGIC	2.40 ± 0.23	-2.66 ± 0.15	—	0.25	3.5
2008	[Uel12]	MAGIC	1.47 ± 1.03	-2.50 ± 0.78	—	0.20	1.2
2007	[Uel09]	MAGIC	2.52 ± 0.42	-2.47 ± 0.19	—	0.20	3.0
	[Sat10]	MAGIC	9.8 ± 0.6	-2.31 ± 0.05	—	0.15	9.0
	[Sat10] cut	MAGIC	60 ± 6	-2.13 ± 0.13	4.19 ± 2.05	0.15	9.0
2006	[Hay08]	MAGIC	2.7 ± 0.3	-2.58 ± 0.18	—	0.15	3.0
	[Bac08]	MAGIC	5.0 ± 2.3	-2.23 ± 0.58	—	0.215	1.25
2005	[Hay08]	MAGIC	1.6 ± 0.3	-2.62 ± 0.25	—	0.15	3.0
	[Zan06]	MAGIC	2.35 ± 0.52	-2.50 ± 0.32	—	0.20	1.8
	[Sch06a]	MAGIC	2.9 ± 0.9	-2.1 ± 0.4	—	0.20	2.0
2004	[Ton06]	MAGIC	4.3 ± 0.5	-2.72 ± 0.14	—	0.15	2.0
2002	[D+05] flare	Whipple 10 m	107 ± 16	-2.81 ± 0.15	—	0.47	10.0
	[D+05] high	Whipple 10 m	123 ± 26	-2.78 ± 0.12	—	0.32	27.6
	[D+05] high cut	Whipple 10 m	137 ± 24	-2.39 ± 0.26	$11.2\,^{+7.7}_{-6.6}$	0.32	27.6
	[A+03a] high	HEGRA	74 ± 13	-2.83 ± 0.14	—	1.30	12.7
	[A+03a] high cut	HEGRA	56 ± 9	-1.83 ± 0.15	$4.2\,^{+0.8}_{-0.6}$	1.30	12.7
	[Khe02] high	CAT	35.2 ± 0.24	-2.64 ± 0.08	—	0.50	12.5
	[Khe02] high cut	CAT	90.6 ± 36.6	-1.27 ± 0.55	1.33 ± 5.08	0.50	12.5
	[Ton06]	HEGRA CT1	8.3 ± 1.3	-3.6 ± 0.17	—	1.00	20.0
	[Ton06] cut	HEGRA CT1	13.2 ± 3.4	-1.8	1.28 ± 0.18	1.00	20.0
2000–2002	[A+03a] low	HEGRA	7.8 ± 1.5	-3.18 ± 0.17	—	1.30	12.7
	[A+03a] low cut	HEGRA	6.0 ± 1.4	-1.8	$2.7\,^{+0.6}_{-0.4}$	1.30	12.7

Table 7.8: Parameters for power-law fits $F(E) = F_{1\,\mathrm{TeV}} \cdot (E/1\,\mathrm{TeV})^{\alpha}$ to the VHE gamma-ray energy spectra of 1ES 1959+650. The notation *cut* indicates a fit with a power-law with exponential cut-off, $F(E) = F_{1\,\mathrm{TeV}} \cdot (E/1\,\mathrm{TeV})^{\alpha} \cdot \exp(-E/E_{\mathrm{cut}})$.

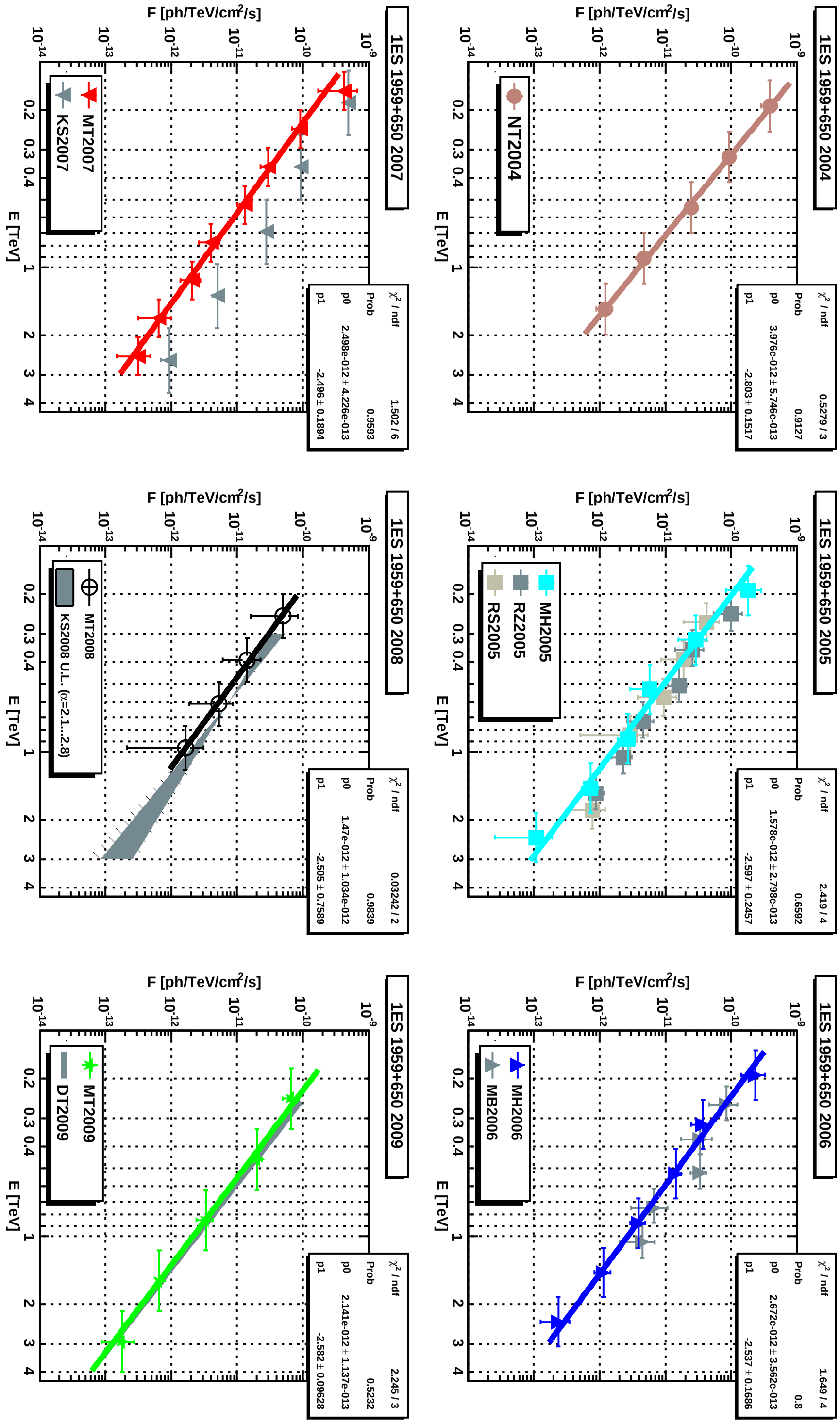

Figure 7.14: Energy spectra of 1ES 1959+650 as measured with MAGIC: NT2004 [Ton06], RZ2005 [Zan06], RS2005 [Sch06a], MH2005 [Hay08], MH2006 [Hay08, T^+08a], MB2006 [Bac08], MT2007 [Uel09], KS2007 and KS2008 [Sat10], MT2008 and MT2009 [Uel12], DT2009 [Tes09].

In Figure 7.15 the flux normalization $F_{1\,\mathrm{TeV}}$ is plotted against the spectral index α of the power-law fits to the energy spectra obtained with MAGIC from 2004–2009. From the covariance matrix of those data points, the error ellipses of the clustered data are drawn for confidence intervals of 1–5 σ. The ellipses are drawn around the average of the data points, with multiples of the standard deviations as radii. The angle of the ellipse is determined by

$$\phi = \frac{1}{2} \arctan\left(2 \frac{cov(x,y)}{\sigma_x^2 - \sigma_y^2}\right). \tag{7.6}$$

One can clearly see that all but the observations of 2004 fit together perfectly well.

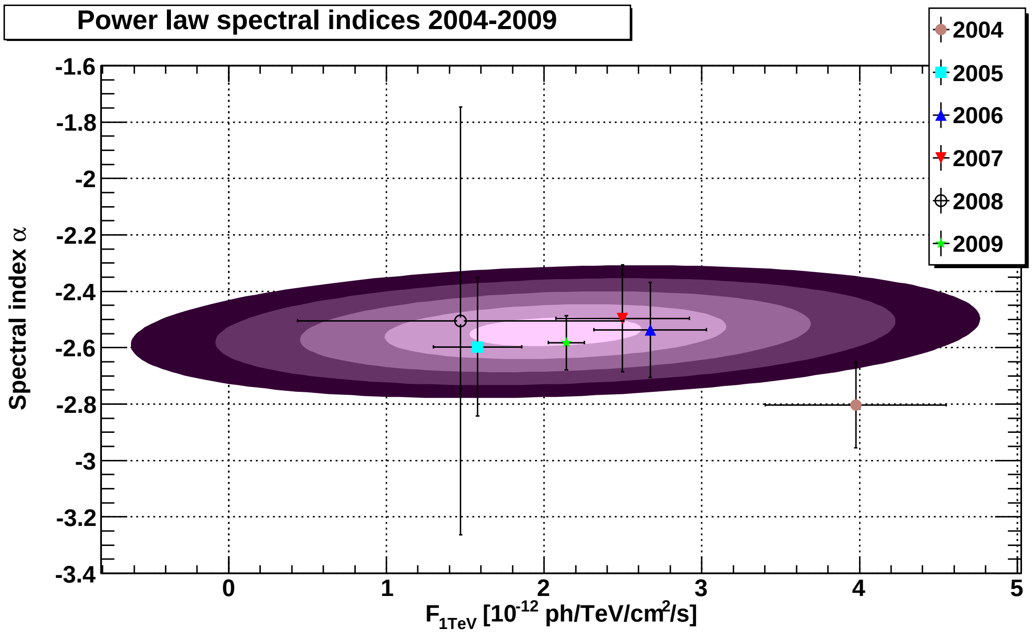

Figure 7.15: Flux normalization vs. spectral index for MAGIC observations of 1ES 1959+650 from 2004–2009.

7.3.2 Steady State VHE Energy Spectrum

As mentioned in subsection 7.2.5 and outlined in subsection 7.2.8 no flux variability has been observed from 1ES 1959+650 during the six years of monitoring observations from 2004 through 2009. Therefore, one would assume that also the spectral behavior of the source might have been the same. This is true for all years except 2004 as indicated by Figure 7.15. To clarify this issue, an additional approach was followed, namely the derivation of a common energy spectrum for all observations. In this context, also the possibility to include data from the HEGRA telescopes for a low emission state between 2000–2002 and from Fermi–LAT during its first two years of operation has been investigated. The data reported by HEGRA CT1 for 2002 have not been taken into consideration as those are comprised of data from different emission states of the source.
As data from different observation seasons, i.e. from different years, are statistically independent, they may be used all together in a fitting procedure. The fit probability derived from a χ^2-test is an appropriate measure of the goodness of the fit, but it is not capable of judging the influence of single data points on the fit or the symmetry of residuals, both have been studied separately.

Influence of Single Data Points – the Cook's Distance

The influence of single data points on a common fit can be estimated by the Cook's distance D_i [Coo77], which is defined as

$$D_i = \frac{1}{N\,p\,MSD} \sum_{j=1}^{N} \left(\hat{Y}_j - \hat{Y}_{j(i)}\right)^2, \tag{7.7}$$

with MSD being the mean squared deviation

$$MSD = \frac{1}{N} \sum_{j=1}^{N} \left(Y_j - \hat{Y}_j\right)^2. \tag{7.8}$$

In a series of $j = 1, \ldots, N$ measurements Y_j, which are described by a model built upon all measurements $\hat{Y}_j$, the Cook's distance D_i for a point i is the sum of squared deviations of the model $\hat{Y}_{j(i)}$ built upon all data points but i from the model $\hat{Y}_j$, divided by mean squared deviation MSD of the model $\hat{Y}_j$ from the measurements Y_j, the number of parameters of the model p, and the number of measurements N. Generally, D_i should not be larger than 1 [CW82], but especially a flat distribution of D_i along the measurements j is desirable.

Symmetry of Fit Residuals

For studying the symmetry of the fit residuals, not only the normalized residuals are depicted in Figure 7.16 but also the histograms of the residuals. These are each fitted with a Gaussian and the fit probability p_{Gauss} gives a handle on the symmetry and quality of the spectral fit. As these Gaussian fit probabilities strongly depend on the binnings of the histograms, this has been changed from $1, \ldots N/2$, where N is the number of data points for the spectral fit. The values of p_{Gauss} for all numbers of bins are also depicted

in Figure 7.16. As expected, a general trend of increasing p_{Gauss} with rising number of bins can be seen. Besides that, a flat distribution of p_{Gauss} and hence a small standard deviation $\sigma_{p_{\text{Gauss}}}$ is expected for good spectral fits, i.e. those with symmetric residuals. For inappropriate spectral fits the variance of the probabilities for the Gaussian fits is considerably higher.
In fact, the histograms of the spectral fit residuals given in Figure 7.16 are drawn (only) for the numbers of bins that are both, ≥ 7 and the smallest number of bins whose Gaussian fit probability $p_{\text{Gauss}} \geq p_{\text{Gauss}}^{\max} - 0.05$.

Results on the Steady State Energy Spectrum

The previously outlined tests have been conducted for all MAGIC data (MAGIC 2004–2009), for all MAGIC data except those of 2004 (MAGIC 2005–2009), for a combination of the latter with HEGRA 2000–2002 low flux data and with Fermi–LAT 2FGL data from a dedicated high energy analysis [Pan11]. As the error on the energy scale is considerably larger for Cherenkov telescopes than for the test beam calibrated Fermi–LAT, additional tests have been performed with the energy scale of MAGIC and HEGRA data shifted w.r.t. that of Fermi–LAT by the values derived in [MHZ10], i.e. an energy shift of +3% for MAGIC and +4.2% for the Hegra CT system. As spectral models a simple power-law (pl)

$$F(E) = F_{1\,\text{TeV}} \cdot (E/1\,\text{TeV})^{\alpha}, \tag{7.9}$$

a power-law with exponential cut-off (cut)

$$F(E) = F_{1\,\text{TeV}} \cdot (E/1\,\text{TeV})^{\alpha} \cdot \exp(-E/E_{\text{cut}}), \tag{7.10}$$

and a curved power-law (curve)

$$F(E) = F_{1\,\text{TeV}} \cdot (E/1\,\text{TeV})^{\alpha+\beta\cdot\log_{10}(E/1\,\text{TeV})} \tag{7.11}$$

have been used.
Summarizing the tests of the Cook's distances, there has only been one case for a spurious data point of strong influence on the model fit. This was the lowest energetic Fermi–LAT data point taken into account. This one strongly influences the different models. Anyway, this is expected as that point lies right at the peak position of the emission spectrum and thus determines the curvature of the model.
The results for the spectral (p_{Spec}) and Gaussian (p_{Gauss}) fit probabilities, the mean Gaussian fit probability $\overline{p}_{\text{Gauss}}$ and its standard deviation $\sigma_{p_{\text{Gauss}}}$ are summarized in Table 7.9. For the combination of MAGIC, HEGRA, and Fermi–LAT the corresponding figures are given in Figure 7.16. For the other combinations the figures can be found in Appendix C. One can clearly see that the MAGIC data of 2004 show a significantly different spectral behavior from those of 2005–2009. The latter are equally well described by all models, hence also by the simple power-law

$$F(E) = (2.12 \pm 0.08) \cdot 10^{-12} \cdot (E/1\,\text{TeV})^{-2.57\pm0.06}\,\text{ph}\,\text{TeV}^{-1}\,\text{cm}^{-2}\,\text{s}^{-1}, \tag{7.12}$$

which is the exactest power-law spectrum derived for that source. Combining theses data with the HEGRA observations, the power-law with an exponential cut-off is favored over

the other models. For the combination of MAGIC and Fermi–LAT data both, a power-law with exponential cut-off and a curved power-law are well suited. The fit parameters for those are given in the inlays in Appendix C.
Combing all, the low state data from HEGRA and those from Fermi–LAT with the MAGIC ones, they complement each other perfectly well. For the first time, this enables the possibility to give a common description of the energy spectrum of 1ES 1959+650 from 10 GeV up to 10 TeV, spanning three orders of magnitude energy, for which a curved power-law model is favored:

$$F(E) = (2.24\pm0.09)\cdot10^{-12}\cdot(E/1\,\mathrm{TeV})^{-2.58\pm0.04-(0.17\pm0.04)\cdot\log_{10}(E/1\,\mathrm{TeV})}\,\mathrm{ph\,TeV^{-1}\,cm^{-2}\,s^{-1}}. \quad (7.13)$$

Concerning the rescaling of the energy values according to [MHZ10] one can note that for the combination of MAGIC and Fermi–LAT data the rescaling slightly improves the fit quality, whereas for the combination of MAGIC and HEGRA data, the fit quality is generally reduced by the rescaling. The latter is also true for the combination of MAGIC, HEGRA and Fermi–LAT data. Thus under the assumption of a single underlying spectral behavior for all the observations, the findings by [MHZ10] cannot be confirmed here.

Measurements	$p^{\mathrm{pl}}_{\mathrm{Spec}}$	$p^{\mathrm{pl}}_{\mathrm{Gauss}}$	$\overline{p}^{\mathrm{pl}}_{\mathrm{Gauss}}$	$\sigma^{\mathrm{pl}}_{p_{\mathrm{Gauss}}}$
MAGIC 2004–2009	0.057	0.988	0.847	0.135
MAGIC 2005–2009	0.897	0.987	0.969	0.044
MAGIC[a] & HEGRA	0.417	1.000	0.862	0.207
MAGIC[a] & HEGRA scaled[b]	0.391	0.994	0.855	0.267
MAGIC[a] & Fermi–LAT	0.447	0.974	0.961	0.084
MAGIC[a] & Fermi–LAT scaled[b]	0.378	0.969	0.965	0.066
MAGIC[a] & HEGRA & Fermi–LAT	0.004	0.986	0.650	0.250
MAGIC[a] & HEGRA & Fermi–LAT scaled[b]	0.002	0.943	0.669	0.232

Measurements	$p^{\mathrm{cut}}_{\mathrm{Spec}}$	$p^{\mathrm{cut}}_{\mathrm{Gauss}}$	$\overline{p}^{\mathrm{cut}}_{\mathrm{Gauss}}$	$\sigma^{\mathrm{pl}}_{p_{\mathrm{Gauss}}}$
MAGIC 2004–2009	0.047	0.991	0.702	0.228
MAGIC 2005–2009	0.873	0.990	0.953	0.061
MAGIC[a] & HEGRA	0.652	0.991	0.964	0.072
MAGIC[a] & HEGRA scaled[b]	0.589	0.988	0.943	0.128
MAGIC[a] & Fermi–LAT	0.915	0.954	0.921	0.115
MAGIC[a] & Fermi–LAT scaled[b]	0.910	0.958	0.908	0.109
MAGIC[a] & HEGRA & Fermi–LAT	0.596	0.974	0.943	0.088
MAGIC[a] & HEGRA & Fermi–LAT scaled[b]	0.498	0.956	0.949	0.083

Measurements	$p^{\mathrm{curve}}_{\mathrm{Spec}}$	$p^{\mathrm{curve}}_{\mathrm{Gauss}}$	$\overline{p}^{\mathrm{curve}}_{\mathrm{Gauss}}$	$\sigma^{\mathrm{curve}}_{p_{\mathrm{Gauss}}}$
MAGIC 2004–2009	0.045	0.984	0.765	0.202
MAGIC 2005–2009	0.870	0.997	0.971	0.044
MAGIC[a] & HEGRA	0.569	0.949	0.882	0.200
MAGIC[a] & HEGRA scaled[b]	0.507	0.949	0.832	0.277
MAGIC[a] & Fermi–LAT	0.934	0.964	0.888	0.197
MAGIC[a] & Fermi–LAT scaled[b]	0.930	0.990	0.915	0.116
MAGIC[a] & HEGRA & Fermi–LAT	0.705	0.998	0.919	0.141
MAGIC[a] & HEGRA & Fermi–LAT scaled[b]	0.643	0.988	0.904	0.122

[a] MAGIC 2005–2009
[b] MAGIC and HEGRA energies scaled by 1.03 and 1.042, respectively, according to [MHZ10].

Table 7.9: Fit probability, maximal and average Gaussian fit probability of the residuals and the according standard deviation of models for the HE–VHE Spectrum of 1ES 1959+650 based on different sets of observations with MAGIC, HEGRA and Fermi–LAT.

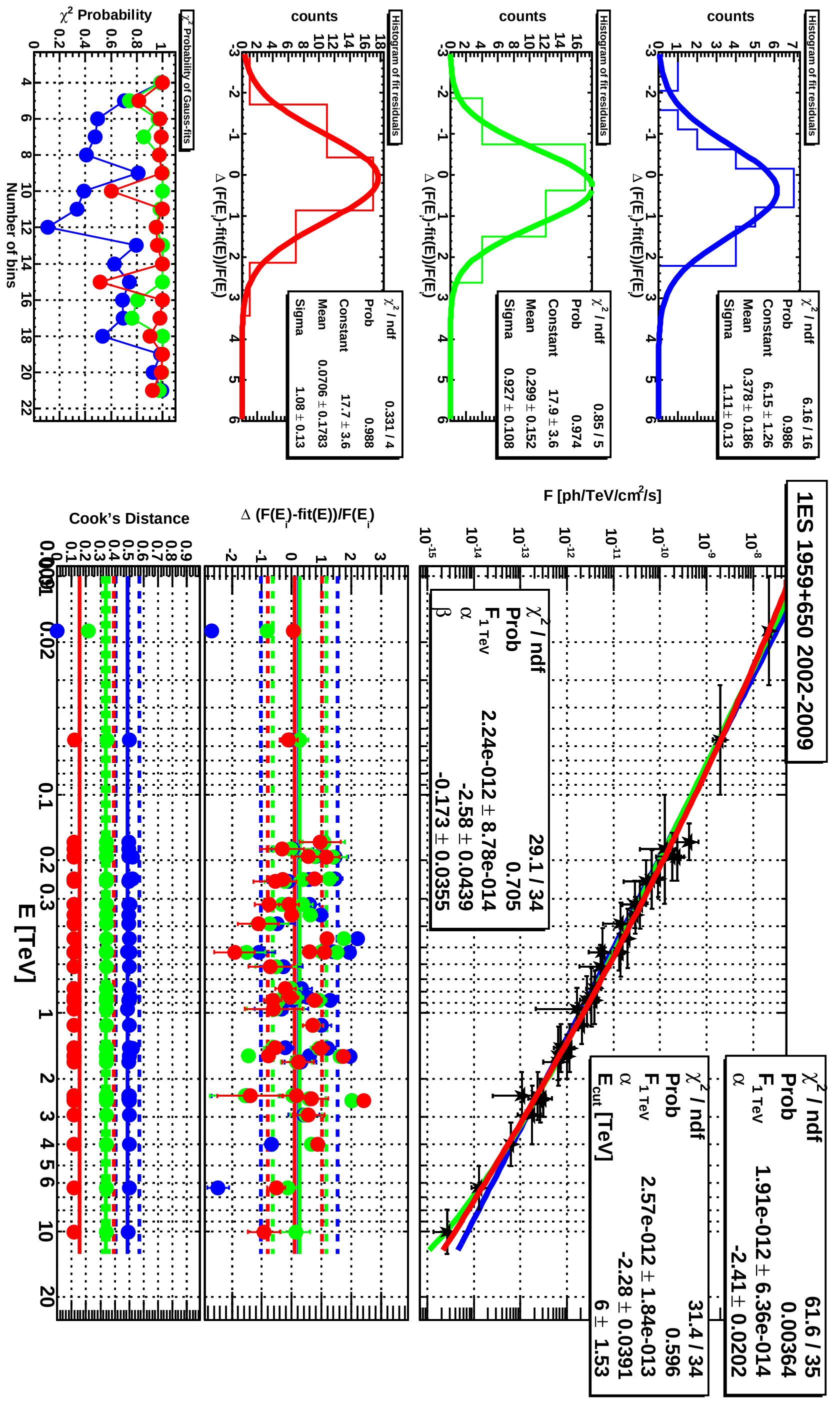

Figure 7.16: Combined MAGIC-HEGRA-Fermi energy spectrum of 1ES 1959+650, along with fit quality test as the Cook's Distance and the Gaussian fit probabilities for the spectral fit residuals. Values stemming from the power-law model are given in blue, for the power-law with cut-off in green and for the curved power-law in red. Solid horizontal lines denote averages, dashed ones denote one standard deviation.

7.4 Spectral Energy Distribution of 1ES 1959+650

In the following the findings presented in section 7.2 and subsection 7.3.2 are taken as motivation to compile and model the time-averaged broad band spectral energy distribution of 1ES 1959+650. In subsection 7.4.1, subsection 7.4.2, and subsection 7.4.3, the data collection is presented, in subsection 7.4.4 the time-averaged frequency and emission level of the synchrotron peak is estimated and afterwards, in subsection 7.4.6 possible emission models matching the broad band SED are discussed. The data are retrieved from the references stated in section 7.2 and additionally given in Appendix D. In the figures, upper limits are denoted by single-sided error bars exceeding the bottom of the figures.

7.4.1 Radio Observations

In Figure 7.17 the low frequency part of the SED is presented. Measurements with the Radio telescopes RATAN–600, Effelsberg 100 m, IRAM, and VLA are depicted besides VLBI and VLBA measurements of the core emission and upper limits by Metsähovi and the Planck satellite. Additionally, NED archival data are shown. Altogether, a wavelength range of 300 MHz–1 THz is covered, whereas the wavelengths of the instruments and the observation epochs are given in the inlay.

7.4.2 Optical Observations

The observations in the IR, optical and UV wavelength bands are depicted in Figure 7.18. The Spitzer far-IR data was retrieved from the Spitzer Heritage Archive[27]. The two available datasets were taken on August 2, 2008 and have been averaged. As the data are so plentiful, any data point with a relative error greater than 46.669%, i.e. an averaged relative error of 33.3%, have been omitted. Near-IR data have been taken with NOT and TwoMASS. The mean, maximum, and minimum fluxes recorded with the KVA in R-band are shown, as well g-band observations with Palomar 60. Several UV measurements have been conducted with Swift–UVOT in U-, B-, V-, UVW1-, UVM2-, and UVW2-bands and twice with Galex in NUV- and FUV-bands. Dates of observation are given in the inlay.

7.4.3 X-Ray Observations

Observations in the X-ray energy range have been conducted by various instruments, namely Swift–XRT, *Beppo*SAX, RXTE–PCA, Swift–BAT, RXTE–HEXTE, and INTEGRAL–IBIS-ISGRI, in the order of rising energy range. The Swift–XRT data for 2007 have been rebinned from 194 to eight bins in energy to achieve reasonable measurement errors. In the soft X-rays, strong and significant flux variations of about a factor of four have been observed. In the hard X-rays instead, the spread of the data can be attributed to the large measurement errors, despite the observations are averaged over several years.

[27] see http://sha.ipac.caltech.edu/applications/Spitzer/SHA

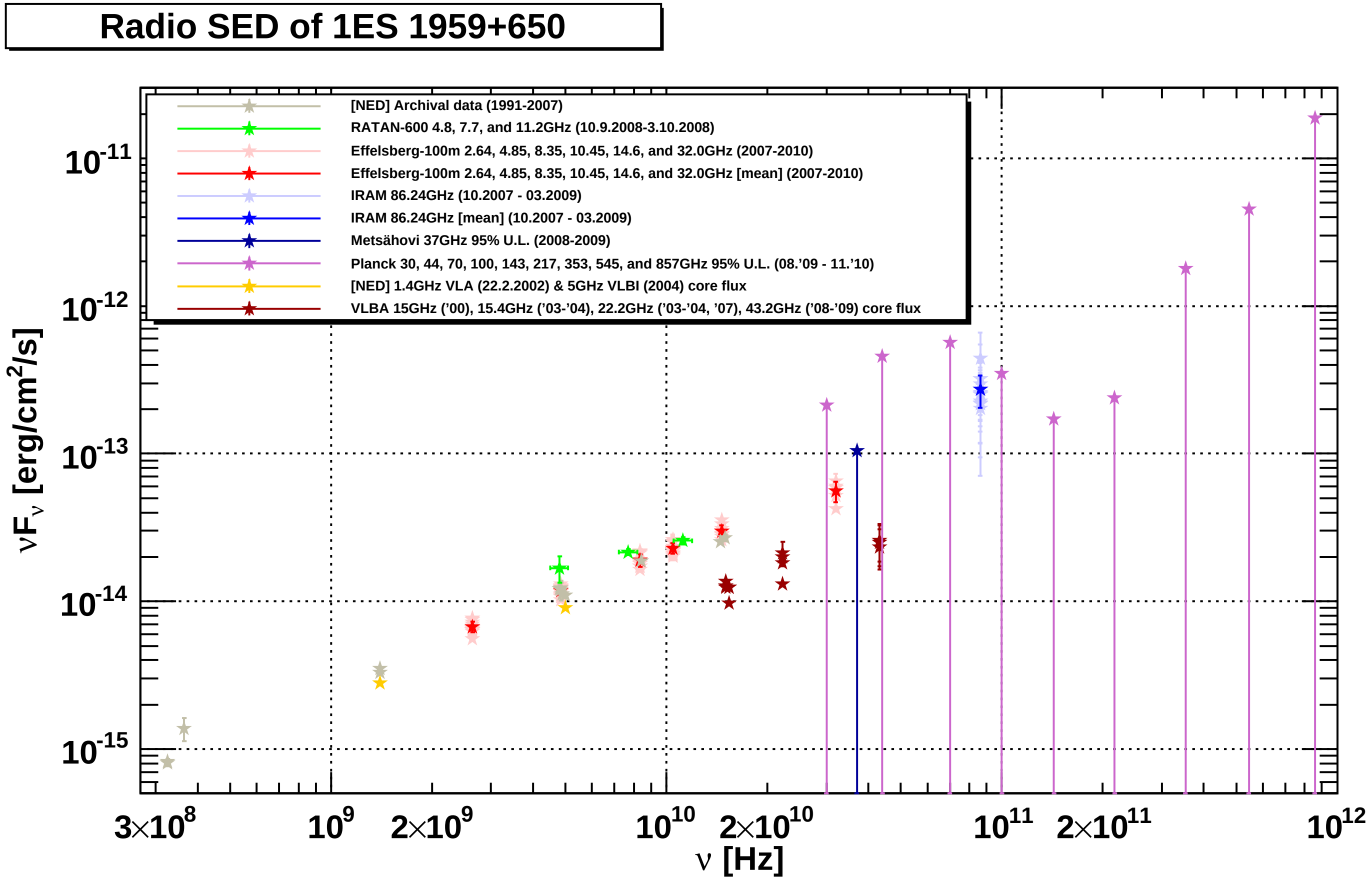

Figure 7.17: Zoom in on the radio frequencies of the SED of 1ES 1959+650.

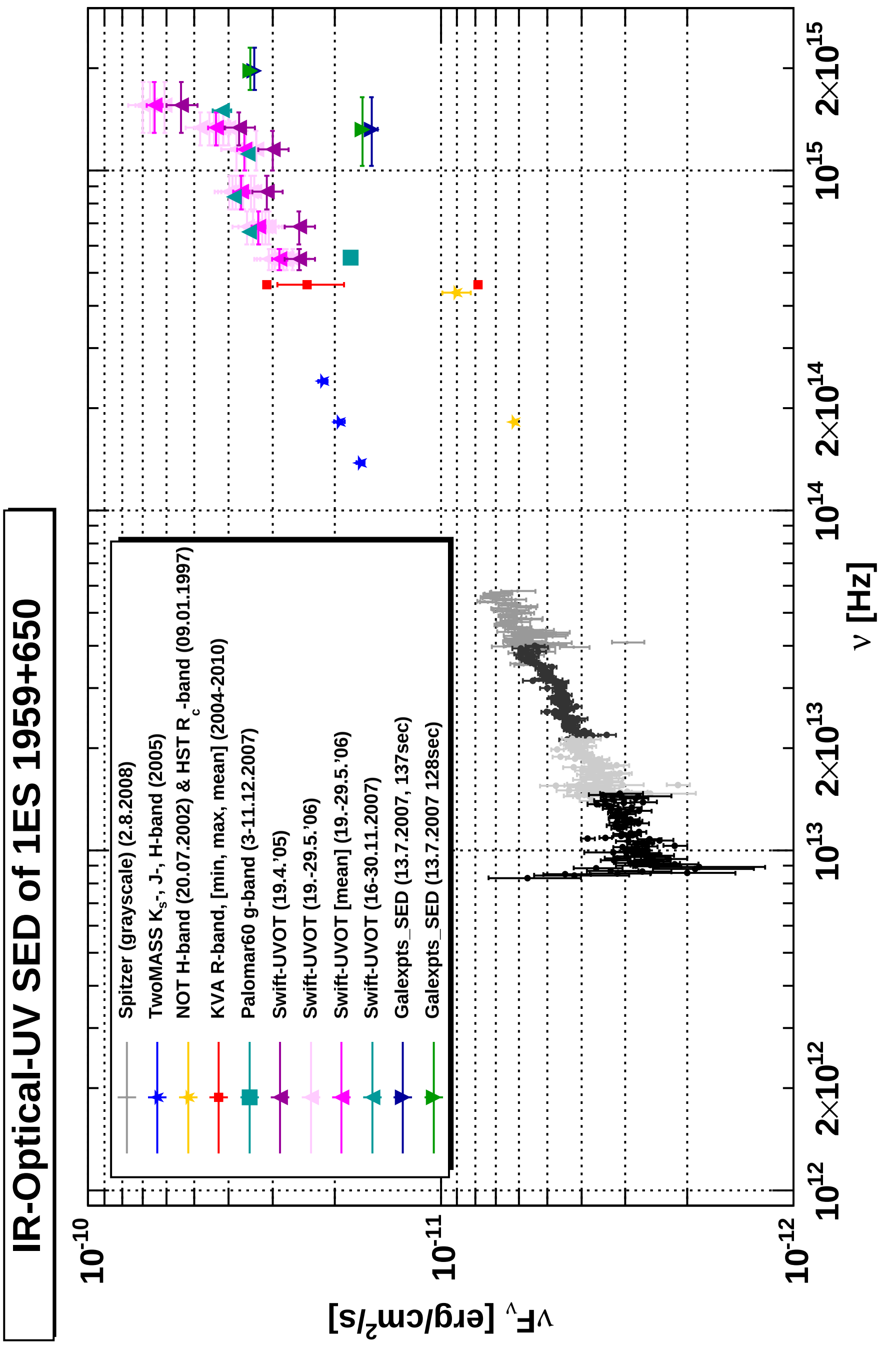

Figure 7.18: Zoom in to the IR, optical, and UV frequencies of the SED of 1ES 1959+650.

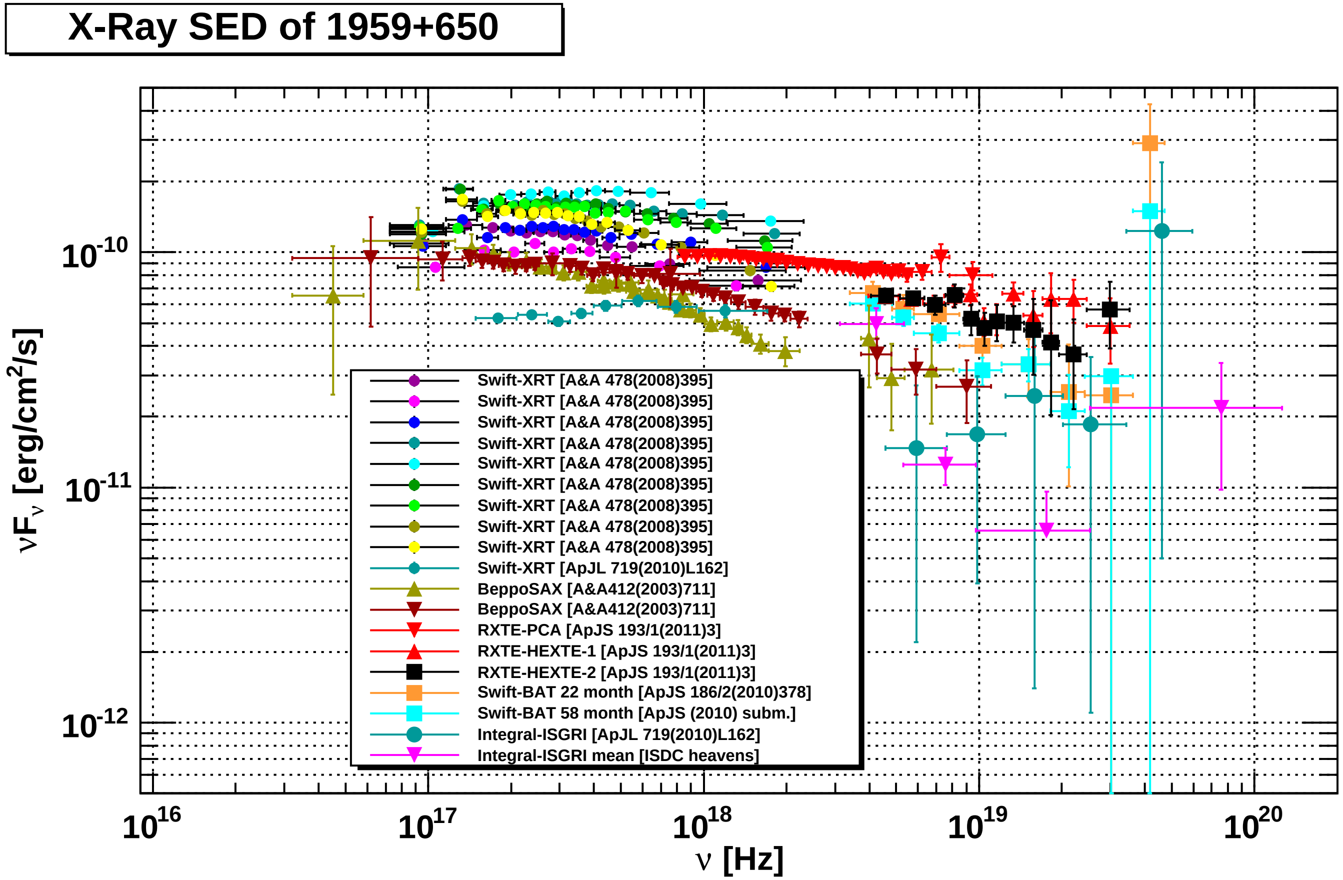

Figure 7.19: Zoom in on the X-ray frequencies of the SED of 1ES 1959+650.

7.4.4 Estimation of the Synchrotron Peak

Comprising the data presented in subsection 7.4.2 and subsection 7.4.3, the synchrotron peak of the SED is well covered and the time-averaged peak position can be estimated. For this purpose a logarithmic parabola is fit to the data in the vertex notation:

$$\nu F_\nu = \nu_{\mathrm{peak}}^{\mathrm{syn}} F_{\nu_{\mathrm{peak}}^{\mathrm{syn}}} \cdot 10^{b \cdot \left[\log\left(\nu / \nu_{\mathrm{peak}}^{\mathrm{syn}}\right)\right]^2}, \tag{7.14}$$

where $\nu_{\mathrm{peak}}^{\mathrm{syn}} F_{\nu_{\mathrm{peak}}^{\mathrm{syn}}}$ is the peak flux at the peak frequency $\nu_{\mathrm{peak}}^{\mathrm{syn}}$ and b the curvature parameter. In accounting the general asymmetric shape of the synchrotron peak, the fit parameters have been determined once including (Figure 7.20) and once excluding (Figure 7.21) the IR and optical data points. In the according figures, the data points included into the fit are marked by blue triangles. The resulting peak positions are given in the inlays and in Table 7.10, along with an overview of values derived in the literature. The ones derived here yield by far the exactest numbers, although the significant variations of X-ray fluxes and spectra lead to a huge χ^2-value. These findings confirm the synchrotron peak of 1ES 1959+650 to be located well above 10^{16} Hz and thus its classification as a HBL.

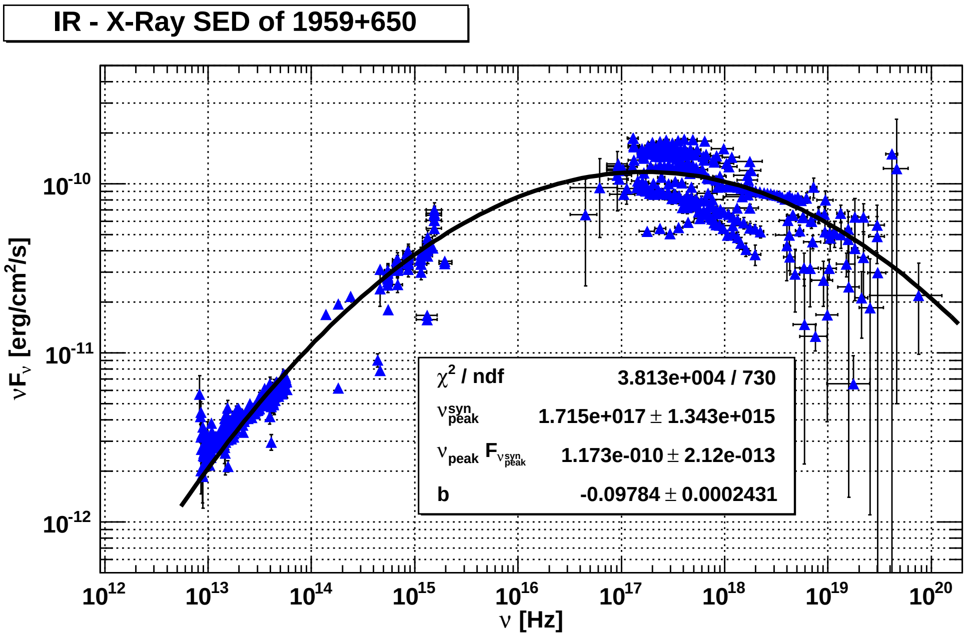

Figure 7.20: Zoom in no the IR–X-ray frequencies of the SED of 1ES 1959+650. An all-time all-instrument log-parabolic fit is applied to find the mean frequency of the synchrotron peak $\nu_{\mathrm{peak}}^{\mathrm{syn}}$.

7.4.5 Gamma-Ray Observations

In Figure 7.22 the spectral data from gamma-ray observations with Cherenkov telescopes and Fermi–LAT are depicted. For Fermi–LAT, the spectra comprised by 6, 11 (1FGL), 24 (2FGL), and 27 months of observation are shown. Additionally, a dedicated high-energy analysis on the 2FGL data has been performed [Pan11]. For the Cherenkov telescopes,

Reference	$\log_{10}\left(\nu^{\mathrm{syn}}_{\mathrm{peak}}/\mathrm{Hz}\right)$	$\log_{10}\left(\nu^{\mathrm{syn}}_{\mathrm{peak}} F_{\nu^{\mathrm{syn}}_{\mathrm{peak}}}/\mathrm{erg\,cm^{-2}\,s^{-1}}\right)$
[B+02]	15.00	—
[P+05]	≥ 18	—
[NTV06]	18.03	—
[T+07b]	17.28	—
[A+10e] SED[a]	16.6	-10
[A+10e] α_{XO-OR}[b,c]	15.9	-10.3
[M+08b] *Beppo*SAX	17.62 ± 0.05	-10.105 ± 0.008
[M+08b] Swift–XRT	17.26 ± 0.05	-9.920 ± 0.007
	17.39 ± 0.07	-9.991 ± 0.014
	17.48 ± 0.05	-9.919 ± 0.011
	17.49 ± 0.04	-9.809 ± 0.006
	17.58 ± 0.03	-9.744 ± 0.008
	17.50 ± 0.02	-9.804 ± 0.006
	17.42 ± 0.04	-9.812 ± 0.005
	17.35 ± 0.03	-9.846 ± 0.006
	17.37 ± 0.03	-9.855 ± 0.006
	17.57 ± 0.03	-9.941 ± 0.008
IR–X-ray (Figure 7.20)	17.234 ± 0.008	-9.931 ± 0.002
UV–X-ray (Figure 7.21)	17.146 ± 0.007	-9.898 ± 0.002

[a] Reported IC peak: $\log_{10}\left(\nu^{\mathrm{IC}}_{\mathrm{peak}}/\mathrm{Hz}\right) = 24.7$, $\log_{10}\left(\nu^{\mathrm{IC}}_{\mathrm{peak}} F_{\nu^{\mathrm{IC}}_{\mathrm{peak}}}/\mathrm{erg\,cm^{-2}\,s^{-1}}\right) = -10.5$.

[b] Reported IC peak: $\log_{10}\left(\nu^{\mathrm{IC}}_{\mathrm{peak}}/\mathrm{Hz}\right) = 24.1$, $\log_{10}\left(\nu^{\mathrm{IC}}_{\mathrm{peak}} F_{\nu^{\mathrm{IC}}_{\mathrm{peak}}}/\mathrm{erg\,cm^{-2}\,s^{-1}}\right) = -10.5$.

[c] Estimated from the difference of the slopes from optical to X-rays and from radio to optical bands: $\alpha_{OX-RO} = \alpha_{OX} - \alpha_{RO}$.

Table 7.10: Position of the synchrotron peak for 1ES 1959+650.

any data which is not explicitly stated as high or flaring state are shown, namely MAGIC observations of 2004 and of 2005–2009, HEGRA low state observations of 2000–2002 and HEGRA CT1 observations of 2002.

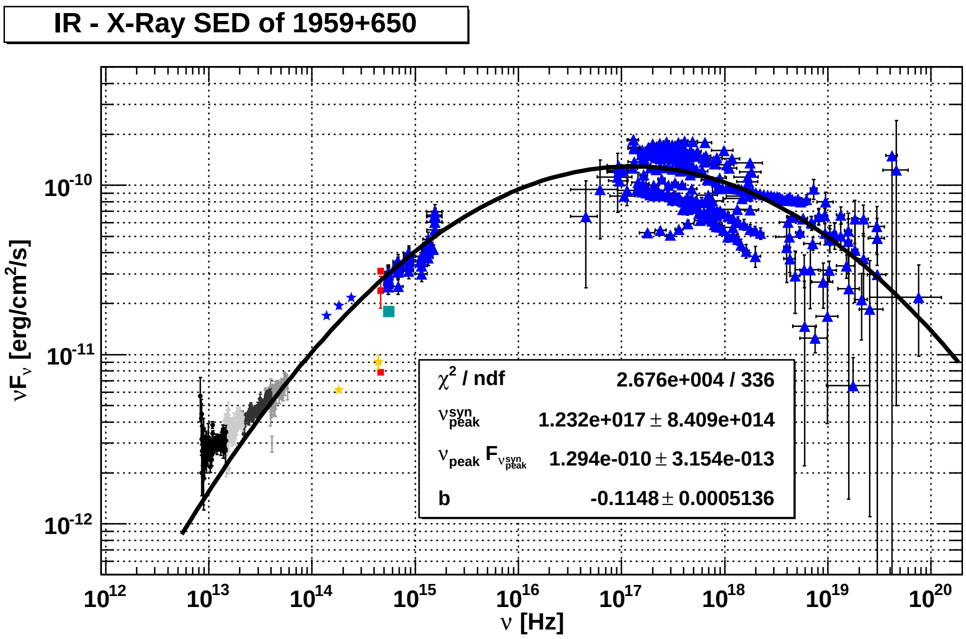

Figure 7.21: Zoom in on the IR–X-ray frequencies of the SED of 1ES 1959+650. An all-time all-instrument log-parabolic fit is applied to find the mean frequency of the synchrotron peak $\nu_{\text{peak}}^{\text{syn}}$, omitting data in the IR and optical wavelengths to account for the asymmetric peak form.

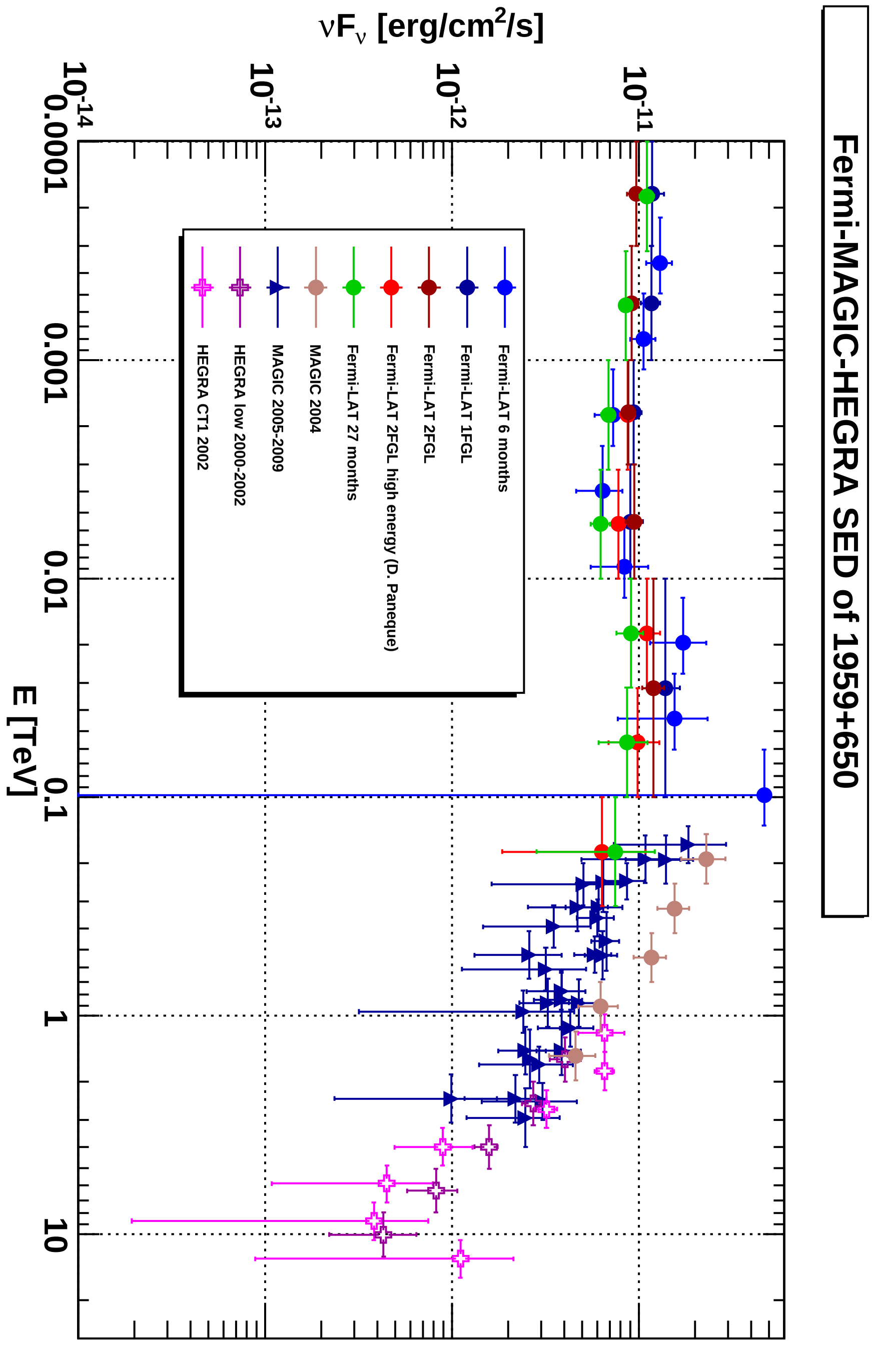

Figure 7.22: Combined gamma-ray SED of 1ES 1959+650 as measured with Fermi–LAT, MAGIC, HEGRA CT System, and Hegra CT1.

7.4.6 Modeling the SED of 1ES 1959+650

The broad band SED of 1ES 1959+650 is depicted in Figure 7.24. In addition to the compilation of data presented in Figure 7.22, Figure 7.17, Figure 7.18, and Figure 7.19, the upper limits derived from CGRO–COMPTEL data (see section 7.2.4) and the VHE data of the flaring state in 2002 (c.f. Figure 7.13) are shown. Though not being comprised by contemporaneous data, the presented SED is probably the most complete one ever compiled for any BL Lac object. The typical two hump structure is clearly visible, but in contrast to the expectations from SSC models, the high energy hump is extremely flat towards lower frequencies, which is a particularly interesting feature concerning the SED modeling. In the following, the modeling of the SED with one-zone SSC models, hadronic model and a two-zone SSC model are discussed. As the redshift of 1ES 1959+650 is comparably small ($z = 0.048$), for all models the effect of extragalactic absorption has been neglected. This might have a small influence on the exact model parameters, but none at all on the general findings. An overview of the obtained model parameters as well as those stated in the literature are given in Table 7.11. As external Compton processes demand for strong seed photon fields, they are generally disfavored for playing a major role in BL Lac objects, as these exhibit no or only weak optical emission lines. Thus, these processes are neglected in the following discussion.

SSC Model

In Figure 7.23 the one-zone SSC model given in [T+08a] is depicted as long-dashed line upon the data collection presented here. Within that model [TMG98b], the spectral slopes of the electron distribution, p_1 and p_2 as well as the maximum Lorenz factor γ_{max} and the one of the spectral break, γ_{break}, are free parameters. Instead in reality, these are interdependent and determined by the underlying acceleration and energy loss processes. Therefore, a self-consistent SSC model was developed [WS10], taking into account these interdependencies. Trying to resemble the shape of the previously published SSC model realization with this self-consistent model leads to the blue solid curve depicted in Figure 7.23. One can see, that this approach slightly overestimates the flux in the hard X-ray regime. But most remarkable is the fact, that both models fail to describe the SED in the Fermi–LAT frequency range. This is highly unusual for high-frequency peaked BL Lac objects (cf. [A+11e] and [A+11f, A+11g] for the exemplary HBLs Mkn 421 and Mkn 501, respectively) and was only once recently observed for a previously unclassified blazar [A+11l].

Hadronic Models

When trying to describe the SED with hadronic emission models, several difficulties occur. In hadronic models, the high energy emission is comprised by synchrotron emission of protons and emission by proton induced cascades (c.f. Equation 2.6). Having the high energy emission described by proton synchrotron emission and trying to model the VHE observations by cascade processes, involves several general problems. Due to the generally featureless cascade emission, this must be very much fine-tuned to be able to explain the spectral shape in the VHE region, strongly relying on the model for the extragalactic absorption. Furthermore, flares in the VHE regime as observed in 2002 have to be explained

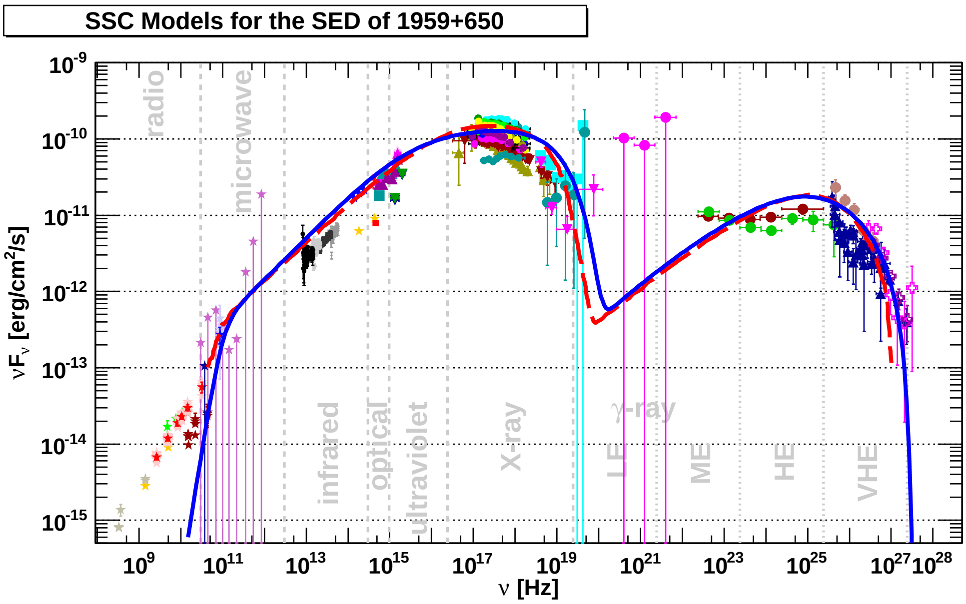

Figure 7.23: SSC Models for the SED of 1ES 1959+650. The data shown is the same as in Figure 7.24, except for redundant data for Swift–BAT and Fermi–LAT, which are left out here. For an explanation of the markers, the reader is referred to the figures of the according frequency ranges. The original model of [T+08a] is shown as red dashed line, the self-consistent one as blue solid line. The model parameters are given in Table 7.11.

by an additional emission region, increasing the number of model parameters even further. Additionally, with the model parameters as magnetic field and the size of emission region adapted to account for the high energy emission by synchrotron radiation of protons, the primary electron population has to be injected into the radiation region with energies higher than explainable in self-consistent models, to be able to explain the synchrotron peak.

A more promising approach is to explain the VHE spectrum by proton synchrotron and the high energy region by cascade emission. This leads to a self-consistent description of the synchrotron peak by the electron population, but the resulting photon densities of the cascade emission generally lead to self-quenching by runaway pair-production [KM92, SK07, PM11]. Hence, also for this approach a strong fine-tuning of the model parameters is necessary to somehow explain the observations.

Altogether, at the current stage of research hadronic processes as underlying emission mechanisms for the SED of 1ES 1959+650 appear to be unfavorable the for mentioned reasons.

Model of two Leptonic Emission Reagions

Dismissing the restriction that the broad band SED can be explained by radiation stemming from only one emission region, the two-zone SSC model[28] is the simplest model extension. Featuring two independent radiation zones, it practically doubles the number of free parameters compared to standard (i.e. one-zone) SSC models but by this offers strong explanatory power. In Figure 7.25 a self-consistent two-zone SSC is overlaid with the observed SED. Additionally to the model parameters given in Table 7.11 the following values have been used for the low energetic emission region and the high energetic one: radius of the acceleration regions $R_{acc} = 1 \cdot 10^{14}\,\mathrm{cm} \wedge 6 \cdot 10^{13}\,\mathrm{cm}$, $t_{\mathrm{acc}}/t_{\mathrm{esc}} = 1.65 \wedge 1.13$. For the efficiency of the shock acceleration compared to stochastic processes $a = 20$ has been used for the low energetic plasmoid and $a \to \infty$, i.e. a shock only model, has been applied to the high energetic emission zone. As shown in Figure 7.25, the applied model of two independent, self-consistent emission regions [WS10] fits the observations reasonably well and is thus the favored model of this study.

Line Absorption Feature

Having a closer look at the latest Fermi–LAT data, comprised by 27 months of observations (see Figure 7.22), there is apparently a dip at 5 GeV present. This feature can also be modeled in a two-zone SSC model, but it might as well be interpreted as an absorption feature. Photons from the He II emission complex within the broad line region or from the accretion dist may cause photon-photon pair-production and here lead to dips in the high energy emission spectra at a few GeV as proposed in [PS10]. Up to now this has only been applied to FSRQs [PS10] and LBLs [S+11], which are both primary candidates for strong external radiation fields. Also for the HBL 1ES 1959+650 this might lead to promising results, independent of the underlying acceleration and radiation processes.

7.5 Conclusion and Outlook

The first multi-year multi-wavelength lightcurve study on 1ES 1959+650 has been presented in section 7.2 and was accomplished by the multi-year and multi-instrument study of the spectral behavior in section 7.3. In the former, the variability has been studied in all wavelengths bands, finding strong optical and X-ray variability whilst no variation in the VHE regime is evident. For studying the interdependence of observations with Cherenkov telescopes and other wavelength bands, the recorded VHE lightcurve is too scarcely populated and the single observations lack a high level of significance. To overcome both, in the future a network of dedicated Cherenkov will be used to conduct such monitoring observations as presented in chapter 8.
The steadiness of the very high energy emission motivated the deduction of a uniform spectral model for HEGRA, MAGIC, and Fermi–LAT data, presented in section 7.3. By this, the high energy spectrum of 1ES 1959+650 has been determined for the first time for more than three orders of magnitude in energy, being well described by a log-parabolic

[28] Generally, two-zone models are referred to a class where the two emission region may or may not interact with each other (see e.g. [C+11]). Instead, throughout this thesis it will be used for a model with two independent emission zones.

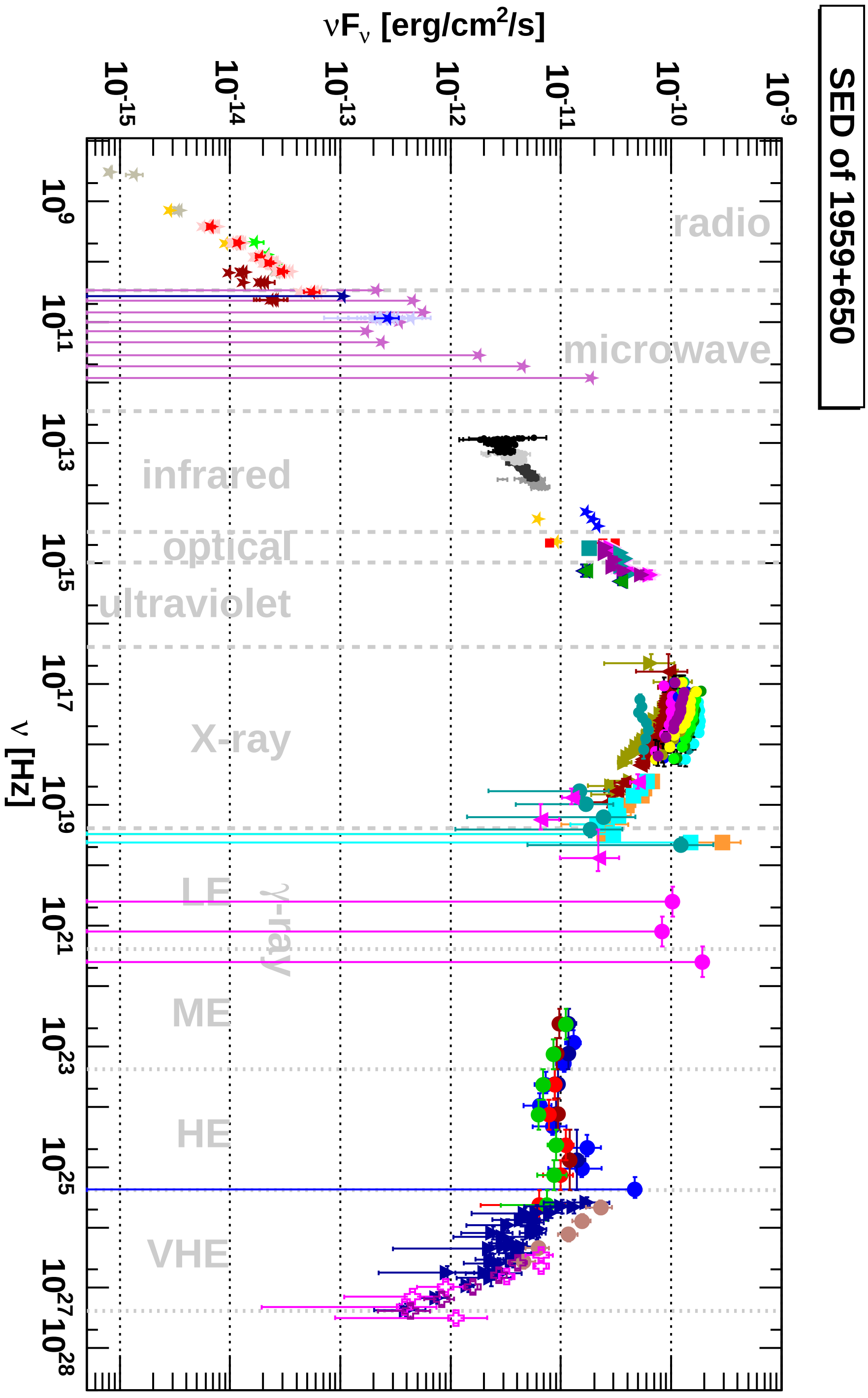

Figure 7.24: Combined SED of 1ES 1959+650. The markers are the same as in Figure 7.17, Figure 7.18, Figure 7.24, and Figure 7.22, thus for clarity an explanation is left out here. For this, the reader is referred to the according figures.

Model	δ	$\gamma_{\rm min}$ [10^3]	$\gamma_{\rm break}$ [10^3]	$\gamma_{\rm max}$ [10^3]
[B+02][a]	14.3^b	0.5	19	—
[K+04b] high	20	0.001	1235	3905
[K+04b] pre-flare	20	0.001	552	3102
[K+04b] orphan	20	0.001	552	3102
[G+06b]	20	0.001	246	1554
[T+08a]	18	0.001	57	600
[T+10a]	18	0.001	57	600
[B+10c] leptonic[c]	19	1	—	60
[B+10c] hadronic[d]	19	0.8	—	45
[S+10]	—			
revised [T+08a]	31	0.003	11^e	650^e
2 zones: LE	20	0.8	8^e	65^e
2 zones: HE	46	1.6	25^e	600^e

Model	R [10^{14} cm]	B [G]	p_1	p_2	ρ [$10^3\,{\rm cm}^{-3}$]	ρ_E [${\rm erg\,cm}^{-3}$]
[B+02][a]	100	1.2	2.6	3.6		
[K+04b] high	58	0.04	2	3		0.22
[K+04b] pre-flare	140	0.04^f	2	3		0.014
[K+04b] orphan	8	0.04	2	3		17
[G+06b]	272	0.02^f	2	3		0.010
[T+08a]	73	0.25	2	3.4	2.2	
[T+10a]	73	0.4	1.9	3.4	0.7	
[B+10c] leptonic[c,g]	0.5	14	1.85	—	—	—
[B+10c] hadronic[d,g]	2	20	1.9	—	—	—
[S+10]	≤ 510	≤ 300	1.4			
revised [T+08a]	70	0.29	1.95^e	2.95^e	800	
2 zones: LE	20	0.81	2.6^e	3.6^e	190	
2 zones: HE	20	0.44	2.13^e	3.13^e	3.75	

[a] Intrinsic luminosity $L' = 8.0 \cdot 10^{40}\,{\rm erg\,s}^{-1}$.
[b] Determined from Lorentz factor $\Gamma = 13$ and viewing angle $\theta = 4.0°$ via $\delta = 1/\Gamma\,(1 - \beta_\Gamma \cos\theta)$.
[c] Kinetic power of electrons $L_e = 8.5 \cdot 10^{42}\,{\rm erg\,s}^{-1}$.
[d] Additional hadronic parameters: $\gamma^{\rm had}_{\rm min} = 10^3$, $\gamma^{\rm had}_{\rm max} = 1.2 \cdot 10^9$, $p^{\rm had} = 1.9$, and kinetic power in protons $L_p = 3.5 \cdot 10^{46}\,{\rm erg\,s}^{-1}$.
[e] These numbers are determined by a self-consistent model [WS10] depending on $t_{\rm acc}/t_{\rm esc} = 0.95$, $R_{\rm acc}$, B and are thus no free parameters as in other models.
[f] The units for these numbers are (probably by mistake) reported as 10^{-4} G in [G+06b].
[f] $\eta_{\rm esc} = t_{\rm esc} \cdot c/R = 10$ and 5, for leptonic and hadronic, respectively.

Table 7.11: Spectral energy distribution model parameters.

model of the form

$$F(E) = (2.24{\pm}0.09)\cdot 10^{-12}\cdot(E/1\,\mathrm{TeV})^{-2.58\pm 0.04-(0.17\pm 0.04)\cdot\log_{10}(E/1\,\mathrm{TeV})}\,\mathrm{ph\,TeV^{-1}\,cm^{-2}\,s^{-1}}. \tag{7.15}$$

In section 7.4 the long-term SED of 1ES 1959+650 has been presented and modeling with leptonic and hadronic emission models has been conducted. For the leptonic case it was found, that neither the one-zone SSC model of [T+08a], nor a self-consistent adaption of this can explain the SED in the HE gamma-ray regime. The hadronic models appear to be disfavored due to their strong an unstable dependence on the model parameters. Instead, the presented two-zone SSC model describes the entire SED from IR through VHE gamma-ray observations perfectly well.

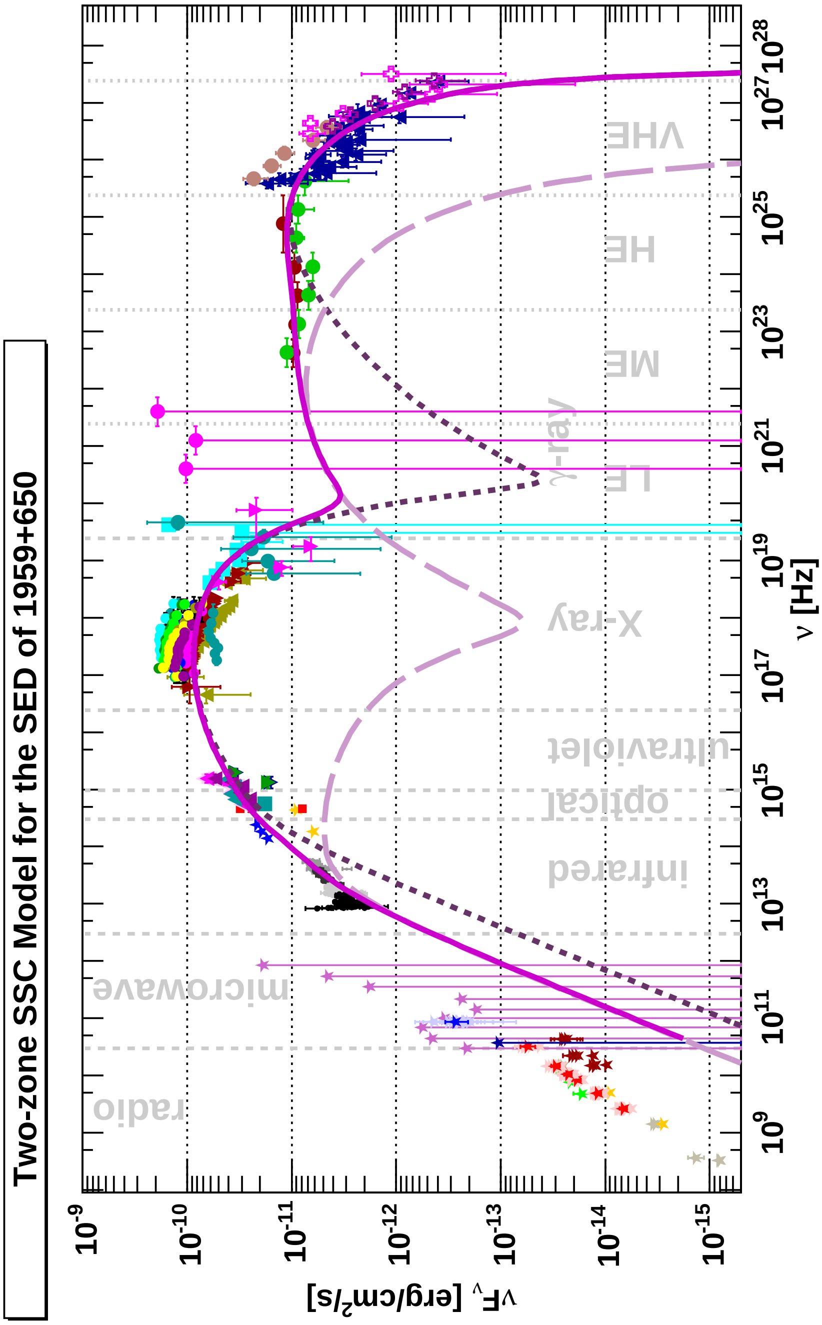

Figure 7.25: Two-zone SSC Model for the SED of 1ES 1959+650. The data shown are the same as in Figure 7.24, except for redundant data for Swift–BAT and Fermi–LAT, which are left out here. For an explanation of the markers, the reader is referred to the figures of the according frequency ranges. The high energy emission region is depicted by the dotted line, the low energetic one by the dashed line and the sum of those as solid line. The model parameters are given in Table 7.11.

Chapter 8
The DWARF Network

To overcome the disadvantages of biased sampling and of time series analyses dominated by gaps rather than by observations, in the course of this thesis a global network of Cherenkov telescopes has been initiated, to be operated in a coordinated way for monitoring observations of nearby blazars – the DWARF[1] network. The aim is to distribute several Cherenkov telescopes around the globe to be able to conduct 24/7 monitoring, preferably with temporal overlap and redundancy to account for weather and duty cycle constraints. The monitored sources will be the brightest TeV blazars: Mrk 421, Mrk 501, 1ES 1959+650, 1ES 2344+514, H 1426+428, and PKS 2155-304. This initiative is pioneered somehow by the Whipple 10 m and TACTIC telescopes which have been dedicated to monitoring observations for several years on the one hand, and on the other hand by building the FACT telescope and starting to coordinate the monitoring network activities. Figure 8.1 depicts the distribution of the Cherenkov telescopes (possibly) contributing to the DWARF network, so far. The following sections give an overview of the instruments already involved and those being build or possibly involved in the future, while section 8.7 summarizes the feasibility of the project.

8.1 FACT – The First G-APD Cherenkov Telescope

The technical details of the FACT telescope as well as the importance of the technological test of G-APDs as photo sensors in IACTs have been outlined in chapter 5. After the successful technological test the telescope will be transferred to scientific operation, dedicated to monitoring observations of the TeV-brightest blazars. In this context, it is foreseen to upgrade the telescope for robotic (remote) operation. This autonomous robotized approach keeps the man power demand on the low side. Additionally, the construction costs per telescope are quite affordable. This concept is especially attractive for countries with smaller budgets for scientific developments, but who still want to contribute to the high-technology spearhead of astrophysics. As such, this telescope will hopefully act as a prototype for many more telescopes built to contribute to the monitoring net-

[1] **D**edicated **W**orldwide **A**GN **R**esearch **F**acility, DWARF

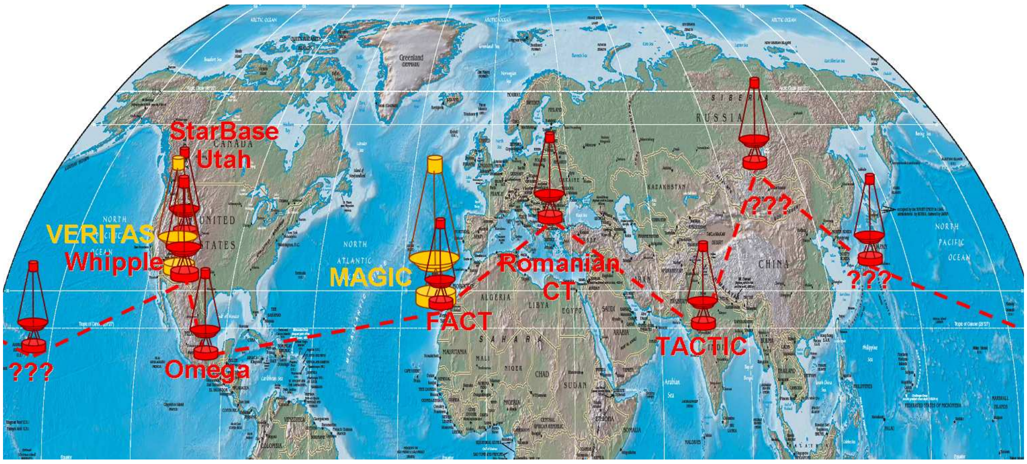

Figure 8.1: The (nearly) worldwide DWARF network.

work DWARF. For multi-wavelength observations, contacts to the F-GAMMA Program[2], conducting radio and optical monitoring of northern Fermi–LAT detected blazars, have been established. Additionally, agreements with the Mesähovi Radio Observatory and the optical KVA telescope of the Tuorla Observatory have been signed. Those will simultaneously complement the FACT telescope observations. In Figure 8.2 the according multi-frequency coverage is depicted, complemented by the all-sky instruments RXTE–ASM, MAXI[3] [M+09a], AGILE–GRID, and Fermi–LAT.

8.2 Whipple 10 m Telescope

The Whipple 10 m telescope[4] is a single 10 m diameter telescope on Mt. Hopkins within the Fred Lawrence Whipple Observatory in Arizona, USA, see Figure 8.3. This pioneering IACT was built in 1968 and in 1989 it finally detected the first source at the VHE gamma-ray sky, the Crab Nebula [W+89]. After several upgrades [K+07a] it has been used until recently in a configuration with a camera consisting of 379 pixels with a field of view of 0.117°, each. Thus, it reached an energy threshold of 300 GeV, see e.g. [C+08]. Being recently put out of operation, the Whipple 10 m telescope has been dedicated to nightly monitoring observations of the five TeV-brightest northern hemisphere blazars since 2005, [S+08c]. Due to the long history of monitoring observations with this telescope there have been lots of multi-wavelength partners providing quasi-simultaneous data from nearly all other wavelength bands, as demonstrated in [H+09a]. Already in 2007 it was decided that Whipple observations would dovetail with those of the FACT telescope and by this, both groups made the first move into the direction of a full time monitoring network of TeV-bright blazars.

[2] **F**ermi–**G**ST **AG**N **M**ulti-frequency **M**onitoring **A**lliance, F-GAMMA, see http://www.mpifr-bonn.mpg.de/div/vlbi/fgamma

[3] **M**onitor of **A**ll-sky **X**-ray **I**mage, MAXI, see http://kibo.jaxa.jp/en/experiment/ef/maxi and http://maxi.riken.jp

[4] see http://veritas.sao.arizona.edu/whipple-10m-topmenu-117

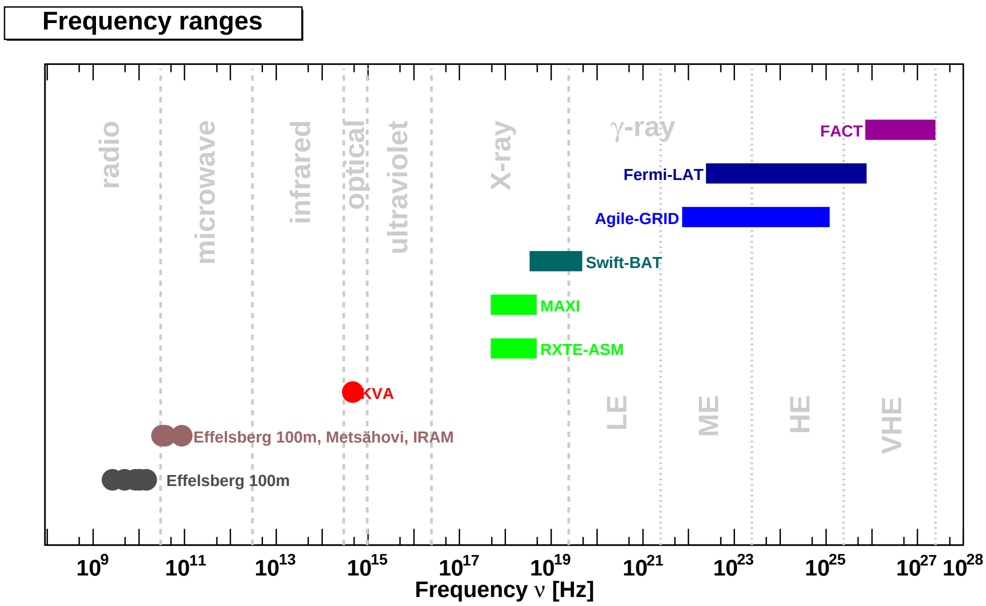

Figure 8.2: The frequency coverage of FACT, its multi-frequency partners and all-sky instruments.

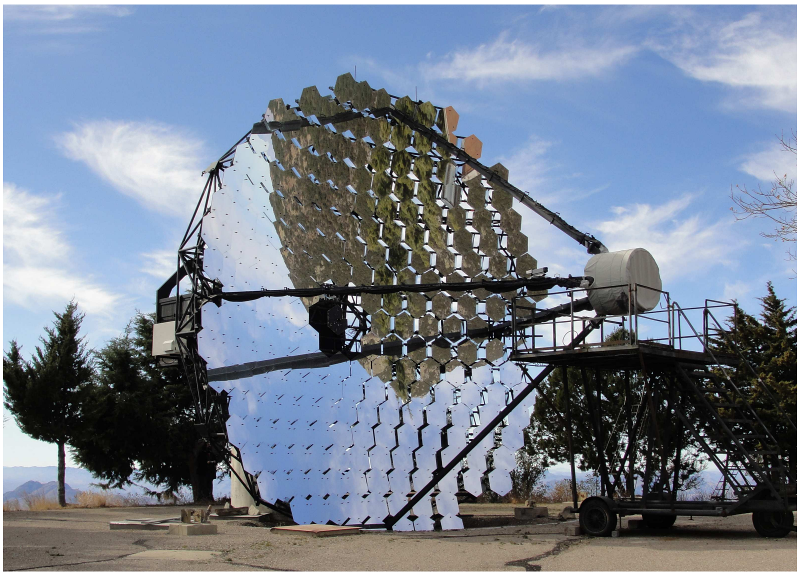

Figure 8.3: Whipple 10 m telescope as in December 2009.

8.3 TACTIC

The TACTIC[5] gamma-ray telescope [K+07b] on Mt. Abu (1300 m a.s.l.), India, has been in operation since 2001 and is depicted in Figure 8.4. With its 9.5 m^2 mirror area and

[5] **T**eV **A**tmospheric **C**herenkov **T**elescope with **I**maging **C**amera, TACTIC, see http://www.barc.ernet.in/pg/nrl-harl

its 349 pixel camera it has a similar performance as a single HEGRA telescope, reaching an energy threshold of 1.2 TeV (c.f. Table 4.2). By this, it is capable of establishing a $3\,\sigma$ signal of a Crab Nebula like source within 9 hours [K+07b]. Except for the high flux states of the sources, the TACTIC telescope is better suited for monitoring on a weekly rather than a daily time scale. The TACTIC telescope is dedicated to monitoring observations on a long-term basis and is perfectly suited to be part of the DWARF network. In the course of this thesis, official contacts to the TACTIC collaboration have been established and the TACTIC collaboration expressed their interest in joining the DWARF network.

Figure 8.4: The TACTIC telescope on Mt. Abu in India [Col11b].

8.4 OMEGA

Beside the HAWC[6] detector on the Volcano Sierra Negra, two of the former HEGRA telescopes ($8.5\,\mathrm{m}^2$ mirror, 271 pixel camera, each, c.f. subsection 4.2.2) have been installed

[6] **H**igh **A**ltitude **W**ater **C**herenkov Experiment, HAWC, see http://hawc.umd.edu

under the name of OMEGA[7] [S+08a] as depicted in Figure 8.5. Due to the higher altitude of 4,100 m a.s.l. (instead of 2,200 m a.s.l. at the HEGRA site), the energy threshold is expected to be lower than 500 GeV which will raise the source detection rate compared to a former two telescope HEGRA system. Hereto, OMEGA will be well suited for a daily monitoring of the TeV brightest blazars. All hardware and software have been checked at UNAM[8], Mexico [A+09g] and have recently been installed at the HAWC site. The primary scientific goal of OMEGA will be to monitor nearby blazars.

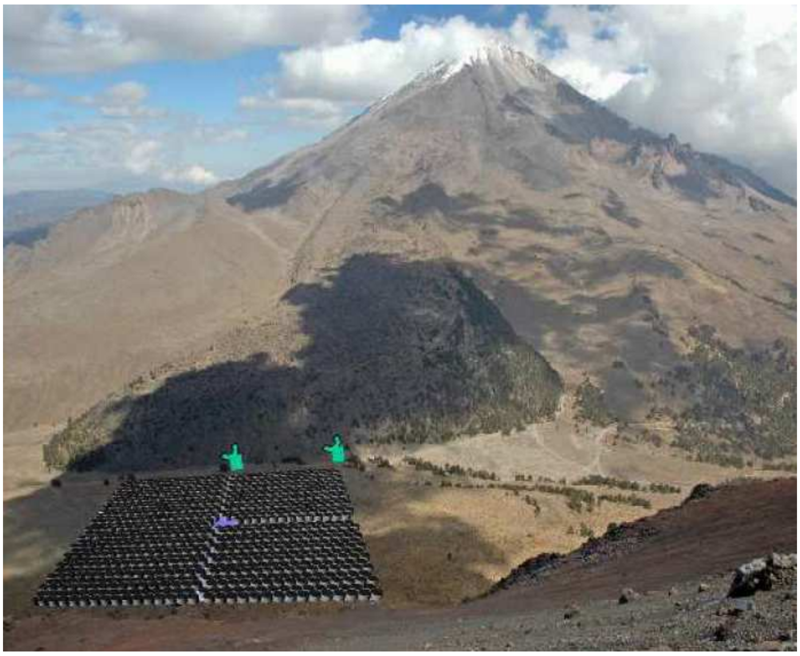

Figure 8.5: The site of the HAWC and OMEGA telescopes as seen from the Sierra Negra. The black array depicts the position of HAWC, whereas the green figures stand for the OMEGA telescopes [A+09g].

8.5 Romanian CT

Lead by the Institute for Space Science, Bucharest, a Romanian consortium has started two projects to prepare the construction of a Cherenkov telescope in their homeland [Rad08]. The first one is engaged in the construction of a dedicated instrument to measure the light of the night sky and the second one is carrying out the site search, based on meteorological, astronomical and social/infrastructural conditions [R+10]. The study on the astroclimatological conditions for the years 2000–2009 of several sites have selected Baisoara as the optimal site in Romania to build the Cherenkov telescope [R+11a]. After the completion of those projects, a Cherenkov telescope will be built and operated within the DWARF network for blazar monitoring. An according Memorandum of Understanding has been worked out and put into force in the course of this thesis.

[7] **O**bservatorio **ME**xicano de **GA**mmas, *mex.* Mexican Observatory of Gammas, OMEGA
[8] **U**niversidad **N**acional **A**utónoma de **M**éxico, UNAM

8.6 Star Base Utah

Star Base Utah[9] consists of two telescopes of the former Telescope Array, each one having a reflector of 3 m diameter with $f/D = 1$ Davis-Cotton optics. The telescopes are built less than 50 miles western of Salt-Lake-City on a 23 m East-West baseline, see Figure 8.6. They were constructed as a test bench for gamma-ray astronomy instrumentation and for intensity interferometry [F+08b]. After Cherenkov cameras will have been built, Star Base Utah will join the monitoring efforts with a stereoscopic system.

Figure 8.6: The Star Base Utah telescopes at night [Col11a].

8.7 Feasibility and Conclusions

The physical motivation of long-term monitoring observations of bright AGN with such ambitious goals as the detection of binary black holes through temporally modulated gamma-ray emission and the detection of hadronic acceleration processes in AGN through cross-correlation of full-time gamma-ray and neutrino observations has been presented in chapter 6. In this chapter, a distributed monitoring network of Cherenkov telescopes for long-term 24/7 observations has been introduced – the DWARF network. In the previous sections, the technical and especially the political build-up of this network has been outlined.

Concerning the feasibility of the project, considerations of the instruments' sensitivity as well as on the temporal coverage are sensible. Statements about the instruments' sensitivities have been given in the previous sections. Figure 8.7 gives an overview about these sensitivities. The minimum integral flux F is depicted against the lower integration boundary in energy E_0. The scaling of the sensitivities is such, that values of F larger than denoted by the corresponding curve result in a $3\,\sigma$ detection within 6 hours of observation time. Additionally, the integral fluxes of the blazars to be monitored with the DWARF network are shown at the lowest published emission states. However, it is obvious that for all instruments besides TACTIC daily measurements of all but the weakest sources are feasible.

[9] see http://www.physics.utah.edu/starbase

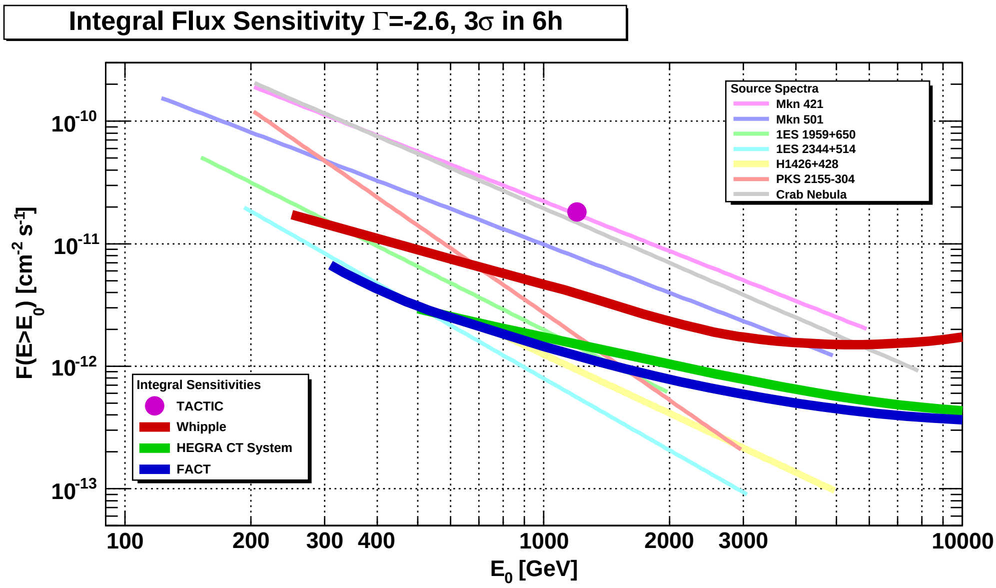

Figure 8.7: Integral spectra of the sources to be monitored with DWARF and the sensitivities of the involved instruments scaled to 3 σ in 6 hours: TACTIC [K+07b], Whipple 10 m [Vas99], HEGRA CT System [Mag97] as an approximation for OMEGA, and FACT as extrapolated in [Bac08]. The spectra are derived from [A+07e] for Mkn 421, [A+07f] for Mkn 501, [T+08a] for 1ES 1959+650, [A+07d] for 1ES 2344+514, [H+03c] for H 1426+428, [A+05b] for PKS 2155-304, and [A+08i] for the Crab Nebula.

Thinking about the goal of conducting 24/7 monitoring of the brightest blazars, the spacial distribution of the telescopes and thus the temporal coverage is a key issue. Figure 8.8 shows the spacial distribution of the telescopes and illustrates the temporal coverage by color coding temporal displacements of approximately 6 hours. Additionally, the local time difference of each telescope location w.r.t. UTC is given as start time for observations lasting 6 hours. As one can see, with only the five actual telescope locations it will be possible to conduct continuous observations for about 18 hours a day, even ensuring temporal overlap between “neighboring” telescopes.
In conclusion, it has been shown that both the telescopes’ sensitivities and the spacial distribution of the presented Cherenkov telescopes ensure that the planned monitoring program of the TeV-brightest blazars can be conducted and will achieve the goal of well sampled, densely populated lightcurves.

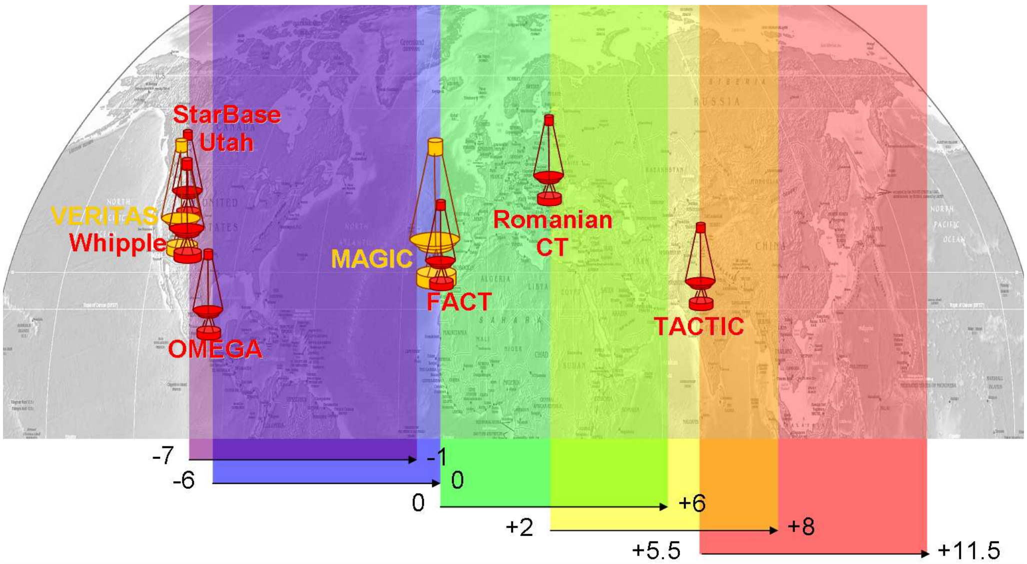

Figure 8.8: The spacial distribution of the Dwarf network telescopes illustrating the temporal coverage by color coding temporal displacements of approximately 6 hours. Additionally, the local time difference w.r.t. UTC is given for each telescope location as start time for observations lasting 6 hours.

Chapter 9
Final Conclusions and Outlook

In the course of this thesis the question for the origin of cosmic rays has been addressed through the long-term behavior of blazars, focusing on the very high energy gamma-ray emission. For this a severalfold approach has been followed as outlined below.

To improve the multivariate separation of gamma-ray events from hadronic background events in data of atmospheric Cherenkov telescopes, two different approaches have been followed in the peripherals of this thesis. The first one focuses on improvements of the execution time of the Ada^{2}Boost algorithm by the re-sampling of training sets. By this, the same classification performance is achieved with a smaller overall training set and simultaneously in far less execution time, as the internal data handling is vastly reduced by the much smaller training samples. The second approach concentrated on optimizing the classification performance, but not for the highest sensitivity but for the smallest error on the estimation of the number of gamma-ray events. This is of particular interest for the determination of lightcurves and energy spectra, being derived from these estimates. Besides that, it reduces the systematic uncertainty of these analyses.

The FACT telescope, the first application of G-APDs as photosensors in an imaging atmospheric Cherenkov telescope has recently been constructed and already during its commissioning phase reported on very promising first results. After the commissioning, it will be devoted to monitoring observations of bright blazars. For the construction of this telescope, the aluminum mirrors of the former HEGRA CT1 have been completely reworked, i.e. re-machined and coated with a protective quartz layer. After that, the mirrors have been characterized, measuring the focal lengths and the spot sizes of a reflected point-like light source. The focal length of all mirrors was found to be on average (4.890 ± 0.008) m, which is a very good value, especially for the extremely small spread. The spot sizes containing 95% of the reflected light have been measured to be on average $(15.95 \pm 6.73)\,\mathrm{mm}^2$, which is well below a quarter of the pixel area used in FACT and thus an excellent value. Hence, the mirrors ensure a high quality imaging well below the camera's resolution and the values determined for every individual mirror will be a valuable input for the telescope simulations needed for data analysis.

The ongoing monitoring campaign of bright blazars with MAGIC was described and the results on Mkn 421 and Mkn 501 were briefly summarized. The results of the monitoring of 1ES 1959+650 have extensively been outlined, including the MAGIC monitoring campaign between 2004–2009, the compilation of multi-wavelength lightcurves and the time-averaged spectral energy distribution. The studies on the fractional variability in the multi-wavelength context yielded modest to strong variations in the optical, X-rays, and high energy gamma-rays, whereas no variability at all has been observed with MAGIC. This finding can hardly be explained in the SSC model, which is commonly used to describe the spectral energy distribution of high-frequency peaked BL Lac objects such as 1ES 1959+650. This gives rise to the assumption of hadronic emission models or of such models with multiple radiation zones. Besides these unexpected consequences, this result enabled the determination of a common multi-year energy spectrum with MAGIC observations from the years of 2005–2009, which can be described by a power-law

$$F(E) = (2.12 \pm 0.08) \cdot 10^{-12} \cdot (E/1\,\mathrm{TeV})^{-2.57\pm0.06}\,\mathrm{ph\,TeV^{-1}\,cm^{-2}\,s^{-1}}. \tag{9.1}$$

This is by far the most exact energy spectrum determined for 1ES 1959+650 in very high energy gamma-rays.
Generalizing this approach also to the energy spectra determined by HEGRA in a comparably low emission state between 2000–2002 and time-integrated measurements by Fermi–LAT, enabled for the first time the determination of the spectral shape of the gamma-ray emission spanning three orders of magnitude in energy from 10 GeV to 10 TeV,

$$F(E) = (2.24\pm0.09)\cdot10^{-12}\cdot(E/1\,\mathrm{TeV})^{-2.58\pm0.04-(0.17\pm0.04)\cdot\log_{10}(E/1\,\mathrm{TeV})}\,\mathrm{ph\,TeV^{-1}\,cm^{-2}\,s^{-1}}. \tag{9.2}$$

During these studies special attention has been paid to the influence of single data points through the Cook's distance and to the Gaussian distribution of the fit residuals for the determination of good fits.
Based on the time-averaged gamma-ray energy spectrum, the time-averaged spectral energy distribution of 1ES 1959+650 has been compiled, resulting in the completest dataset presented so far for any HBL, spanning 20 orders of magnitude in frequency with essentially no gaps. Although not being recorded simultaneously, the variability amplitudes in the different frequency ranges can clearly be seen. Just as the steady VHE gamma-ray emission level and the coexistent variability in X-rays, the very flat spectral shape in the Fermi–LAT energy range obviously cannot be explained by a simple SSC model. By this, 1ES 1959+650 is one of the very first HBLs whose non-thermal emission cannot be explained with a SSC model.
Furthermore it was outlined, that hadronic emission models, though generally being able to explain the shape of the SED, are disfavored for being extremely sensitive to parameter variations throughout the modeling. Instead, it was shown, that a model of two independent, self-consistent emission regions explains the overall SED extremely well.
Finally, it was presented, that a global network of a small number of Cherenkov telescopes dedicated to monitoring observations of TeV-bright blazars will be well suited to obtain plentiful, well sampled lightcurves, needed for studying possible temporal correlations between very high energy gamma-rays and other wavelengths.
Summarizing, the long-term gamma-ray monitoring of blazars has been addressed in various ways throughout this thesis, bearing unexpected results on the steadiness of the

very high energy gamma-ray emission as well as on the spectral shape of the blazar 1ES 1959+650, which are both hardly explainable in SSC models.
In the future, these findings will have to be confirmed by simultaneous multi-wavelength campaigns and high quality long-term observations, especially in the very high energy gamma-rays, to ensure that none of the findings is caused by averaging over different emission states. For this, the FACT telescope and the DWARF network, both of them having been set-up in the course of this thesis, will be perfectly suited.

Appendix A
Energy Ranges

The energy ranges of electromagnetic radiation. The conversion of the different physical units is based on $E = h\nu = hc/\lambda$.

Radiation type	Abbrev.	Energy E [eV]	Frequency ν [Hz]	Wavelength λ [m]
Radio		$1.2 \cdot 10^{-8} - 1.2 \cdot 10^{-4}$	$3 \cdot 10^{6} - 3 \cdot 10^{10}$ (MHz – GHz)	$100 - 0.01$ (cm – m)
Microwave		$1.2 \cdot 10^{-4} - 1.2 \cdot 10^{-2}$	$3 \cdot 10^{10} - 3 \cdot 10^{12}$ (GHz – THz)	$0.01 - 10^{-4}$ (mm)
Infrared	IR	$1.2 \cdot 10^{-2} - 1.2$ (eV)	$3 \cdot 10^{12} - 3 \cdot 10^{14}$	$10^{-4} - 10^{-6}$ (μm)
Optical	Vis	$1 - 4$ (eV)	$3 \cdot 10^{14} - 3 \cdot 10^{15}$	$10^{-6} - 3 \cdot 10^{-7}$ (nm – μm)
Ultraviolet	UV	$4 - 125$ (eV)	$3 \cdot 10^{15} - 3 \cdot 10^{16}$	$3 \cdot 10^{-7} - 10^{-8}$
X-ray	X-ray	$125 - 1.3 \cdot 10^{5}$ (keV)	$3 \cdot 10^{16} - 3 \cdot 10^{19}$	$10^{-8} - 10^{-11}$
Gamma-ray	γ-ray		$> 3 \cdot 10^{19}$	$< 10^{-11}$
Low energy	LE	$10^{5} - 10^{7}$ (MeV)	$3 \cdot 10^{19} - 3 \cdot 10^{21}$	
Medium energy	ME	$10^{7} - 10^{9}$ (MeV – GeV)	$3 \cdot 10^{21} - 3 \cdot 10^{23}$	
High energy	HE	$10^{9} - 10^{11}$ (GeV)	$3 \cdot 10^{23} - 3 \cdot 10^{25}$	
Very high energy	VHE	$10^{11} - 10^{13}$ (TeV)	$3 \cdot 10^{25} - 3 \cdot 10^{27}$	
Ultra high energy	UHE	$> 10^{13}$	$> 3 \cdot 10^{27}$	

Appendix B
Data for Lightcurves

B.1 Radio Observations

Date [MJD]	$Flux_{14.5\,GHz}$ [erg/cm^2/s]	σ_{date} [MJD]	σ_{flux} [erg/cm^2/s]
52764.5	0.190141	-	-
52766.5	0.110916	-	0.080546
52767.5	0.319543	-	0.180898
52768.5	0.528169	-	0.129401
52769.5	0.311620	-	0.130721
52770.5	0.079226	-	0.048856
52773.5	0.163733	-	-
52774.5	0.200705	-	-

Table B.1: Lightcurve data from UMRAO (14.5 GHz) [G+06b].

Date [MJD]	$Flux_{14\,GHz}$ [Jy]	σ_{date} [MJD]	σ_{flux} [Jy]
54686.2	0.202	-	0.005
54692.1	0.197	-	0.005
54698.1	0.203	-	0.005
54700.1	0.22	-	0.005
54712.1	0.215	-	0.005
54763	0.215	-	0.005
54772.9	0.216	-	0.005
54785.9	0.211	-	0.005
54787.9	0.21	-	0.004
54789.9	0.21	-	0.004
54791.9	0.225	-	0.005

54793.9	0.222	-	0.005
54803.8	0.231	-	0.005
54805.8	0.228	-	0.005
54819.8	0.198	-	0.004
54821.8	0.208	-	0.005
54823.8	0.213	-	0.005
54859.7	0.202	-	0.005
54861.7	0.202	-	0.004
54863.7	0.198	-	0.004
54865.7	0.202	-	0.004
54873.6	0.206	-	0.004
54879.6	0.204	-	0.005
54881.6	0.208	-	0.005
54883.6	0.215	-	0.005
54887.6	0.209	-	0.005
54889.6	0.219	-	0.005
54891.6	0.22	-	0.005
54895.6	0.211	-	0.005
54899.6	0.209	-	0.004
54901.6	0.202	-	0.004
54903.6	0.214	-	0.005
54905.6	0.208	-	0.005
54909.5	0.227	-	0.004
54918.8	0.212	-	0.004
54931.4	0.232	-	0.004
54940.4	0.225	-	0.003
54943.4	0.22	-	0.003
54949.3	0.229	-	0.004
54955.3	0.225	-	0.004
54962.3	0.24	-	0.004
54965.3	0.242	-	0.004
54968.3	0.233	-	0.004
54971.3	0.247	-	0.004
54974.3	0.229	-	0.004
54977.3	0.227	-	0.004
54999.2	0.231	-	0.004
55018.2	0.23	-	0.004
55024.2	0.226	-	0.004
55027.2	0.236	-	0.004
55039.2	0.215	-	0.007
55048.2	0.224	-	0.006

Table B.4: Lightcurve data from OVRO (14 GHz) [Pan11].

Date [MJD]	$\text{Flux}_{15\,\text{GHz}}$ [Jy]	σ_{date} [MJD]	σ_{flux} [Jy]
51609	0.131	-	-
51704	0.147	-	-
52799	0.167	-	-
52943	0.151	-	-
53043	0.092	-	-
54616	0.194	-	-
54742	0.172	-	-
54762	0.19	-	-
54887	0.179	-	-
54983	0.219	-	-
54985	0.219	-	-
55035	0.218	-	-

Table B.2: Lightcurve data from MOJAVE (15 GHz) [L+11a].

Date [MJD]	$\text{Flux}_{14.6\,\text{GHzV}}$ [Jy]	σ_{date} [MJD]	σ_{flux} [Jy]
54184.2	0.213	-	0.006
54218.3	0.195	-	0.006
54274.3	0.189	-	0.006
54338.0	0.203	-	0.005
54359.8	0.205	0.001	0.009
54454.2	0.196	0.001	0.011
54513.6	0.179	-	0.004
54934.5	0.228	0.001	0.005
55010.3	0.244	0.002	0.006
55101.9	0.197	0.002	0.005

Table B.3: Lightcurve data from Effelsberg 100 m (14.6 GHz) [FA11].

B.2 Optical Observations

These values have been corrected for the host galaxy flux, in R-band according to [N+07b] and in V-band following the $z = 0$ approximation from the model of [FSI95], stating $F_V - F_R = 0.61$ mJ.

Date [MJD]	$\text{Flux}_{\text{R-band}}$ [Jy]	σ_{date} [MJD]	σ_{flux} [Jy]
52527.8	0.00389898	-	6.41068e-005
52528.8	0.00402301	-	6.6146e-005
52543.8	0.00416247	-	7.2208e-005
52549.8	0.00407146	-	9.26779e-005
52554.8	0.0040978	-	6.73758e-005
52566.8	0.0043707	-	8.37245e-005
52569.8	0.00455985	-	7.91017e-005
52576.8	0.00450973	-	7.82322e-005
52638.8	0.00400452	-	9.11541e-005
52641.7	0.00366565	-	7.68356e-005
52751	0.00382781	-	6.29367e-005
52762	0.00443558	-	7.69459e-005
52763.9	0.00450558	-	7.40805e-005
52868.9	0.00446839	-	7.7515e-005
52880.9	0.00407897	-	6.70662e-005
52882.9	0.00408273	-	6.7128e-005
52883.9	0.00406397	-	6.68196e-005
52886.9	0.00391697	-	6.44027e-005
52891.8	0.00400821	-	6.59028e-005
52892.9	0.00396051	-	6.87046e-005
52895.8	0.0038384	-	6.31108e-005
52902.8	0.00398612	-	6.55396e-005
52906.8	0.0041243	-	6.78116e-005
52917.8	0.0041663	-	6.85021e-005
52926.8	0.00372349	-	6.12215e-005
52930.7	0.00400821	-	6.59028e-005
52931.7	0.00396781	-	6.52385e-005
52935.8	0.00410535	-	6.75e-005
52938.8	0.00438279	-	7.20616e-005
52951.7	0.00386323	-	6.70171e-005
52954.8	0.00385612	-	6.34021e-005
52955.7	0.0039242	-	6.80747e-005
52959.8	0.00374413	-	6.15607e-005
52960.8	0.00382429	-	6.28788e-005
52961.8	0.00380672	-	6.25898e-005
52979.8	0.00380672	-	6.60367e-005
52981.8	0.00391697	-	6.79494e-005
53107.9	0.00349422	-	5.74518e-005

53174.1	0.00346219	-	5.69251e-005
53179	0.00346857	-	6.01708e-005
53190	0.003459	-	6.93835e-005
53203.1	0.00349744	-	6.06716e-005
53220	0.00343045	-	5.95094e-005
53227	0.00355591	-	5.84661e-005
53235	0.00356247	-	6.17996e-005
53243	0.00352007	-	6.42484e-005
53251.9	0.0037098	-	6.43555e-005
53252.9	0.00371322	-	6.10526e-005
53253.9	0.00363204	-	5.64261e-005
53253.9	0.00364209	-	5.65822e-005
53254	0.00365217	-	6.00487e-005
53254.9	0.00354283	-	5.50402e-005
53254.9	0.00356575	-	5.53962e-005
53255	0.00352981	-	5.48378e-005
53255.9	0.00358221	-	6.53826e-005
53256.9	0.00356247	-	5.85739e-005
53257.9	0.00363874	-	6.64144e-005
53258.9	0.00368936	-	6.40008e-005
53260.9	0.0036589	-	6.34725e-005
53261.9	0.00360206	-	6.24864e-005
53262.9	0.00369276	-	6.07161e-005
53269.9	0.00364881	-	6.32973e-005
53270.9	0.00363539	-	5.97728e-005
53292.7	0.00357232	-	5.87359e-005
53350.8	0.00428303	-	7.04213e-005
53466.2	0.00489498	-	8.93434e-005
53469.2	0.00491305	-	8.078e-005
53473.2	0.00516834	-	0.000112992
53477.2	0.00504139	-	9.20158e-005
53478.2	0.00501361	-	7.78897e-005
53480.2	0.00507868	-	8.8102e-005
53493.2	0.00474407	-	9.08767e-005
53498.2	0.00461053	-	7.58061e-005
53501.2	0.00465748	-	8.07952e-005
53509.2	0.00453055	-	7.4491e-005
53511.2	0.00460204	-	7.56665e-005
53514.2	0.00443967	-	0.000101059
53518.2	0.00437473	-	9.56415e-005
53520.2	0.00435864	-	7.95541e-005
53521.2	0.00443558	-	8.09585e-005
53522.2	0.0044152	-	7.65924e-005
53523.2	0.00439897	-	7.63107e-005
53524.2	0.00455565	-	8.72675e-005
53527.2	0.00439087	-	8.01424e-005

53528.2	0.00453055	-	7.85933e-005
53531.2	0.00456826	-	8.7509e-005
53532.2	0.00459781	-	7.97601e-005
53533.2	0.00445606	-	7.73011e-005
53539.2	0.00447662	-	7.76579e-005
53547.2	0.0043028	-	8.63091e-005
53551.1	0.00446839	-	7.7515e-005
53552.1	0.00443967	-	7.70168e-005
53555.1	0.00423205	-	7.72436e-005
53558.1	0.00427514	-	7.80302e-005
53559.1	0.00425158	-	7.3754e-005
53562.2	0.00427121	-	7.40944e-005
53564.1	0.0042555	-	7.76717e-005
53565.2	0.00423985	-	7.7386e-005
53566.1	0.00414334	-	7.18763e-005
53567.1	0.00417014	-	7.61136e-005
53569.1	0.00406772	-	7.79206e-005
53570.1	0.00411292	-	8.62109e-005
53571.2	0.0041663	-	9.85848e-005
53574.1	0.00400452	-	7.67101e-005
53576.1	0.00411671	-	7.88592e-005
53585.1	0.00406023	-	7.77772e-005
53586.1	0.00400821	-	7.31581e-005
53587.1	0.00398245	-	7.2688e-005
53595	0.00360206	-	7.55027e-005
53597	0.00357561	-	6.8494e-005
53605.9	0.00361868	-	6.27748e-005
53612.9	0.00365553	-	6.01041e-005
53613.8	0.00373036	-	6.13344e-005
53639	0.00356903	-	6.51422e-005
53641.9	0.00354283	-	6.4664e-005
53642.9	0.00365217	-	6.99604e-005
53654.9	0.00363539	-	6.63533e-005
53675.8	0.00366227	-	6.02149e-005
53720.7	0.00394231	-	7.19553e-005
53722.8	0.00406397	-	7.41759e-005
53725.7	0.00409403	-	6.73138e-005
53747.7	0.00453055	-	7.4491e-005
53754.7	0.00467467	-	8.53223e-005
53811.8	0.00544692	-	8.95579e-005
53816	0.00571414	-	9.39515e-005
53817.9	0.00559952	-	9.2067e-005
53818.3	0.00542189	-	9.89607e-005
53819.3	0.00528872	-	0.000106086
53820.3	0.00545194	-	0.000104437
53825.2	0.00561501	-	0.00010756

53826.2	0.00550745	-	0.000110473
53827.2	0.00572995	-	0.000104583
53830.2	0.00578297	-	0.000105551
53831.2	0.00585802	-	0.000101622
53833.2	0.0057194	-	0.000104391
53840.2	0.0058311	-	0.000169353
53844.2	0.00595046	-	0.000108608
53845.2	0.00596143	-	0.000108808
53848.9	0.00617377	-	0.000101509
53859.2	0.00589591	-	0.000102279
53860.2	0.00610591	-	0.000105922
53861.2	0.0063409	-	0.000109998
53872.2	0.00540195	-	0.000108357
53874.2	0.00535243	-	9.76928e-005
53875.2	0.00546199	-	8.98057e-005
53877.2	0.00538705	-	9.83247e-005
53878.2	0.00529359	-	9.18302e-005
53879.2	0.00540195	-	8.88186e-005
53880.2	0.00560984	-	8.71525e-005
53880.2	0.00563055	-	9.25772e-005
53882.2	0.00556353	-	9.65129e-005
53883.2	0.00565133	-	9.8036e-005
53884.2	0.00585802	-	9.1008e-005
53885.2	0.00589591	-	0.000102279
53886.2	0.00589048	-	0.000112837
53887.2	0.00604437	-	0.000104854
53888.2	0.00604994	-	0.000104951
53889.2	0.00600552	-	0.00010418
53891.2	0.00585802	-	0.000101622
53892.2	0.00605551	-	0.000110526
53893.2	0.00598344	-	0.000103797
53897.1	0.00598895	-	0.000109311
53898.1	0.00585263	-	0.000101528
53901.2	0.00571414	-	0.000109459
53902.1	0.00583648	-	0.000101248
53904.2	0.00577764	-	0.000100227
53905.1	0.00585802	-	0.000101622
53906.2	0.00592312	-	0.000102751
53907.2	0.00584185	-	0.000101341
53908.2	0.00601659	-	0.000109815
53909.2	0.00601106	-	0.000104276
53910.1	0.00595595	-	0.00010332
53911.2	0.00611154	-	0.000106019
53913.1	0.00617946	-	0.000107198
53914.1	0.00615107	-	0.000106705
53915.1	0.0060388	-	0.000104758

53918.1	0.00593404	-	0.00010294
53919.1	0.00609468	-	0.000105727
53920.1	0.00635259	-	0.000110201
53921.1	0.0063643	-	0.000110404
53922.1	0.00617377	-	0.000107099
53925.2	0.00613975	-	0.000194766
53926.1	0.0063643	-	0.000110404
53927.1	0.00629435	-	0.000126257
53928.1	0.00677565	-	0.000135912
53930.1	0.0072003	-	0.000124907
53931.1	0.00697189	-	0.000127251
53932.1	0.00693347	-	0.00012655
53933.2	0.00700407	-	0.000146812
53934.1	0.00709497	-	0.000123079
53935.2	0.00704938	-	0.000128666
53936.2	0.00718043	-	0.000131058
53938.1	0.00707539	-	0.000135535
53939.1	0.00693986	-	0.000139206
53940.2	0.00683834	-	0.000137169
53941.2	0.00681947	-	0.000130633
53948.1	0.00695266	-	0.000120611
53949.1	0.00664585	-	0.000115288
53953.1	0.00651855	-	0.000118977
53954.9	0.00659706	-	0.000126373
53958	0.0062309	-	0.000119358
53958.9	0.00633506	-	0.000121354
53967	0.00691434	-	0.000126201
53971	0.00675073	-	0.000123215
53975	0.00656071	-	0.000125676
53979	0.00631758	-	0.000132423
53992.8	0.00655467	-	0.000107772
53993	0.00639957	-	0.000116805
53996.9	0.0062539	-	0.000119799
54000.9	0.0064469	-	0.000117669
54004.9	0.00718043	-	0.000131058
54045.8	0.00643503	-	0.000123269
54047.8	0.00653658	-	0.000113393
54062.8	0.00630015	-	0.000114991
54097.7	0.00528872	-	9.17457e-005
54228.2	0.00428303	-	7.8174e-005
54230.2	0.00425942	-	7.77432e-005
54231.2	0.00430676	-	8.63886e-005
54233.2	0.00434261	-	7.92615e-005
54235.2	0.00462755	-	8.44622e-005
54236.2	0.00459357	-	8.38422e-005
54238.2	0.0045809	-	8.36108e-005

54239.2	0.00459357	-	8.38422e-005
54245.2	0.00469192	-	8.56372e-005
54247.2	0.00466606	-	8.51653e-005
54249.2	0.00472662	-	8.62705e-005
54253.2	0.00469624	-	9.42012e-005
54255.2	0.00466606	-	8.51653e-005
54256.2	0.00483672	-	9.26515e-005
54257.2	0.00457668	-	8.35339e-005
54261.2	0.00456826	-	8.33801e-005
54263.2	0.00466606	-	8.93825e-005
54265.2	0.00457668	-	8.76703e-005
54266.2	0.00453055	-	8.67866e-005
54268.2	0.00458934	-	8.3765e-005
54269.1	0.0045389	-	8.28443e-005
54270.1	0.00449315	-	8.60701e-005
54271.1	0.00458512	-	8.78319e-005
54272.1	0.00435864	-	7.95541e-005
54277.1	0.00412051	-	7.52077e-005
54278.1	0.00421261	-	8.06961e-005
54279.1	0.00424376	-	8.12929e-005
54280.1	0.0042555	-	8.15178e-005
54281.1	0.0044152	-	8.4577e-005
54282.2	0.00431868	-	8.2728e-005
54283.1	0.00420485	-	8.05476e-005
54284.1	0.00410914	-	7.87141e-005
54285.1	0.00415098	-	7.57639e-005
54286.1	0.00411671	-	7.51385e-005
54287.1	0.00417783	-	8.38024e-005
54291.1	0.00427121	-	8.18187e-005
54299.1	0.00427908	-	0.000162369
54300.1	0.00417398	-	8.37253e-005
54311.9	0.00481893	-	0.000109692
54313	0.00470057	-	0.000115452
54313.9	0.00483672	-	9.70189e-005
54314.9	0.00503675	-	9.64834e-005
54315.9	0.00501823	-	9.61286e-005
54316.9	0.00475281	-	0.000103907
54317.9	0.00485904	-	9.30792e-005
54319.9	0.00479237	-	9.18021e-005
54320.9	0.00477036	-	9.13803e-005
54321.9	0.00480121	-	9.19713e-005
54322.9	0.00466177	-	8.93002e-005
54323.9	0.00476596	-	9.98993e-005
54324.9	0.00459357	-	8.79939e-005
54325.9	0.00463608	-	8.88081e-005
54326.9	0.00453472	-	8.68665e-005

54327.9	0.00446839	-	8.96306e-005
54328.9	0.00433861	-	8.31098e-005
54329.9	0.00440302	-	8.43437e-005
54330.9	0.00444786	-	8.52025e-005
54331.9	0.00439087	-	8.41109e-005
54333.9	0.00451805	-	7.83764e-005
54334.9	0.00458934	-	8.3765e-005
54335.9	0.00452638	-	8.26157e-005
54338.9	0.00444376	-	8.91367e-005
54340.9	0.00471358	-	0.00010305
54342.9	0.00465319	-	9.75354e-005
54345.9	0.00478796	-	9.6041e-005
54347.9	0.00458512	-	8.78319e-005
54348.9	0.00467467	-	8.95473e-005
54349.9	0.00473534	-	9.07094e-005
54350.9	0.00475719	-	8.68286e-005
54351.9	0.00480563	-	8.77127e-005
54352.9	0.00477036	-	8.70688e-005
54354.9	0.00483226	-	9.25662e-005
54356.9	0.00515408	-	9.40725e-005
54358.9	0.00526442	-	9.60865e-005
54360.9	0.00525473	-	9.59097e-005
54362.8	0.00530336	-	0.00010159
54363.9	0.00540195	-	0.000108357
54367.9	0.0052499	-	0.000100566
54370.9	0.00497222	-	9.97371e-005
54371.8	0.0049221	-	9.42871e-005
54372.8	0.00493572	-	9.4548e-005
54373.8	0.00493572	-	9.00871e-005
54375.9	0.00471358	-	9.02927e-005
54381.9	0.004868	-	8.8851e-005
54385.9	0.0052499	-	9.10721e-005
54388.9	0.00494027	-	9.46352e-005
54389.8	0.00489047	-	8.92612e-005
54391.8	0.00501361	-	9.60401e-005
54393.8	0.00520176	-	0.000104341
54396.8	0.00533766	-	0.000102247
54398.8	0.00546199	-	0.000104629
54401.9	0.00547206	-	0.000104822
54404.8	0.00541191	-	0.000108557
54405.8	0.00540195	-	9.85967e-005
54406.9	0.00554818	-	0.000101266
54407.8	0.00557379	-	0.000106771
54409.8	0.00545696	-	9.96007e-005
54413.8	0.00546702	-	0.000114594
54415.8	0.00580966	-	0.000116535

54417.8	0.00622516	-	0.000119248
54419.8	0.00593404	-	0.000108309
54447.8	0.0052499	-	9.58214e-005
54568.2	0.00456826	-	8.33801e-005
54570.2	0.00479679	-	8.75513e-005
54571.2	0.00460628	-	8.40742e-005
54572.2	0.00452638	-	8.26157e-005
54573.2	0.00462755	-	8.44622e-005
54574.2	0.0047397	-	8.65092e-005
54575.2	0.00489949	-	8.94257e-005
54576.2	0.00496307	-	9.5072e-005
54577.2	0.00518264	-	9.45938e-005
54578.2	0.00506467	-	9.24406e-005
54579.2	0.00501361	-	9.15087e-005
54581.2	0.00487249	-	9.77364e-005
54582.2	0.00476596	-	9.98993e-005
54583.2	0.00481006	-	0.000182517
54584.2	0.0048501	-	9.29079e-005
54586.2	0.00494482	-	9.91874e-005
54588.2	0.0053475	-	0.000107265
54590.2	0.00519698	-	9.48555e-005
54591.2	0.00511624	-	9.33819e-005
54592.2	0.00488147	-	9.35088e-005
54596.2	0.00470924	-	8.59533e-005
54597.2	0.00481006	-	8.77935e-005
54598.2	0.00478796	-	8.73902e-005
54600.2	0.00474844	-	8.66688e-005
54601.2	0.00483672	-	8.828e-005
54602.2	0.00489498	-	8.93434e-005
54605.2	0.00487698	-	8.90149e-005
54606.2	0.00485457	-	9.29935e-005
54607.2	0.00481006	-	9.64843e-005
54608.2	0.00480121	-	9.63067e-005
54609.2	0.00467467	-	8.95473e-005
54610.2	0.00458512	-	9.19722e-005
54612.2	0.00468329	-	8.97124e-005
54613.2	0.00478355	-	9.16331e-005
54614.2	0.00477036	-	8.70688e-005
54615.2	0.00470057	-	9.4288e-005
54616.2	0.00469624	-	8.99606e-005
54618.2	0.0046876	-	8.97951e-005
54619.2	0.00467467	-	8.95473e-005
54620.2	0.00463608	-	8.88081e-005
54621.2	0.00471358	-	9.02927e-005
54622.2	0.00471358	-	9.02927e-005
54623.1	0.00473098	-	8.635e-005

54624.1	0.00466606	-	8.51653e-005
54625.1	0.00464463	-	8.4774e-005
54626.1	0.00461478	-	8.42292e-005
54627.2	0.00450973	-	8.63878e-005
54628.2	0.00463181	-	8.45401e-005
54629.2	0.00470057	-	9.00435e-005
54630.2	0.00467036	-	8.94649e-005
54631.2	0.00482782	-	9.2481e-005
54635.2	0.00452638	-	9.07939e-005
54636.1	0.00434661	-	8.7188e-005
54637.2	0.00430676	-	8.63886e-005
54639.2	0.00454308	-	9.1129e-005
54640.2	0.00472662	-	9.05425e-005
54641.2	0.00485457	-	9.29935e-005
54642.2	0.00477475	-	9.14645e-005
54643.2	0.00481006	-	9.21409e-005
54644.1	0.00488147	-	0.000115508
54645.1	0.00476596	-	0.000104195
54646.1	0.00487698	-	0.000106622
54647.1	0.0047049	-	9.86194e-005
54648.1	0.0048501	-	9.72874e-005
54649.1	0.00483672	-	8.828e-005
54650.2	0.00479679	-	8.75513e-005
54651.2	0.00485457	-	9.7377e-005
54652.1	0.00479237	-	8.74707e-005
54653.1	0.00472662	-	9.48105e-005
54654.1	0.00471358	-	8.60325e-005
54655.1	0.00465319	-	8.91359e-005
54656.1	0.00465748	-	9.34236e-005
54657.1	0.00455146	-	9.54031e-005
54658.1	0.00464035	-	9.308e-005
54659.1	0.0047049	-	9.01265e-005
54660.1	0.00460628	-	8.82374e-005
54662.1	0.00457668	-	9.18029e-005
54663.1	0.00466177	-	8.93002e-005
54664.1	0.00462329	-	8.8563e-005
54665.1	0.00464463	-	8.89718e-005
54666.1	0.00462329	-	9.27377e-005
54667.1	0.00457247	-	0.000116412
54669.1	0.00455146	-	0.000103604
54670	0.00454727	-	9.94138e-005
54670.1	0.00467898	-	9.38548e-005
54671.1	0.00465319	-	9.33376e-005
54722.9	0.00485457	-	8.86059e-005
54730.8	0.00453472	-	8.2768e-005
54732.8	0.00474844	-	9.09604e-005

54734.8	0.00502286	-	9.62171e-005
54745.7	0.00532783	-	8.75999e-005
54745.8	0.00532783	-	9.72439e-005
54746.8	0.00526927	-	0.000105696
54747.8	0.00514459	-	0.000107836
54749.8	0.0053475	-	0.000102436
54751.8	0.00532783	-	0.00010687
54752.8	0.0054169	-	0.000108657
54753.9	0.00550238	-	0.000105403
54755.8	0.00547206	-	9.98763e-005
54761.7	0.00568788	-	9.86701e-005
54774.8	0.00496307	-	0.000121899
54781.8	0.00494027	-	8.57009e-005
54784.8	0.00478796	-	9.6041e-005
54785.8	0.00472662	-	0.000208574
54786.8	0.00460204	-	8.39968e-005
54787.8	0.00457247	-	8.34569e-005
54788.8	0.00477475	-	0.000100084
54789.8	0.0047049	-	9.01265e-005
54793.8	0.0048501	-	9.72874e-005
54794.8	0.00489949	-	0.000102698
54795.8	0.00494938	-	0.000121563
54798.8	0.00490852	-	9.4027e-005
54800.8	0.00532783	-	0.000164257
54801.8	0.00521136	-	9.9828e-005
54805.8	0.00526927	-	0.000105696
54932.2	0.00587964	-	0.000123243
54933.2	0.00606109	-	0.000148868
54936.2	0.00611717	-	0.000128222
54937.2	0.0063643	-	0.000121914
54954.2	0.00638191	-	0.000128014
54957.2	0.00658492	-	0.00012614
54958.2	0.00659706	-	0.000126373
54960.2	0.00670735	-	0.000134542
54961.2	0.0067321	-	0.000128959
54962.2	0.00685095	-	0.000131236
54963.2	0.00686358	-	0.000131478
54964.2	0.00680066	-	0.000142548
54965.2	0.00694626	-	0.000133062
54966.2	0.00693986	-	0.000126667
54967.2	0.00701053	-	0.000134293
54969.2	0.00686358	-	0.000131478
54970.2	0.00684464	-	0.000124929
54971.2	0.00676941	-	0.000135787
54972.2	0.00670117	-	0.00012231
54974.2	0.00698475	-	0.000127486

54975.2	0.00696547	-	0.000127134
54976.2	0.00681947	-	0.000124469
54977.2	0.00668884	-	0.000122085
54978.2	0.00663973	-	0.000121189
54979.2	0.00650655	-	0.000118758
54980.2	0.00664585	-	0.000121301
54981.2	0.00675073	-	0.000117108
54982.2	0.00680066	-	0.000117974
54983.2	0.00664585	-	0.000115288
54986.2	0.00699763	-	0.000127721
54987.2	0.00700407	-	0.000127839
54988.2	0.00701053	-	0.000127957
54989.2	0.00692709	-	0.000126434
54990.2	0.00710805	-	0.000136161
54991.2	0.00702345	-	0.00013454
54992.2	0.00715403	-	0.000130576
54993.2	0.00720694	-	0.000131541
54994.2	0.00716722	-	0.000143766
54996.2	0.00727362	-	0.000139332
54997.2	0.00732741	-	0.00013374
55002.1	0.00688257	-	0.000125621
55003.2	0.00680692	-	0.00012424
55004.2	0.00675073	-	0.000135412
55005.2	0.00682576	-	0.000124584
55006.1	0.00667038	-	0.000139818
55007.2	0.00662751	-	0.000120966
55008.1	0.00665811	-	0.000163532
55009.1	0.00659706	-	0.000132329
55010.1	0.00657281	-	0.000125908
55012.1	0.00678189	-	0.000136037
55013.1	0.00702993	-	0.000128311
55014.1	0.00688891	-	0.000125737
55015.1	0.00689526	-	0.000125853
55020.1	0.00801218	-	0.000167943
55022.1	0.0078587	-	0.000157636
55023	0.0076094	-	0.000145765
55024.1	0.00784424	-	0.000143174
55025.1	0.00766568	-	0.000139914
55027.1	0.00811616	-	0.000148137
55028.1	0.00824424	-	0.000172807
55030.1	0.00776517	-	0.000162766
55032.1	0.00801218	-	0.000167943
55033.1	0.00816866	-	0.000163854
55034.1	0.00814612	-	0.000178093
55035.1	0.00826705	-	0.000158363
55036.1	0.00845183	-	0.000169534

55037.1	0.00828993	-	0.000158801
55038.1	0.00810123	-	0.000147864
55039.1	0.00774374	-	0.000162316
55040.1	0.00779383	-	0.000149298
55041.1	0.00770816	-	0.000147657
55042.1	0.0074499	-	0.000149436
55046.1	0.00706237	-	0.000141663
55047	0.00691434	-	0.000138694
55048.1	0.00670117	-	0.000134418
55052	0.00675695	-	0.000369159
55054.1	0.00630595	-	0.000120796
55056.1	0.00645284	-	0.00012361
55056.9	0.00643503	-	0.000105804
55057.9	0.00632923	-	0.000115521
55058.9	0.00646474	-	0.000117995
55059.9	0.00640547	-	0.000116913
55061	0.00639957	-	0.000134141
55063.9	0.00649457	-	0.000130274
55066	0.00626543	-	0.00012002
55068	0.00641728	-	0.000134512
55070	0.00635259	-	0.000121689
55071	0.00621943	-	0.000119139
55072.9	0.00615107	-	0.000128933
55075.9	0.00589591	-	0.000128898
55078.9	0.00562537	-	0.000117913
55080.9	0.00553797	-	0.000106085
55081.9	0.00539698	-	0.000113126
55083	0.00565654	-	0.000118567
55083.9	0.00548215	-	0.000105015
55085.9	0.00591222	-	0.000139898
55086.9	0.0057458	-	0.000110066
55087.9	0.00568265	-	0.00010372
55089.9	0.00584724	-	0.000112009
55099.9	0.00544692	-	0.00010434
55100.9	0.0054771	-	0.000104919
55107.8	0.00559436	-	0.000117263
55110.8	0.00528385	-	0.000101217
55111.8	0.00533274	-	0.000102153
55112.9	0.00544692	-	0.00010434
55113.9	0.00545696	-	0.000104533
55114.9	0.00544692	-	0.00010434
55115.9	0.00559436	-	0.000107165
55116.8	0.00569837	-	0.000109157
55117.8	0.00561501	-	0.00010756
55118.9	0.00556866	-	0.000106673
55119.9	0.00547206	-	0.000104822

55120.9	0.00553797	-	0.000106085
55121.8	0.00566175	-	0.000108456
55122.8	0.00561501	-	0.00010756
55124.9	0.00566175	-	0.000108456
55126.9	0.00557379	-	0.000106771
55127.9	0.00565654	-	0.000108356
55128.8	0.00552778	-	0.000105889
55129.8	0.00540195	-	0.000103479
55130.8	0.00543689	-	0.000118863
55131.8	0.00546702	-	0.000163665
55133.8	0.00543689	-	8.93931e-005
55311.2	0.00367579	-	7.04129e-005
55312.2	0.00379971	-	7.27868e-005
55313.2	0.00387035	-	8.11264e-005
55319.2	0.00364881	-	8.63396e-005
55331.2	0.00353631	-	7.41246e-005
55333.2	0.00346538	-	6.63823e-005
55335.2	0.00347817	-	6.66273e-005
55336.2	0.00340213	-	6.51707e-005
55337.2	0.00346219	-	6.94475e-005
55342.2	0.00359543	-	7.86043e-005
55344.2	0.00367579	-	8.03612e-005
55347.2	0.00360538	-	7.55723e-005
55348.2	0.00372349	-	7.80481e-005
55349.2	0.0036589	-	8.65785e-005
55350.2	0.00384194	-	9.43629e-005
55354.2	0.00394231	-	7.90782e-005
55355.2	0.00388464	-	7.79214e-005
55361.1	0.00407522	-	8.17441e-005
55362.2	0.00398245	-	8.70656e-005
55363.2	0.0040193	-	8.78712e-005
55364.2	0.00394958	-	7.92239e-005
55365.2	0.00407897	-	8.91757e-005
55366.1	0.00405649	-	8.13685e-005
55367.1	0.00409403	-	7.47244e-005
55368.1	0.00400452	-	7.67101e-005
55431.9	0.00433861	-	7.13352e-005
55447.9	0.00476596	-	7.83617e-005
55469.8	0.00528872	-	8.69569e-005

Table B.5: Lightcurve data from KVA R-band [L+10].

Date [MJD]	$\text{Flux}_{\text{R-band}}$ [Jy]	σ_{date} [MJD]	σ_{flux} [Jy]
53860	0.0066	-	0.0002
53861	0.0073	-	0.0003
53871	0.0058	-	0.0003
53872	0.0059	-	0.0003
53878	0.0053	-	0.0004
53880	0.0061	-	0.0003
53882	0.0061	-	0.0003
53885	0.0066	-	0.0003
53886	0.0067	-	0.0002
53887	0.0071	-	0.0002
53894	0.0067	-	0.0002
53898	0.0062	-	0.0002
53899	0.0063	-	0.0003
53900	0.0066	-	0.0003
53901	0.0065	-	0.0002
53908	0.0063	-	0.0005
53909	0.0071	-	0.0004
53910	0.0068	-	0.0003
53912	0.0073	-	0.0003
53916	0.0068	-	0.0002

Table B.6: Lightcurve data from Perugia–AIT R-band [T+08a].

Date [MJD]	$Flux_{R\text{-band}}$ [Jy]	σ_{date} [MJD]	σ_{flux} [Jy]
54961.3	0.008395	-	0.000268991
54970.3	0.009128	-	0.000498607
54972.3	0.008650	-	0.000477678
54974.3	0.008358	-	0.000232467
54975.3	0.009088	-	0.000581378
54983.3	0.008066	-	0.000252192
55003.3	0.008717	-	0.000259106
55005.3	0.008612	-	0.000147526
55015.3	0.009587	-	0.000540482
55016.3	0.008555	-	0.000355259
55018.3	0.009850	-	0.000400005
55019.3	0.010339	-	0.000309595
55026.3	0.009978	-	0.000175616
55028.2	0.01	-	0.000175616
55029.2	0.010284	-	0.00015911
55031.2	0.010563	-	0.00015138
55034.2	0.010417	-	0.000685169
55037.2	0.010218	-	0.000264047

Table B.7: Lightcurve data from GRT R-band [Pan11].

Date [MJD]	$Flux_{R\text{-band}}$ [Jy]	σ_{date} [MJD]	σ_{flux} [Jy]
54379.7	0.00470	-	0.000145602
54381.8	0.00514	-	0.000164924
54437.7	0.00835	-	0.000184391
54438.6	0.00741	-	0.000213776
54453.7	0.00463	-	0.000184391
54463.6	0.00596	-	0.000233452

Table B.8: Lightcurve data from NMS R-band [Pan11].

Date [MJD]	$\text{Flux}_{\text{R-band}}$ [Jy]	σ_{date} [MJD]	σ_{flux} [Jy]
53664.6	0.00296	-	4.47214e-005
53664.6	0.00248	-	8.06226e-005
53665.6	0.00259	-	4.47214e-005
53665.6	0.00344	-	4.47214e-005
53665.7	0.00312	-	4.47214e-005
53666.6	0.00293	-	4.47214e-005
53666.6	0.00351	-	4.47214e-005
53666.7	0.00350	-	4.47214e-005
53667.6	0.00300	-	4.12311e-005
53667.6	0.00344	-	4.47214e-005
53667.7	0.00261	-	4.12311e-005
53669.6	0.00325	-	5e-005
53669.7	0.00328	-	5e-005
53669.7	0.00324	-	5e-005
53671.6	0.00314	-	4.47214e-005
53671.7	0.00310	-	4.47214e-005
53672.6	0.00319	-	4.47214e-005
53672.6	0.00329	-	4.47214e-005
53672.7	0.00323	-	4.47214e-005
53673.6	0.00314	-	4.47214e-005
53673.6	0.00314	-	4.47214e-005
53673.7	0.00307	-	4.47214e-005
53818.0	0.00648	-	5e-005
53832.0	0.00688	-	5e-005
53859.0	0.00686	-	5e-005
53865.9	0.00738	-	5e-005
53866.0	0.00737	-	5e-005
53875.9	0.00564	-	4.47214e-005
53876.0	0.00571	-	4.47214e-005
53887.8	0.00713	-	5e-005
53887.9	0.00714	-	5e-005
53888.0	0.00705	-	5e-005
53895.8	0.00751	-	5.65685e-005
53895.9	0.00741	-	5.65685e-005
53895.9	0.00722	-	5e-005
53897.8	0.00744	-	0.000107703
53897.9	0.00713	-	0.000107703
53897.9	0.00713	-	8.94427e-005

Table B.9: Lightcurve data from Tenagra-II R-band [Pan11].

Date [MJD]	$\text{Flux}_{\text{V-band}}$ [Jy]	σ_{date} [MJD]	σ_{flux} [Jy]
54961.3	0.0016268	-	0.000305629
54970.3	0.006706	-	0.000619293
54972.3	0.007678	-	0.000608317
54974.3	0.007210	-	0.000228528
54975.3	0.008991	-	0.000658217
54983.3	0.006292	-	0.000291755
55003.3	0.007396	-	0.000345324
55005.3	0.006985	-	0.000183415
55015.3	0.006260	-	0.000610312
55016.3	0.007245	-	0.000473692
55018.3	0.007298	-	0.000476681
55019.3	0.008815	-	0.000413937
55026.3	0.007873	-	0.000217706
55028.2	0.008693	-	0.000214758
55029.2	0.008462	-	0.000181463
55031.2	0.008673	-	0.000185367
55037.2	0.010082	-	0.000351285

Table B.10: Lightcurve data from GRT V-band [Pan11].

Date [MJD]	$\text{Flux}_{\text{V-band}}$ [Jy]	σ_{date} [MJD]	σ_{flux} [Jy]
54379.7	0.00383	-	0.000117047
54381.8	0.00360	-	0.000107703
54437.7	0.00567	-	0.000117047
54438.6	0.00528	-	0.000107703
54453.7	0.00363	-	0.000145602
54463.6	0.00536	-	0.000282843

Table B.11: Lightcurve data from NMS V-band [Pan11].

Date [MJD]	$Flux_{V\text{-band}}$ [erg/cm^2/s]	σ_{date} [MJD]	σ_{flux} [erg/cm^2/s]
53664.6	0.00153	-	4.47214e-005
53664.6	0.00135	-	5e-005
53664.7	0.00132	-	0.000155242
53665.6	0.00133	-	4.47214e-005
53665.6	0.00132	-	4.47214e-005
53665.7	0.00150	-	5e-005
53666.6	0.00179	-	5e-005
53666.6	0.00138	-	4.47214e-005
53666.7	0.00176	-	4.47214e-005
53667.6	0.00151	-	4.47214e-005
53667.6	0.00186	-	5e-005
53667.7	0.00157	-	4.47214e-005
53669.6	0.00189	-	5e-005
53669.7	0.00179	-	5e-005
53669.7	0.00183	-	5e-005
53670.6	0.00160	-	4.47214e-005
53671.6	0.00137	-	4.47214e-005
53672.6	0.00172	-	4.47214e-005
53672.6	0.00172	-	5e-005
53672.7	0.00165	-	5e-005
53673.6	0.00168	-	4.47214e-005
53673.6	0.00165	-	4.47214e-005
53673.7	0.00223	-	4.47214e-005
53818.0	0.00497	-	5.65685e-005
53832.0	0.00522	-	5e-005
53859.0	0.00520	-	5e-005
53865.9	0.00583	-	5.65685e-005
53866.0	0.00567	-	5e-005
53875.9	0.00415	-	5e-005
53876.0	0.00415	-	5e-005
53887.8	0.00538	-	5e-005
53887.9	0.00534	-	5e-005
53888.0	0.00539	-	5e-005
53895.8	0.00570	-	5.65685e-005
53895.9	0.00578	-	5.65685e-005
53896.0	0.00578	-	5.65685e-005
53897.8	0.00522	-	0.000117047
53897.9	0.00573	-	8.94427e-005
53898.0	0.00519	-	8.94427e-005

Table B.12: Lightcurve data from Tenagra-II V-band [Pan11].

Date [MJD]	$\text{Flux}_{\text{V-band}}$ [Jy]	σ_{date} [MJD]	σ_{flux} [Jy]
54502.6	0.0013502	0.105606	0.000388564
54504.9	0.0030596	0.106967	0.000662500
54511.5	0.0025448	0.106617	0.000342733
54513.8	0.0031279	0.141918	0.000446664

Table B.13: Lightcurve data from INTEGRAL–OMC V-band [W+11b].

Date [MJD]	$\text{Flux}_{\text{V-band}}$ [Jy]	σ_{date} [MJD]	σ_{flux} [Jy]
53479	0.0046	-	0.00046
53874	0.0050	-	0.00050
53876	0.0052	-	0.00052
53878	0.0048	-	0.00048
53879	0.0051	-	0.00051
53880	0.0051	-	0.00051
53881	0.0055	-	0.00055
53882	0.0056	-	0.00056
53883	0.0054	-	0.00054
53884	0.0054	-	0.00054

Table B.14: Lightcurve data from Swift–UVOT V-band [T+08a].

B.3 X-Ray Observations

Date [MJD]	$\text{Rate}_{0.3\text{–}10\,\text{keV}}$ [photons/s]	σ_{date} [MJD]	σ_{rate} [photons/s]
53479.3	8.91137	0.269618	0.04692
53874.7	7.73295	0.011560	0.07652
53876.2	9.52493	0.073519	0.07539
53878.5	12.4835	0.106696	0.05854
53879.6	13.5959	0.136152	0.07940
53880.7	11.9533	0.270475	0.05405
53881.6	11.9436	0.270394	0.05440
53882.8	10.4255	0.239928	0.05143
53883.2	10.7260	0.103212	0.05469
53884.2	7.98009	0.039306	0.12381
54273.2	5.94847	0.002484	0.20498
54420.1	6.24413	0.039960	0.08548
54427.1	7.67971	0.005549	0.15501
54427.2	8.09051	0.006217	0.15222
54434.8	8.56265	0.007437	0.14542
54744.3	5.97578	0.137977	0.07032
54752.1	6.46200	0.035791	0.14670
54754.9	5.13872	0.036168	0.13008
54755.1	4.62108	0.068967	0.11226
54757.4	5.26026	0.035994	0.13821
54766.7	4.57262	0.005781	0.11597
54767.1	4.71314	0.005534	0.11619
54769.6	4.22019	0.006972	0.10939
54770.2	4.18515	0.005854	0.10468
54983.7	5.23594	0.070274	0.10119
54989.1	8.33616	0.005712	0.09985
54996.3	6.19328	0.072932	0.07769
55005.0	6.03983	0.024243	0.14221
55007.6	6.57944	0.028920	0.17138
55010.0	9.28039	0.035448	0.09187
55013.2	6.44545	0.169904	0.17709
55016.5	10.7852	0.034181	0.09665
55020.3	9.57632	0.002673	0.27650
55031.0	5.43441	0.005941	0.12225
55038.9	7.59821	0.003490	0.12310
55045.3	8.91374	0.003750	0.12314
55052.8	6.90319	0.001598	0.27675
55059.6	7.43414	0.006173	0.14866
55066.1	9.51246	0.099959	0.13028
55070.4	9.62500	0.007112	0.10437
55087.1	6.01227	0.005544	0.08279

55100.8	5.91115	0.141181	0.03254
55318.5	4.34619	0.007471	0.06191
55325.6	7.14108	0.006279	0.08715
55332.4	6.05369	0.005880	0.08345
55346.1	5.71236	0.006476	0.07947
55353.6	4.67401	0.006262	0.07127
55360.1	4.94710	0.036215	0.07761
55367.7	3.96604	0.005859	0.06739
55375.2	5.09298	0.006736	0.07283
55381.3	5.67030	0.006690	0.07366
55396.9	5.01549	0.006424	0.07230
55404.0	5.65637	0.004470	0.09593
55409.0	4.32565	0.005903	0.07056
55458.2	5.93316	0.036994	0.07399
55463.7	8.78699	0.007159	0.08795

Table B.15: Lightcurve data from Swift–XRT (0.3–10 keV) [F^+11b].

Date [MJD]	$\text{Flux}_{2\text{–}10\,\text{keV}}$ [10^{-11} erg/cm^2/s]	σ_{date} [MJD]	σ_{flux} [10^{-11} erg/cm^2/s]
50150	4.26818	14.5606	1.09626
50181.8	3.9211	16.1005	0.843136
50213	4.31613	14.3527	0.799857
50243	1.51836	14.2817	0.958273
50273	3.14032	14.573	0.64995
50303	3.00184	14.4432	0.737021
50333	5.66171	14.5776	0.676191
50363	3.55859	14.7374	0.835216
50393.2	3.09728	14.5426	0.850611
50424.7	1.41162	14.8195	0.638732
50455	5.13192	14.5409	1.06881
50485	6.62035	14.2033	0.701769
50515	5.10361	14.5132	0.705375
50544.9	2.83448	14.544	0.695187
50575	2.60684	14.5394	1.44753
50606.3	2.81503	15.8604	1.03968
50637	2.4844	14.4424	0.796232
50669.9	3.86918	17.3332	1.41765
50702	5.18155	14.5527	0.799012
50732	3.8652	14.3998	1.19646
50762	4.6877	14.4426	0.805493
50793.7	2.29328	16.6133	3.09364
50824	1.19426	14.2788	0.936368
50854	3.84785	14.3928	0.770998

50884.8	2.77009	15.306	1.20014
50915.9	2.27614	14.3652	0.807514
50950.6	3.13589	19.0445	1.08694
50983.3	2.44494	15.6041	1.2379
51016.1	2.08023	14.5449	0.954161
51046.8	3.13563	15.2458	0.874391
51078	4.54161	14.8013	0.696741
51110	4.2883	16.7017	0.960685
51141	5.69258	14.259	1.06743
51171.1	2.13939	14.5465	0.968854
51201	4.57366	14.651	1.09172
51231	3.00724	14.5124	0.945006
51261	5.28411	14.8979	1.01494
51291	8.36586	14.6456	0.810988
51323.2	5.75659	16.5194	1.83769
51354	4.0041	14.6872	2.13923
51384	4.60574	14.7052	0.830562
51414.1	5.91247	14.3975	5.16799
51444.1	7.3209	14.4514	0.682644
51474	8.60909	14.5118	0.709545
51504	10.2388	14.3878	1.40694
51534.8	10.5306	15.0986	1.2701
51567.6	10.032	16.7753	1.35768
51599	7.97051	14.4281	2.30432
51629.5	8.71157	14.988	1.61433
51660	8.9324	14.4115	1.37961
51690	5.82176	14.4746	1.61258
51720.1	6.94056	14.5826	1.32344
51750	6.02327	14.7775	1.02258
51780.2	11.091	14.7521	0.864062
51816.1	4.63875	14.5551	0.70501
51847	7.74772	14.3677	0.926061
51877	10.6524	14.4398	1.23666
51908.4	6.48663	15.7931	3.21307
51940.4	2.51599	14.9644	0.948506
51973.2	5.71794	15.546	1.62087
52011.7	9.82719	16.6283	1.69771
52042.4	8.70829	15.0344	1.1601
52073	4.14251	14.5816	1.51635
52104.5	6.01811	15.944	1.37407
52135.1	7.14629	14.6318	1.0269
52165	6.55043	14.626	0.965709
52195	7.64322	14.3935	0.779333
52225.4	4.53706	14.8383	1.79536
52260.3	3.06492	15.8533	1.90625
52291	5.30017	14.5031	0.858261

52321.3	5.7831	14.9186	1.03306
52352	3.61649	14.6046	0.954537
52382	5.69689	14.6601	1.41122
52413.9	11.238	16.4065	1.37257
52445.1	6.51273	14.5331	1.27685
52474.9	14.6209	14.6561	1.11396
52505	14.6783	14.4569	1.44304
52535	8.43016	14.5298	0.737302
52565	9.99134	14.3939	0.719475
52595	17.2394	14.429	1.51124
52626.2	6.83936	15.5606	0.989977
52661.9	3.11764	14.4031	0.969387
52699.5	8.01911	14.9348	1.36743
52736	6.23328	20.4374	0.744916
52767	13.4636	14.5314	1.5065
52797.5	7.90968	15.0103	1.22867
52835.5	8.20693	15.9464	1.04115
52866	6.84936	14.5717	1.18044
52896	5.47977	14.5262	1.04817
52926.5	6.66076	15.0651	1.0605
52957.1	4.57689	14.2429	1.3146
52987	4.16753	14.5676	1.13936
53016.9	4.24323	14.5364	1.11096
53047	4.1024	14.4763	1.19552
53078	2.30978	15.2337	1.64337
53110.4	7.53077	15.9586	1.24994
53142.9	8.10401	16.2674	1.36459
53173.9	10.4225	15.4249	1.26905
53205	9.16434	14.5022	1.17319
53236	9.43642	14.6021	1.12501
53266.1	7.43569	14.5361	0.766391
53296	9.07007	14.3587	0.756756
53326.1	5.57776	14.7026	1.17299
53356	4.15241	14.5881	1.74342
53388	7.1906	15.5875	1.66147
53419	7.85478	14.5256	1.64933
53449	7.60351	14.6539	0.94291
53485	9.57913	20.4418	1.14109
53516.1	7.11304	14.9171	1.38809
53546	8.46788	14.4587	0.977277
53576.1	6.62606	14.6005	0.892267
53606	5.06682	14.5687	0.834877
53636	7.9089	14.324	0.814942
53666	8.05164	14.3916	0.968762
53696	12.0765	14.1724	1.84502
53725.9	9.94096	14.3642	1.76205

53756	11.6571	14.3342	1.0727
53786	11.716	14.4215	0.846986
53816	9.07832	14.5099	0.82098
53845.9	9.85128	14.3262	0.990405
53876	11.72	14.5259	1.20385
53906	14.2334	14.4339	1.13181
53936.1	14.0448	14.5912	0.968447
53966	12.8642	14.5351	0.985922
53996	7.62182	14.4389	0.772163
54026	13.3699	14.6104	0.939733
54056	10.931	14.5146	2.52758
54086.4	10.4471	14.9605	1.33171
54117	5.94423	14.2918	1.06452
54147	9.51793	14.2543	1.08259
54177	7.12867	14.4812	0.897431
54207	5.0296	14.4744	0.968215
54237	7.01609	14.5289	1.27364
54267	6.41754	14.5303	1.44821
54297	8.84305	14.3982	1.2833
54327	7.91842	14.4847	0.859757
54357	8.42875	14.665	0.80105
54387	8.7338	14.5153	0.918964
54417	10.3619	14.77	1.0799
54447.7	8.91235	15.3832	2.11915
54478	9.10355	14.3472	1.3105
54508	6.29165	14.6368	1.0831
54538	6.30977	14.5247	1.0697
54568	5.88631	14.3881	0.823764
54598	6.21497	14.5899	0.930413
54628.1	7.68723	14.4867	1.1557
54658	8.34242	14.3409	1.11165
54688	9.25018	14.4644	1.11259
54718	10.8795	14.5914	1.01343
54748	10.6766	14.4846	0.997554
54778	5.18518	14.4456	1.57899
54808	10.4461	14.4931	1.24725
54838	4.9568	14.4603	1.61501
54868	7.02309	14.5703	1.1008
54898	7.95875	14.3341	1.10398
54928	10.67	14.491	0.804267
54958	11.4112	14.5151	1.08866
54988.1	7.52959	14.4722	1.09072
55018.1	10.9719	14.381	1.34347
55048	8.04401	14.3829	1.26265
55078.1	8.69973	14.4815	1.01839
55108.9	7.91597	15.4158	1.02459

55138.9	11.0382	14.5593	1.48274
55169	7.07105	14.5244	1.18468
55199	8.62352	14.6821	1.42162
55229.1	3.00963	14.4039	1.2145
55259	9.04953	14.3155	1.37442
55289	8.27756	14.6649	1.29164
55319	6.87426	14.8147	1.55519
55349	8.05586	14.5799	1.41794
55379.1	9.69624	14.3621	1.79219
55409	0.959847	14.5246	2.23798
55439.1	10.8669	14.5262	1.5422
55469	10.1062	14.4595	1.25022
55500.6	10.4575	15.9094	2.27978
55532	11.9332	14.6915	2.83763
55563.8	7.00024	15.6011	2.90846

Table B.16: Lightcurve data from RXTE–ASM (2–10 keV) in 20 days bins [B+11a].

Date [MJD]	$\text{Flux}_{2\text{–}10\,\text{keV}}$ $[10^{-11}\,\text{erg/cm}^2/\text{s}]$	σ_{date} [MJD]	σ_{flux} $[10^{-11}\,\text{erg/cm}^2/\text{s}]$
51753.9	14.0	-	-
51754.0	13.8	-	-
51754.1	14.0	-	-
51754.9	13.2	-	-
51755.0	12.8	-	-
51755.1	12.7	-	-
51755.9	11.9	-	-
51757.0	12.2	-	-
51757.1	11.9	-	-
51757.9	10.6	-	-
51758.0	10.2	-	-
51758.1	10.8	-	-
51788.0	8.6	-	-
51789.9	8.4	-	-
51790.9	10.4	-	-
51791.9	11.9	-	-
51792.9	13.8	-	-

Table B.17: Lightcurve data from RXTE–PCA (2–10 keV) [G+02].

Date [MJD]	$\mathrm{Flux}_{2\text{–}10\,\mathrm{keV}}$ [10^{-11} erg/cm^2/s]	σ_{date} [MJD]	σ_{flux} [10^{-11} erg/cm^2/s]
51823	7.14	-	-
51823	6.97	-	-
51825	8.84	-	-
51825	8.84	-	-
51826	8.5	-	-
51827	9.01	-	-
51828	6.8	-	-
51829	5.95	-	-
51831	4.59	-	-
51832	5.44	-	-
51833	6.63	-	-
51834	6.63	-	-
51836	6.97	-	-
51837	5.61	-	-
51839	4.42	-	-
51840	4.25	-	-
51841	4.59	-	-
51844	6.97	-	-
51845	6.97	-	-
51846	7.99	-	-
51850	6.29	-	-
51851	5.78	-	-
51853	6.63	-	-
51855	7.48	-	-
51856	6.63	-	-
51857	8.33	-	-
51858	10.2	-	-
51859	14.79	-	-
51860	17.68	-	-
51862	19.72	-	-
51863	18.36	-	-

Table B.18: Lightcurve data from ARGOS–USA (2–10keV) [G+02].

Date [MJD]	$\mathrm{Flux}_{2\text{–}10\,\mathrm{keV}}$ [10^{-11} erg/cm^2/s]	σ_{date} [MJD]	σ_{flux} [10^{-11} erg/cm^2/s]
52297	29	-	-
52655	7.7	-	-
52884	6.9	-	-

Table B.19: Lightcurve data from XMM–Newton (2–10 keV) [P+05].

Date [MJD]	$\text{Flux}_{2\text{–}10\,\text{keV}}$ $[10^{-11}\,\text{erg/cm}^2/\text{s}]$	σ_{date} [MJD]	σ_{flux} $[10^{-11}\,\text{erg/cm}^2/\text{s}]$
50572	1.38	-	-
52175	8.34	-	-
52180	10.6	-	-

Table B.20: Lightcurve data from BeppoSAX (2–10keV) [DSG05].

Date [MJD]	$\text{Flux}_{2\text{–}10\,\text{keV}}$ $[10^{-11}\,\text{erg/cm}^2/\text{s}]$	σ_{date} [MJD]	σ_{flux} $[10^{-11}\,\text{erg/cm}^2/\text{s}]$
53479	11.7	-	-
53874	11	-	-
53876	15	-	-
53878	23	-	-
53879	24	-	-
53880	20	-	-
53881	20	-	-
53882	15	-	-
53883	15	-	-
53884	14	-	-
55100	7.17	-	-

Table B.21: Lightcurve data from Swift–XRT (2–10 keV) [M+08b, G+11].

Date [MJD]	$\text{Flux}_{15\text{–}50\,\text{keV}}$ [10^{-3} photons/cm^2/s]	σ_{date} [MJD]	σ_{flux} [10^{-3} photons/cm^2/s]
53465.3	0.565623	51.2637	0.157437
53577.2	0.282143	61.2418	0.339102
53702.0	0.631198	57.0440	0.335065
53812.1	0.599994	54.1099	0.396014
53915.5	0.688242	51.5495	0.512257
54021.0	0.493870	51.9670	0.365034
54136.8	0.350539	52.8352	0.235840
54245.6	0.163662	48.6484	0.495294
54362.5	0.036500	69.5055	0.275996
54479.7	0.516348	56.6923	0.601573
54591.2	-0.22622	45.1538	0.134889
54684.0	0.332429	45	0.139181
54777.9	0.553518	47.9231	0.237863
54882.5	0.441027	51.5275	0.226384
54977.0	0.247108	45	0.164764
55070.9	0.358202	47.8901	0.192048
55166.2	0.753584	45.2308	0.290238
55265.8	0.707768	49.7912	0.354304
55357.7	0.462458	45.7363	0.178940
55451.7	0.367354	45.7473	0.159784

Table B.22: Lightcurve data from Swift–BAT (15–50 keV) in 91 days bins [B+11c].

B.4 HE Gamma-Ray Observations

Date [MJD]	$\text{Flux}_{>300\,\text{MeV}}$ [10^-6 photons/cm^2/s]	σ_{date} [MJD]	σ_{flux} [10^-6 photons/cm^2/s]
54683	0.122	3.5	0.073
54690	0.235	3.5	0.093
54697	0.215	3.5	0.083
54704	0.098	3.5	0.07
54711	0.293	3.5	0.1
54718	0	3.5	0.007
54725	0.376	3.5	0.109
54732	0.28	3.5	0.094
54739	0.242	3.5	0.096
54746	0.079	3.5	0.053
54753	0.271	3.5	0.092
54760	0.168	3.5	0.087
54767	0.355	3.5	0.107
54774	0.281	3.5	0.099
54781	0.053	3.5	0.051
54788	0.085	3.5	0.064
54795	0.279	3.5	0.098
54802	0.127	3.5	0.068
54809	0.344	3.5	0.112
54816	0.28	3.5	0.095
54823	0.142	3.5	0.082
54830	0.246	3.5	0.13
54837	0.204	3.5	0.092
54844	0.334	3.5	0.107
54851	0.215	3.5	0.095
54858	0.346	3.5	0.105
54865	0.231	3.5	0.086
54872	0.521	3.5	0.128
54879	0.205	3.5	0.106
54886	0.448	3.5	-
54893	0.407	3.5	-
54900	0.58	3.5	0.232
54907	0.483	3.5	0.116
54914	0.247	3.5	0.099
54921	0.103	3.5	0.064
54928	0.17	3.5	0.079
54935	0.363	3.5	0.117
54942	0.185	3.5	0.11
54949	0.297	3.5	0.099
54956	0.043	3.5	0.081
54963	0.43	3.5	0.102

54970	0.296	3.5	0.092
54977	0.418	3.5	0.108
54984	0.18	3.5	0.087
54991	0.261	3.5	0.106
54998	0.109	3.5	0.064
55005	0.243	3.5	0.098

Table B.23: Lightcurve data from Fermi–LAT (>300 MeV) for 11 months in weekly time bins [A+10c].

B.5 VHE Gamma-Ray Observations

Date [MJD]	Flux [erg/cm^2/s]	σ_{date} [MJD]	σ_{flux} [erg/cm^2/s]
53499.2	0.67495	0.0213542	0.656651
53504.2	1.02857	0.0539410	0.053941
553522.2	0.91886	0.0307407	0.436436
53523.2	1.44114	0.0172106	0.607910
53526.2	1.28434	0.0175810	0.610726
53527.2	0.71619	0.0163773	0.601113
53530.2	0.63597	0.0227720	0.507663
53532.2	0.97602	0.0234722	0.491189
53536.2	0.99795	0.0344734	0.413468
53553.1	1.30117	0.0245486	0.491459
53555.1	1.31175	0.0197106	0.558748
53561.1	1.06421	0.0404398	0.365360
53563.1	0.87689	0.0395428	0.374700
53876.2	1.09191	0.0452257	0.395779
53877.2	1.48503	0.0381481	0.442647
53878.1	1.65163	0.0633333	0.419564
53879.2	1.26649	0.0570081	0.421729
53880.2	1.14184	0.0519907	0.405099
53881.1	0.53027	0.0523553	0.374955
53882.1	2.08558	0.0538715	0.450116
53924.2	1.67898	0.0082176	0.923820
53948.9	0.87513	0.0264062	0.478953
53962.9	1.99862	0.0232465	0.494379
53997.0	1.70235	0.0100521	0.876136
54004.9	2.45757	0.0228241	0.843753
54018.9	1.81789	0.0276678	0.540969
54232.1	1.40632	0.0157351	0.595910
54240.1	0.53513	0.0205955	0.491564
54263.2	1.47410	0.0229354	0.464044
54354.9	0.91342	0.0197203	0.545437

54361.9	1.78590	0.0265761	0.451717
54373.9	0.57128	0.0317069	0.417178
54380.9	1.21719	0.0246561	0.422023
54388.9	0.87309	0.0234582	0.464154
54389.9	1.86549	0.0384278	0.396519
54404.8	2.08749	0.0014907	1.998980
54405.8	1.46832	0.0304851	0.477824
54406.8	1.45935	0.0040125	1.343430
54409.8	2.75114	0.0043604	1.211520
54558.2	2.09493	0.0051255	0.937354
54570.2	1.58276	0.0051358	0.858062
54571.2	1.32571	0.0046177	0.865101
54597.2	1.14586	0.0070455	0.726403
54599.2	2.31522	0.0067045	0.862485
54616.1	0.33983	0.0184202	0.311700
54620.1	0.63612	0.0183132	0.448013
54661.1	0.97376	0.0046109	0.737565
55001.2	0.92793	0.0445279	0.283034
55002.2	1.44903	0.0297905	0.374557
55005.2	1.30506	0.0301432	0.373188
55009.2	1.87421	0.0062872	0.846648
55010.2	2.20648	0.0069033	0.861719
55013.2	1.32337	0.0081090	0.795197
55014.2	1.08933	0.0073724	0.780596
55015.1	2.38961	0.0058932	0.950898
55017.2	1.35378	0.0032726	1.058460
55041.0	1.79180	0.0036554	1.099280
55041.0	0.54239	0.0355868	0.301243
55042.0	0.49405	0.0296930	0.312063
55098.9	0.48491	0.0107588	0.608410

Table B.24: Lightcurve data from MAGIC [A+06c, Hay08, T+08a, Uel09, Uel12].

Appendix C
Figures for the Combined VHE Spectrum

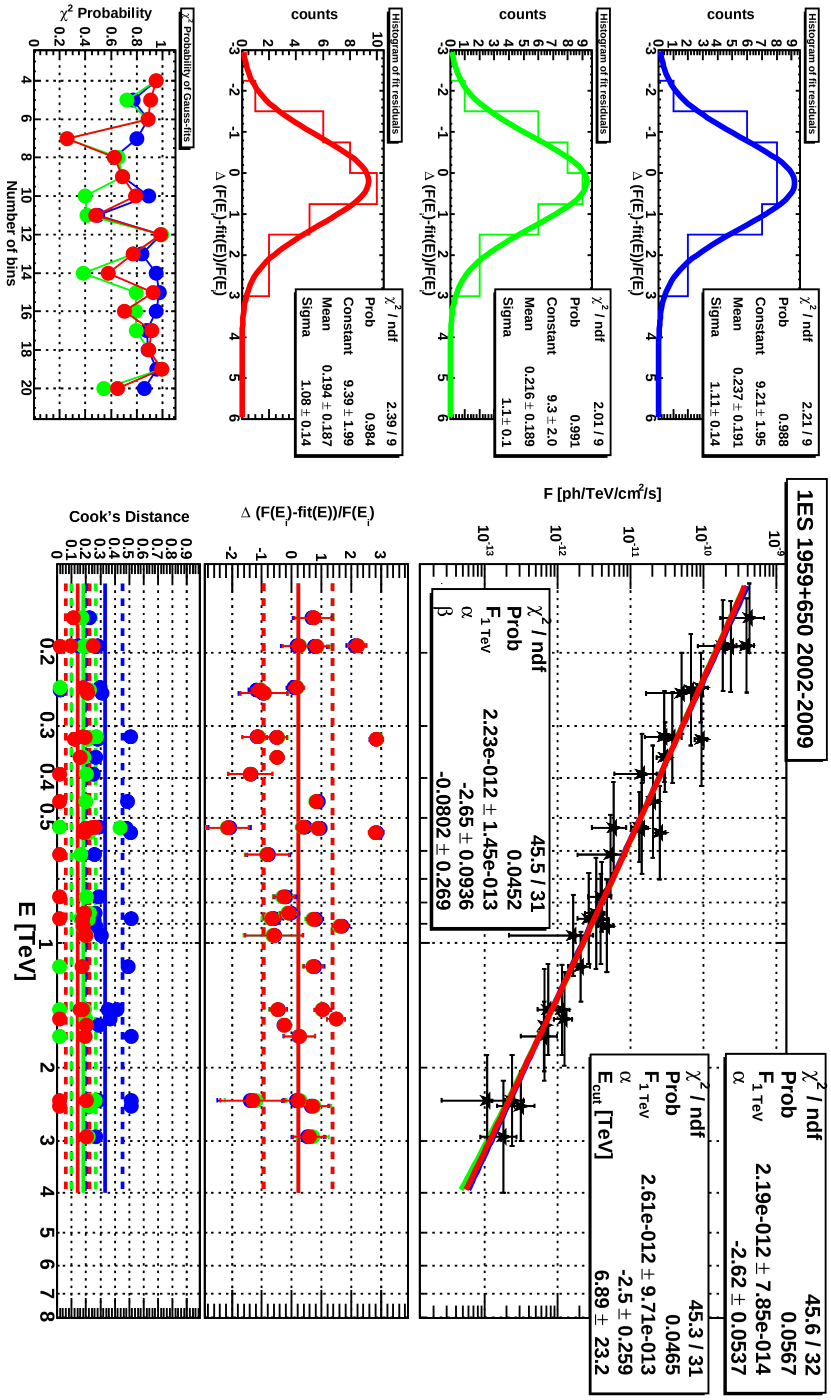

Figure C.1: Combined MAGIC (2004–2009) energy spectrum of 1ES 1959+650, along with fit quality test as the Cook's Distance and the Gaussian fit probabilities for the spectral fit residuals. Values stemming from the power-law model are given in blue, for the power-law with cut-off in green and for the curved power-law in red. Solid horizontal lines denote averages, dashed ones denote one standard deviation.

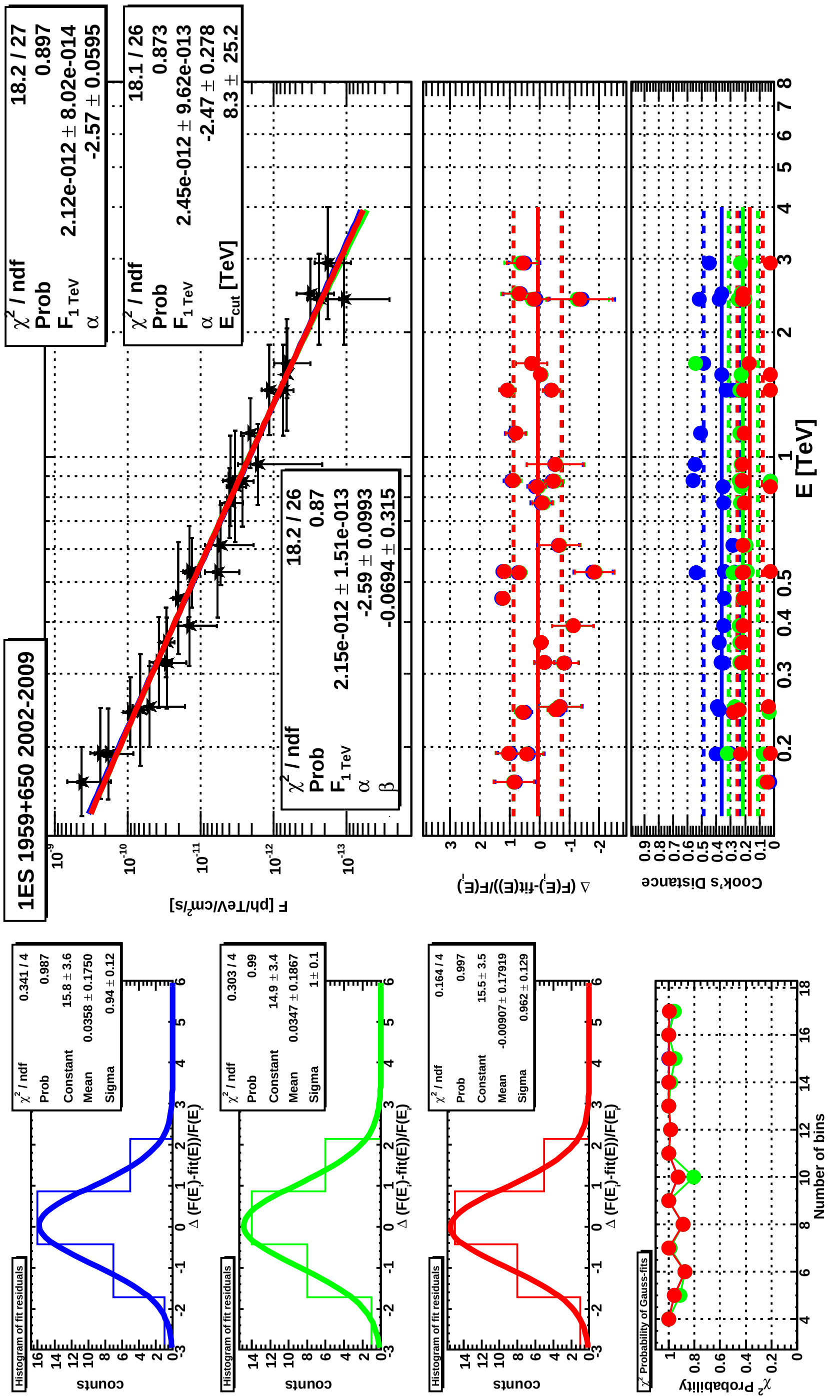

Figure C.2: Combined MAGIC (2005–2009) energy spectrum of 1ES 1959+650, along with fit quality test as the Cook's Distance and the Gaussian fit probabilities for the spectral fit residuals. Values stemming from the power-law model are given in blue, for the power-law with cut-off in green and for the curved power-law in red. Solid horizontal lines denote averages, dashed ones denote one standard deviation.

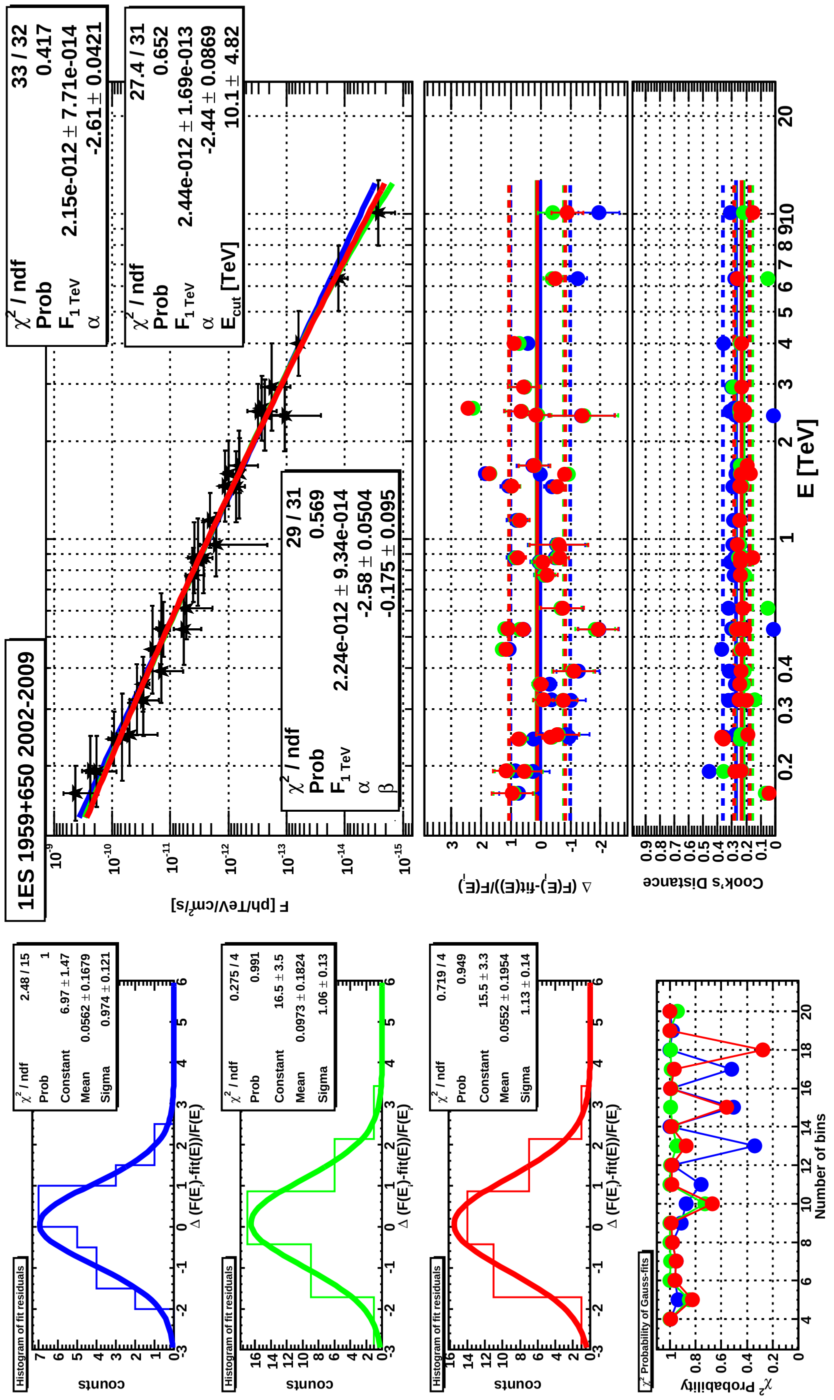

Figure C.3: Combined MAGIC-HEGRA energy spectrum of 1ES 1959+650, along with fit quality test as the Cook's Distance and the Gaussian fit probabilities for the spectral fit residuals. Values stemming from the power-law model are given in blue, for the power-law with cut-off in green and for the curved power-law in red. Solid horizontal lines denote averages, dashed ones denote one standard deviation.

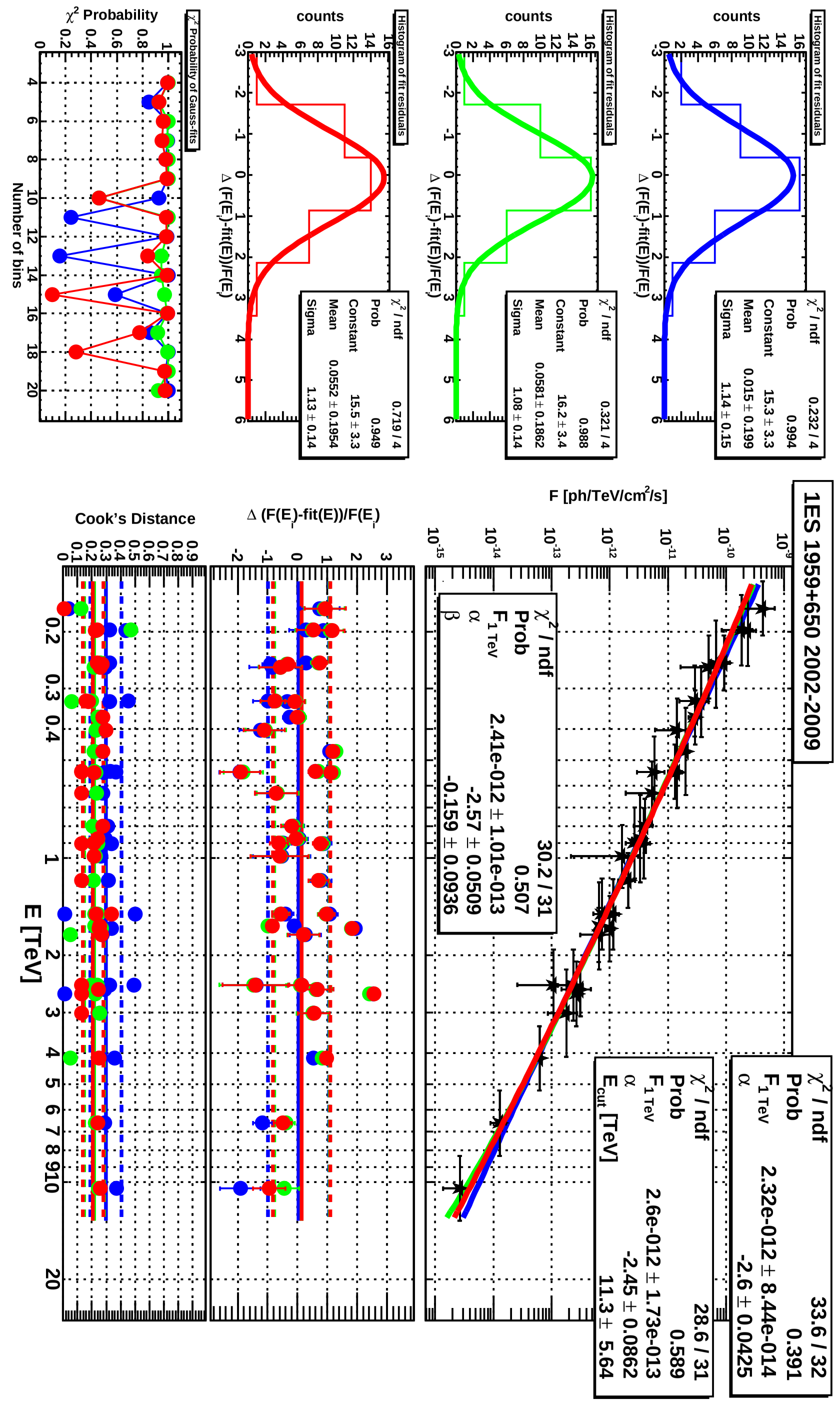

Figure C.4: Combined MAGIC-HEGRA energy spectrum of 1ES 1959+650, rescaled according to [MHZ10], along with fit quality test as the Cook's Distance and the Gaussian fit probabilities for the spectral fit residuals. Values stemming from the power-law model are given in blue, for the power-law with cut-off in green and for the curved power-law in red. Solid horizontal lines denote averages, dashed ones denote one standard deviation.

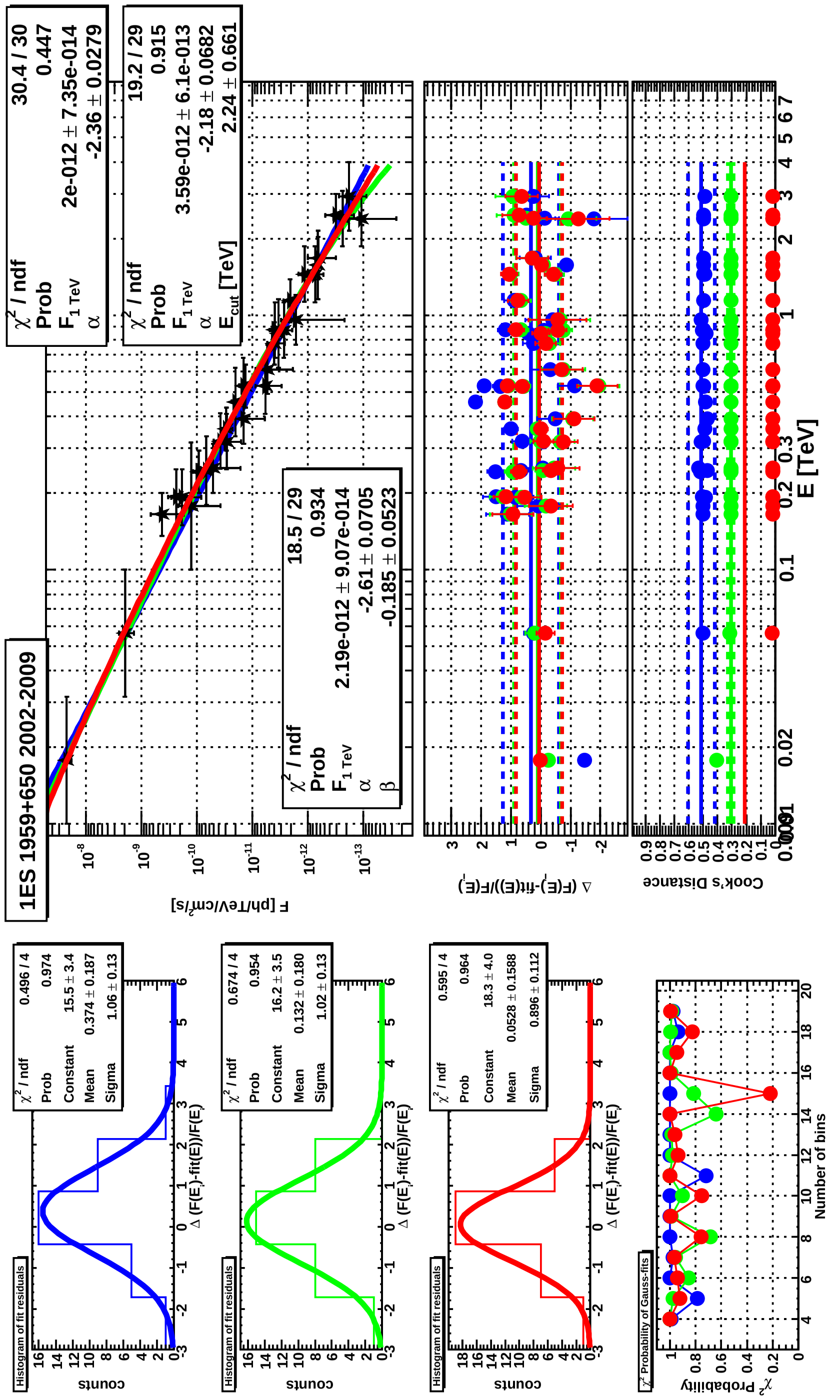

Figure C.5: Combined MAGIC-Fermi–LAT energy spectrum of 1ES 1959+650, along with fit quality test as the Cook's Distance and the Gaussian fit probabilities for the spectral fit residuals. Values stemming from the power-law model are given in blue, for the power-law with cut-off in green and for the curved power-law in red. Solid horizontal lines denote averages, dashed ones denote one standard deviation.

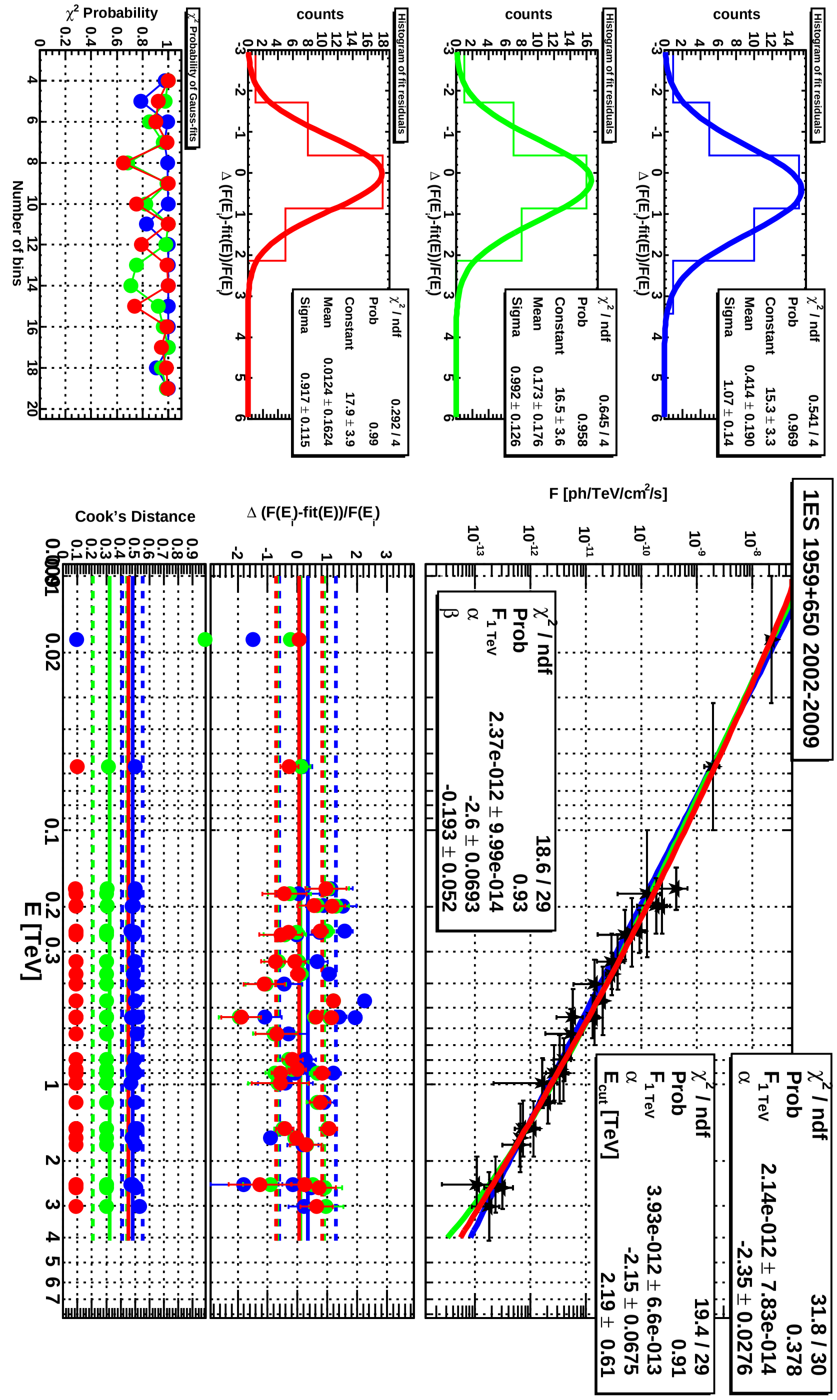

Figure C.6: Combined MAGIC-Fermi–LAT energy spectrum of 1ES 1959+650, rescaled according to [MHZ10], along with fit quality test as the Cook's Distance and the Gaussian fit probabilities for the spectral fit residuals. Values stemming from the power-law model are given in blue, for the power-law with cut-off in green and for the curved power-law in red. Solid horizontal lines denote averages, dashed ones denote one standard deviation.

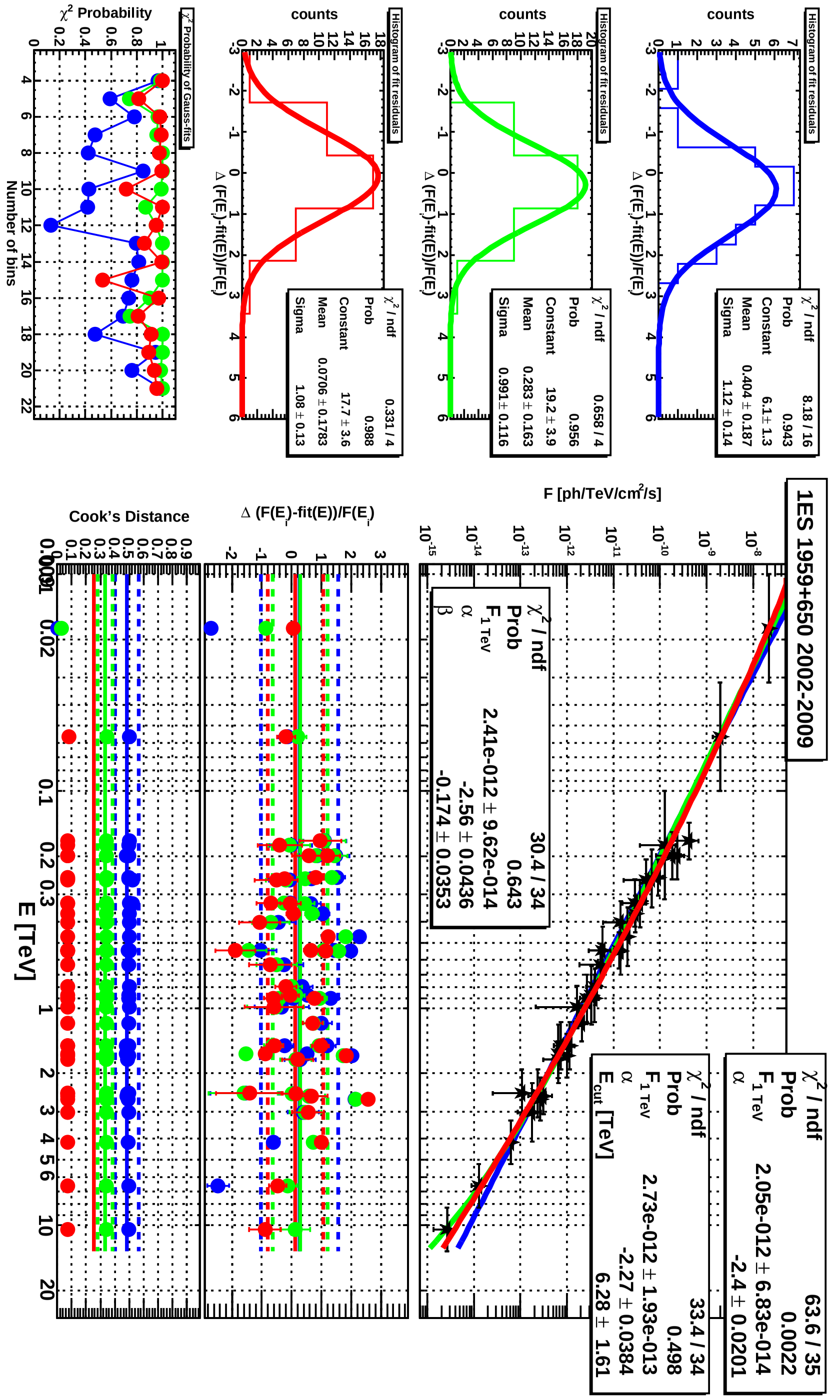

Figure C.7: Combined MAGIC-HEGRA-Fermi–LAT energy spectrum of 1ES 1959+650, rescaled according to [MHZ10], along with fit quality test as the Cook's Distance and the Gaussian fit probabilities for the spectral fit residuals. Values stemming from the power-law model are given in blue, for the power-law with cut-off in green and for the curved power-law in red. Solid horizontal lines denote averages, dashed ones denote one standard deviation.

Appendix D
Data for SED Modeling

D.1 Radio Observations

ν [Hz]	νF_ν [erg/cm^2/s]	σ_ν^- [Hz]	σ_ν^+ [Hz]	$\sigma_{\nu F_\nu}^-$ [erg/cm^2/s]	$\sigma_{\nu F_\nu}^+$ [erg/cm^2/s]
3.250e+008	8.190e-016	-	-	-	-
3.259e+008	8.016e-016	-	-	3.519e-017	3.519e-017
3.259e+008	8.212e-016	-	-	3.617e-017	3.617e-017
3.650e+008	1.372e-015	-	-	2.446e-016	2.446e-016
1.400e+009	3.304e-015	-	-	-	-
1.400e+009	3.494e-015	-	-	1.050e-016	1.050e-016
4.800e+009	1.219e-014	-	-	7.680e-016	7.680e-016
4.850e+009	1.193e-014	-	-	1.790e-015	1.790e-015
4.850e+009	1.227e-014	-	-	1.115e-015	1.115e-015
4.885e+009	1.124e-014	-	-	4.885e-016	4.885e-016
5.000e+009	1.100e-014	-	-	-	-
8.400e+009	1.872e-014	-	-	-	-
1.450e+010	2.523e-014	-	-	5.800e-016	5.800e-016
1.497e+010	2.694e-014	-	-	1.497e-015	1.497e-015

Table D.1: Spectral energy distribution data from 1991–2007 by NED (radio data) [NI11].

ν [Hz]	νF_ν [erg/cm^2/s]	σ_ν^- [Hz]	σ_ν^+ [Hz]	$\sigma_{\nu F_\nu}^-$ [erg/cm^2/s]	$\sigma_{\nu F_\nu}^+$ [erg/cm^2/s]
1.400e+009	2.800e-015	-	-	-	-
5.000e+009	9.085e-015	-	-	-	-
1.820e+014	6.200e-012	-	-	-	-
4.370e+014	9.050e-012	-	-	8.340e-013	8.340e-013

Table D.2: Spectral energy distribution data from 1997, 2002, 2004 via NED (core flux) from HST, NOT, VLA, VLBI [NI11].

ν [Hz]	νF_ν [erg/cm^2/s]	σ_ν^- [Hz]	σ_ν^+ [Hz]	$\sigma_{\nu F_\nu}^-$ [erg/cm^2/s]	$\sigma_{\nu F_\nu}^+$ [erg/cm^2/s]
1.500e+010	1.365e-014	-	-	-	-
1.500e+010	1.245e-014	-	-	-	-
1.500e+010	1.275e-014	-	-	-	-
1.540e+010	1.247e-014	-	-	-	-
1.540e+010	1.247e-014	-	-	-	-
1.540e+010	9.702e-015	-	-	-	-
2.220e+010	1.998e-014	-	-	-	-
2.220e+010	1.820e-014	-	-	-	-
2.220e+010	1.310e-014	-	-	-	-
2.220e+010	2.131e-014	-	-	3.996e-015	3.996e-015
4.320e+010	2.592e-014	-	-	7.344e-015	7.344e-015
4.320e+010	2.333e-014	-	-	6.912e-015	7.344e-015
4.320e+010	2.506e-014	-	-	7.776e-015	7.776e-015

Table D.3: Spectral energy distribution data from 2000–2009 VLBA [PE04, PPE08, PPE10].

ν [Hz]	νF_ν [erg/cm^2/s]	σ_ν^- [Hz]	σ_ν^+ [Hz]	$\sigma_{\nu F_\nu}^-$ [erg/cm^2/s]	$\sigma_{\nu F_\nu}^+$ [erg/cm^2/s]
4.800e+009	1.680e-014	3.000e+008	3.000e+008	3.360e-015	3.360e-015
7.700e+009	2.156e-014	5.000e+008	5.000e+008	9.600e-016	9.600e-016
1.120e+010	2.576e-014	7.000e+008	7.000e+008	1.440e-015	1.440e-015

Table D.4: Spectral energy distribution data from 2008.09–10 by RATAN–600 [G+11].

ν [Hz]	νF_ν [erg/cm^2/s]	σ_ν^- [Hz]	σ_ν^+ [Hz]	$\sigma_{\nu F_\nu}^-$ [erg/cm^2/s]	$\sigma_{\nu F_\nu}^+$ [erg/cm^2/s]
2.640e+009	6.720e-015	-	-	5.184e-016	5.184e-016
4.850e+009	1.179e-014	-	-	7.748e-016	7.748e-016
8.350e+009	1.893e-014	-	-	1.741e-015	1.741e-015
1.045e+010	2.289e-014	-	-	1.770e-015	1.770e-015
1.460e+010	2.992e-014	-	-	2.650e-015	2.650e-015
3.200e+010	5.562e-014	-	-	7.897e-015	7.897e-015

Table D.5: Spectral energy distribution data from 2007.01.27–2009.09.27 by Effelsberg 100 m [FA11].

ν [Hz]	νF_ν [erg/cm^2/s]	σ_ν^- [Hz]	σ_ν^+ [Hz]	$\sigma_{\nu F_\nu}^-$ [erg/cm^2/s]	$\sigma_{\nu F_\nu}^+$ [erg/cm^2/s]
3.700e+010	1.051e-013	-	-	1.998e-013	-

Table D.6: Spectral energy distribution data from 2005.02–2009.10 Metsähovi (upper limit) [LTN11].

ν [Hz]	νF_ν [erg/cm^2/s]	σ_ν^- [Hz]	σ_ν^+ [Hz]	$\sigma_{\nu F_\nu}^-$ [erg/cm^2/s]	$\sigma_{\nu F_\nu}^+$ [erg/cm^2/s]
8.624e+010	2.719e-013	-	-	6.396e-014	6.396e-014

Table D.7: Spectral energy distribution data from 2007.10.09–2010.03.22 by IRAM [FA11].

ν [Hz]	νF_ν [erg/cm^2/s]	σ_ν^- [Hz]	σ_ν^+ [Hz]	$\sigma_{\nu F_\nu}^-$ [erg/cm^2/s]	$\sigma_{\nu F_\nu}^+$ [erg/cm^2/s]
3.000e+010	2.130e-013	-	-	2.130e-013	-
4.400e+010	4.576e-013	-	-	4.576e-013	-
7.000e+010	5.670e-013	-	-	5.670e-013	-
1.000e+011	3.500e-013	-	-	3.500e-013	-
1.430e+011	1.716e-013	-	-	1.716e-013	-
2.170e+011	2.387e-013	-	-	2.387e-013	-
3.530e+011	1.800e-012	-	-	1.800e-012	-
5.450e+011	4.523e-012	-	-	4.523e-012	-
8.570e+011	1.868e-011	-	-	1.868e-011	-

Table D.8: Spectral energy distribution data from 2009.08.12–2010.11.14 by Planck ($2\,\sigma$ upper limits) [G+11].

D.2 Infrared Observations

ν [Hz]	νF_ν [erg/cm^2/s]	σ_ν^- [Hz]	σ_ν^+ [Hz]	$\sigma_{\nu F_\nu}^-$ [erg/cm^2/s]	$\sigma_{\nu F_\nu}^+$ [erg/cm^2/s]
5.780e+013	6.070e-012	-	-	6.71879314e-013	6.71879314e-013
5.746e+013	6.748e-012	-	-	4.53448795e-013	4.53448795e-013
5.713e+013	6.767e-012	-	-	4.98504686e-013	4.98504686e-013
5.680e+013	6.937e-012	-	-	5.92448435e-013	5.92448435e-013
5.648e+013	7.196e-012	-	-	3.917836e-013	3.917836e-013
5.616e+013	6.829e-012	-	-	3.86387342e-013	3.86387342e-013
5.584e+013	7.029e-012	-	-	4.08297313e-013	4.08297313e-013
5.553e+013	7.320e-012	-	-	3.95408482e-013	3.95408482e-013
5.522e+013	7.218e-012	-	-	4.07263015e-013	4.07263015e-013
5.492e+013	6.695e-012	-	-	3.80931861e-013	3.80931861e-013
5.461e+013	6.144e-012	-	-	4.10499384e-013	4.10499384e-013
5.431e+013	6.660e-012	-	-	3.58322628e-013	3.58322628e-013
5.402e+013	7.511e-012	-	-	3.66683187e-013	3.66683187e-013
5.372e+013	7.346e-012	-	-	3.93567825e-013	3.93567825e-013
5.344e+013	6.574e-012	-	-	3.99759065e-013	3.99759065e-013
5.315e+013	6.467e-012	-	-	3.86341362e-013	3.86341362e-013
5.287e+013	6.350e-012	-	-	3.85775768e-013	3.85775768e-013
5.258e+013	6.468e-012	-	-	4.01949245e-013	4.01949245e-013
5.231e+013	5.723e-012	-	-	3.91691346e-013	3.91691346e-013
5.203e+013	5.937e-012	-	-	3.83380765e-013	3.83380765e-013
5.176e+013	5.737e-012	-	-	3.74424952e-013	3.74424952e-013
5.149e+013	6.829e-012	-	-	3.77577013e-013	3.77577013e-013
5.123e+013	6.758e-012	-	-	3.68019309e-013	3.68019309e-013
5.096e+013	6.076e-012	-	-	4.32794376e-013	4.32794376e-013
5.070e+013	6.557e-012	-	-	3.75369052e-013	3.75369052e-013
5.044e+013	6.682e-012	-	-	4.00924533e-013	4.00924533e-013
5.019e+013	6.152e-012	-	-	3.64115141e-013	3.64115141e-013
4.994e+013	5.803e-012	-	-	3.54159772e-013	3.54159772e-013
4.969e+013	5.897e-012	-	-	3.40088222e-013	3.40088222e-013
4.944e+013	6.285e-012	-	-	3.79642571e-013	3.79642571e-013
4.919e+013	6.441e-012	-	-	3.5132261e-013	3.5132261e-013
4.895e+013	6.519e-012	-	-	3.34357819e-013	3.34357819e-013
4.871e+013	6.452e-012	-	-	3.20660134e-013	3.20660134e-013
4.847e+013	6.406e-012	-	-	3.04011718e-013	3.04011718e-013
4.824e+013	6.083e-012	-	-	3.54375793e-013	3.54375793e-013
4.800e+013	5.541e-012	-	-	4.00857927e-013	4.00857927e-013
4.777e+013	5.535e-012	-	-	3.71902815e-013	3.71902815e-013
4.754e+013	6.232e-012	-	-	3.35494214e-013	3.35494214e-013
4.731e+013	6.438e-012	-	-	3.32220231e-013	3.32220231e-013
4.709e+013	6.401e-012	-	-	3.26313567e-013	3.26313567e-013
4.687e+013	5.914e-012	-	-	3.27090727e-013	3.27090727e-013

4.665e+013	6.646e-012	-	-	3.20603604e-013	3.20603604e-013
4.643e+013	6.521e-012	-	-	3.1581922e-013	3.1581922e-013
4.621e+013	6.423e-012	-	-	3.14020316e-013	3.14020316e-013
4.600e+013	6.708e-012	-	-	3.33053979e-013	3.33053979e-013
4.578e+013	6.561e-012	-	-	3.53854312e-013	3.53854312e-013
4.557e+013	6.278e-012	-	-	3.97020837e-013	3.97020837e-013
4.537e+013	5.982e-012	-	-	3.91354676e-013	3.91354676e-013
4.516e+013	5.943e-012	-	-	3.97235703e-013	3.97235703e-013
4.495e+013	6.087e-012	-	-	3.83355248e-013	3.83355248e-013
4.475e+013	6.191e-012	-	-	3.83839836e-013	3.83839836e-013
4.455e+013	5.499e-012	-	-	4.62128446e-013	4.62128446e-013
4.435e+013	5.234e-012	-	-	4.45321532e-013	4.45321532e-013
4.415e+013	5.597e-012	-	-	4.54265545e-013	4.54265545e-013
4.396e+013	6.442e-012	-	-	4.96077763e-013	4.96077763e-013
4.376e+013	5.242e-012	-	-	9.33621383e-013	9.33621383e-013
4.357e+013	5.819e-012	-	-	4.88019411e-013	4.88019411e-013
4.338e+013	5.259e-012	-	-	5.30361968e-013	5.30361968e-013
4.319e+013	4.933e-012	-	-	5.54621884e-013	5.54621884e-013
4.300e+013	5.621e-012	-	-	6.56516765e-013	6.56516765e-013
4.282e+013	5.943e-012	-	-	7.01821717e-013	7.01821717e-013
4.263e+013	5.459e-012	-	-	6.29766403e-013	6.29766403e-013
4.245e+013	5.071e-012	-	-	6.36375187e-013	6.36375187e-013
4.227e+013	5.636e-012	-	-	5.75077978e-013	5.75077978e-013
4.209e+013	5.531e-012	-	-	5.21146713e-013	5.21146713e-013
4.191e+013	6.092e-012	-	-	5.07385012e-013	5.07385012e-013
4.174e+013	6.020e-012	-	-	4.99640928e-013	4.99640928e-013
4.156e+013	6.041e-012	-	-	5.14885461e-013	5.14885461e-013
4.139e+013	6.012e-012	-	-	5.30295366e-013	5.30295366e-013
4.122e+013	5.778e-012	-	-	7.46379837e-013	7.46379837e-013
4.105e+013	6.138e-012	-	-	5.34030832e-013	5.34030832e-013
4.088e+013	5.697e-012	-	-	5.20266729e-013	5.20266729e-013
4.071e+013	4.794e-012	-	-	5.32522908e-013	5.32522908e-013
4.054e+013	5.130e-012	-	-	4.9565775e-013	4.9565775e-013
4.038e+013	5.802e-012	-	-	4.88499947e-013	4.88499947e-013
4.021e+013	5.448e-012	-	-	5.10403651e-013	5.10403651e-013
4.005e+013	4.915e-012	-	-	5.15420966e-013	5.15420966e-013
3.989e+013	6.052e-012	-	-	5.85836238e-013	5.85836238e-013
3.973e+013	6.540e-012	-	-	6.30684498e-013	6.30684498e-013
3.957e+013	4.196e-012	-	-	4.09917524e-013	4.09917524e-013
4.088e+013	2.962e-012	-	-	3.14183297e-013	3.14183297e-013
4.054e+013	6.057e-012	-	-	3.27380654e-013	3.27380654e-013
4.021e+013	6.138e-012	-	-	3.16763046e-013	3.16763046e-013
3.989e+013	5.611e-012	-	-	2.93059149e-013	2.93059149e-013
3.957e+013	5.015e-012	-	-	2.78967762e-013	2.78967762e-013
3.926e+013	5.298e-012	-	-	2.92581103e-013	2.92581103e-013
3.895e+013	5.220e-012	-	-	2.83396521e-013	2.83396521e-013

3.865e+013	5.565e-012	-	-	2.57139992e-013	2.57139992e-013
3.835e+013	4.986e-012	-	-	2.43220235e-013	2.43220235e-013
3.805e+013	6.204e-012	-	-	2.42160035e-013	2.42160035e-013
3.776e+013	5.508e-012	-	-	2.34707887e-013	2.34707887e-013
3.748e+013	5.315e-012	-	-	2.18093215e-013	2.18093215e-013
3.720e+013	5.845e-012	-	-	2.14089618e-013	2.14089618e-013
3.692e+013	5.885e-012	-	-	1.98920485e-013	1.98920485e-013
3.665e+013	5.567e-012	-	-	2.06777998e-013	2.06777998e-013
3.638e+013	5.687e-012	-	-	2.02688366e-013	2.02688366e-013
3.611e+013	5.775e-012	-	-	2.05041942e-013	2.05041942e-013
3.585e+013	5.420e-012	-	-	1.94939832e-013	1.94939832e-013
3.559e+013	5.590e-012	-	-	1.91778337e-013	1.91778337e-013
3.534e+013	6.137e-012	-	-	2.2839337e-013	2.2839337e-013
3.509e+013	5.823e-012	-	-	3.77629779e-013	3.77629779e-013

Table D.9: Spectral energy distribution data from 2008.08.02 by Spitzer band 1 [IRS11].

ν [Hz]	νF_ν [erg/cm^2/s]	σ_ν^- [Hz]	σ_ν^+ [Hz]	$\sigma_{\nu F_\nu}^-$ [erg/cm^2/s]	$\sigma_{\nu F_\nu}^+$ [erg/cm^2/s]
3.989e+013	5.424e-012	-	-	3.393168e-013	3.393168e-013
3.957e+013	5.327e-012	-	-	3.57593581e-013	3.57593581e-013
3.926e+013	5.943e-012	-	-	3.19785039e-013	3.19785039e-013
3.895e+013	5.736e-012	-	-	2.75960461e-013	2.75960461e-013
3.865e+013	5.790e-012	-	-	2.53041054e-013	2.53041054e-013
3.835e+013	5.294e-012	-	-	2.57862256e-013	2.57862256e-013
3.805e+013	5.699e-012	-	-	2.39469368e-013	2.39469368e-013
3.776e+013	5.955e-012	-	-	2.25629311e-013	2.25629311e-013
3.748e+013	5.630e-012	-	-	2.14648243e-013	2.14648243e-013
3.720e+013	5.489e-012	-	-	1.99887113e-013	1.99887113e-013
3.692e+013	5.933e-012	-	-	1.85345859e-013	1.85345859e-013
3.665e+013	5.652e-012	-	-	1.78533886e-013	1.78533886e-013
3.638e+013	5.532e-012	-	-	1.7336543e-013	1.7336543e-013
3.611e+013	5.733e-012	-	-	1.77720039e-013	1.77720039e-013
3.585e+013	5.453e-012	-	-	1.72632023e-013	1.72632023e-013
3.559e+013	5.482e-012	-	-	1.640938e-013	1.640938e-013
3.534e+013	5.437e-012	-	-	1.59925335e-013	1.59925335e-013
3.509e+013	5.221e-012	-	-	1.60777987e-013	1.60777987e-013
3.484e+013	5.120e-012	-	-	1.6383617e-013	1.6383617e-013
3.460e+013	4.854e-012	-	-	1.60979863e-013	1.60979863e-013
3.436e+013	5.240e-012	-	-	1.48688117e-013	1.48688117e-013
3.412e+013	5.233e-012	-	-	1.57074568e-013	1.57074568e-013
3.389e+013	5.161e-012	-	-	1.46415223e-013	1.46415223e-013
3.366e+013	5.026e-012	-	-	1.52085151e-013	1.52085151e-013
3.343e+013	4.972e-012	-	-	1.56732998e-013	1.56732998e-013
3.321e+013	5.025e-012	-	-	1.65310258e-013	1.65310258e-013

3.299e+013	5.141e-012	-	-	1.61877624e-013	1.61877624e-013
3.277e+013	5.060e-012	-	-	1.72161329e-013	1.72161329e-013
3.255e+013	4.995e-012	-	-	1.68038039e-013	1.68038039e-013
3.234e+013	4.944e-012	-	-	1.69457232e-013	1.69457232e-013
3.213e+013	4.900e-012	-	-	1.72448275e-013	1.72448275e-013
3.192e+013	5.110e-012	-	-	3.0249331e-013	3.0249331e-013
3.172e+013	4.892e-012	-	-	3.78612832e-013	3.78612832e-013
3.152e+013	5.483e-012	-	-	3.67290195e-013	3.67290195e-013
3.132e+013	4.687e-012	-	-	3.37951143e-013	3.37951143e-013
3.112e+013	4.722e-012	-	-	3.1404216e-013	3.1404216e-013
3.093e+013	4.648e-012	-	-	1.80426033e-013	1.80426033e-013
3.036e+013	4.591e-012	-	-	1.72602324e-013	1.72602324e-013
3.018e+013	4.550e-012	-	-	1.50641076e-013	1.50641076e-013
2.999e+013	4.986e-012	-	-	2.43469393e-013	2.43469393e-013
2.981e+013	4.679e-012	-	-	1.43137153e-013	1.43137153e-013
2.963e+013	4.596e-012	-	-	1.37880966e-013	1.37880966e-013
2.946e+013	4.601e-012	-	-	1.26021522e-013	1.26021522e-013
2.928e+013	4.676e-012	-	-	1.50125352e-013	1.50125352e-013
2.911e+013	4.553e-012	-	-	1.25982233e-013	1.25982233e-013
2.894e+013	4.557e-012	-	-	1.22176763e-013	1.22176763e-013
2.877e+013	4.532e-012	-	-	1.28588757e-013	1.28588757e-013
2.861e+013	4.388e-012	-	-	1.27239758e-013	1.27239758e-013
2.844e+013	4.567e-012	-	-	1.21883561e-013	1.21883561e-013
2.828e+013	4.697e-012	-	-	1.19988272e-013	1.19988272e-013
2.812e+013	4.831e-012	-	-	1.26664744e-013	1.26664744e-013
2.796e+013	4.453e-012	-	-	1.29509245e-013	1.29509245e-013
2.781e+013	4.594e-012	-	-	1.30748915e-013	1.30748915e-013
2.765e+013	4.461e-012	-	-	1.28455309e-013	1.28455309e-013
2.750e+013	4.360e-012	-	-	1.30659237e-013	1.30659237e-013
2.735e+013	4.691e-012	-	-	1.46760825e-013	1.46760825e-013
2.720e+013	4.722e-012	-	-	1.3710972e-013	1.3710972e-013
2.705e+013	4.561e-012	-	-	1.41907854e-013	1.41907854e-013
2.690e+013	4.395e-012	-	-	1.31246691e-013	1.31246691e-013
2.675e+013	4.528e-012	-	-	1.33565139e-013	1.33565139e-013
2.661e+013	4.483e-012	-	-	1.41315742e-013	1.41315742e-013
2.647e+013	4.135e-012	-	-	1.40561009e-013	1.40561009e-013
2.633e+013	4.404e-012	-	-	1.3832505e-013	1.3832505e-013
2.619e+013	4.458e-012	-	-	1.45557274e-013	1.45557274e-013
2.605e+013	4.390e-012	-	-	1.51976489e-013	1.51976489e-013
2.592e+013	4.354e-012	-	-	1.68224252e-013	1.68224252e-013
2.578e+013	4.400e-012	-	-	1.96334655e-013	1.96334655e-013
2.565e+013	4.738e-012	-	-	1.90784775e-013	1.90784775e-013
2.552e+013	5.005e-012	-	-	1.8366841e-013	1.8366841e-013
2.538e+013	4.667e-012	-	-	1.73393989e-013	1.73393989e-013
2.526e+013	4.646e-012	-	-	1.83761078e-013	1.83761078e-013
2.513e+013	4.598e-012	-	-	1.88870577e-013	1.88870577e-013

2.500e+013	4.591e-012	-	-	1.74128941e-013	1.74128941e-013
2.488e+013	4.547e-012	-	-	1.81170319e-013	1.81170319e-013
2.475e+013	4.509e-012	-	-	1.94266912e-013	1.94266912e-013
2.463e+013	4.592e-012	-	-	1.79544055e-013	1.79544055e-013
2.451e+013	4.235e-012	-	-	1.65140216e-013	1.65140216e-013
2.439e+013	4.094e-012	-	-	2.48302242e-013	2.48302242e-013
2.427e+013	4.295e-012	-	-	1.71416252e-013	1.71416252e-013
2.415e+013	4.180e-012	-	-	2.75593619e-013	2.75593619e-013
2.403e+013	4.218e-012	-	-	1.65166254e-013	1.65166254e-013
2.391e+013	4.365e-012	-	-	1.537157e-013	1.537157e-013
2.380e+013	4.337e-012	-	-	1.47424001e-013	1.47424001e-013
2.369e+013	4.232e-012	-	-	1.39517442e-013	1.39517442e-013
2.357e+013	4.301e-012	-	-	1.44021365e-013	1.44021365e-013
2.346e+013	4.318e-012	-	-	1.47819042e-013	1.47819042e-013
2.335e+013	4.361e-012	-	-	1.83449118e-013	1.83449118e-013
2.324e+013	4.231e-012	-	-	1.92121048e-013	1.92121048e-013
2.313e+013	4.337e-012	-	-	1.85335564e-013	1.85335564e-013
2.303e+013	4.321e-012	-	-	1.5402724e-013	1.5402724e-013
2.292e+013	4.229e-012	-	-	1.45211715e-013	1.45211715e-013
2.281e+013	4.321e-012	-	-	1.49382996e-013	1.49382996e-013
2.271e+013	4.285e-012	-	-	1.56406408e-013	1.56406408e-013
2.261e+013	4.326e-012	-	-	1.51537031e-013	1.51537031e-013
2.250e+013	4.252e-012	-	-	1.53554176e-013	1.53554176e-013
2.240e+013	3.924e-012	-	-	1.6173074e-013	1.6173074e-013
2.230e+013	4.142e-012	-	-	1.64630022e-013	1.64630022e-013
2.220e+013	3.922e-012	-	-	1.62793653e-013	1.62793653e-013
2.210e+013	4.067e-012	-	-	1.75664594e-013	1.75664594e-013
2.200e+013	3.965e-012	-	-	1.80952874e-013	1.80952874e-013
2.191e+013	3.967e-012	-	-	1.82786393e-013	1.82786393e-013
2.181e+013	3.392e-012	-	-	1.98175458e-013	1.98175458e-013
2.171e+013	3.723e-012	-	-	1.97000212e-013	1.97000212e-013
2.162e+013	4.018e-012	-	-	2.0179727e-013	2.0179727e-013
2.153e+013	4.111e-012	-	-	2.07161656e-013	2.07161656e-013
2.143e+013	4.062e-012	-	-	2.23543142e-013	2.23543142e-013
2.134e+013	3.967e-012	-	-	2.30880182e-013	2.30880182e-013
2.125e+013	3.975e-012	-	-	2.36952434e-013	2.36952434e-013
2.116e+013	4.381e-012	-	-	2.35491989e-013	2.35491989e-013

Table D.10: Spectral energy distribution data from 2008.08.02 by Spitzer band 2 [IRS11].

ν [Hz]	νF_ν [erg/cm^2/s]	σ_ν^- [Hz]	σ_ν^+ [Hz]	$\sigma_{\nu F_\nu}^-$ [erg/cm^2/s]	$\sigma_{\nu F_\nu}^+$ [erg/cm^2/s]
2.131e+013	4.246e-012	-	-	2.87933608e-013	2.87933608e-013
2.118e+013	3.788e-012	-	-	2.67939001e-013	2.67939001e-013
2.105e+013	4.235e-012	-	-	2.07389219e-013	2.07389219e-013
2.093e+013	4.143e-012	-	-	1.67831411e-013	1.67831411e-013
2.081e+013	3.867e-012	-	-	1.8420632e-013	1.8420632e-013
2.069e+013	4.146e-012	-	-	2.3052149e-013	2.3052149e-013
2.057e+013	4.343e-012	-	-	2.29037131e-013	2.29037131e-013
2.045e+013	4.233e-012	-	-	2.47377293e-013	2.47377293e-013
2.033e+013	4.102e-012	-	-	2.37619267e-013	2.37619267e-013
2.021e+013	3.888e-012	-	-	2.65134356e-013	2.65134356e-013
2.010e+013	4.012e-012	-	-	2.82957426e-013	2.82957426e-013
1.999e+013	4.212e-012	-	-	2.08299759e-013	2.08299759e-013
1.987e+013	4.158e-012	-	-	1.96450773e-013	1.96450773e-013
1.976e+013	4.673e-012	-	-	1.83476546e-013	1.83476546e-013
1.965e+013	4.110e-012	-	-	1.81485323e-013	1.81485323e-013
1.954e+013	4.042e-012	-	-	2.01765577e-013	2.01765577e-013
1.944e+013	4.080e-012	-	-	1.92411779e-013	1.92411779e-013
1.933e+013	3.920e-012	-	-	1.86030415e-013	1.86030415e-013
1.923e+013	3.968e-012	-	-	1.89370403e-013	1.89370403e-013
1.912e+013	3.874e-012	-	-	1.65767618e-013	1.65767618e-013
1.902e+013	3.987e-012	-	-	1.78863408e-013	1.78863408e-013
1.892e+013	3.889e-012	-	-	2.05998353e-013	2.05998353e-013
1.882e+013	4.579e-012	-	-	2.53734521e-013	2.53734521e-013
1.872e+013	3.814e-012	-	-	3.20950785e-013	3.20950785e-013
1.862e+013	4.171e-012	-	-	2.5962325e-013	2.5962325e-013
1.852e+013	3.561e-012	-	-	2.36262715e-013	2.36262715e-013
1.843e+013	3.564e-012	-	-	1.96990184e-013	1.96990184e-013
1.833e+013	3.746e-012	-	-	1.94544573e-013	1.94544573e-013
1.824e+013	3.748e-012	-	-	2.19717826e-013	2.19717826e-013
1.814e+013	3.724e-012	-	-	1.95373054e-013	1.95373054e-013
1.805e+013	3.649e-012	-	-	1.76892e-013	1.76892e-013
1.796e+013	3.584e-012	-	-	1.96819511e-013	1.96819511e-013
1.787e+013	3.483e-012	-	-	1.9986919e-013	1.9986919e-013
1.778e+013	3.172e-012	-	-	2.49524737e-013	2.49524737e-013
1.769e+013	3.327e-012	-	-	3.03061789e-013	3.03061789e-013
1.760e+013	3.751e-012	-	-	2.38083067e-013	2.38083067e-013
1.751e+013	4.212e-012	-	-	2.87431875e-013	2.87431875e-013
1.743e+013	3.606e-012	-	-	3.56134876e-013	3.56134876e-013
1.734e+013	3.679e-012	-	-	2.3581075e-013	2.3581075e-013
1.726e+013	3.779e-012	-	-	2.42715168e-013	2.42715168e-013
1.717e+013	3.975e-012	-	-	1.9284162e-013	1.9284162e-013
1.709e+013	3.689e-012	-	-	1.92756628e-013	1.92756628e-013
1.701e+013	3.799e-012	-	-	2.08788744e-013	2.08788744e-013

1.693e+013	3.502e-012	-	-	2.20238726e-013	2.20238726e-013
1.685e+013	3.104e-012	-	-	2.27529474e-013	2.27529474e-013
1.677e+013	3.214e-012	-	-	2.83835656e-013	2.83835656e-013
1.669e+013	3.823e-012	-	-	2.88633852e-013	2.88633852e-013
1.661e+013	3.480e-012	-	-	3.01021195e-013	3.01021195e-013
1.653e+013	3.408e-012	-	-	2.85353829e-013	2.85353829e-013
1.646e+013	3.681e-012	-	-	3.41391513e-013	3.41391513e-013
1.638e+013	3.567e-012	-	-	2.88041103e-013	2.88041103e-013
1.630e+013	3.714e-012	-	-	2.59968559e-013	2.59968559e-013
1.623e+013	3.315e-012	-	-	2.7094107e-013	2.7094107e-013
1.616e+013	3.937e-012	-	-	2.86497005e-013	2.86497005e-013
1.601e+013	3.380e-012	-	-	2.44625655e-013	2.44625655e-013
1.594e+013	3.304e-012	-	-	2.46003652e-013	2.46003652e-013
1.587e+013	3.352e-012	-	-	2.64197142e-013	2.64197142e-013
1.579e+013	3.628e-012	-	-	2.48722891e-013	2.48722891e-013
1.572e+013	3.657e-012	-	-	2.52288111e-013	2.52288111e-013
1.565e+013	4.048e-012	-	-	3.37184425e-013	3.37184425e-013
1.559e+013	3.052e-012	-	-	3.87278511e-013	3.87278511e-013
1.552e+013	4.098e-012	-	-	3.61111859e-013	3.61111859e-013
1.545e+013	4.728e-012	-	-	5.00793921e-013	5.00793921e-013
1.532e+013	4.017e-012	-	-	3.5393425e-013	3.5393425e-013
1.525e+013	3.788e-012	-	-	3.64702982e-013	3.64702982e-013
1.518e+013	3.446e-012	-	-	3.16753319e-013	3.16753319e-013
1.512e+013	3.590e-012	-	-	2.95728071e-013	2.95728071e-013
1.506e+013	3.793e-012	-	-	3.10120159e-013	3.10120159e-013
1.499e+013	4.326e-012	-	-	3.72095004e-013	3.72095004e-013
1.493e+013	3.676e-012	-	-	4.12117741e-013	4.12117741e-013
1.487e+013	2.964e-012	-	-	3.68759815e-013	3.68759815e-013
1.468e+013	2.551e-012	-	-	6.58686923e-013	6.58686923e-013
1.462e+013	3.730e-012	-	-	4.4227353e-013	4.4227353e-013
1.456e+013	3.926e-012	-	-	4.66194296e-013	4.66194296e-013
1.444e+013	4.084e-012	-	-	3.93665372e-013	3.93665372e-013
1.438e+013	3.798e-012	-	-	4.28476016e-013	4.28476016e-013
1.559e+013	2.133e-012	-	-	1.60135366e-013	1.60135366e-013
1.545e+013	3.349e-012	-	-	2.5105245e-013	2.5105245e-013
1.532e+013	3.616e-012	-	-	2.96641955e-013	2.96641955e-013
1.518e+013	3.415e-012	-	-	1.92628968e-013	1.92628968e-013
1.506e+013	3.542e-012	-	-	2.21331895e-013	2.21331895e-013
1.493e+013	3.907e-012	-	-	2.10914766e-013	2.10914766e-013
1.480e+013	3.091e-012	-	-	2.16687825e-013	2.16687825e-013
1.468e+013	3.415e-012	-	-	2.06170564e-013	2.06170564e-013
1.456e+013	3.813e-012	-	-	2.31037986e-013	2.31037986e-013
1.444e+013	3.499e-012	-	-	2.03827778e-013	2.03827778e-013
1.432e+013	3.215e-012	-	-	2.13523092e-013	2.13523092e-013
1.421e+013	3.052e-012	-	-	1.63478877e-013	1.63478877e-013
1.410e+013	2.875e-012	-	-	1.62775075e-013	1.62775075e-013

1.399e+013	3.732e-012	-	-	3.14473616e-013	3.14473616e-013

Table D.11: Spectral energy distribution data from 2008.08.02 by Spitzer band 3 [IRS11].

ν [Hz]	νF_ν [erg/cm^2/s]	σ_ν^- [Hz]	σ_ν^+ [Hz]	$\sigma_{\nu F_\nu}^-$ [erg/cm^2/s]	$\sigma_{\nu F_\nu}^+$ [erg/cm^2/s]
1.468e+013	3.107e-012	-	-	4.3777506e-013	4.3777506e-013
1.456e+013	3.483e-012	-	-	3.25141693e-013	3.25141693e-013
1.444e+013	2.761e-012	-	-	5.42757835e-013	5.42757835e-013
1.432e+013	3.073e-012	-	-	3.35073239e-013	3.35073239e-013
1.421e+013	2.809e-012	-	-	2.2678047e-013	2.2678047e-013
1.410e+013	3.257e-012	-	-	2.67238198e-013	2.67238198e-013
1.399e+013	3.436e-012	-	-	2.48908834e-013	2.48908834e-013
1.388e+013	2.673e-012	-	-	2.34104528e-013	2.34104528e-013
1.377e+013	3.030e-012	-	-	1.98210343e-013	1.98210343e-013
1.366e+013	3.618e-012	-	-	2.24791744e-013	2.24791744e-013
1.356e+013	3.356e-012	-	-	2.03226781e-013	2.03226781e-013
1.345e+013	3.305e-012	-	-	1.62677676e-013	1.62677676e-013
1.335e+013	2.873e-012	-	-	1.72025204e-013	1.72025204e-013
1.325e+013	3.285e-012	-	-	1.91634366e-013	1.91634366e-013
1.315e+013	3.126e-012	-	-	2.18021136e-013	2.18021136e-013
1.306e+013	2.741e-012	-	-	2.08195929e-013	2.08195929e-013
1.296e+013	2.955e-012	-	-	1.55164069e-013	1.55164069e-013
1.287e+013	3.181e-012	-	-	1.81058566e-013	1.81058566e-013
1.277e+013	3.034e-012	-	-	2.25819045e-013	2.25819045e-013
1.268e+013	3.135e-012	-	-	1.65998566e-013	1.65998566e-013
1.259e+013	3.135e-012	-	-	1.42735201e-013	1.42735201e-013
1.250e+013	3.157e-012	-	-	1.57818254e-013	1.57818254e-013
1.242e+013	3.154e-012	-	-	1.88317033e-013	1.88317033e-013
1.233e+013	2.901e-012	-	-	1.72533162e-013	1.72533162e-013
1.224e+013	2.916e-012	-	-	1.59824815e-013	1.59824815e-013
1.216e+013	2.916e-012	-	-	2.28890132e-013	2.28890132e-013
1.208e+013	3.172e-012	-	-	1.624263e-013	1.624263e-013
1.200e+013	2.754e-012	-	-	1.83378637e-013	1.83378637e-013
1.191e+013	3.007e-012	-	-	1.81386195e-013	1.81386195e-013
1.183e+013	3.207e-012	-	-	1.83771936e-013	1.83771936e-013
1.168e+013	3.053e-012	-	-	1.61610338e-013	1.61610338e-013
1.160e+013	3.139e-012	-	-	1.55382671e-013	1.55382671e-013
1.131e+013	2.746e-012	-	-	1.25191698e-013	1.25191698e-013
1.123e+013	2.900e-012	-	-	1.54344659e-013	1.54344659e-013
1.116e+013	3.074e-012	-	-	1.66553571e-013	1.66553571e-013
1.109e+013	2.867e-012	-	-	1.54135914e-013	1.54135914e-013
1.102e+013	3.086e-012	-	-	1.56605942e-013	1.56605942e-013
1.096e+013	2.934e-012	-	-	1.55714197e-013	1.55714197e-013
1.089e+013	3.414e-012	-	-	1.42206478e-013	1.42206478e-013

1.082e+013	3.837e-012	-	-	1.76078377e-013	1.76078377e-013
1.076e+013	2.564e-012	-	-	1.98738482e-013	1.98738482e-013
1.069e+013	2.400e-012	-	-	2.02376443e-013	2.02376443e-013
1.063e+013	2.938e-012	-	-	2.52034314e-013	2.52034314e-013
1.056e+013	2.670e-012	-	-	1.83154505e-013	1.83154505e-013
1.050e+013	2.651e-012	-	-	1.56599317e-013	1.56599317e-013
1.044e+013	2.669e-012	-	-	1.57078351e-013	1.57078351e-013
1.038e+013	2.794e-012	-	-	1.77438306e-013	1.77438306e-013
1.032e+013	2.173e-012	-	-	1.69035754e-013	1.69035754e-013
1.026e+013	2.602e-012	-	-	1.72915927e-013	1.72915927e-013
1.020e+013	3.060e-012	-	-	1.79996462e-013	1.79996462e-013
1.014e+013	2.775e-012	-	-	1.85275118e-013	1.85275118e-013
1.008e+013	2.868e-012	-	-	1.80441339e-013	1.80441339e-013
1.003e+013	2.790e-012	-	-	1.71054601e-013	1.71054601e-013
9.969e+012	2.753e-012	-	-	1.86726891e-013	1.86726891e-013
9.913e+012	2.987e-012	-	-	2.91173936e-013	2.91173936e-013
9.858e+012	3.247e-012	-	-	6.70905889e-013	6.70905889e-013
9.803e+012	2.694e-012	-	-	2.82057001e-013	2.82057001e-013
9.749e+012	2.630e-012	-	-	2.38934717e-013	2.38934717e-013
9.696e+012	2.632e-012	-	-	2.59907793e-013	2.59907793e-013
9.643e+012	2.493e-012	-	-	3.08676608e-013	3.08676608e-013
9.591e+012	2.976e-012	-	-	2.67670855e-013	2.67670855e-013
9.539e+012	2.622e-012	-	-	3.14455873e-013	3.14455873e-013
9.488e+012	3.168e-012	-	-	2.63862299e-013	2.63862299e-013
9.437e+012	2.262e-012	-	-	2.59719641e-013	2.59719641e-013
9.387e+012	2.536e-012	-	-	2.8761502e-013	2.8761502e-013
9.338e+012	3.237e-012	-	-	2.89597287e-013	2.89597287e-013
9.289e+012	2.628e-012	-	-	2.86435707e-013	2.86435707e-013
9.240e+012	2.534e-012	-	-	3.00491028e-013	3.00491028e-013
9.192e+012	2.906e-012	-	-	3.2824527e-013	3.2824527e-013
9.145e+012	2.438e-012	-	-	3.37736371e-013	3.37736371e-013
9.098e+012	2.178e-012	-	-	3.1451402e-013	3.1451402e-013
9.051e+012	2.547e-012	-	-	3.53035191e-013	3.53035191e-013
9.005e+012	2.804e-012	-	-	3.92947392e-013	3.92947392e-013
8.960e+012	2.469e-012	-	-	3.86143569e-013	3.86143569e-013
8.915e+012	1.852e-012	-	-	6.48820489e-013	6.48820489e-013
8.870e+012	3.635e-012	-	-	5.76829073e-013	5.76829073e-013
8.826e+012	1.901e-012	-	-	6.06903956e-013	6.06903956e-013
8.696e+012	3.306e-012	-	-	5.53074906e-013	5.53074906e-013
8.653e+012	2.683e-012	-	-	4.63853921e-013	4.63853921e-013
8.569e+012	2.003e-012	-	-	5.40558968e-013	5.40558968e-013
8.528e+012	3.169e-012	-	-	6.16890136e-013	6.16890136e-013
8.487e+012	4.440e-012	-	-	6.87808538e-013	6.87808538e-013
8.447e+012	4.185e-012	-	-	1.25324353e-012	1.25324353e-012
8.288e+012	5.675e-012	-	-	1.66095093e-012	1.66095093e-012

Table D.12: Spectral energy distribution data from 2008.08.02 by Spitzer band 4 [IRS11].

ν [Hz]	νF_ν [erg/cm^2/s]	σ_ν^- [Hz]	σ_ν^+ [Hz]	$\sigma_{\nu F_\nu}^-$ [erg/cm^2/s]	$\sigma_{\nu F_\nu}^+$ [erg/cm^2/s]
1.380e+014	1.690e-011	-	-	4.520e-013	4.520e-013
1.820e+014	1.940e-011	-	-	6.790e-013	6.790e-013
2.400e+014	2.160e-011	-	-	6.380e-013	6.380e-013

Table D.13: Spectral energy distribution data from 1999.06.03 by 2MASS [S+06].

D.3 Optical and UV Observations

ν [Hz]	νF_ν [erg/cm^2/s]	σ_ν^- [Hz]	σ_ν^+ [Hz]	$\sigma_{\nu F_\nu}^-$ [erg/cm^2/s]	$\sigma_{\nu F_\nu}^+$ [erg/cm^2/s]
4.612e+014	7.841e-012	-	-	-	-
4.612e+014	3.113e-011	-	-	-	-
4.612e+014	2.391e-011	-	-	5.112e-012	5.112e-012

Table D.14: Spectral energy distribution data from 2004–2010 by KVA [L+10].

ν [Hz]	νF_ν [erg/cm^2/s]	σ_ν^- [Hz]	σ_ν^+ [Hz]	$\sigma_{\nu F_\nu}^-$ [erg/cm^2/s]	$\sigma_{\nu F_\nu}^+$ [erg/cm^2/s]
5.530e+014	1.800e-011	-	-	2.970e-013	2.970e-013

Table D.15: Spectral energy distribution data from 2007.12.3–11 Palomar60 [B+10c].

ν [Hz]	νF_ν [erg/cm^2/s]	σ_ν^- [Hz]	σ_ν^+ [Hz]	$\sigma_{\nu F_\nu}^-$ [erg/cm^2/s]	$\sigma_{\nu F_\nu}^+$ [erg/cm^2/s]
5.483e+014	2.522e-011	3.855e+013	3.855e+013	2.522e-012	2.522e-012
6.826e+014	2.526e-011	7.577e+013	7.577e+013	2.526e-012	2.526e-012
8.652e+014	3.115e-011	9.801e+013	9.801e+013	3.115e-012	3.115e-012
1.153e+015	2.998e-011	1.537e+014	1.537e+014	2.998e-012	2.998e-012
1.335e+015	3.737e-011	1.480e+014	1.480e+014	3.737e-012	3.737e-012
1.555e+015	5.442e-011	2.649e+014	2.649e+014	5.442e-012	5.442e-012

Table D.16: Spectral energy distribution data from 2005.04.19 by Swift–UVOT [T+08a, T+07b].

ν [Hz]	νF_ν [erg/cm^2/s]	σ_ν^- [Hz]	σ_ν^+ [Hz]	$\sigma_{\nu F_\nu}^-$ [erg/cm^2/s]	$\sigma_{\nu F_\nu}^+$ [erg/cm^2/s]
5.483e+014	2.869e-011	3.855e+013	3.855e+013	1.343e-012	1.343e-012
6.826e+014	3.292e-011	7.577e+013	7.577e+013	1.394e-012	1.394e-012
8.652e+014	3.682e-011	9.801e+013	9.801e+013	1.829e-012	1.829e-012
1.153e+015	3.600e-011	1.537e+014	1.537e+014	1.700e-012	1.700e-012
1.335e+015	4.331e-011	1.480e+014	1.480e+014	2.278e-012	2.278e-012
1.555e+015	6.486e-011	2.649e+014	2.649e+014	3.078e-012	3.078e-012

Table D.17: Spectral energy distribution data from 2006.05.19–29 by Swift–UVOT (mean) [T+08a].

ν [Hz]	νF_ν [erg/cm^2/s]	σ_ν^- [Hz]	σ_ν^+ [Hz]	$\sigma_{\nu F_\nu}^-$ [erg/cm^2/s]	$\sigma_{\nu F_\nu}^+$ [erg/cm^2/s]
6.600e+014	3.500e-011	-	-	2.070e-013	2.070e-013
8.370e+014	3.870e-011	-	-	2.140e-013	2.140e-013
1.120e+015	3.530e-011	-	-	3.540e-013	3.540e-013
1.500e+015	4.180e-011	-	-	2.540e-012	2.540e-012

Table D.18: Spectral energy distribution data from 2007.11.16–30 by Swift–UVOT [B+10c].

ν [Hz]	νF_ν [erg/cm^2/s]	σ_ν^- [Hz]	σ_ν^+ [Hz]	$\sigma_{\nu F_\nu}^-$ [erg/cm^2/s]	$\sigma_{\nu F_\nu}^+$ [erg/cm^2/s]
1.962e+015	3.375e-011	2.363e+014	3.313e+014	9.051e-013	9.051e-013
1.320e+015	1.572e-011	2.906e+014	3.255e+014	6.411e-013	6.411e-013

Table D.19: Spectral energy distribution data from 2007.07.13 by Galex (137sec) [Lev11].

ν [Hz]	νF_ν [erg/cm^2/s]	σ_ν^- [Hz]	σ_ν^+ [Hz]	$\sigma_{\nu F_\nu}^-$ [erg/cm^2/s]	$\sigma_{\nu F_\nu}^+$ [erg/cm^2/s]
1.962e+015	3.475e-011	2.363e+014	3.313e+014	9.693e-013	9.693e-013
1.320e+015	1.668e-011	2.906e+014	3.255e+014	4.744e-013	4.744e-013

Table D.20: Spectral energy distribution data from 2007.07.13 by Galex (128sec) [Lev11].

D.4 X-Ray Observations

ν [Hz]	νF_ν [erg/cm^2/s]	σ_ν^- [Hz]	σ_ν^+ [Hz]	$\sigma_{\nu F_\nu}^-$ [erg/cm^2/s]	$\sigma_{\nu F_\nu}^+$ [erg/cm^2/s]
4.505e+016	6.562e-011	1.297e+016	1.297e+016	4.078e-011	4.078e-011
9.176e+016	1.120e-010	3.373e+016	3.373e+016	4.271e-011	4.271e-011
1.437e+017	1.039e-010	1.816e+016	1.816e+016	1.505e-011	1.505e-011
1.722e+017	9.855e-011	1.038e+016	1.038e+016	9.169e-012	9.169e-012
1.968e+017	9.176e-011	1.427e+016	1.427e+016	8.333e-012	8.333e-012
2.267e+017	9.208e-011	1.557e+016	1.557e+016	7.693e-012	7.693e-012
2.552e+017	8.715e-011	1.297e+016	1.297e+016	6.326e-012	6.326e-012
2.799e+017	8.684e-011	1.168e+016	1.168e+016	5.960e-012	5.960e-012
3.097e+017	8.177e-011	1.816e+016	1.816e+016	6.079e-012	6.079e-012
3.512e+017	8.247e-011	2.335e+016	2.335e+016	6.478e-012	6.478e-012
3.915e+017	7.202e-011	1.687e+016	1.687e+016	5.073e-012	5.073e-012
4.343e+017	7.202e-011	2.595e+016	2.595e+016	5.516e-012	5.516e-012
4.823e+017	7.482e-011	2.206e+016	2.206e+016	5.348e-012	5.348e-012
5.433e+017	7.442e-011	3.892e+016	3.892e+016	6.455e-012	6.455e-012
6.302e+017	6.913e-011	4.801e+016	4.801e+016	6.616e-012	6.616e-012
7.210e+017	6.328e-011	4.282e+016	4.282e+016	5.853e-012	5.853e-012
8.404e+017	6.640e-011	7.655e+016	7.655e+016	7.159e-012	7.159e-012
4.340e+017	7.566e-011	2.247e+016	2.247e+016	4.792e-012	4.792e-012
4.902e+017	7.351e-011	3.370e+016	3.370e+016	5.476e-012	5.476e-012
5.576e+017	6.830e-011	3.370e+016	3.370e+016	4.702e-012	4.702e-012
6.249e+017	6.650e-011	3.370e+016	3.370e+016	4.342e-012	4.342e-012
6.811e+017	6.536e-011	2.247e+016	2.247e+016	3.749e-012	3.749e-012
7.541e+017	6.174e-011	5.055e+016	5.055e+016	4.634e-012	4.634e-012
8.271e+017	5.714e-011	2.247e+016	2.247e+016	3.545e-012	3.545e-012
8.945e+017	5.668e-011	4.493e+016	4.493e+016	3.703e-012	3.703e-012
9.732e+017	5.440e-011	3.370e+016	3.370e+016	3.417e-012	3.417e-012
1.063e+018	4.953e-011	5.616e+016	5.616e+016	3.453e-012	3.453e-012
1.203e+018	5.051e-011	8.424e+016	8.424e+016	4.100e-012	4.100e-012
1.333e+018	4.795e-011	4.493e+016	4.493e+016	3.608e-012	3.608e-012
1.434e+018	4.443e-011	5.616e+016	5.616e+016	3.488e-012	3.488e-012
1.608e+018	4.080e-011	1.179e+017	1.179e+017	3.775e-012	3.775e-012
1.978e+018	3.813e-011	2.527e+017	2.527e+017	5.341e-012	5.341e-012
3.993e+018	4.300e-011	2.723e+017	2.723e+017	1.633e-011	1.633e-011
4.810e+018	2.919e-011	5.445e+017	5.445e+017	1.173e-011	1.173e-011
6.715e+018	3.166e-011	1.361e+018	1.361e+018	1.297e-011	1.297e-011

Table D.21: Spectral energy distribution data from 2001.09.25 by BeppoSAX [T+03].

ν [Hz]	νF_ν [erg/cm^2/s]	σ_ν^- [Hz]	σ_ν^+ [Hz]	$\sigma_{\nu F_\nu}^-$ [erg/cm^2/s]	$\sigma_{\nu F_\nu}^+$ [erg/cm^2/s]
6.192e+016	9.447e-011	2.984e+016	2.984e+016	4.629e-011	4.629e-011
1.125e+017	9.351e-011	2.076e+016	2.076e+016	1.778e-011	1.778e-011
1.411e+017	9.478e-011	7.785e+015	7.785e+015	7.325e-012	7.325e-012
1.566e+017	9.171e-011	7.785e+015	7.785e+015	6.156e-012	6.156e-012
1.722e+017	9.055e-011	7.785e+015	7.785e+015	5.430e-012	5.430e-012
1.878e+017	8.786e-011	7.785e+015	7.785e+015	4.859e-012	4.859e-012
2.072e+017	8.666e-011	1.168e+016	1.168e+016	5.445e-012	5.445e-012
2.267e+017	8.742e-011	7.785e+015	7.785e+015	4.116e-012	4.116e-012
2.436e+017	8.838e-011	9.082e+015	9.082e+015	4.177e-012	4.177e-012
2.825e+017	8.956e-011	2.984e+016	2.984e+016	9.568e-012	9.568e-012
3.279e+017	8.726e-011	1.557e+016	1.557e+016	4.601e-012	4.601e-012
3.603e+017	8.506e-011	1.687e+016	1.687e+016	4.443e-012	4.443e-012
3.967e+017	7.970e-011	1.946e+016	1.946e+016	4.338e-012	4.338e-012
4.823e+017	8.183e-011	6.617e+016	6.617e+016	1.129e-011	1.129e-011
7.586e+017	8.082e-011	2.102e+017	2.102e+017	2.242e-011	2.242e-011
4.340e+017	8.474e-011	2.247e+016	2.247e+016	4.529e-012	4.529e-012
4.789e+017	8.274e-011	2.247e+016	2.247e+016	4.022e-012	4.022e-012
5.295e+017	8.091e-011	2.808e+016	2.808e+016	4.400e-012	4.400e-012
5.969e+017	7.926e-011	3.931e+016	3.931e+016	5.304e-012	5.304e-012
6.643e+017	7.940e-011	2.808e+016	2.808e+016	3.551e-012	3.551e-012
7.148e+017	7.404e-011	2.247e+016	2.247e+016	2.660e-012	2.660e-012
7.710e+017	7.274e-011	3.370e+016	3.370e+016	3.360e-012	3.360e-012
8.384e+017	7.008e-011	3.370e+016	3.370e+016	3.033e-012	3.033e-012
9.058e+017	7.047e-011	3.370e+016	3.370e+016	2.879e-012	2.879e-012
9.844e+017	6.782e-011	4.493e+016	4.493e+016	3.278e-012	3.278e-012
1.085e+018	6.578e-011	5.616e+016	5.616e+016	3.552e-012	3.552e-012
1.198e+018	6.355e-011	5.616e+016	5.616e+016	3.174e-012	3.174e-012
1.338e+018	6.117e-011	8.424e+016	8.424e+016	3.987e-012	3.987e-012
1.535e+018	5.855e-011	1.123e+017	1.123e+017	4.406e-012	4.406e-012
1.759e+018	5.479e-011	1.123e+017	1.123e+017	3.703e-012	3.703e-012
1.967e+018	5.397e-011	9.548e+016	9.548e+016	3.098e-012	3.098e-012
2.226e+018	5.203e-011	1.629e+017	1.629e+017	4.159e-012	4.159e-012
4.265e+018	3.684e-011	5.445e+017	5.445e+017	6.248e-012	6.248e-012
5.899e+018	3.176e-011	1.089e+018	1.089e+018	6.939e-012	6.939e-012
9.030e+018	2.684e-011	2.042e+018	2.042e+018	7.981e-012	7.981e-012

Table D.22: Spectral energy distribution data from 2001.09.28-29 by BeppoSAX [T+03].

ν [Hz]	νF_ν [erg/cm^2/s]	σ_ν^- [Hz]	σ_ν^+ [Hz]	$\sigma_{\nu F_\nu}^-$ [erg/cm^2/s]	$\sigma_{\nu F_\nu}^+$ [erg/cm^2/s]
9.551e+016	1.088e-010	2.297e+016	2.297e+016	2.101e-012	2.101e-012
1.378e+017	1.304e-010	1.934e+016	1.934e+016	2.549e-012	2.549e-012
1.717e+017	1.271e-010	1.451e+016	1.451e+016	2.523e-012	2.523e-012
1.995e+017	1.233e-010	1.330e+016	1.330e+016	2.450e-012	2.450e-012
2.273e+017	1.212e-010	1.451e+016	1.451e+016	2.312e-012	2.312e-012
2.551e+017	1.221e-010	1.330e+016	1.330e+016	2.433e-012	2.433e-012
2.829e+017	1.224e-010	1.451e+016	1.451e+016	2.385e-012	2.385e-012
3.131e+017	1.184e-010	1.572e+016	1.572e+016	2.350e-012	2.350e-012
3.470e+017	1.179e-010	1.813e+016	1.813e+016	2.313e-012	2.313e-012
3.881e+017	1.122e-010	2.297e+016	2.297e+016	2.235e-012	2.235e-012
4.473e+017	1.072e-010	3.627e+016	3.627e+016	2.143e-012	2.143e-012
5.489e+017	1.058e-010	6.529e+016	6.529e+016	2.105e-012	2.105e-012
7.508e+017	8.909e-011	1.366e+017	1.366e+017	1.774e-012	1.774e-012
1.574e+018	7.592e-011	6.867e+017	6.867e+017	1.643e-012	1.643e-012

Table D.23: Spectral energy distribution data from 2005.04.19 by Swift–XRT [M+08b, T+07b].

ν [Hz]	νF_ν [erg/cm^2/s]	σ_ν^- [Hz]	σ_ν^+ [Hz]	$\sigma_{\nu F_\nu}^-$ [erg/cm^2/s]	$\sigma_{\nu F_\nu}^+$ [erg/cm^2/s]
1.064e+017	8.639e-011	2.902e+016	2.902e+016	2.858e-012	2.858e-012
1.596e+017	1.023e-010	2.418e+016	2.418e+016	3.326e-012	3.326e-012
2.043e+017	1.005e-010	2.055e+016	2.055e+016	3.296e-012	3.296e-012
2.442e+017	1.090e-010	1.934e+016	1.934e+016	3.525e-012	3.525e-012
2.853e+017	9.988e-011	2.176e+016	2.176e+016	3.285e-012	3.285e-012
3.313e+017	1.032e-010	2.418e+016	2.418e+016	3.387e-012	3.387e-012
3.869e+017	1.010e-010	3.143e+016	3.143e+016	3.353e-012	3.353e-012
4.788e+017	9.544e-011	6.045e+016	6.045e+016	3.165e-012	3.165e-012
6.928e+017	8.766e-011	1.535e+017	1.535e+017	2.898e-012	2.898e-012
1.314e+018	7.189e-011	4.679e+017	4.679e+017	2.890e-012	2.890e-012

Table D.24: Spectral energy distribution data from 2006.05.19 by Swift–XRT [T+08a].

ν [Hz]	νF_ν [erg/cm^2/s]	σ_ν^- [Hz]	σ_ν^+ [Hz]	$\sigma_{\nu F_\nu}^-$ [erg/cm^2/s]	$\sigma_{\nu F_\nu}^+$ [erg/cm^2/s]
9.551e+016	1.063e-010	2.055e+016	2.055e+016	3.430e-012	3.430e-012
1.330e+017	1.377e-010	1.693e+016	1.693e+016	4.496e-012	4.496e-012
1.644e+017	1.155e-010	1.451e+016	1.451e+016	3.761e-012	3.761e-012
1.910e+017	1.268e-010	1.209e+016	1.209e+016	4.090e-012	4.090e-012
2.152e+017	1.240e-010	1.209e+016	1.209e+016	4.022e-012	4.022e-012
2.382e+017	1.286e-010	1.088e+016	1.088e+016	4.239e-012	4.239e-012
2.611e+017	1.269e-010	1.209e+016	1.209e+016	4.069e-012	4.069e-012
2.853e+017	1.289e-010	1.209e+016	1.209e+016	4.178e-012	4.178e-012
3.107e+017	1.246e-010	1.330e+016	1.330e+016	4.050e-012	4.050e-012
3.385e+017	1.250e-010	1.451e+016	1.451e+016	4.094e-012	4.094e-012
3.700e+017	1.216e-010	1.693e+016	1.693e+016	3.998e-012	3.998e-012
4.074e+017	1.232e-010	2.055e+016	2.055e+016	4.074e-012	4.074e-012
4.618e+017	1.152e-010	3.385e+016	3.385e+016	3.776e-012	3.776e-012
5.453e+017	1.195e-010	4.957e+016	4.957e+016	3.968e-012	3.968e-012
6.795e+017	1.083e-010	8.463e+016	8.463e+016	3.591e-012	3.591e-012
8.971e+017	1.105e-010	1.330e+017	1.330e+017	3.652e-012	3.652e-012
1.681e+018	8.627e-011	6.504e+017	6.504e+017	3.289e-012	3.289e-012

Table D.25: Spectral energy distribution data from 2006.05.21 by Swift–XRT [T+08a].

ν [Hz]	νF_ν [erg/cm^2/s]	σ_ν^- [Hz]	σ_ν^+ [Hz]	$\sigma_{\nu F_\nu}^-$ [erg/cm^2/s]	$\sigma_{\nu F_\nu}^+$ [erg/cm^2/s]
9.309e+016	1.308e-010	2.055e+016	2.055e+016	2.609e-012	2.609e-012
1.294e+017	1.858e-010	1.572e+016	1.572e+016	3.673e-012	3.673e-012
1.584e+017	1.611e-010	1.330e+016	1.330e+016	3.173e-012	3.173e-012
1.838e+017	1.607e-010	1.209e+016	1.209e+016	3.077e-012	3.077e-012
2.067e+017	1.581e-010	1.088e+016	1.088e+016	3.151e-012	3.151e-012
2.285e+017	1.636e-010	1.088e+016	1.088e+016	3.205e-012	3.205e-012
2.503e+017	1.582e-010	1.088e+016	1.088e+016	3.145e-012	3.145e-012
2.720e+017	1.664e-010	1.088e+016	1.088e+016	3.273e-012	3.273e-012
2.950e+017	1.631e-010	1.209e+016	1.209e+016	3.169e-012	3.169e-012
3.192e+017	1.666e-010	1.209e+016	1.209e+016	3.314e-012	3.314e-012
3.458e+017	1.606e-010	1.451e+016	1.451e+016	3.107e-012	3.107e-012
3.772e+017	1.584e-010	1.693e+016	1.693e+016	3.103e-012	3.103e-012
4.147e+017	1.594e-010	2.055e+016	2.055e+016	3.142e-012	3.142e-012
4.655e+017	1.604e-010	3.022e+016	3.022e+016	3.179e-012	3.179e-012
5.416e+017	1.589e-010	4.594e+016	4.594e+016	3.139e-012	3.139e-012
6.589e+017	1.491e-010	7.133e+016	7.133e+016	2.963e-012	2.963e-012
8.378e+017	1.458e-010	1.076e+017	1.076e+017	2.902e-012	2.902e-012
1.170e+018	1.437e-010	2.249e+017	2.249e+017	2.857e-012	2.857e-012
1.813e+018	1.198e-010	4.183e+017	4.183e+017	4.581e-012	4.581e-012

Table D.26: Spectral energy distribution data from 2006.05.23 by Swift–XRT [T+08a].

ν [Hz]	νF_ν [erg/cm^2/s]	σ_ν^- [Hz]	σ_ν^+ [Hz]	$\sigma_{\nu F_\nu}^-$ [erg/cm^2/s]	$\sigma_{\nu F_\nu}^+$ [erg/cm^2/s]
1.040e+017	1.223e-010	3.143e+016	3.143e+016	2.434e-012	2.434e-012
1.584e+017	1.574e-010	2.297e+016	2.297e+016	3.134e-012	3.134e-012
1.995e+017	1.754e-010	1.813e+016	1.813e+016	3.433e-012	3.433e-012
2.358e+017	1.772e-010	1.813e+016	1.813e+016	3.438e-012	3.438e-012
2.720e+017	1.804e-010	1.814e+016	1.814e+016	3.537e-012	3.537e-012
3.107e+017	1.735e-010	2.055e+016	2.055e+016	3.411e-012	3.411e-012
3.542e+017	1.792e-010	2.297e+016	2.297e+016	3.547e-012	3.547e-012
4.074e+017	1.830e-010	3.022e+016	3.022e+016	3.634e-012	3.634e-012
4.896e+017	1.821e-010	5.199e+016	5.199e+016	3.632e-012	3.632e-012
6.444e+017	1.789e-010	1.028e+017	1.028e+017	3.567e-012	3.567e-012
9.769e+017	1.610e-010	2.297e+017	2.297e+017	3.219e-012	3.219e-012
1.755e+018	1.353e-010	5.489e+017	5.489e+017	4.691e-012	4.691e-012

Table D.27: Spectral energy distribution data from 2006.05.24 by Swift–XRT [T+08a].

ν [Hz]	νF_ν [erg/cm^2/s]	σ_ν^- [Hz]	σ_ν^+ [Hz]	$\sigma_{\nu F_\nu}^-$ [erg/cm^2/s]	$\sigma_{\nu F_\nu}^+$ [erg/cm^2/s]
9.430e+016	1.196e-010	2.176e+016	2.176e+016	2.301e-012	2.301e-012
1.306e+017	1.856e-010	1.451e+016	1.451e+016	3.704e-012	3.704e-012
1.584e+017	1.527e-010	1.330e+016	1.330e+016	2.999e-012	2.999e-012
1.826e+017	1.600e-010	1.088e+016	1.088e+016	3.164e-012	3.164e-012
2.043e+017	1.541e-010	1.088e+016	1.088e+016	3.028e-012	3.028e-012
2.261e+017	1.517e-010	1.088e+016	1.088e+016	3.007e-012	3.007e-012
2.478e+017	1.606e-010	1.088e+016	1.088e+016	3.077e-012	3.077e-012
2.696e+017	1.650e-010	1.088e+016	1.088e+016	3.176e-012	3.176e-012
2.926e+017	1.555e-010	1.209e+016	1.209e+016	2.999e-012	2.999e-012
3.168e+017	1.614e-010	1.209e+016	1.209e+016	3.162e-012	3.162e-012
3.421e+017	1.581e-010	1.330e+016	1.330e+016	3.108e-012	3.108e-012
3.712e+017	1.574e-010	1.572e+016	1.572e+016	3.068e-012	3.068e-012
4.050e+017	1.602e-010	1.813e+016	1.813e+016	3.165e-012	3.165e-012
4.510e+017	1.538e-010	2.781e+016	2.781e+016	3.014e-012	3.014e-012
5.187e+017	1.482e-010	3.990e+016	3.990e+016	2.938e-012	2.938e-012
6.226e+017	1.456e-010	6.408e+016	6.408e+016	2.905e-012	2.905e-012
7.798e+017	1.390e-010	9.309e+016	9.309e+016	2.767e-012	2.767e-012
1.047e+018	1.321e-010	1.741e+017	1.741e+017	2.641e-012	2.641e-012
1.662e+018	1.121e-010	4.413e+017	4.413e+017	3.200e-012	3.200e-012

Table D.28: Spectral energy distribution data from 2006.05.25 by Swift–XRT [T+08a].

ν [Hz]	νF_ν [erg/cm^2/s]	σ_ν^- [Hz]	σ_ν^+ [Hz]	$\sigma_{\nu F_\nu}^-$ [erg/cm^2/s]	$\sigma_{\nu F_\nu}^+$ [erg/cm^2/s]
9.309e+016	1.277e-010	2.055e+016	2.055e+016	2.489e-012	2.489e-012
1.282e+017	1.261e-010	1.451e+016	1.451e+016	2.499e-012	2.499e-012
1.560e+017	1.519e-010	1.330e+016	1.330e+016	3.019e-012	3.019e-012
1.801e+017	1.663e-010	1.088e+016	1.088e+016	3.252e-012	3.252e-012
2.019e+017	1.569e-010	1.088e+016	1.088e+016	3.052e-012	3.052e-012
2.237e+017	1.606e-010	1.088e+016	1.088e+016	3.088e-012	3.088e-012
2.454e+017	1.581e-010	1.088e+016	1.088e+016	3.049e-012	3.049e-012
2.672e+017	1.566e-010	1.088e+016	1.088e+016	3.087e-012	3.087e-012
2.902e+017	1.528e-010	1.209e+016	1.209e+016	2.970e-012	2.970e-012
3.143e+017	1.560e-010	1.209e+016	1.209e+016	3.087e-012	3.087e-012
3.397e+017	1.556e-010	1.330e+016	1.330e+016	3.067e-012	3.067e-012
3.687e+017	1.562e-010	1.572e+016	1.572e+016	3.029e-012	3.029e-012
4.038e+017	1.467e-010	1.934e+016	1.934e+016	2.923e-012	2.923e-012
4.510e+017	1.479e-010	2.781e+016	2.781e+016	2.949e-012	2.949e-012
5.187e+017	1.497e-010	3.990e+016	3.990e+016	2.958e-012	2.958e-012
6.275e+017	1.375e-010	6.891e+016	6.891e+016	2.737e-012	2.737e-012
7.967e+017	1.342e-010	1.003e+017	1.003e+017	2.666e-012	2.666e-012
1.105e+018	1.263e-010	2.079e+017	2.079e+017	2.517e-012	2.517e-012
1.701e+018	1.050e-010	3.881e+017	3.881e+017	3.605e-012	3.605e-012

Table D.29: Spectral energy distribution data from 2006.05.26 by Swift–XRT [T+08a].

ν [Hz]	νF_ν [erg/cm^2/s]	σ_ν^- [Hz]	σ_ν^+ [Hz]	$\sigma_{\nu F_\nu}^-$ [erg/cm^2/s]	$\sigma_{\nu F_\nu}^+$ [erg/cm^2/s]
9.430e+016	1.218e-010	2.176e+016	2.176e+016	2.366e-012	2.366e-012
1.330e+017	1.650e-010	1.693e+016	1.693e+016	3.227e-012	3.227e-012
1.632e+017	1.456e-010	1.330e+016	1.330e+016	2.907e-012	2.907e-012
1.886e+017	1.502e-010	1.209e+016	1.209e+016	2.943e-012	2.943e-012
2.128e+017	1.488e-010	1.209e+016	1.209e+016	2.909e-012	2.909e-012
2.370e+017	1.439e-010	1.209e+016	1.209e+016	2.798e-012	2.798e-012
2.611e+017	1.501e-010	1.209e+016	1.209e+016	2.909e-012	2.909e-012
2.865e+017	1.449e-010	1.330e+016	1.330e+016	2.787e-012	2.787e-012
3.131e+017	1.461e-010	1.330e+016	1.330e+016	2.893e-012	2.893e-012
3.421e+017	1.396e-010	1.572e+016	1.572e+016	2.737e-012	2.737e-012
3.772e+017	1.354e-010	1.934e+016	1.934e+016	2.663e-012	2.663e-012
4.232e+017	1.282e-010	2.660e+016	2.660e+016	2.545e-012	2.545e-012
4.909e+017	1.282e-010	4.111e+016	4.111e+016	2.544e-012	2.544e-012
6.081e+017	1.210e-010	7.617e+016	7.617e+016	2.415e-012	2.415e-012
8.245e+017	1.050e-010	1.402e+017	1.402e+017	2.098e-012	2.098e-012
1.475e+018	8.360e-011	5.102e+017	5.102e+017	1.941e-012	1.941e-012

Table D.30: Spectral energy distribution data from 2006.05.27 by Swift–XRT [T+08a].

ν [Hz]	νF_ν [erg/cm^2/s]	σ_ν^- [Hz]	σ_ν^+ [Hz]	$\sigma_{\nu F_\nu}^-$ [erg/cm^2/s]	$\sigma_{\nu F_\nu}^+$ [erg/cm^2/s]
9.430e+016	1.256e-010	2.176e+016	2.176e+016	2.464e-012	2.464e-012
1.330e+017	1.684e-010	1.693e+016	1.693e+016	3.348e-012	3.348e-012
1.644e+017	1.416e-010	1.451e+016	1.451e+016	2.804e-012	2.804e-012
1.910e+017	1.502e-010	1.209e+016	1.209e+016	2.989e-012	2.989e-012
2.164e+017	1.456e-010	1.330e+016	1.330e+016	2.795e-012	2.795e-012
2.418e+017	1.473e-010	1.209e+016	1.209e+016	2.914e-012	2.914e-012
2.672e+017	1.468e-010	1.330e+016	1.330e+016	2.812e-012	2.812e-012
2.938e+017	1.479e-010	1.330e+016	1.330e+016	2.906e-012	2.906e-012
3.216e+017	1.432e-010	1.451e+016	1.451e+016	2.848e-012	2.848e-012
3.530e+017	1.417e-010	1.693e+016	1.693e+016	2.772e-012	2.772e-012
3.917e+017	1.317e-010	2.176e+016	2.176e+016	2.624e-012	2.624e-012
4.449e+017	1.339e-010	3.143e+016	3.143e+016	2.675e-012	2.675e-012
5.320e+017	1.243e-010	5.561e+016	5.561e+016	2.477e-012	2.477e-012
7.000e+017	1.074e-010	1.124e+017	1.124e+017	2.133e-012	2.133e-012
1.101e+018	9.681e-011	2.890e+017	2.890e+017	1.925e-012	1.925e-012
1.762e+018	7.182e-011	3.712e+017	3.712e+017	3.535e-012	3.535e-012

Table D.31: Spectral energy distribution data from 2006.05.28 by Swift–XRT [T+08a].

ν [Hz]	νF_ν [erg/cm^2/s]	σ_ν^- [Hz]	σ_ν^+ [Hz]	$\sigma_{\nu F_\nu}^-$ [erg/cm^2/s]	$\sigma_{\nu F_\nu}^+$ [erg/cm^2/s]
1.789e+017	5.239e-011	2.989e+016	3.011e+016	1.502e-012	1.502e-012
2.379e+017	5.435e-011	2.694e+016	3.106e+016	1.787e-012	1.787e-012
2.966e+017	5.075e-011	2.458e+016	3.042e+016	2.038e-012	2.038e-012
3.584e+017	5.508e-011	2.835e+016	3.665e+016	2.517e-012	2.517e-012
4.406e+017	5.926e-011	4.158e+016	6.242e+016	2.788e-012	2.788e-012
5.782e+017	6.208e-011	7.119e+016	9.581e+016	3.254e-012	3.254e-012
7.943e+017	5.876e-011	1.113e+017	1.497e+017	3.389e-012	3.389e-012
1.199e+018	5.631e-011	2.401e+017	5.009e+017	3.309e-012	3.309e-012

Table D.32: Spectral energy distribution data from 2007.11.30 by Swift–XRT [B+10c].

D.5 LE and ME Gamma-Ray Observations

ν [Hz]	νF_ν [erg/cm^2/s]	σ_ν^- [Hz]	σ_ν^+ [Hz]	$\sigma_{\nu F_\nu}^-$ [erg/cm^2/s]	$\sigma_{\nu F_\nu}^+$ [erg/cm^2/s]
4.111e+018	6.721e-011	7.254e+017	7.254e+017	7.647e-012	7.647e-012
5.320e+018	5.747e-011	4.836e+017	4.836e+017	8.213e-012	8.213e-012
7.133e+018	5.447e-011	1.330e+018	1.330e+018	6.687e-012	6.687e-012
1.028e+019	3.994e-011	1.813e+018	1.813e+018	7.600e-012	7.600e-012
1.511e+019	3.344e-011	3.022e+018	3.022e+018	9.327e-012	9.327e-012
2.116e+019	2.539e-011	3.022e+018	3.022e+018	1.526e-011	1.526e-011
3.022e+019	2.465e-011	6.045e+018	6.045e+018	2.465e-011	-
4.171e+019	2.911e-010	5.440e+018	5.440e+018	1.349e-010	1.349e-010

Table D.33: Spectral energy distribution data from 2004.11–2006.08 by Swift–BAT (22 months) [T+10e].

ν [Hz]	νF_ν [erg/cm^2/s]	σ_ν^- [Hz]	σ_ν^+ [Hz]	$\sigma_{\nu F_\nu}^-$ [erg/cm^2/s]	$\sigma_{\nu F_\nu}^+$ [erg/cm^2/s]
4.111e+018	6.049e-011	7.254e+017	7.254e+017	3.504e-012	3.504e-012
5.320e+018	5.272e-011	4.836e+017	4.836e+017	4.103e-012	4.103e-012
7.133e+018	4.526e-011	1.330e+018	1.330e+018	4.003e-012	4.003e-012
1.028e+019	3.147e-011	1.813e+018	1.813e+018	4.219e-012	4.219e-012
1.511e+019	3.347e-011	3.022e+018	3.022e+018	5.287e-012	5.287e-012
2.116e+019	2.114e-011	3.022e+018	3.022e+018	8.964e-012	8.964e-012
3.022e+019	2.970e-011	6.045e+018	6.045e+018	2.970e-011	-
4.171e+019	1.498e-010	5.440e+018	5.440e+018	1.498e-010	-

Table D.34: Spectral energy distribution data from 2004.11–2009.08 by Swift–BAT (58 months) [B+10b].

ν [Hz]	νF_ν [erg/cm^2/s]	σ_ν^- [Hz]	σ_ν^+ [Hz]	$\sigma_{\nu F_\nu}^-$ [erg/cm^2/s]	$\sigma_{\nu F_\nu}^+$ [erg/cm^2/s]
5.920e+018	1.470e-011	1.340e+018	1.716e+018	1.250e-011	1.250e-011
9.850e+018	1.680e-011	2.214e+018	2.665e+018	1.290e-011	1.290e-011
1.590e+019	2.450e-011	3.385e+018	4.236e+018	2.310e-011	2.310e-011
2.550e+019	1.850e-011	5.364e+018	8.786e+018	1.740e-011	1.740e-011
4.610e+019	1.230e-010	1.181e+019	1.348e+019	1.180e-010	1.180e-010

Table D.35: Spectral energy distribution data from 2007.11.24–12.01 by Integral–IBIS-ISGRI [B+10c].

ν [Hz]	νF_ν [erg/cm^2/s]	σ_ν^- [Hz]	σ_ν^+ [Hz]	$\sigma_{\nu F_\nu}^-$ [erg/cm^2/s]	$\sigma_{\nu F_\nu}^+$ [erg/cm^2/s]
4.231e+018	4.967e-011	1.112e+018	1.112e+018	7.050e-012	8.171e-012
7.544e+018	1.250e-011	2.225e+018	2.200e+018	2.243e-012	2.243e-012
1.758e+019	6.569e-012	7.858e+018	7.762e+018	-	3.044e-012
7.568e+019	2.179e-011	5.034e+019	5.039e+019	1.202e-011	1.202e-011

Table D.36: Spectral energy distribution data from Integral–IBIS-ISGRI (mean) [W+11b].

ν [Hz]	νF_ν [erg/cm^2/s]	σ_ν^- [Hz]	σ_ν^+ [Hz]	$\sigma_{\nu F_\nu}^-$ [erg/cm^2/s]	$\sigma_{\nu F_\nu}^+$ [erg/cm^2/s]
3.985e+020	1.030e-010	1.744e+020	3.067e+020	1.030e-010	-
1.248e+021	8.300e-011	5.428e+020	9.821e+020	8.300e-011	-
3.985e+021	1.920e-010	1.755e+021	3.101e+021	1.920e-010	-

Table D.37: Spectral energy distribution data from 1991.04–2000.06 by CGRO–Comptel ($2\,\sigma$ upper limits) [Col11c].

D.6 HE Gamma-Ray Observations

ν [Hz]	νF_ν [erg/cm^2/s]	σ_ν^- [Hz]	σ_ν^+ [Hz]	$\sigma_{\nu F_\nu}^-$ [erg/cm^2/s]	$\sigma_{\nu F_\nu}^+$ [erg/cm^2/s]
8.688e+022	1.302e-011	3.303e+022	3.303e+022	2.060e-012	2.060e-012
1.935e+023	1.065e-011	7.357e+022	7.357e+022	1.611e-012	1.611e-012
4.309e+023	7.293e-012	1.638e+023	1.638e+023	1.498e-012	1.498e-012
9.595e+023	6.398e-012	3.648e+023	3.648e+023	1.782e-012	1.782e-012
2.137e+024	8.418e-012	8.125e+023	8.125e+023	2.859e-012	2.859e-012
4.759e+024	1.727e-011	1.809e+024	1.809e+024	5.759e-012	5.759e-012
1.060e+025	1.554e-011	4.029e+024	4.029e+024	7.806e-012	7.806e-012
2.360e+025	4.690e-011	8.973e+024	8.973e+024	4.690e-011	-

Table D.38: Spectral energy distribution data from 2008.08.04–2009.02.01 by Fermi–LAT (LBAS) [A+09c].

ν [Hz]	νF_ν [erg/cm^2/s]	σ_ν^- [Hz]	σ_ν^+ [Hz]	$\sigma_{\nu F_\nu}^-$ [erg/cm^2/s]	$\sigma_{\nu F_\nu}^+$ [erg/cm^2/s]
4.188e+022	1.178e-011	1.770e+022	3.066e+022	1.923e-012	1.923e-012
1.324e+023	1.167e-011	5.990e+022	1.094e+023	1.373e-012	1.373e-012
4.188e+023	9.373e-012	1.770e+023	3.066e+023	9.613e-013	9.613e-013
1.324e+024	8.995e-012	5.990e+023	1.094e+024	1.511e-012	1.511e-012
7.646e+024	1.389e-011	5.228e+024	1.653e+025	2.670e-012	2.670e-012

Table D.39: Spectral energy distribution data from 2008.08.04–2009.07.04 by Fermi–LAT (1FGL) [A+10b].

ν [Hz]	νF_ν [erg/cm^2/s]	σ_ν^- [Hz]	σ_ν^+ [Hz]	$\sigma_{\nu F_\nu}^-$ [erg/cm^2/s]	$\sigma_{\nu F_\nu}^+$ [erg/cm^2/s]
4.188e+022	9.736e-012	1.770e+022	3.066e+022	1.045e-012	1.045e-012
1.324e+023	9.157e-012	5.990e+022	1.094e+023	6.472e-013	6.472e-013
4.188e+023	8.777e-012	1.770e+023	3.066e+023	6.824e-013	6.824e-013
1.324e+024	9.478e-012	5.990e+023	1.094e+024	9.674e-013	9.674e-013
7.646e+024	1.203e-011	5.228e+024	1.653e+025	1.615e-012	1.615e-012

Table D.40: Spectral energy distribution data from 2008.08.04–2010.07.31-Fermi–LAT (2FGL) [The11a].

ν [Hz]	νF_ν [erg/cm^2/s]	σ_ν^- [Hz]	σ_ν^+ [Hz]	$\sigma_{\nu F_\nu}^-$ [erg/cm^2/s]	$\sigma_{\nu F_\nu}^+$ [erg/cm^2/s]
4.298e+022	1.109e-011	1.880e+022	3.343e+022	9.619e-013	9.619e-013
1.359e+023	8.556e-012	5.952e+022	1.059e+023	5.569e-013	5.569e-013
4.298e+023	6.886e-012	1.880e+023	3.343e+023	5.569e-013	5.569e-013
1.359e+024	6.278e-012	5.952e+023	1.059e+024	7.594e-013	7.594e-013
4.298e+024	9.063e-012	1.880e+024	3.343e+024	1.468e-012	1.468e-012
1.359e+025	8.658e-012	5.952e+024	1.059e+025	2.531e-012	2.531e-012
4.298e+025	7.493e-012	1.880e+025	3.343e+025	4.658e-012	4.658e-012

Table D.41: Spectral energy distribution data from 2008.08.04–2010.11.04 by Fermi–LAT (27 months) [G+11].

ν [Hz]	νF_ν [erg/cm^2/s]	σ_ν^- [Hz]	σ_ν^+ [Hz]	$\sigma_{\nu F_\nu}^-$ [erg/cm^2/s]	$\sigma_{\nu F_\nu}^+$ [erg/cm^2/s]
4.300e+023	8.753e-012	1.882e+023	3.346e+023	8.266e-013	8.266e-013
1.360e+024	7.781e-012	5.951e+023	1.058e+024	1.054e-012	1.054e-012
4.300e+024	1.108e-011	1.882e+024	3.347e+024	1.924e-012	1.924e-012
1.360e+025	9.901e-012	5.951e+024	1.058e+025	2.985e-012	2.985e-012
4.300e+025	6.376e-012	1.882e+025	3.346e+025	4.508e-012	4.508e-012

Table D.42: Spectral energy distribution data from 2008.08.04–2010.07.31 by Fermi–LAT (2FGL-HE) [Pan11].

D.7 VHE Gamma-Ray Observations

ν [Hz]	νF_ν [erg/cm^2/s]	σ_ν^- [Hz]	σ_ν^+ [Hz]	$\sigma_{\nu F_\nu}^-$ [erg/cm^2/s]	$\sigma_{\nu F_\nu}^+$ [erg/cm^2/s]
4.643e+025	2.300e-011	1.064e+025	1.378e+025	6.177e-012	6.177e-012
7.810e+025	1.563e-011	1.789e+025	2.297e+025	3.012e-012	3.012e-012
1.311e+026	1.174e-011	2.998e+025	3.869e+025	2.313e-012	2.313e-012
2.200e+026	6.252e-012	5.029e+025	6.504e+025	1.505e-012	1.505e-012
3.695e+026	4.600e-012	8.439e+025	1.093e+026	1.277e-012	1.277e-012

Table D.43: Spectral energy distribution data from 2004 by MAGIC [A+06c, Ton06].

ν [Hz]	νF_ν [erg/cm^2/s]	σ_ν^- [Hz]	σ_ν^+ [Hz]	$\sigma_{\nu F_\nu}^-$ [erg/cm^2/s]	$\sigma_{\nu F_\nu}^+$ [erg/cm^2/s]
4.653e+025	1.087e-011	1.037e+025	1.335e+025	5.920e-012	5.920e-012
7.705e+025	4.699e-012	1.718e+025	2.211e+025	2.150e-012	2.150e-012
1.276e+026	2.593e-012	2.845e+025	3.661e+025	1.275e-012	1.275e-012
2.113e+026	3.263e-012	4.712e+025	6.064e+025	9.611e-013	9.611e-013
3.500e+026	2.477e-012	7.803e+025	1.004e+026	7.025e-013	7.025e-013
5.797e+026	9.918e-013	1.292e+026	1.663e+026	7.560e-013	7.560e-013

Table D.44: Spectral energy distribution data from 2005 by MAGIC [Hay08].

ν [Hz]	νF_ν [erg/cm^2/s]	σ_ν^- [Hz]	σ_ν^+ [Hz]	$\sigma_{\nu F_\nu}^-$ [erg/cm^2/s]	$\sigma_{\nu F_\nu}^+$ [erg/cm^2/s]
4.669e+025	1.399e-011	1.040e+025	1.330e+025	5.483e-012	5.483e-012
7.729e+025	6.127e-012	1.717e+025	2.225e+025	2.058e-012	2.058e-012
1.280e+026	6.426e-012	2.853e+025	3.675e+025	1.261e-012	1.261e-012
2.119e+026	4.784e-012	4.715e+025	6.069e+025	1.203e-012	1.203e-012
3.508e+026	3.860e-012	7.810e+025	1.006e+026	1.029e-012	1.029e-012
5.808e+026	2.191e-012	1.294e+026	1.666e+026	1.021e-012	1.021e-012

Table D.45: Spectral energy distribution data from 2006 by MAGIC [T+08a, Hay08].

ν [Hz]	νF_ν [erg/cm^2/s]	σ_ν^- [Hz]	σ_ν^+ [Hz]	$\sigma_{\nu F_\nu}^-$ [erg/cm^2/s]	$\sigma_{\nu F_\nu}^+$ [erg/cm^2/s]
3.985e+025	1.840e-011	7.009e+024	8.505e+024	1.101e-011	1.101e-011
5.868e+025	8.650e-012	1.032e+025	1.252e+025	2.169e-012	2.169e-012
8.640e+025	6.018e-012	1.520e+025	1.844e+025	1.366e-012	1.366e-012
1.272e+026	5.837e-012	2.237e+025	2.715e+025	1.317e-012	1.317e-012
1.873e+026	3.857e-012	3.294e+025	3.997e+025	1.342e-012	1.342e-012
2.758e+026	4.313e-012	4.850e+025	5.885e+025	1.420e-012	1.420e-012
4.060e+026	2.928e-012	7.141e+025	8.665e+025	1.530e-012	1.530e-012
5.978e+026	3.067e-012	1.051e+026	1.276e+026	1.618e-012	1.618e-012

Table D.46: Spectral energy distribution data from 2007 by MAGIC [Uel09].

ν [Hz]	νF_ν [erg/cm^2/s]	σ_ν^- [Hz]	σ_ν^+ [Hz]	$\sigma_{\nu F_\nu}^-$ [erg/cm^2/s]	$\sigma_{\nu F_\nu}^+$ [erg/cm^2/s]
6.050e+025	5.047e-012	1.214e+025	1.519e+025	3.406e-012	3.406e-012
9.469e+025	3.511e-012	1.900e+025	2.377e+025	2.039e-012	2.039e-012
1.482e+026	3.184e-012	2.974e+025	3.720e+025	2.055e-012	2.055e-012
2.319e+026	2.409e-012	4.654e+025	5.822e+025	2.092e-012	2.092e-012

Table D.47: Spectral energy distribution data from 2008 by MAGIC [Uel12].

ν [Hz]	νF_ν [erg/cm^2/s]	σ_ν^- [Hz]	σ_ν^+ [Hz]	$\sigma_{\nu F_\nu}^-$ [erg/cm^2/s]	$\sigma_{\nu F_\nu}^+$ [erg/cm^2/s]
5.935e+025	6.466e-012	1.582e+025	2.158e+025	1.680e-012	1.680e-012
1.103e+026	6.725e-012	2.942e+025	4.012e+025	1.124e-012	1.124e-012
2.052e+026	3.869e-012	5.471e+025	7.460e+025	1.116e-012	1.116e-012
3.815e+026	2.613e-012	1.017e+026	1.387e+026	1.217e-013	1.217e-013
7.093e+026	2.485e-012	1.891e+026	2.579e+026	1.282e-012	1.282e-012

Table D.48: Spectral energy distribution data from 2009 by MAGIC [Uel12].

ν [Hz]	νF_ν [erg/cm^2/s]	σ_ν^- [Hz]	σ_ν^+ [Hz]	$\sigma_{\nu F_\nu}^-$ [erg/cm^2/s]	$\sigma_{\nu F_\nu}^+$ [erg/cm^2/s]
2.902e+026	6.575e-012	5.223e+025	6.529e+025	1.813e-012	1.813e-012
4.352e+026	6.593e-012	7.979e+025	9.575e+025	7.838e-013	7.838e-013
6.480e+026	3.211e-012	1.170e+026	1.436e+026	4.511e-013	4.511e-013
9.672e+026	8.947e-013	1.755e+026	2.034e+026	3.999e-013	3.999e-013
1.417e+027	4.500e-013	2.464e+026	3.105e+026	3.417e-013	3.417e-013
2.106e+027	3.829e-013	3.787e+026	4.650e+026	3.634e-013	3.634e-013
3.139e+027	1.112e-012	5.675e+026	6.889e+026	1.023e-012	1.023e-012

Table D.49: Spectral energy distribution data from 2002 by Hegra CT1 [Ton06].

ν [Hz]	νF_ν [erg/cm^2/s]	σ_ν^- [Hz]	σ_ν^+ [Hz]	$\sigma_{\nu F_\nu}^-$ [erg/cm^2/s]	$\sigma_{\nu F_\nu}^+$ [erg/cm^2/s]
4.594e+026	3.008e-012	5.126e+025	5.682e+025	8.676e-013	8.676e-013
5.803e+026	2.123e-012	6.408e+025	6.843e+025	6.460e-013	6.460e-013
7.254e+026	1.442e-012	7.665e+025	9.092e+025	5.768e-013	5.768e-013
9.188e+026	1.180e-012	1.025e+026	1.245e+026	4.627e-013	4.627e-013
1.185e+027	4.232e-013	1.415e+026	1.480e+026	3.847e-013	3.847e-013
1.499e+027	4.927e-013	1.664e+026	1.881e+026	4.311e-013	4.311e-013

Table D.50: Spectral energy distribution data from 2000–2002 HEGRA (Götting) [Göt06].

ν [Hz]	νF_ν [erg/cm^2/s]	σ_ν^- [Hz]	σ_ν^+ [Hz]	$\sigma_{\nu F_\nu}^-$ [erg/cm^2/s]	$\sigma_{\nu F_\nu}^+$ [erg/cm^2/s]
3.840e+026	4.042e-012	7.907e+025	1.001e+026	6.995e-013	8.460e-013
6.103e+026	2.729e-012	1.262e+026	1.567e+026	3.550e-013	2.716e-013
9.641e+026	1.583e-012	1.971e+026	2.503e+026	2.573e-013	1.716e-013
1.530e+027	8.243e-013	3.153e+026	3.997e+026	2.462e-013	2.445e-013
2.434e+027	4.320e-013	5.044e+026	6.321e+026	2.113e-013	2.160e-013

Table D.51: Spectral energy distribution data from 2000–2002 HEGRA [A+03a].

D.8 VHE Gamma-Ray Flare Observations

ν [Hz]	νF_ν [erg/cm^2/s]	σ_ν^- [Hz]	σ_ν^+ [Hz]	$\sigma_{\nu F_\nu}^-$ [erg/cm^2/s]	$\sigma_{\nu F_\nu}^+$ [erg/cm^2/s]
9.261e+025	6.463e-010	1.620e+025	1.959e+025	2.350e-010	2.350e-010
1.359e+026	1.812e-010	2.370e+025	2.877e+025	1.063e-010	1.063e-010
1.835e+026	1.892e-010	5.658e+025	8.124e+025	6.922e-011	6.922e-011
1.997e+026	1.782e-010	3.506e+025	4.207e+025	7.433e-011	7.433e-011
2.418e+026	1.527e-010	7.447e+025	1.078e+026	8.812e-011	8.812e-011
2.926e+026	1.893e-010	5.078e+025	6.238e+025	5.630e-011	5.630e-011
3.820e+026	1.380e-010	1.173e+026	1.710e+026	3.680e-011	3.680e-011
4.304e+026	1.254e-010	7.544e+025	9.067e+025	4.873e-011	4.873e-011
5.054e+026	1.624e-010	1.557e+026	2.254e+026	5.389e-011	5.389e-011
6.311e+026	3.525e-011	1.100e+026	1.335e+026	4.147e-011	4.147e-011
8.004e+026	1.260e-010	2.474e+026	3.569e+026	3.511e-011	3.511e-011
9.261e+026	5.547e-011	1.615e+026	1.956e+026	3.760e-011	3.760e-011
1.057e+027	1.680e-010	3.259e+026	4.698e+026	4.284e-011	4.284e-011
1.359e+027	9.260e-011	2.372e+026	2.885e+026	3.340e-011	3.340e-011
1.673e+027	4.412e-011	5.160e+026	7.489e+026	2.532e-011	2.532e-011
1.997e+027	4.744e-011	3.499e+026	4.200e+026	3.389e-011	3.389e-011
2.205e+027	1.234e-010	6.787e+026	9.861e+026	3.465e-011	3.465e-011
2.926e+027	2.932e-011	5.085e+026	6.229e+026	2.580e-011	2.580e-011
3.506e+027	5.390e-012	1.084e+027	1.563e+027	1.415e-011	1.415e-011
4.304e+027	1.924e-011	7.554e+026	9.109e+026	1.371e-011	1.371e-011
4.618e+027	1.303e-011	1.427e+027	2.059e+027	3.390e-011	3.390e-011

Table D.52: Spectral energy distribution data from 2002.05 by Whipple 10 m high [D+05].

ν [Hz]	νF_ν [erg/cm^2/s]	σ_ν^- [Hz]	σ_ν^+ [Hz]	$\sigma_{\nu F_\nu}^-$ [erg/cm^2/s]	$\sigma_{\nu F_\nu}^+$ [erg/cm^2/s]
3.675e+026	9.254e-011	4.836e+025	5.610e+025	1.851e-011	1.851e-011
4.884e+026	5.557e-011	6.480e+025	7.423e+025	1.046e-011	1.046e-011
6.480e+026	4.603e-011	8.536e+025	9.769e+025	8.055e-012	8.055e-012
8.584e+026	6.057e-011	1.127e+026	1.294e+026	8.077e-012	8.077e-012
1.136e+027	4.601e-011	1.487e+026	1.719e+026	1.062e-011	1.062e-011
1.506e+027	2.798e-011	1.980e+026	2.270e+026	7.462e-012	7.462e-012
1.995e+027	1.200e-011	2.614e+026	3.022e+026	5.452e-012	5.452e-012
2.645e+027	1.342e-011	3.482e+026	4.004e+026	5.753e-012	5.753e-012

Table D.53: Spectral energy distribution data from 2002.05 by HEGRA high [A+03a].

ν [Hz]	νF_ν [erg/cm^2/s]	σ_ν^- [Hz]	σ_ν^+ [Hz]	$\sigma_{\nu F_\nu}^-$ [erg/cm^2/s]	$\sigma_{\nu F_\nu}^+$ [erg/cm^2/s]
1.364e+026	2.647e-010	2.370e+025	2.877e+025	8.331e-011	1.026e-010
2.000e+026	2.479e-010	3.482e+025	4.231e+025	5.999e-011	6.308e-011
2.933e+026	2.017e-011	5.126e+025	6.190e+025	2.017e-011	4.409e-011
4.304e+026	9.972e-011	7.496e+025	9.164e+025	3.793e-011	3.520e-011
6.333e+026	4.883e-011	1.112e+026	1.327e+026	3.311e-011	2.998e-011
9.266e+026	5.569e-011	1.606e+026	1.949e+026	2.449e-011	2.557e-011
1.357e+027	5.473e-011	2.360e+026	2.882e+026	2.249e-011	2.121e-011
1.995e+027	3.564e-012	3.492e+026	4.212e+026	3.564e-012	2.251e-011

Table D.54: Spectral energy distribution data from 2002.06.04 by Whipple 10 m flare [D+05].

Glossary of Abbreviations

Abbreviation	Meaning
2MASS	**2 M**icron **A**ll **S**ky **S**urvey
ADC	**A**nalog to **D**igital **C**onverter
AGASA	**A**keno **G**iant **A**ir **S**hower **A**rray
AGILE	**A**strorivelatore **G**amma a **I**mmagini **Le**ggero, *ital.:* Light Imager for Gamma-ray Astrophysics
AGN	**A**ctive **G**alactic **N**ucleus
AIT	**A**utomatic **I**maging **T**elescope
AMANDA	**A**ntarctic **M**uon **A**nd **N**eutrino **D**etector **A**rray
ARGOS	**A**dvanced **R**esearch and **G**lobal **O**bservation **S**atellite
ASM	**A**ll-**S**ky **M**onitor
BAT	**B**urst **A**lert **T**elescope
BBH	**B**inary **B**lack **H**ole
BH	**B**lack **H**ole
CANGAROO	**C**ollaboration of **A**ustralia and **N**ippon (Japan) for a **GA**mma **R**ay **O**bservatory in the **O**utback
CAT	**C**herenkov **A**rray at **T**hémis
CCD	**C**harge **C**oupled **D**evice
CGRO	**C**ompton **G**amma-**R**ay **O**bservatory
CMB	**C**osmic **M**icrowave **B**ackground
COMPTEL	Imaging **Compt**on **Tel**escope
CREAM	**C**osmic **R**ay **E**nergy **A**nd **M**ass
CTA	**C**herenkov **T**elescope **A**rray
DAQ	**D**ata **AQ**uisition
DRS	**D**omino **R**ing **S**ampling chip
DWARF	**D**edicated **W**orldwide **A**GN **R**esearch **F**acility
EBL	**E**xtragalactic **B**ackground **L**ight
EC	**E**xternal **C**ompton
EGRET	**E**nergetic **G**amma **R**ay **E**xperiment **T**elescope
EPIC	**E**uropean **P**hoton **I**maging **C**amera
FACT	**F**irst G-**A**PD **C**herenkov **T**elescope
FADC	**F**lash **A**nalog to **D**igital **C**onverter
F-GAMMA	**F**ermi–**G**ST **A**GN **M**ulti-frequency **M**onitoring **A**lliance
FGST or Fermi	**F**ermi **G**amma-ray **S**pace **T**elescope
FoV	**F**ield **o**f **V**iew
FSRQ	**F**lat **S**pectrum **R**adio **Q**uasar

Abbreviation	Meaning
FUV	**F**ar **U**ltra**v**iolet
GALEX	**Gal**axy **E**volution E**x**plorer
G-APD	**G**eiger-mode **A**valanche **P**hoto**d**iode
GBT 91 m	91 m **G**reen **B**ank **T**elescope
GRB	**G**amma-**R**ay **B**urst
GRID	**G**amma-**R**ay **I**maging **D**etector
GRT	**G**oddard **R**obotic **T**elescope
GZK	**G**reisen-**Z**atsepin-**K**uzmin
H.E.S.S.	**H**igh **E**nergy **S**tereoscopic **S**ystem
HAWC	**H**igh **A**ltitude **W**ater **C**herenkov Experiment
HBL	**H**igh-frequency peaked **BL** **L**ac object
HEAO 2	**H**igh **E**nergy **A**stronomy **O**bservatory 2
HEAVENS	**H**igh-**E**nergy **A**strophysics **V**irtually **En**lightened **S**ky
HEGRA	**H**igh **E**nergy **G**amma **R**ay **A**stronomy
HEXTE	**H**igh **E**nergy **X**-ray **T**iming **E**xperiment
HiRes	**Hi**gh **Res**olution Fly's Eye Detector
HST	**H**ubble **S**pace **T**elescope
IACT	**I**maging **A**tmospheric **C**herenkov **T**elescope
IBIS	**I**mager on-**B**oard the **I**NTEGRAL **S**atellite
IFAM	Fraunhofer-**I**nstitut für **F**ertigungstechnik und **A**ngewandte **M**aterialforschung, *ger.:* Fraunhofer Institute for Manufacturing Technology and Applied Materials Research
INTEGRAL	**Inte**rnational **G**amma-**R**ay **A**strophysics **L**aboratory
IRAM	**I**nstitut de **R**adio**a**stronomie **M**illimétrique
IRS	**I**nfra**R**ed **S**pectrograph
ISGRI	**I**NTEGRAL **S**oft **G**amma-**R**ay **I**mager
JEM-X	**J**oint **E**uropean X-Ray **M**onitor
KM3NeT	**km**^{3} **Ne**utrino **T**elescope
LAT	**L**arge **A**rea **T**elescope
LBAS	**L**AT **B**right **A**GN **S**ample
LBL	**L**ow-frequency peaked **BL** **L**ac object
LECS	**L**ow **E**nergy **C**oncentrator **S**pectrometer
LISA	**L**aser **I**nterferometer **S**pace **A**ntenna
MAGIC	**M**ajor **A**tmospheric **G**amma **I**maging **C**herenkov telescopes
MAXI	**M**onitor of **A**ll-sky **X**-ray **I**mage
MECS	**M**edium **E**nergy **C**oncentrator **S**pectrometer
MHD	**M**agneto**h**ydro**d**ynamics
MOS	**M**etal **O**xide **S**emi-conductor
MWL	**M**ulti-**W**ave**l**ength
NASA	**N**ational **A**eronautics and **S**pace **A**dministration
NED	**N**ASA/IPAC **E**xtragalactic **D**atabase
NMS	**N**ew **M**exico **S**kies
NOT	**N**ordic **O**ptical **T**elescope

Abbreviation	Meaning
NSB	**N**ight-**s**ky **b**ackground
NUV	**N**ear **U**ltra**v**iolet
OMC	**O**ptical **M**onitoring **C**amera
OMEGA	**O**bservatorio **ME**xicano de **GA**mmas, *mex.* Mexican Observatory of Gammas
OVRO	**O**wens **V**alley **R**adio **O**bservatory
PAO	**P**ierre **A**uger **O**bservatory
PCA	**P**roportional **C**ounter **A**rray
PDE	**P**hoton **D**etection **E**fficiency
PDS	**P**hoswich **D**etector **S**ystem
PMT	**P**hoto**m**ultiplier **T**ube
PSF	**P**oint **S**pread **F**unktion
PWN	**P**ulsar **W**ind **N**ebula
QE	**Q**uantum **E**fficiency
QSO	**Q**uasi **S**tellar **O**bject
RATAN	RATAN *rus.:* Academy of Science Radio Telescope
ROSAT	**Rö**ntgen**sat**ellit *ger.:* X-ray Satellite
RXTE	**R**ossi **X**-ray **T**iming **E**xplorer
SAX	**S**atellite per **A**stronomia **X**, *ital.:* X-Ray Astronomy Satellite
SED	**S**pectral **E**nergy **D**istribution
SiPM	**Si**lizium **P**hoto**M**ultiplier
SUPERKAMIOKANDE	**Super Kamioka n**ucleon **d**ecay **e**xperiment
SMBH	**S**uper**M**assive **B**lack **H**ole
SNO	**S**udbury **N**eutrino **O**bservatory
SNR	**S**uper**n**ova **R**emnant
SSC	**S**ynchrotron **S**elf **C**ompton
SST	**S**pitzer **S**pace **T**elescope
TA	**T**elescope **A**rray
TACTIC	**T**eV **A**tmospheric **C**herenkov **T**elescope with **I**maging **C**amera
ToO	**T**arget **o**f **O**pportunity
UMRAO	**U**niversity of **M**ichigan **R**adio **A**stronomy **O**bservatory
USA	**U**nconventional **S**tellar **A**spect
UTRAO	**U**niversity of **T**exas **R**adio **A**stronomy **O**bservatory
UVOT	**U**ltra**v**iolet/**O**ptical **T**elescope
VERITAS	**V**ery **E**nergetic **R**adiation **I**maging **T**elescope
VHE	**V**ery **H**igh **E**nergy
VLA	**V**ery **L**arge **A**rray
VLBA	**V**ery **L**ong **B**aseline **A**rray
VLBI	**V**ery **L**ong **B**aseline **I**nterferrometry
WFC	**W**ide **F**ield **C**amera
WFPC2	**W**ide **F**ield **P**lanetary **C**amera **2**
WIYN	University of **W**isconsin, **I**ndiana University, **Y**ale University, and **N**ational Optical Astronomy Observatory (NOAO)

Abbreviation	Meaning
WSRT	**W**esterbork **S**ynthesis **R**adio **T**elescope
XMM-Newton	**X**-ray **M**ulti-Mirror **M**ission-**Newton**
XRB	**X**-**R**ay **B**inary
XRT	**X**-**R**ay **T**elescope

List of Figures

List of Tables

Bibliography

The references are appearing in the alphabetic order of the abbreviations and thus not necessarily in the alphabetic order of the name of the first author. The last numbers refer back to the pages of citations within this thesis.

[A+03a] F. Aharonian et al. Detection of TeV gamma-rays from the BL Lac 1ES 1959+650 in its low states and during a major outburst in 2002. *Astronomy & Astrophysics*, 406:L9, July 2003. 78, 85, 193, 194

[A+03b] H. D. Aller et al. The University of Michigan Radio Variability Program. In *American Astronomical Society Meeting Abstracts #202*, volume 35 of *Bulletin of the American Astronomical Society*, page 723, May 2003. 26

[A+05a] M. Ackermann et al. Multiwavelength comparison of selected neutrino point source candidates. In *29th International Cosmic Ray Conference*, volume 5 of *International Cosmic Ray Conference*, page 1, 2005. 78

[A+05b] F. Aharonian et al. H.E.S.S. observations of PKS 2155-304. *Astronomy & Astrophysics*, 430:865–875, February 2005, arXiv:astro-ph/0411582. 115

[A+06a] R. U. Abbasi et al. Search for Cross-Correlations of Ultrahigh-Energy Cosmic Rays with BL Lacertae Objects. *Astrophysical Journal*, 636:680–684, January 2006, arXiv:astro-ph/0507120. 79

[A+06b] F. Aharonian et al. A low level of extragalactic background light as revealed by γ-rays from blazars. *Nature*, 440:1018–1021, April 2006, arXiv:astro-ph/0508073. 16

[A+06c] J. Albert et al. Observation of Very High Energy Gamma-Ray Emission from the Active Galactic Nucleus 1ES 1959+650 Using the MAGIC Telescope. *Astrophysical Journal*, 639:761–765, March 2006, arXiv:astro-ph/0508543. 78, 156, 191

[A+07a] J. Abraham et al. Correlation of the highest energy cosmic rays with nearby extragalactic objects. *Science*, 318:938, 2007. arXiv:astro-ph/0711.2256. 10

[A+07b] M. Ackermann et al. The MAGIC/IceCube Target of Opportunity Program test run. *Astronomische Nachrichten*, 328:605, September 2007. 79

[A+07c] F. Aharonian et al. An Exceptional Very High Energy Gamma-Ray Flare of PKS 2155-304. *Astrophysical Journal Letters*, 664:L71–L74, August 2007, 0706.0797. 19

[A+07d] J. Albert et al. Observation of Very High Energy γ-Rays from the AGN 1ES 2344+514 in a Low Emission State with the MAGIC Telescope. *Astrophysical Journal*, 662:892–899, June 2007, arXiv:astro-ph/0612383. 115

[A+07e] J. Albert et al. Observations of Markarian 421 with the MAGIC Telescope. *Astrophysical Journal*, 663:125–138, July 2007, arXiv:astro-ph/0603478. 65, 115

[A+07f] J. Albert et al. Variable Very High Energy γ-Ray Emission from Markarian 501. *Astrophysical Journal*, 669:862–883, November 2007, arXiv:astro-ph/0702008. 19, 65, 115

[A+07g] J. Albert et al. Very high energy gamma-ray observations during moonlight and twilight with the MAGIC telescope. *Astroparticle Physics*, February 2007, arXiv:astro-ph/0702475. Submitted for publication. 39

[A+08a] R. U. Abbasi et al. First Observation of the Greisen-Zatsepin-Kuzmin Suppression. *Physical Review Letters*, 100(10):101101–+, March 2008, arXiv:astro-ph/0703099. 9

[A+08b] R. U. Abbasi et al. Search for correlations between HiRes stereo events and active galactic nuclei. *Astroparticle Physics*, 30:175–179, November 2008, 0804.0382. 11

[A+08c] J. Abraham et al. Correlation of the highest-energy cosmic rays with the positions of nearby active galactic nuclei. *Astroparticle Physics*, 29:188–204, April 2008, 0712.2843. 10

[A+08d] J. Abraham et al. Observation of the Suppression of the Flux of Cosmic Rays above $4{\times}10^{19}$ eV. *Physical Review Letters*, 101(6):061101–+, August 2008, 0806.4302. 9

[A+08e] M. Ackermann et al. Neutrino Triggered Target of Opportunity (NToO) test run with AMANDA-II and MAGIC. In *30th International Cosmic Ray Conference*, volume 3 of *International Cosmic Ray Conference*, pages 1257–1260, 2008, 0709.2640. 79

[A+08f] F. Aharonian et al. High energy astrophysics with ground-based gamma ray detectors. *Reports on Progress in Physics*, 71(9):096901–+, September 2008. 33

[A+08g] J. Albert et al. Implementation of the random forest method for the imaging atmospheric cherenkov telescope magic. *Nuclear Instruments and Methods in Physics Research Section A: Accelerators, Spectrometers, Detectors and Associated Equipment*, 588(3):424–432, 2008. 42

[A+08h] J. Albert et al. Very-High-Energy gamma rays from a Distant Quasar: How Transparent Is the Universe? *Science*, 320:1752–, June 2008, 0807.2822. 16

[A+08i] J. Albert et al. VHE γ-Ray Observation of the Crab Nebula and its Pulsar with the MAGIC Telescope. *Astrophysical Journal*, 674:1037–1055, February 2008, 0705.3244. 38, 115

[A+08j] E. Angelakis et al. Monitoring the radio spectra of selected blazars in the Fermi-GST era . The Effelsberg 100-m telescope covering the cm band. *Memorie della Societá Astronomica Italiana*, 79:1042–+, 2008, 0809.3912. 26

[A+09a] R. Abbasi et al. First Neutrino Point-Source Results from the 22 String Icecube Detector. *Astrophysical Journal Letters*, 701:L47–L51, August 2009, 0905.2253. 79

[A+09b] R. Abbasi et al. Search for point sources of high energy neutrinos with final data from AMANDA-II. *Physical Review D*, 79(6):062001, March 2009, 0809.1646. 79

[A+09c] A. A. Abdo et al. Bright Active Galactic Nuclei Source List from the First Three Months of the Fermi Large Area Telescope All-Sky Survey. *Astrophysical Journal*, 700:597–622, July 2009, 0902.1559. 77, 189

[A+09d] A. A. Abdo et al. Fermi Observations of TeV-Selected Active Galactic Nuclei. *Astrophysical Journal*, 707:1310–1333, December 2009, 0910.4881. 77

[A+09e] V. A. Acciari et al. Radio Imaging of the Very-High-Energy γ-Ray Emission Region in the Central Engine of a Radio Galaxy. *Science*, 325:444–, July 2009, 0908.0511. 17

[A+09f] V. A. Acciari et al. Simultaneous Multiwavelength Observations of Markarian 421 During Outburst. *Astrophysical Journal*, 703:169–178, September 2009, 0907.3923. 65

[A+09g] R. Alfaro et al. A High Altitude Mexican ACT Project, OMEGA. In *31st International Cosmic Ray Conference, Łódź, Poland*, International Cosmic Ray Conference, page 0868, July 2009. Published online: http://icrc2009.uni.lodz.pl/proc/html. 113

[A+09h] E. Aliu et al. Improving the performance of the single-dish Cherenkov telescope MAGIC through the use of signal timing. *Astroparticle Physics*, 30:293–305, January 2009, 0810.3568. 39, 48

[A+09i] H. Anderhub et al. A novel camera type for very high energy gamma-ray astronomy based on Geiger-mode avalanche photodiodes. *Journal of Instrumentation*, 4:P10010, October 2009, 0911.4920. 47

[A+09j] H. Anderhub et al. Simultaneous Multiwavelength Observation of Mkn 501 in a Low State in 2006. *Astrophysical Journal*, 705:1624–1631, November 2009, 0910.2093. 65

[A+09k] W. B. Atwood et al. The Large Area Telescope on the Fermi Gamma-Ray Space Telescope Mission. *Astrophysical Journal*, 697:1071–1102, June 2009, 0902.1089. 31

[A+10a] R. U. Abbasi et al. Indications of Proton-Dominated Cosmic-Ray Composition above 1.6 EeV. *Physical Review Letters*, 104(16):161101–+, April 2010, 0910.4184. 5, 6

[A+10b] A. A. Abdo et al. Fermi Large Area Telescope First Source Catalog. *Astrophysical Journal Supplements*, 188:405–436, June 2010, 1002.2280. 77, 189

[A+10c] A. A. Abdo et al. Gamma-ray Light Curves and Variability of Bright Fermi-detected Blazars. *Astrophysical Journal*, 722:520–542, October 2010, 1004.0348. 77, 155

[A+10d] A. A. Abdo et al. Spectral Properties of Bright Fermi-Detected Blazars in the Gamma-Ray Band. *Astrophysical Journal*, 710:1271–1285, February 2010. 77

[A+10e] A. A. Abdo et al. The Spectral Energy Distribution of Fermi Bright Blazars. *Astrophysical Journal*, 716:30–70, June 2010, 0912.2040. 70, 98

[A+10f] J. Abraham et al. Measurement of the energy spectrum of cosmic rays above 10^{18} eV using the Pierre Auger Observatory. *Physics Letters B*, 685:239–246, March 2010, 1002.1975. 9

[A+10g] P. Abreu et al. Update on the correlation of the highest energy cosmic rays with nearby extragalactic matter. *Astroparticle Physics*, 34:314–326, December 2010, 1009.1855. 11

[A+10h] J. Aleksić et al. MAGIC TeV gamma-ray observations of Markarian 421 during multiwavelength campaigns in 2006. *Astronomy & Astrophysics*, 519:A32+, September 2010, 1001.1291. 65

[A+11a] R. Abbasi et al. Limits on Neutrino Emission from Gamma-Ray Bursts with the 40 String IceCube Detector. *Physical Review Letters*, 106(14):141101–+, April 2011, 1101.1448. 12

[A+11b] R. Abbasi et al. Measurement of the atmospheric neutrino energy spectrum from 100 GeV to 400 TeV with IceCube. *Physical Review D*, 83(1):012001–+, January 2011, 1010.3980. 12

[A+11c] R. Abbasi et al. Time-Dependent Searches for Point Sources of Neutrinos with the 40-String and 22-String Configurations of IceCube. *ArXiv e-prints*, April 2011, 1104.0075. 79

[A+11d] R. Abbasi et al. Time-integrated Searches for Point-like Sources of Neutrinos with the 40-string IceCube Detector. *Astrophysical Journal*, 732:18, May 2011, 1012.2137. 12, 79

[A+11e] A. A. Abdo et al. Fermi Large Area Telescope Observations of Markarian 421: The Missing Piece of its Spectral Energy Distribution. *Astrophysical Journal*, 736:131–+, August 2011, 1106.1348. 19, 101

[A+11f] A. A. Abdo et al. Insights into the High-energy γ-ray Emission of Markarian 501 from Extensive Multifrequency Observations in the Fermi Era. *Astrophysical Journal*, 727:129–+, February 2011, 1011.5260. 20, 101

[A+11g] V. A. Acciari et al. Spectral Energy Distribution of Markarian 501: Quiescent State Versus Extreme Outburst. *Astrophysical Journal*, 729:2–+, March 2011, 1012.2200. 19, 65, 101

[A+11h] P. A. R. Ade et al. Planck early results: first assessment of the High Frequency Instrument in-flight performance. *Astronomy & Astrophysics*, January 2011, 1101.2039. 27

[A+11i] P. A. R. Ade et al. Planck Early Results: The Planck mission. *Astronomy & Astrophysics*, January 2011, 1101.2022. 27

[A+11j] I. Agudo et al. Gamma-ray emission region located in the parsec scale jet of OJ287. *Journal of Physics: Conference Series*, August 2011, 1108.0925. Submitted for publication in the proceedings of the workshop "Beamed and Unbeamed Gamma-rays from Galaxies". 17

[A+11k] J. Aleksić et al. Performance of the MAGIC stereo system obtained with Crab Nebula data. *Astroparticle Physics*, August 2011, 1108.1477. Submitted for publication. 39

[A+11l] E. Aliu et al. Multiwavelength Observations of the Previously Unidentified Blazar RX J0648.7+1516. *Astrophysical Journal*, 742:127, December 2011, 1110.5949. 101

[A+11m] V. Allevato et al. The XMM-Newton Wide Field Survey in the COSMOS Field: Redshift Evolution of AGN Bias and Subdominant Role of Mergers in Triggering Moderate-luminosity AGNs at Redshifts up to 2.2. *Astrophysical Journal*, 736:99–+, August 2011, 1105.0520. 20

[A+11n] H. Anderhub et al. A G-APD based Camera for Imaging Atmospheric Cherenkov Telescopes. *Nuclear Instruments and Methods in Physics Research A*, 628:107–110, February 2011. 48

[A+11o] H. Anderhub et al. Electronics for the camera of the First G-APD Cherenkov Telescope (FACT) for ground based gamma-ray astronomy. In *32nd International Cosmic Ray Conference, Beijing, China*, International Cosmic Ray Conference, page 0389, August 2011. 48

[A+11p] H. Anderhub et al. Electronics for the camera of the First G-APD Cherenkov Telescope (FACT) for ground based gamma-ray astronomy. *Journal of Instrumentation*, page P11141, October 2011. Submitted for publication. 48

[A+11q] H. Anderhub et al. Results of the prototype camera for FACT. *Nuclear Instruments and Methods in Physics Research A*, 639:55–57, May 2011. 47

[Ack07] M. Ackermann. Upper limits on neutrino fluxes from point-like sources with AMANDA-II. *Astrophysics and Space Science*, 309:421–427, June 2007. 79

[Aha04] Felix A. Aharonian. *Very High Energy Cosmic Gamma Radiation – A Crutial Window on the Extreme Universe*. World Scientific Publishing Co.Pte. Ltd., 2004. 3

[Alf11] L. Alfredo Anchordoqui. Ultrahigh Energy Cosmic Rays: Facts, Myths, and Legends. *CERN Yellow Report*, April 2011, 1104.0509. Lectures given at the 6^th CERN-Latin-American School of High-Energy Physics, Natal, Brazil, March - April, 2011: http://physicschool.web.cern.ch/PhysicSchool/CLASHEP/CLASHEP2011. Submitted for publication. 3

[Arg00] S. Argiro. *The fluorescence detector of the Pierre Auger Cosmic Ray Observatory and its readout electronics*. PhD thesis, Universita degli Studi di Milano, November 2000. 11

[Ast07] Astroteilchenphysik Deutschland. Official website, November 2007. http://www.astroteilchenphysik.de. 38

[B+97] G. Boella et al. The medium-energy concentrator spectrometer on board the BeppoSAX X-ray astronomy satellite. *Astronomy and Astrophysics Supplement*, 122:327–340, April 1997. 30

[B+02] V. Beckmann et al. BeppoSAX spectral survey of BL Lacs - New spectra and results. *Astronomy & Astrophysics*, 383:410–422, February 2002, arXiv:astro-ph/0112311. 73, 98, 105

[B+03a] K. Bernlöhr et al. The optical system of the H.E.S.S. imaging atmospheric Cherenkov telescopes. Part I: layout and components of the system. *Astroparticle Physics*, 20:111–128, November 2003, arXiv:astro-ph/0308246. 51

[B+03b] D. Bettoni et al. The black hole mass of low redshift radiogalaxies. *Astronomy & Astrophysics*, 399:869–878, March 2003, arXiv:astro-ph/0212162. 68

[B+04a] C. Baixeras et al. Commissioning and first tests of the MAGIC telescope. *Nuclear Instruments and Methods in Physics Research A*, 518:188–192, February 2004. 38

[B+04b] C. Bigongiari et al. The MAGIC telescope reflecting surface. *Nuclear Instruments and Methods in Physics Research A*, 518(1-2):193–194, 2004. Proc. Frontier Detectors for Frontier Physics. 51

[B+04c] R. K. Bock et al. Methods for multidimensional event classification: a case study using images from a Cherenkov gamma-ray telescope. *Nuclear Instruments and Methods in Physics Research A*, 516:511–528, January 2004. 42

[B+04d] M. Bondi et al. VLBA polarization observations of BL Lac objects and passive elliptical galaxies. *Monthly Notices of the Royal Astronomical Society*, 352:112–124, July 2004. 69, 71

[B+04e] C. Budtz-Jørgensen et al. JEM-X: the x-ray monitor on INTEGRAL. In K. A. Flanagan & O. H. W. Siegmund, editor, *Society of Photo-Optical Instrumentation Engineers (SPIE) Conference Series*, volume 5165 of *Society of Photo-Optical Instrumentation Engineers (SPIE) Conference Series*, pages 139–150, February 2004. 30

[B+05a] S. D. Barthelmy et al. The Burst Alert Telescope (BAT) on the SWIFT Midex Mission. *Space Science Reviews*, 120:143–164, October 2005, arXiv:astro-ph/0507410. 30

[B+05b] M. Błażejowski et al. A Multiwavelength View of the TeV Blazar Markarian 421: Correlated Variability, Flaring, and Spectral Evolution. *Astrophysical Journal*, 630:130–141, September 2005, arXiv:astro-ph/0505325. 19

[B+05c] T. Bretz et al. MAGIC - Roadmap to a standard analysis. In F. A. Aharonian, H. J. Völk, and D. Horns, editors, *High Energy Gamma-Ray Astronomy*, volume 745 of *American Institute of Physics Conference Series*, pages 730–735, February 2005. 58

[B+05d] D. N. Burrows et al. The Swift X-Ray Telescope. *Space Science Reviews*, 120:165–195, October 2005, arXiv:astro-ph/0508071. 29

[B+06a] J. G. Baker et al. Gravitational-Wave Extraction from an Inspiraling Configuration of Merging Black Holes. *Physical Review Letters*, 96(11):111102, March 2006. arXiv:gr-qc/0511103. 21

[B+06b] K. Bammel et al. *Der Brockhaus Astronomie*. F. A. Brockhaus, 2006. 13, 16, 17

[B+07a] M. Backes et al. Long term monitoring of bright TeV Blazars with the MAGIC Telescope. *Astronomische Nachrichten*, 328:677, July 2007. 66

[B+07b] V. Beckmann et al. Swift and INTEGRAL observation of 1ES 1959+650. *The Astronomer's Telegram*, 1317:1, December 2007. 75

[B+07c] A. Biland et al. First detection of Cherenkov light from cosmic-particle-induced air showers by Geiger-mode avalanche photodiodes. *Nuclear Instruments and Methods in Physics Research A*, 581:143–146, October 2007. 46

[B+07d] E. Bottacini et al. Blazar 1ES 1959+650 shows high and hard X-ray state. *The Astronomer's Telegram*, 1315:1, November 2007. 75

[B+07e] T. Bretz et al. Long-term VHE γ-ray monitoring of bright blazars with a dedicated telescope. *Astronomische Nachrichten*, 328:676, July 2007. 58

[B+08a] T. Bretz et al. Long-term monitoring of bright blazars with a dedicated Cherenkov telescope. In F. A. Aharonian, W. Hofmann, and F. Rieger, editors, *American Institute of Physics Conference Series*, volume 1085 of *American Institute of Physics Conference Series*, pages 850–853, December 2008. 45

[B+08b] T. Bretz et al. Long term VHE gamma ray monitoring of bright blazars with a dedicated Cherenkov telescope. In *Blazar Variability across the Electromagnetic Spectrum*, volume BLAZARS2008 of *Proceedings of Science*, 2008. 45

[B+08c] T. Bretz et al. Long-term VHE γ-ray monitoring of bright blazars with a dedicated Cherenkov telescope. In *30th International Cosmic Ray Conference, Mérida, Mexico*, volume 3 of *International Cosmic Ray Conference*, pages 1495–1498, 2008. 58, 66

[B+08d] J. Buckley et al. The Status and future of ground-based TeV gamma-ray astronomy. A White Paper prepared for the Division of Astrophysics of the American Physical Society. *ArXiv e-prints*, page 0810.0444, October 2008, 0810.0444. 46

[B+09a] M. Backes et al. Long-term monitoring of blazars - the DWARF network. In *31st International Cosmic Ray Conference, Łódź, Poland*, International Cosmic Ray Conference, page 1452, July 2009. Published online: http://icrc2009.uni.lodz.pl/proc/html. 58, 64

[B+09b] M. Backes et al. Long-Term Monitoring of Bright Blazars with a Dedicated Cherenkov Telescope. *International Journal of Modern Physics D*, 18:1645–1649, 2009. 45

[B+09c] M. Bass et al. *Handbook of Optics: Optical properties of materials, nonlinear optics, quantum optics*. Handbook of Optics. McGraw-Hill, 2009. 53

[B+09d] J. L. Bazo Alba et al. Search for neutrino flares from point sources with IceCube. In *31st International Cosmic Ray Conference, Łódź, Poland*, International Cosmic Ray Conference, page 1282, July 2009, 0908.4209. Published online: http://icrc2009.uni.lodz.pl/proc/html. 79

[B+09e] V. Beckmann et al. The second INTEGRAL AGN catalogue. *Astronomy & Astrophysics*, 505:417–439, October 2009, 0907.0654. 75

[B+09f] P. L. Biermann et al. Active Galactic Nuclei: Sources for ultra high energy cosmic rays? *Nuclear Physics B Proceedings Supplements*, 190:61–78, May 2009, 0811.1848. 10

[B+09g] I. Braun et al. First Avalanche-photodiode camera test (FACT): A novel camera using G-APDs for the observation of very high-energy γ-rays with Cherenkov telescopes. *Nuclear Instruments and Methods in Physics Research A*, 610:400–403, October 2009. 46

[B+09h] I. Braun et al. Solid Light Concentrators for Cherenkov Astronomy. In *31st International Cosmic Ray Conference, Łódź, Poland*, International Cosmic Ray Conference, page 1248, July 2009. Published online: http://icrc2009.uni.lodz.pl/proc/html. 48

[B+09i] T. Bretz et al. Status of the DWARF project for long-term monitoring of bright blazars. In *31st International Cosmic Ray Conference, Łódź, Poland*, International Cosmic Ray Conference, page 1275, July 2009. Published online: http://icrc2009.uni.lodz.pl/proc/html. 58

[B+09j] T. Bretz et al. The drive system of the major atmospheric gamma-ray imaging Cherenkov telescope. *Astroparticle Physics*, 31:92–101, March 2009, 0810.4593. 48

[B+09k] D. Britzger et al. Studies of the Influence of Moonlight on Observations with the MAGIC Telescope. In *31st International Cosmic Ray Conference, Łódź, Poland*, International Cosmic Ray Conference, page 1269, July 2009, 0907.0973. Published online: http://icrc2009.uni.lodz.pl/proc/html. 39

[B+10a] M. V. Barkov et al. Rapid TeV variability in Blazars as result of Jet-Star Interaction. *ArXiv e-prints*, December 2010, 1012.1787. 18

[B+10b] W. H. Baumgartner et al. The Swift-BAT 58 Month Survey. In *AAS/High Energy Astrophysics Division #11*, volume 42 of *Bulletin of the American Astronomical Society*, page 675, February 2010. 74, 187

[B+10c] E. Bottacini et al. Probing the Transition Between the Synchrotron and Inverse-compton Spectral Components of 1ES 1959+650. *Astrophysical Journal Letters*, 719:L162–L166, August 2010, 1010.3259. 75, 105, 178, 179, 186, 187

[B+11a] HM. Bardt et al. ASM official lightcurve website, February 2011. http://xte.mit.edu/ASM_lc.html. 150

[B+11b] B. Bartoli et al. Long-term Monitoring of the TeV Emission from Mrk 421 with the ARGO-YBJ Experiment. *Astrophysical Journal*, 734:110–+, June 2011, 1106.0896. 64

[B+11c] W. H. Baumgartner et al. Swift–BAT official 58 months catalog website, November 2011. http://heasarc.gsfc.nasa.gov/docs/swift/results/bs58mon. 153

[B+11d] W. Benbow et al. Highlights of the VERITAS Blazar Observation Program. In *32nd International Cosmic Ray Conference, Beijing, China*, International Cosmic Ray Conference, page 1030, August 2011, 1110.0038. 64, 78

[B+11e] A. Biland et al. First Results from the First G-APD Cherenkov Telescope. In *32nd International Cosmic Ray Conference, Beijing, China*, International Cosmic Ray Conference, page 1125, August 2011. 57

[B+11f] T. Bretz et al. A status report: FACT – a fact! In *13th ICATPP Conference on Astroparticle, Particle, Space Physics and Detectors for Physics Applications, Como, Italy*, International Conference on Advanced Technology and Particle Physics, October 2011. Submitted for publication. 57

[B+11g] T. Bretz et al. Status of the First G-APD Cherenkov Telescope (FACT). In *32nd International Cosmic Ray Conference, Beijing, China*, International Cosmic Ray Conference, August 2011. 57

[B+11h] K. A. Brodatzki et al. Internal $\gamma\gamma$ Opacity in Active Galactic Nuclei and the Consequences for the TeV Observations of M87 and Cen A. *Astrophysical Journal*, 736:98–+, August 2011, 1103.5552. 15

[Bac08] Michael Backes. Langzeitbeobachtung von TeV Blazaren – Quellenanalyse mit MAGIC und Konzeption eines dedizierten Teleskops. Diplomarbeit, Technische Universität Dortmund, January 2008. 78, 85, 86, 115

[BBR80] M. C. Begelman, R. D. Blandford, and M. J. Rees. Massive black hole binaries in active galactic nuclei. *Nature*, 287:307–309, September 1980. 20

[BD08] T. Bretz and D. Dorner. MARS – The Cherenkov Observatory edition. In F. A. Aharonian, W. Hofmann, and F. Rieger, editors, *American Institute of Physics Conference Series*, volume 1085 of *American Institute of Physics Conference Series*, pages 664–+, December 2008. 58

[BD09] T. Bretz and D. Dorner. MARS - CheObs goes Monte Carlo. In *31st International Cosmic Ray Conference, Łódź, Poland*, International Cosmic Ray Conference, page 1259, July 2009. Published online: http://icrc2009.uni.lodz.pl/proc/html. 58

[Bd11] P. L. Biermann and V. de Souza. On a common origin of galactic and extragalactic cosmic rays. *ArXiv e-prints*, June 2011, 1106.0625. 10

[Bec08] J. K. Becker. High-energy neutrinos in the context of multimessenger astrophysics. *Physics Reports*, 458:173–246, March 2008, 0710.1557. 3, 7, 8, 23

[Bes10] Vasily S. Beskin. *MHD Flows in Compact Astrophysical Objects – Accretion, Winds and Jets*. Springer-Verlag Berlin Heidelberg, 2010. 17

[Bf05] E. Bernardini and for the IceCube Collaboration. Multi-Messenger Studies with AMANDA/IceCube: Observations and Strategies. In *Proceedings of Towards a Network of Atmospheric Cherenkov Detectors VII: Cherenkov 2005*, Towards a Network of Atmospheric Cherenkov Detectors, September 2005, arXiv:astro-ph/0509396. Ecole Polytechnique, Palaiseau, France. 64, 78

[BHK11] M. Böttcher, D. E. Harris, and H. Krawczynski, editors. *Relativistic Jets from Active Galactic Nuclei*. Wiley VCH, 2011. in preperation. 17

[BK79] R. D. Blandford and A. Königl. Relativistic jets as compact radio sources. *Astrophysical Journal*, 232:34, August 1979. 19

[BL09] T. A. Boroson and T. R. Lauer. A candidate sub-parsec supermassive binary black hole system. *Nature*, 458:53–55, March 2009, 0901.3779. 20

[Bla07] O. Blaes. Accretion Disks in AGNs. In L. C. Ho & J.-W. Wang, editor, *The Central Engine of Active Galactic Nuclei*, volume 373 of *Astronomical Society of the Pacific Conference Series*, pages 75–+, October 2007, arXiv:astro-ph/0703589. 16

[Bla08] Pasquale Blasi. Rapporteur talk, session og-1. In 30^{th} *International Cosmic Ray Conference ICRC, Mérida, Mexico*, International Cosmic Ray Conference, August 2008. http://www.icrc2007.unam.mx/. 5

[Boe05] M. Boettcher. A Hadronic Synchrotron Mirror Model for the "Orphan" TeV Flare in 1ES 1959+650. *Astrophysical Journal*, 621:176–180, March 2005, arXiv:astro-ph/0411248. 19

[Boj02] Heidrun Bojahr. *Suche nach TeV-Blazaren mir dem HEGRA-System der abbildenden Cherenkov-Teleskope*. PhD thesis, Bergische Universität Wuppertal, December 2002. WUB-DIS 2002-3. 33

[Bra03] Hale Bradt. *Astronomy Methods: A Physical Approach to Astronomical Observations*. Cambridge University Press, 2003. 26

[Bra07] Hale Bradt. *Astrophysics Processes – The Physics of Astronomical Phenomena*. Springer-Verlag Berlin Heidelberg, 2007. 13

[Bre01] L. Breiman. Random forests. *Machine Learning*, 45:5, 2001. 42

[BRM09] M. Böttcher, A. Reimer, and A. P. Marscher. Implications of the very High Energy Gamma-Ray Detection of the Quasar 3C279. *Astrophysical Journal*, 703:1168–1175, September 2009. 19

[BRS09] V. Beckmann, C. Ricci, and S. Soldi. Fermi detected blazars seen by INTEGRAL. *ArXiv e-prints*, December 2009, 0912.2254. 75

[Buc99] J. H. Buckley. Observations of blazars with the Whipple Observatory gamma-ray telescope. *Astroparticle Physics*, 11:119–129, June 1999. 77

[BW97] H. M. Badran and T. C. Weekes. Improvement of gamma-hadron discrimination at TeV energies using a new parameter, image Surface Brightness. *Astroparticle Physics*, 7:307–314, October 1997. 42

[BWE91] R. H. Becker, R. L. White, and A. L. Edwards. A new catalog of 53,522 4.85 GHz sources. *Astrophysical Journal Supplements*, 75:1–229, January 1991. 25

[BWM03] T. Bretz, R. Wagner, and MAGIC collaboration. The MAGIC Analysis and Reconstruction Software. In *International Cosmic Ray Conference*, volume 5 of *International Cosmic Ray Conference*, pages 2947–+, July 2003. 39

[BZ69] V. S. Berezinskij and G. T. Zatsepin. Cosmic rays at ultrahigh energies (neutrino?). *Physics Letters B*, 28:423, 1969. 12

[BZ77] R. D. Blandford and R. L. Znajek. Electromagnetic extraction of energy from Kerr black holes. *Monthly Notices of the Royal Astronomical Society*, 179:433–456, May 1977. 17

[C^+97] M. Catanese et al. First Results from a Search for TeV Emission from BL Lacs Out to Z = 0.2. In *International Cosmic Ray Conference*, volume 3 of *International Cosmic Ray Conference*, page 277, 1997, arXiv:astro-ph/9706136. 77

[C^+00] J. Cortina et al. The new data acquisition system of the first telescope in HEGRA. In B. L. Dingus, M. H. Salamon, and D. B. Kieda, editors, *American Institute of Physics Conference Series*, volume 515 of *American Institute of Physics Conference Series*, pages 368–372, June 2000. 34, 43, 50, 51

[C^+06] S. B. Cenko et al. The Automated Palomar 60 Inch Telescope. *The Publications of the Astronomical Society of the Pacific*, 118:1396–1406, October 2006, arXiv:astro-ph/0608323. 29

[C+08] E. Collins-Hughes et al. Gamma-ray observations of blazars with the Whipple 10 m telescope. In *8th INTEGRAL Workshop "The Restless Gamma-ray Universe"*, volume INTEGRAL 2010 of *Proceedings of Science*, 2008. 110

[C+11] X. Chen et al. Time-dependent simulations of multiwavelength variability of the blazar Mrk 421 with a Monte Carlo multizone code. *Monthly Notices of the Royal Astronomical Society*, 416:2368–2387, September 2011, 1106.1865. 103

[Cam04] A. M. Campbell. *The character of optical variability for X-ray selected blazars*. PhD thesis, Georgia State University, Georgia, USA, December 2004. 68

[Cam07] Max Camenzind. *Compact Objects in Astrophysics – White Dwarfs, Neutron Stars and Black Holes*. Springer-Verlag Berlin Heidelberg, 2007. 17

[CG08] J.-M. Casandjian and I. A. Grenier. A revised catalogue of EGRET γ-ray sources. *Astronomy & Astrophysics*, 489:849–883, October 2008, 0806.0113. 76

[Che34] P. A. Cherenkov. Visible emission of clean liquids by action of gamma radiation. *Doklady Akademii Nauk SSSR*, 2:451+, 1934. 33

[CIA07] CIA. *The World Fact Book*. Central Intelligence Agency, December 2007. https://www.cia.gov/library/publications/the-world-factbook. 40

[Cir08] V. Cirkel-Bartelt. History of astroparticle physics and its components. *Living Reviews in Relativity*, 11(2), 2008. http://www.livingreviews.org/lrr-2008-2. 3

[CLN08] P. M. Chadwick, I. J. Latham, and S. J. Nolan. TOPICAL REVIEW: TeV gamma-ray astronomy. *Journal of Physics G Nuclear Physics*, 35(3):033201–+, March 2008. 33

[Col07a] CANGAROO Collaboration. Official website, December 2007. http://icrhp9.icrr.u-tokyo.ac.jp/. 40

[Col07b] VERITAS Collaboration. Official website, December 2007. http://veritas.sao.arizona.edu/. 40

[Col11a] Star Base Utah Collaboration. Official website, October 2011. http://www.physics.utah.edu/starbase/. 114

[Col11b] TACTIC Collaboration. Official website, October 2011. http://www.barc.ernet.in/pg/nrl-harl. 112

[Col11c] W. Collmar. Private communication, July 2011. 76, 188

[Coo77] R. D. Cook. Detection of Influential Observation in Linear Regression. *Technometrics*, 18/1:15–18, February 1977. 88

[CW82] R. D. Cook and S. Weisberg. *Residuals and influence in regression*. Monographs on statistics and applied probability. Chapman and Hall, 1982. 88

[D+96] J. N. Douglas et al. The Texas Survey of Radio Sources Covering -35.5 degrees $<$ declination $<$ 71.5 degrees at 365 MHz. *Astronomical Journal*, 111:1945–+, May 1996. 26

[D+97] A. Daum et al. First results on the performance of the HEGRA IACT array. *Astroparticle Physics*, 8:1–11, December 1997. 36, 43

[D+03] F. De Paolis et al. Binary black holes in Mkns as sources of gravitational radiation for space based interferometers. *Astronomy & Astrophysics*, 410:741–747, November 2003, arXiv:astro-ph/0310213. 21

[D+05] M. K. Daniel et al. Spectrum of Very High Energy Gamma-Rays from the blazar 1ES 1959+650 during Flaring Activity in 2002. *Astrophysical Journal*, 621:181, March 2005. arXiv:astro-ph/0503.085. 83, 85, 194, 195

[D+09a] V. K. Dhar et al. ANN-based energy reconstruction procedure for TACTIC γ-ray telescope and its comparison with other conventional methods. *Nuclear Instruments and Methods in Physics Research A*, 606:795–805, July 2009, 0904.4096. 42

[D+09b] I. Donnarumma et al. The June 2008 Flare of Markarian 421 from Optical to TeV Energies. *Astrophysical Journal Letters*, 691:L13–L19, January 2009, 0812.1500. 65

[D+11a] M. Doert et al. Correlated neutrino and gamma-ray emission from Active Galactic Nuclei - an estimation. *Journal of Physics: Conference Series*, 2011. Accepted for publication. 19

[D+11b] A. Domínguez et al. Extragalactic background light inferred from AEGIS galaxy-SED-type fractions. *Monthly Notices of the Royal Astronomical Society*, 410:2556–2578, February 2011, 1007.1459. 16

[de 48] G. de Vaucouleurs. Recherches sur les Nebuleuses Extragalactiques. *Annales d'Astrophysique*, 11:247, January 1948. 67

[Der02] C. D. Dermer. Neutrino, Neutron, and Cosmic-Ray Production in the External Shock Model of Gamma-Ray Bursts. *Astrophysical Journal*, 574:65–87, July 2002, arXiv:astro-ph/0005440. 10

[Der11] C. D. Dermer. Are Gamma-Ray Bursts the Sources of the Ultra-High Energy Cosmic Rays? *ArXiv e-prints*, March 2011, 1103.4834. 10

[Df11] G. Di Sciascio and for the ARGO-YBJ Collaboration. Gamma-Ray Astronomy with ARGO-YBJ. *ArXiv e-prints*, July 2011, 1107.3404. 64

[DHH97] A. Daum, G. Hermann, and HEGRA Collaboration. The Stereoscopic System of Imaging Atmospheric Cherenkov Telescopes of the HEGRA-Collaboration. In *International Cosmic Ray Conference*, volume 5 of *International Cosmic Ray Conference*, pages 117–+, 1997. 36, 43

[DM09] Charles D. Dermer and Govind Menon. *High Energy Radiation from Black Holes: Gamma Rays, Cosmic Rays, and Neutrinos*. Princeton University Press, 2009. 3, 13

[DR10] C. D. Dermer and S. Razzaque. Acceleration of Ultra-high-energy Cosmic Rays in the Colliding Shells of Blazars and Gamma-ray Bursts: Constraints from the Fermi Gamma-ray Space Telescope. *Astrophysical Journal*, 724:1366–1372, December 2010, 1004.4249. 10

[Dre09] Jens Dreyer. *Neutrinos from Starbust-Galaxies - A source stacking analysis of AMANDA II and IcdCube data*. PhD thesis, Technische Universität Dortmund, December 2009. 4

[DS93] C. D. Dermer and R. Schlickeiser. Model for the High-Energy Emission from Blazars. *Astrophysical Journal*, 416:458–+, October 1993. 19

[DSG05] D. Donato, R. M. Sambruna, and M. Gliozzi. Six years of BeppoSAX observations of blazars: A spectral catalog. *Astronomy & Astrophysics*, 433:1163–1169, April 2005, arXiv:physics/0412114. 73, 152

[DT03] A. Djannati-Ataí and The CAT Collaboration. Two new VHE BL Lac objects, 1ES 1426+428 and 1ES 1959+650, detected by the CAT Telescope. In S. Collin, F. Combes, & I. Shlosman, editor, *Active Galactic Nuclei: From Central Engine to Host Galaxy*, volume 290 of *Astronomical Society of the Pacific Conference Series*, page 291, 2003. 78, 83

[E+92] M. Elvis et al. The Einstein Slew Survey. *Astrophysical Journal Supplements*, 80:257–303, May 1992. 67

[E+11] S. L. Ellison et al. Galaxy pairs in the Sloan Digital Sky Survey - IV: Interactions trigger AGN. *Monthly Notices of the Royal Astronomical Society*, August 2011, 1108.2711. accepted for publication. 21

[EBHL11] M. Eracleous, T. A. Boroson, J. P. Halpern, and J. Liu. A Large Systematic Search for Recoiling and Close Supermassive Binary Black Holes. *Astrophysical Journal Supplements*, June 2011, 1106.2952. 20

[ESS07] E/PO, Sonoma State University, and Aurore Simonnet. Official website of the Fermi Gamma-ray Space Telescope, November 2007. http://glast.sonoma.edu/images/agnnotext.html. 18

[F+94] V. P. Fomin et al. New methods of atmospheric Cherenkov imaging for gamma-ray astronomy. I. The false source method. *Astroparticle Physics*, 2:137–150, May 1994. 64

[F+97] F. Frontera et al. The high energy instrument PDS on-board the BeppoSAX X–ray astronomy satellite. *Astronomy and Astrophysics Supplement*, 122:357–369, April 1997. 30

[F+98] G. Fossati et al. A unifying view of the spectral energy distributions of blazars. *Monthly Notices of the Royal Astronomical Society*, 299:433–448, September 1998, arXiv:astro-ph/9804103. 18

[F+00] R. Falomo et al. The Hubble Space Telescope Survey of BL Lacertae Objects. III. Morphological Properties of Low-Redshift Host Galaxies. *Astrophysical Journal*, 542:731–739, October 2000, arXiv:astro-ph/0006388. 67

[F+03] R. Falomo et al. Black Hole Masses and the Fundamental Plane of BL Lacertae Objects. *Astrophysical Journal*, 595:624–630, October 2003, arXiv:astro-ph/0306163. 68

[F+07] L. Fuhrmann et al. Simultaneous Radio to (Sub-) mm-Monitoring of Variability and Spectral Shape Evolution of potential GLAST Blazars. In S. Ritz, P. Michelson, & C. A. Meegan, editor, *The First GLAST Symposium*, volume 921 of *American Institute of Physics Conference Series*, pages 249–251, July 2007, 0704.3944. 26

[F+08a] J. H. Fan et al. A possible disk mechanism for the 23-day QPO in Mkn 501. *Astroparticle Physics*, 28:508–515, January 2008, 0710.1340. 21

[F+08b] G. Finnegan et al. Deployment of a Pair of 3 M telescopes in Utah. In F. A. Aharonian, W. Hofmann, and F. Rieger, editors, *American Institute of Physics Conference Series*, volume 1085 of *American Institute of Physics Conference Series*, pages 746–748, December 2008. 114

[F+11a] G. Fabbiano et al. A close nuclear black-hole pair in the spiral galaxy ngc 3393. *Nature*, August 2011. `http://dx.doi.org/10.1038/nature10364`. 20

[F+11b] A. Falcone et al. Swift official lightcurve website, February 2011. `http://www.swift.psu.edu/monitoring`. 146

[FA11] L. Fuhrmann and E. Angelakis. Private communication, November 2011. 70, 72, 125, 167

[Fan00] J. Fan. Long-term variability properties and periodicity analysis for blazars. In K. S. Cheng, H. F. Chau, K. L. Chan, & K. C. Leung, editor, *Stellar Astrophysics*, pages 319–+, 2000, arXiv:astro-ph/0001029. 21

[FCT03] R. Falomo, N. Carangelo, and A. Treves. Host galaxies and black hole masses of low- and high-luminosity radio-loud active nuclei. *Monthly Notices of the Royal Astronomical Society*, 343:505–511, August 2003, arXiv:astro-ph/0304190. 68

[Fer49] E. Fermi. On the origin of the cosmic radiation. *Physical Review*, 75(8):1169–1174, Apr 1949. 6

[Fid06] V. V. Fidelis. Tera-electron-volt radiation from the blazar 1ES 1959+650 in 2004. *Astronomy Reports*, 50:809–813, October 2006. 78

[Fie07] N. Fields. A Multi-Wavelength Blazar Campaign. In *American Astronomical Society Meeting Abstracts*, volume 38 of *Bulletin of the American Astronomical Society*, page 730, December 2007. 71

[Fie11] N. Fields. Official website, REU 2007 Wisconsin-Madison, November 2011. http://www.astro.wisc.edu/~fields/pages/Plots.html. 72

[FKT02] R. Falomo, J. K. Kotilainen, and A. Treves. The Black Hole Mass of BL Lacertae Objects from the Stellar Velocity Dispersion of the Host Galaxy. *Astrophysical Journal Letters*, 569:L35–L38, April 2002, arXiv:astro-ph/0203199. 68

[FMV+10] Fermi-LAT Collaboration: A. A. Abdo, MAGIC Collaboration: J. Aleksić, VERITAS Collaboration: V. A. Acciari, GASP-WEBT Consortium, and Multi-Wavelength Partners. Insights Into the High-Energy Gamma-ray Emission of Markarian 501 from Extensive Multifrequency Observations in the Fermi Era. *ArXiv e-prints*, November 2010, 1011.5260. accepted for publication in Astrophysical Journal. 65

[FRV08] A. Franceschini, G. Rodighiero, and M. Vaccari. Extragalactic optical-infrared background radiation, its time evolution and the cosmic photon-photon opacity. *Astronomy & Astrophysics*, 487:837–852, September 2008, 0805.1841. 16

[FSI95] M. Fukugita, K. Shimasaku, and T. Ichikawa. Galaxy Colors in Various Photometric Band Systems. *The Publications of the Astronomical Society of the Pacific*, 107:945, October 1995. 72, 126

[G+79] R. Giacconi et al. The Einstein /HEAO 2/ X-ray Observatory. *Astrophysical Journal*, 230:540–550, June 1979. 67

[G+00] K. Gebhardt et al. A Relationship between Nuclear Black Hole Mass and Galaxy Velocity Dispersion. *Astrophysical Journal Letters*, 539:L13–L16, August 2000, arXiv:astro-ph/0006289. 68

[G+02] B. Giebels et al. Observation of X-Ray Variability in the BL Lacertae Object 1ES 1959+65. *Astrophysical Journal*, 571:763–770, June 2002, arXiv:astro-ph/0203335. 73, 74, 150, 151

[G+04a] N. Gehrels et al. The Swift Gamma-Ray Burst Mission. *Astrophysical Journal*, 611:1005–1020, August 2004. 29, 30

[G+04b] M. Giroletti et al. A Sample of Low-Redshift BL Lacertae Objects. I. The Radio Data. *Astrophysical Journal*, 613:752–769, October 2004, arXiv:astro-ph/0406255. 69, 70, 71

[G+06a] M. Giroletti et al. A Sample of Low-Redshift BL Lacertae Objects. II. EVN and MERLIN Data and Multiwavelength Analysis. *Astrophysical Journal*, 646:801–814, August 2006, arXiv:astro-ph/0604224. 71

[G+06b] K. Gutierrez et al. Multiwavelength Observations of 1ES 1959+650, 1 Year after the Strong Outburst of 2002. *Astrophysical Journal*, 644:742–747, June 2006, arXiv:astro-ph/0603013. 70, 72, 78, 105, 123

[G+08] F. Goebel et al. Upgrade of the MAGIC Telescope with a Multiplexed Fiber-Optic 2 GSamples/s FADC Data Acquisition system. In 30th *International Cosmic Ray Conference ICRC, Mérida, Mexico*, volume 3 of *International Cosmic Ray Conference*, pages 1481–1484, 2008. arXiv:astro-ph/0709.2363. 38

[G+09] R. C. Gilmore et al. GeV gamma-ray attenuation and the high-redshift UV background. *Monthly Notices of the Royal Astronomical Society*, 399:1694–1708, November 2009, 0905.1144. 16

[G+11] P. Giommi et al. Simultaneous Planck, Swift, and Fermi observations of X-ray and gamma-ray selected blazars. *Astronomy & Astrophysics*, August 2011, 1108.1114. Submitted for publication. 152, 166, 167, 190

[Gai90] Thomas K. Gaisser. *Cosmic Rays and Particles*. Cambridge University Press, 1990. 3, 6, 9

[GB+08] F. Goebel, M. Backes, et al. Long term monitoring of bright TeV Blazars with the MAGIC telescope. In 30th *International Cosmic Ray Conference ICRC, Mérida, Mexico*, volume 3 of *International Cosmic Ray Conference*, pages 1025–1028, 2008, 0709.2032. arXiv:astro-ph/0709.2032. 66, 78

[GG99] Gorachand and Ghosh. Dispersion-equation coefficients for the refractive index and birefringence of calcite and quartz crystals. *Optics Communications*, 163(1-3):95 – 102, 1999. 53

[GHF81] P. Gorenstein, F. R. Harnden, Jr., and D. G. Fabricant. In orbit performance of the Einstein Observatory/HEAO-2 Imaging Proportional Counter. *IEEE Transactions on Nuclear Science*, 28:869–874, February 1981. 67

[Ghi11] G. Ghisellini. Extragalactic relativistic jets. *ArXiv e-prints*, March 2011, 1104.0006. Invited plenary talk at the Texas Symposium, Heidelberg, December 2010. 17

[Gre66] K.I. Greisen. End to the Cosmic-Ray Spectrum? *Physical Review Letters*, 16:748, 1966. 9

[Gro06] Andreas Gross. *Search for High Energy Neutrinos from AGN classes with AMANDA-II*. PhD thesis, Universität Dortmund, February 2006. 23

[Gru00] Claus Grupen. *Astroteilchenphysik*. Springer-Verlag Berlin Heidelberg, 2000. 3

[Gru05] Claus Grupen. *Astroparticle Physics*. Springer-Verlag Berlin Heidelberg, 2005. 3

[Göt06] Niels Götting. *Nachweis von TeV-Gamma-Strahlung aus der Richtung der Blazare H1426+428 und 1ES1959+650 sowie der Radiogalaxie M87 mit den HEGRA-Cherenkov-Teleskopen*. PhD thesis, Universität Hamburg, 2006. ISBN 978-3-86624-243-2. 83, 193

[H+95a] J. A. Holtzman et al. The performance and calibration of WFPC2 on the Huble Space Telescope. *The Publications of the Astronomical Society of the Pacific*, 107:156–178, February 1995. 28

[H+95b] J. A. Holtzman et al. The Photometric Performance and Calibration of WFPC2. *The Publications of the Astronomical Society of the Pacific*, 107:1065–+, November 1995. 28

[H+98] N. Hayashida et al. Observations of TeV Gamma Ray Flares from Markarian 501 with the Telescope Array Prototype. *Astrophysical Journal Letters*, 504:L71+, September 1998. 21, 65

[H+99a] R. C. Hartman et al. The Third EGRET Catalog of High-Energy Gamma-Ray Sources. *Astrophysical Journal Supplements*, 123:79–202, July 1999. 76

[H+99b] J. Heidt et al. High-resolution imaging of Einstein Slew Survey BL Lacertae objects. *Astronomy & Astrophysics*, 341:683–692, January 1999, arXiv:astro-ph/9811050. 67, 69

[H+03a] J. Holder et al. Detection of TeV Gamma Rays from the BL Lacertae Object 1ES 1959+650 with the Whipple 10 Meter Telescope. *Astrophysical Journal Letters*, 583:L9–L12, January 2003, arXiv:astro-ph/0212170. 68, 78

[H+03b] J. Holder et al. Whipple Observations of 1ES1959+650: An Update. In *International Cosmic Ray Conference*, volume 5 of *International Cosmic Ray Conference*, page 2619, July 2003, arXiv:astro-ph/0305577. 78

[H+03c] D. Horan et al. Observations of H1426+428 from 1999 to 2002 with the Whipple Observatory 10 m Telescope. In *28^{th} International Cosmic Ray Conference*, volume 5 of *International Cosmic Ray Conference*, page 2647, July 2003, arXiv:astro-ph/0305579. 115

[H+04a] D. Horan et al. Constraints on the Very High Energy Emission from BL Lacertae Objects. *Astrophysical Journal*, 603:51–61, March 2004, arXiv:astro-ph/0311397. 77, 84

[H+04b] J. R. Houck et al. The Infrared Spectrograph (IRS) on the Spitzer Space Telescope. *Astrophysical Journal Supplements*, 154:18–24, September 2004, arXiv:astro-ph/0406167. 27

[H+06] D. S. Hudson et al. X-ray detection of the proto supermassive binary black hole at the centre of Abell 400. *Astronomy & Astrophysics*, 453:433–446, July 2006, arXiv:astro-ph/0603272. 20

[H+08] M. Hayashida et al. First simultaneous multiwavelength observation for the BL Lac object, 1ES1959+650 in a low state with MAGIC and Suzaku/Swift. In 30^{th} *International Cosmic Ray Conference ICRC, Mérida, Mexico*, volume 3 of *International Cosmic Ray Conference*, pages 1021–1024, 2008, 0709.2349. 78

[H+09a] D. Horan et al. Multiwavelength Observations of Markarian 421 in 2005-2006. *Astrophysical Journal*, 695:596–618, April 2009, 0901.1225. 110

[H+09b] C. C. Hsu et al. Monitoring of bright blazars with MAGIC telescope. In *31st International Cosmic Ray Conference, Łódź, Poland*, International Cosmic Ray Conference, page 1058, July 2009, 0907.0893. Published online: http://icrc2009.uni.lodz.pl/proc/html. 39, 41, 65, 66, 78

[H+10] S. Hümmer et al. Simplified Models for Photohadronic Interactions in Cosmic Accelerators. *Astrophysical Journal*, 721:630–652, September 2010, 1002.1310. 13, 16

[H+11] B. Huber et al. Solid Light Concentrators for small-sized photosensors used in Cherenkov telescopes. In *32nd International Cosmic Ray Conference, Beijing, China*, International Cosmic Ray Conference, page 0136, August 2011. 48

[Ham09] Hamamatsu Photonics. MPPC - Multi-Pixel Photon Counter – technical information. http://sales.hamamatsu.com/assets/\applications/SSD/mppc_kapd9003e02.pdf, 2009. 46

[Hay04] Elisabeth A. Hays. *A Search for TeV Emission from Active Galaxies using the Milagro Observatory*. PhD thesis, University of Maryland (College Park, Md.), August 2004. 84

[Hay05] E. Hays. A Search for Tev Emission From X-ray Selected Agn with Milagro. *Astrophysics and Space Science*, 297:43–52, June 2005. 84

[Hay08] Masaaki Hayashida. *Observation of Very-High-Energy Gamma-Rays from Blazars with the MAGIC Telescope*. PhD thesis, Ludwig-Maximilians-Universität München, March 2008. 78, 85, 86, 156, 191

[HB08] R. Hudec and M. Basta. Very long term observations of blazars candidates for supermassive black hole binaries. In *Blazar Variability across the Electromagnetic Spectrum*, volume BLAZARS2008 of *Proceedings of Science*, 2008. 19

[HC07] H.E.S.S.-Collaboration. Official website, December 2007. http://www.mpi-hd.mpg.de/hfm/HESS/. 40

[Hei10] Max Heikenfeld. Der Einfluss von erhöhtem Nachthimmeluntergrund auf Beobachtungen mit den MAGIC-Teleskopen. Bachelorarbeit, Technische Universität Dortmund, August 2010. 39

[Hel11] Marius Helf. Gamma-Hadron-Separation im MAGIC-Experiment durch verteilungsgestütztes Sampling. Diplomarbeit, Technische Universität Dortmund, April 2011. 42

[Hes11] V. F. Hess. Über die Absorption der Gamma–Strahlung in der Atmosphäre. *Physikalische Zeitschrift*, 12(22|23):998, 1911. 3

[Hes12] V. F. Hess. Über Beobachtungen der durchdringenden Strahlung bei sieben Freiballonfahrten. *Physikalische Zeitschrift*, 13:1084, 1912. 3

[HH05] F. Halzen and D. Hooper. High energy neutrinos from the TeV Blazar 1ES 1959+650. *Astroparticle Physics*, 23:537–542, July 2005, arXiv:astro-ph/0502449. 19, 78

[HH09] J. A. Hinton and W. Hofmann. Teraelectronvolt Astronomy. *Annual Review of Astronomy & Astrophysics*, 47:523–565, September 2009, 1006.5210. 3, 33

[Hil85] A. M. Hillas. Cerenkov light images of EAS produced by primary gamma. In F. C. Jones, editor, 19^{th} *International Cosmic Ray Conference ICRC, San Diego, USA*, volume 3 of *International Cosmic Ray Conference*, page 445, August 1985. 34

[Hin09] J. Hinton. Ground-based gamma-ray astronomy with Cherenkov telescopes. *New Journal of Physics*, 11(5):055005–+, May 2009, 0803.1609. 33

[HK10] D. Heck and J. Knapp. *EAS Simulation with CORSIKA: A User's Manual.* Forschungszentrum Karlsruhe, 2010. http://www-ik.fzk.de/corsika. 58

[Hor03] D. Horns. Multi-wavelength Observations of the TeV Blazars Mkn 421, 1ES1959+650, and H1426+428 with the HEGRA Cherenkov Telescopes and the RXTE X-ray Satellite. In L. O. Takalo & E. Valtaoja, editor, *High Energy Blazar Astronomy*, volume 299 of *Astronomical Society of the Pacific Conference Series*, page 13, July 2003, arXiv:astro-ph/0209454. 78

[Hud11] R. Hudec. Astronomical Plate Archives and Binary Blazars Studies. *Journal of Astrophysics and Astronomy*, pages 2–+, May 2011. 19

[IRS11] IRSA. Spitzer Heritage Arxhive, November 2011. http://sha.ipac.caltech.edu. 170, 172, 175, 177

[J+97] R. Jager et al. The Wide Field Cameras onboard the BeppoSAX X-ray Astronomy Satellite. *Astronomy and Astrophysics Supplement*, 125:557–572, November 1997. 73

[J+01] F. Jansen et al. XMM-Newton observatory. I. The spacecraft and operations. *Astronomy & Astrophysics*, 365:L1–L6, January 2001. 29

[J+03] P. L. Jensen et al. The INTEGRAL spacecraft - in-orbit performance. *Astronomy & Astrophysics*, 411:L7–L17, November 2003. 28

[J+06] K. Jahoda et al. Calibration of the Rossi X-Ray Timing Explorer Proportional Counter Array. *Astrophysical Journal Supplements*, 163:401–423, April 2006, arXiv:astro-ph/0511531. 30

[K+98] M. Kestel et al. The Upgrade of the HEGRA CT1 telescope with new mirrors and new Trigger system. In J. Medina, editor, *16*th *European cosmic ray symposium*, Nuclear Physics B, Proc. Suppl., 1998. 34, 37, 43

[K+99a] A. Konopelko et al. Performance of the stereoscopic system of the HEGRA imaging air Čerenkov telescopes: Monte Carlo simulations and observations. *Astroparticle Physics*, 10:275–289, May 1999, arXiv:astro-ph/9901199. 36

[K+99b] Y. Y. Kovalev et al. Survey of instantaneous 1-22 GHz spectra of 550 compact extragalactic objects with declinations from -30^{deg} to +43^{deg}. *Astronomy and Astrophysics Supplement*, 139:545–554, November 1999, arXiv:astro-ph/0408264. 26

[K+01] D. Kranich et al. QPO analysis of the TeV and X-ray lightcurve of Mkn 501 in 1997 final results. In *International Cosmic Ray Conference*, volume 7 of *International Cosmic Ray Conference*, pages 2630–+, August 2001. 21, 65

[K+02] Y. Y. Kovalev et al. Broad-band Radio Spectra Variability of 550 AGN in 1997-2001. *Publications of the Astronomical Society of Australia*, 19:83–87, 2002. 26

[K+03] S. Komossa et al. Discovery of a Binary Active Galactic Nucleus in the Ultraluminous Infrared Galaxy NGC 6240 Using Chandra. *Astrophysical Journal Letters*, 582:L15–L19, January 2003, arXiv:astro-ph/0212099. 20

[K+04a] T. M. Kneiske et al. Implications of cosmological gamma-ray absorption. II. Modification of gamma-ray spectra. *Astronomy & Astrophysics*, 413:807, January 2004. arXiv:astro-ph/0309.141. 16

[K+04b] H. Krawczynski et al. Multiwavelength Observations of Strong Flares from the TeV Blazar 1ES 1959+650. *Astrophysical Journal*, 601:151–164, January 2004, arXiv:astro-ph/0310158. 19, 70, 72, 78, 83, 105

[K+07a] J. Kildea et al. The Whipple Observatory 10 m gamma-ray telescope, 1997–2006. *Astroparticle Physics*, 28:182–195, October 2007. 43, 110

[K+07b] R. Koul et al. The TACTIC atmospheric Cherenkov imaging telescope. *Nuclear Instruments and Methods in Physics Research A*, 578:548–564, August 2007, 0706.2055. 111, 112, 115

[K+09a] T. Krähenbühl et al. Geiger-mode Avalanche Photodiodes as Photodetectors in Cherenkov Astronomy. In *31st International Cosmic Ray Conference, Łódź, Poland*, International Cosmic Ray Conference, page 1282, July 2009. Published online: http://icrc2009.uni.lodz.pl/proc/html. 46

[K+09b] T. Krähenbühl et al. Geiger-mode avalanche photodiodes as photodetectors in Cherenkov astronomy. In *International Workshop on New Photon Detectors (PD09)*, 2009. 46, 48

[K+09c] O. M. Kurtanidze et al. Ten Years Optical Photometry of TeV BL Lacertae Objects. In W. Wang, Z. Yang, Z. Luo, & Z. Chen, editor, *The Starburst-AGN Connection*, volume 408 of *Astronomical Society of the Pacific Conference Series*, page 266, October 2009. 70

[K+11a] T. Krähenbühl et al. Calibrating the camera for the First G-APD Cherenkov Telescope (FACT). In *32nd International Cosmic Ray Conference, Beijing, China*, International Cosmic Ray Conference, page 0529, August 2011. 48

[K+11b] T. Krähenbühl et al. G-APDs in Cherenkov Astronomy: the FACT camera. *Nuclear Instruments and Methods in Physics Research A*, July 2011. Proceedings of the 6^{th} International Conference on New Developments In Photodetection (NDIP2011). Submitted for publication. 48

[KA08] S. R. Kelner and F. A. Aharonian. Energy spectra of gamma rays, electrons, and neutrinos produced at interactions of relativistic protons with low energy radiation. *Physical Review D*, 78(3):034013–+, August 2008, 0803.0688. 13

[Kap07] A. Kappes. Vorlesung Astroteilchenphysik, November 2007. http://www.pi1.physik.uni-erlangen.de/~kappes/lehre/WS05-VAT/. 11

[Kap09] B. Z. Kapanadze. Observational evidences of multiple shock waves in X-ray selected BL Lacerate objects. *Astrophysics*, 52:358–368, September 2009. 70, 72

[KD10] T. M. Kneiske and H. Dole. A lower-limit flux for the extragalactic background light. *Astronomy & Astrophysics*, 515:A19+, June 2010, 1001.2132. 16

[Khe02] B. Khelifi. *Recherche de sources gamma par une mêthode de maximum de vraisemblance: Application aux AGN et aux sources galactiques suivis par le télescope CAT*. PhD thesis, Caen University, 2002. Caen. 77, 78, 85

[KM92] J. G. Kirk and A. Mastichiadis. X-ray flares from runaway pair production in active galactic nuclei. *Nature*, 360:135–137, November 1992. 102

[KN29] O. Klein and T. Nishina. Über die Streuung von Strahlung durch freie Elektronen nach der neuen relativistischen Quantendynamik von Dirac. *Zeitschrift fur Physik*, 52:853–868, November 1929. 15

[Kol10] H. Kolanosky. Einführung in die astroteilchenphysik, February 2010. http://www-zeuthen.desy.de/~kolanosk/astro0910/skript.html. 3

[Kom06] S. Komossa. Observational evidence for binary black holes and active double nuclei. *Memorie della Societa Astronomica Italiana*, 77:733–+, 2006. 21

[KP79] D. V. Korolkov and I. N. Pariiskii. The Soviet RATAN-600 radio telescope. *Sky and Telescope*, 57:324–329, April 1979. 26

[Kra99] D. Kranich. Evidence for a QPO structure in the TeV and x-ray light curve during the 1997 high state γ emission of Mkn 501. In 26^{th} *International Cosmic Ray Conference ICRC, Salt Lake City, USA*, volume 3 of *International Cosmic Ray Conference*, page 358, August 1999. 21, 65

[Kra03] D. Kranich. TeV Observations of BL Lac Objects (Invited Talk). In L. O. Takalo & E. Valtaoja, editor, *High Energy Blazar Astronomy*, volume 299 of *Astronomical Society of the Pacific Conference Series*, page 3, July 2003. 78, 83

[Kro99] Julian H. Krolik. *Active Galactic Nuclei – From the Central Black Hole to the Galactic Environment*. Princeton University Press, 1999. 17

[KS11] U. F. Katz and C. Spiering. High-Energy Neutrino Astrophysics: Status and Perspectives. *Progress in Particle and Nuclear Physics*, November 2011, 1111.0507. Accepted for publication. 3

[KT06] M. Kusunose and F. Takahara. A Structured Leptonic Jet Model of the "Orphan" TeV Gamma-Ray Flares in TeV Blazars. *Astrophysical Journal*, 651:113–119, November 2006, arXiv:astro-ph/0607063. 19

[KTR+10] R. Krivonos, S. Tsygankov, M. Revnivtsev, S. Grebenev, E. Churazov, and R. Sunyaev. INTEGRAL/IBIS 7-year All-Sky Hard X-Ray Survey. II. Catalog of sources. *Astronomy & Astrophysics*, 523:A61, November 2010, 1006.4437. 75

[L+96] A. M. Levine et al. First Results from the All-Sky Monitor on the Rossi X-Ray Timing Explorer. *Astrophysical Journal Letters*, 469:L33+, September 1996, arXiv:astro-ph/9608109. 30

[L+03] F. Lebrun et al. ISGRI: The INTEGRAL Soft Gamma-Ray Imager. *Astronomy & Astrophysics*, 411:L141–L148, November 2003, arXiv:astro-ph/0310362. 31

[L+09a] P. Lachowicz et al. A ~4.6 h quasi-periodic oscillation in the BL Lacertae PKS 2155-304? *Astronomy & Astrophysics*, 506:L17–L20, November 2009, 0909.2113. 21

[L+09b] J.-P. Lenain et al. Very High Energy Active Galactic Nuclei Synchrotron Self-Compton Modeling Tour. *International Journal of Modern Physics D*, 18:1535–1539, 2009, 0904.1660. 19

[L+09c] H. Z. Li et al. The Periodicity Analysis of the Light Curve of 3C 279 and Implications for the Precession Jet. *The Publications of the Astronomical Society of the Pacific*, 121:1172–1179, November 2009. 21

[L+09d] E. J. Lindfors et al. The connection between optical and VHE gamma-ray high states in the blazar jets. *ArXiv e-prints*, July 2009, 0907.0550. 71

[L+09e] M. L. Lister et al. MOJAVE: Monitoring of Jets in Active Galactic Nuclei with VLBA Experiments. V. Multi-Epoch VLBA Images. *Astronomical Journal*, 137:3718–3729, March 2009, 0812.3947. 27, LVII

[L+10] EA. Lindfors et al. Private communication, December 2010. 138, 178

[L+11a] M. Lister et al. MOJAVE official website, November 2011. `http://www.physics.purdue.edu/astro/MOJAVE/sourcepages/1959+650.shtml`. 69, 70, 71, 125

[L+11b] M. L. Lister et al. γ-Ray and Parsec-scale Jet Properties of a Complete Sample of Blazars From the MOJAVE Program. *Astrophysical Journal*, 742:27, November 2011, 1107.4977. 71

[LB09] T. R. Lauer and T. A. Boroson. Hubble Space Telescope Images and KPNO Spectroscopy of the Binary Black Hole Candidate SDSS J153636.22+044127.0. *Astrophysical Journal*, 703:930–938, September 2009, 0906.0020. 20

[Lev11] K. Levay. Multimission Archive at the Space Telescope Science Institute (MAST), December 2011. http://galex.stsci.edu/GR6/?page=explore&photo=true&objid=6372569432789616572. 179

[LM83] T.-P. Li and Y.-Q. Ma. Analysis methods for results in gamma-ray astronomy. *Astrophysical Journal*, 272:317, September 1983. 41

[Lob06] A. P. Lobanov. Nuclear activity in galaxies driven by binary supermassive black holes. *ArXiv Astrophysics e-prints*, June 2006, arXiv:astro-ph/0606198. Contribution to ESO Astrophysical Symposia, "Relativistic Astrophysics and Cosmology", eds. B. Aschenbach, V. Burwitz, G. Hasinger, B. Leibundgut (Springer: Heidelberg 2006). 21

[Lon10] Malcom Sim Longair. *High Energy Astrophysics*. Cambridge University Press, third edition, 2010. 3

[Lon11] F. Longo. Private communication, November 2011. 76

[LS11] A. Letessier-Selvon and T. Stanev. Ultrahigh Energy Cosmic Rays. *ArXiv e-prints*, February 2011, 1103.0031. 3

[LTN11] A. Lähteenmäki, M. Tornikoski, and E. Nieppola. Private communication, February 2011. 70, 167

[M+96] M. J. M. Marcha et al. Optical spectroscopy and polarization of a new sample of optically bright flat radio spectrum sources. *Monthly Notices of the Royal Astronomical Society*, 281:425–448, July 1996. 67

[M+00] A. Mücke et al. Monte Carlo simulations of photohadronic processes in astrophysics. *Computer Physics Communications*, 124:290–314, February 2000, arXiv:astro-ph/9903478. 13

[M+03] J. M. Mas-Hesse et al. OMC: An Optical Monitoring Camera for INTEGRAL. Instrument description and performance. *Astronomy & Astrophysics*, 411:L261–L268, November 2003. 28

[M+05] D. C. Martin et al. The Galaxy Evolution Explorer: A Space Ultraviolet Survey Mission. *Astrophysical Journal Letters*, 619:L1–L6, January 2005, arXiv:astro-ph/0411302. 29

[M+07] L. Mayer et al. Rapid Formation of Supermassive Black Hole Binaries in Galaxy Mergers with Gas. *Science*, 316:1874, June 2007. arXiv:astro-ph/0706.1562. 20

[M+08a] A. P. Marscher et al. The inner jet of an active galactic nucleus as revealed by a radio-to-γ-ray outburst. *Nature*, 452:966–969, April 2008. 17

[M+08b] F. Massaro et al. X-ray spectral evolution of TeV BL Lacertae objects: eleven years of observations with BeppoSAX, XMM-Newton and Swift satellites. *Astronomy & Astrophysics*, 478:395–401, February 2008, 0712.2116. 74, 98, 152, 182

[M+09a] M. Matsuoka et al. The MAXI Mission on the ISS: Science and Instruments for Monitoring All-Sky X-Ray Images. *Publications of the Astronomical Society of Japan*, 61:999–, October 2009, 0906.0631. 110

[M+09b] H. Miyamoto et al. SiPM development and application for astroparticle physics experiments. In *31st International Cosmic Ray Conference, Łódź, Poland*, International Cosmic Ray Conference, page 1320, July 2009. Published online: http://icrc2009.uni.lodz.pl/proc/html. 48

[M+09c] A. Moralejo et al. MARS, the MAGIC Analysis and Reconstruction Software. In *31st International Cosmic Ray Conference, Łódź, Poland*, International Cosmic Ray Conference, page 0469, July 2009, 0907.0943. Published online: http://icrc2009.uni.lodz.pl/proc/html. 39

[M+10] L. Ma et al. CCD photometry of five X-ray selected BL Lacertae objects. *Astrophysics and Space Science*, 327:35–58, May 2010. 68

[M+11] A. Mennella et al. Planck early results: First assessment of the Low Frequency Instrument in-flight performance. *Astronomy & Astrophysics*, January 2011, 1101.2038. 27

[Mag97] N. Magnussen. The MAGIC Telescope Project for Gamma Astronomy above 10 GeV. In *36th INFN ELOISATRON Workshop on New Detectors, Erice, Italy*, November 1997. arXiv:astro-ph/9805.184. 115

[MAL65] I. H. MALITSON. Interspecimen comparison of the refractive index of fused silica. *J. Opt. Soc. Am.*, 55(10):1205–1208, Oct 1965. 53

[Man93] K. Mannheim. The proton blazar. *Astronomy & Astrophysics*, 269:67, March 1993. 19

[Man95] K. Mannheim. High-energy neutrinos from extragalactic jets. *Astroparticle Physics*, 3:295–302, May 1995. 19

[McK06] M. McKee. Black holes collide in the best simulation yet. *New Scientist*, April 2006.
http://www.newscientist.com/article/dn9012.html. 21

[MD03] R. J. McLure and J. S. Dunlop. On the Black Hole – Bulge Mass Relation in Active and Inactive Galaxies. In R. Bender & A. Renzini, editor, *The Mass of Galaxies at Low and High Redshift*, page 26, 2003, arXiv:astro-ph/0201081. 68

[Méz10] Pétér Mézároz. *The High Energy Universe – Ultra-High Energy Events in Astrophysics and Cosmology*. Cambridge University Press, 2010. 3

[MF01a] D. Merritt and L. Ferrarese. Relationship of Black Holes to Bulges. In J. H. Knapen, J. E. Beckman, I. Shlosman, & T. J. Mahoney, editor, *The Central Kiloparsec of Starbursts and AGN: The La Palma Connection*, volume 249 of *Astronomical Society of the Pacific Conference Series*, page 335, 2001, arXiv:astro-ph/0107134. 68

[MF01b] D. Merritt and L. Ferrarese. The M.-σ Relation for Supermassive Black Holes. *Astrophysical Journal*, 547:140–145, January 2001, arXiv:astro-ph/0008310. 68

[MHZ10] M. Meyer, D. Horns, and H.-S. Zechlin. The Crab Nebula as a standard candle in very high-energy astrophysics. *Astronomy & Astrophysics*, 523:A2+, November 2010, 1008.4524. 31, 89, 90, 91, 161, 163, 164

[MP01] A. Muecke and R. J. Protheroe. A proton synchrotron blazar model for flaring in Markarian 501. *Astroparticle Physics*, 15:121–136, March 2001, arXiv:astro-ph/0004052. 13, 19

[MR07] D. Mazin and M. Raue. New limits on the density of the extragalactic background light in the optical to the far infrared from the spectra of all known TeV blazars. *Astronomy & Astrophysics*, 471:439–452, August 2007, arXiv:astro-ph/0701694. 16

[MT10] H. Miyamoto and M. Teshima. SiPM development for the imaging Cherenkov and fluorescence telescopes. *Nuclear Instruments and Methods in Physics Research A*, 623:198–200, November 2010. 48

[Mun06] J. L. Munõz. *Measurement of the invariance of the speed of light observing the active galactic nucleus Mkn421 with the MAGIC Telescope*. PhD thesis, Universitat Autonoma de Barcelona, June 2006. 35

[Mur00] P. Murdin. *Michigan Radio Astronomy Observatory*. November 2000. 25

[N+94] P. J. Napier et al. The Very Long Baseline Array. *IEEE Proceedings*, 82:658–672, May 1994. 27

[N+07a] E. Nieppola et al. 37 GHz Observations of a Large Sample of BL Lacertae Objects. *Astronomical Journal*, 133:1947–1953, May 2007, 0705.0887. 26

[N+07b] K. Nilsson et al. Host galaxy subtraction of TeV candidate BL Lacertae objects. *Astronomy & Astrophysics*, 475:199–207, November 2007, 0709.2533. 72, 126

[NCS11] NASA, CXC, and SAO. Official website, July 2011. http://chandra.harvard.edu/xray_astro/absorption.html. 14

[NCW07] NASA, CXC, and M. Weiss. Official website of the NASA, November 2007. http://www.nasa.gov/missions/deepspace/Chandra_black_hole_engines_prt.htm. 22

[NI11] NASA and IPAC. Nasa/ipac extragalactic database (ned), November 2011. http://ned.ipac.caltech.edu. 165, 166

[Nis99] T. Nishiyama. Detection of a new TeV gamma-ray source of BL Lac object 1ES 1959+650. In 26th *International Cosmic Ray Conference ICRC, Salt Lake City, USA*, volume 3 of *International Cosmic Ray Conference*, page 370, August 1999. 77

[NST11] A. Neronov, D. V. Semikoz, and A. M. Taylor. Very hard gamma-ray emission from a flare of Mrk 501. *ArXiv e-prints*, April 2011, 1104.2801. 19

[NTE83] P. J. Napier, A. R. Thompson, and R. D. Ekers. The Very Large Array - Design and performance of a modern synthesis radio telescope. *IEEE Proceedings*, 71:1295–1320, November 1983. 27

[NTV06] E. Nieppola, M. Tornikoski, and E. Valtaoja. Spectral energy distributions of a large sample of BL Lacertae objects. *Astronomy & Astrophysics*, 445:441–450, January 2006, arXiv:astro-ph/0509045. 98

[Oso06] S. Osone. Study of 23 day periodicity of Blazar Mkn501 in 1997. *Astroparticle Physics*, 26:209, October 2006. arXiv:astro-ph/0506.328. 21

[OvE09] S. Ohm, C. van Eldik, and K. Egberts. γ/hadron separation in very-high-energy γ-ray astronomy using a multivariate analysis method. *Astroparticle Physics*, 31:383–391, June 2009, 0904.1136. 42

[P^+92] M. Punch et al. Detection of TeV photons from the active galaxy Markarian 421. *Nature*, 358:477–+, August 1992. 64

[P^+96] E. S. Perlman et al. The Einstein Slew Survey Sample of BL Lacertae Objects. *Astrophysical Journal Supplements*, 104:251, June 1996. 67, 68, 69

[P^+97] A. N. Parmar et al. The low-energy concentrator spectrometer on-board the BeppoSAX X-ray astronomy satellite. *Astronomy and Astrophysics Supplement*, 122:309–326, April 1997. 30

[P^+98] R. J. Protheroe et al. Very High Energy Gamma Rays from Markarian 501. In M. S. Potgieter, B. C. Raubenheimer, & D. J. van der Walt, editor, *25th International Cosmic Ray Conference, Durban, South Africa*, volume 8 of *International Cosmic Ray Conference*, pages 317–+, 1998, arXiv:astro-ph/9710118. 65

[P^+03a] M. Prest et al. The AGILE silicon tracker: an innovative /γ-ray instrument for space. *Nuclear Instruments and Methods in Physics Research A*, 501:280–287, March 2003. 31

[P^+03b] G. Pühlhofer et al. The technical performance of the HEGRA system of imaging air Cherenkov telescopes. *Astroparticle Physics*, 20:267–291, December 2003, arXiv:astro-ph/0306123. 36

[P^+05] E. S. Perlman et al. Intrinsic Curvature in the X-Ray Spectra of BL Lacertae Objects. *Astrophysical Journal*, 625:727–740, June 2005, arXiv:astro-ph/0502298. 73, 98, 151

[P^+07a] I. H. Park et al. Silicon charge detector for the CREAM experiment. *Nuclear Instruments and Methods in Physics Research A*, 570:286, January 2007. 5

[P+07b] R. Pegna et al. A GHz sampling DAQ system for the MAGIC-II telescope. *Nuclear Instruments and Methods in Physics Research A*, 572:382–384, March 2007. 47

[P+08] T. S. Poole et al. Photometric calibration of the Swift ultraviolet/optical telescope. *Monthly Notices of the Royal Astronomical Society*, 383:627–645, January 2008, 0708.2259. 29

[P+09a] C. Pittori et al. First AGILE catalog of high-confidence gamma-ray sources. *Astronomy & Astrophysics*, 506:1563–1574, November 2009, 0902.2959. 76

[P+09b] A. B. Pushkarev et al. Jet opening angles and gamma-ray brightness of AGN. *Astronomy & Astrophysics*, 507:L33–L36, November 2009, 0910.1813. 71

[P+10] E. Prandini et al. Constraining blazar distances with combined Fermi and TeV data: an empirical approach. *Monthly Notices of the Royal Astronomical Society*, 405:L76–L80, June 2010, 1003.1674. 16

[Pal09] D. M. Palmer. A Fast Chi-Squared Technique for Period Search of Irregularly Sampled Data. *Astrophysical Journal*, 695:496–502, April 2009, 0901.1913. 80

[Pan11] D. Paneque. Private communication, February 2011. 70, 72, 89, 97, 124, 140, 141, 142, 143, 190

[PE04] B. G. Piner and P. G. Edwards. The Parsec-Scale Structure and Jet Motions of the TeV Blazars 1ES 1959+650, PKS 2155-304, and 1ES 2344+514. *Astrophysical Journal*, 600:115–126, January 2004, arXiv:astro-ph/0309547. 69, 71, 166

[Per10] Donald H. Perkins. *Particle Astrophysics*. Oxford University Press, second edition, 2010. 3

[Pf09] A. Pichel and for the VERITAS Collaboration. Highlights from the Whipple 10-m Blazar Monitoring Program. In *31st International Cosmic Ray Conference, Łódź, Poland*, International Cosmic Ray Conference, page 0636, July 2009, 0908.0010. Published online: http://icrc2009.uni.lodz.pl/proc/html. 64

[PM11] M. Petropoulou and A. Mastichiadis. Implications of automatic photon quenching on compact gamma-ray sources. *Astronomy & Astrophysics*, 532:A11, August 2011, 1105.3852. 102

[Pog06] R. Poggiani. Search for Rapid Optical Variability in Three Gamma-Ray Loud Blazars. *Astrophysics and Space Science*, 306:17–22, December 2006. 68

[PPE08] B. G. Piner, N. Pant, and P. G. Edwards. The Parsec-Scale Jets of the TeV Blazars H1426+428, 1ES 1959+650, and PKS 2155-304: 2001-2004. *Astrophysical Journal*, 678:64–77, May 2008, 0801.2749. 69, 71, 166

[PPE10] B. G. Piner, N. Pant, and P. G. Edwards. The Jets of TeV Blazars at Higher Resolution: 43 GHz and Polarimetric VLBA Observations from 2005 to 2009. *Astrophysical Journal*, 723:1150–1167, November 2010, 1009.2269. 69, 70, 71, 166

[PS10] J. Poutanen and B. Stern. GeV Breaks in Blazars as a Result of Gamma-ray Absorption Within the Broad-line Region. *Astrophysical Journal Letters*, 717:L118–L121, July 2010, 1005.3792. 103

[PU92] P. Padovani and C. M. Urry. Luminosity functions, relativistic beaming, and unified theories of high-luminosity radio sources. *Astrophysical Journal*, 387:449, March 1992. 17

[Pun08] Brian Punsly. *Black Hole Gravitohydromagnetics*. Springer-Verlag Berlin Heidelberg, second edition, 2008. 17

[Q+96] J. Quinn et al. Detection of Gamma Rays with E > 300 GeV from Markarian 501. *Astrophysical Journal Letters*, 456:L83+, January 1996. 65

[R+97] R. B. Rengelink et al. The Westerbork Northern Sky Survey (WENSS), I. A 570 square degree Mini-Survey around the North Ecliptic Pole. *Astronomy and Astrophysics Supplement*, 124:259–280, August 1997. 26

[R+98] R. E. Rothschild et al. In-Flight Performance of the High-Energy X-Ray Timing Experiment on the Rossi X-Ray Timing Explorer. *Astrophysical Journal*, 496:538–+, March 1998, arXiv:astro-ph/9710328. 30

[R+01] P. S. Ray et al. The USA X-ray timing experiment. *X-ray Astronomy: Stellar Endpoints, AGN, and the Diffuse X-ray Background*, 599:336–345, December 2001. 73

[R+05a] B. Riegel et al. A systematic study of the interdependence of IACT image parameters. In *International Cosmic Ray Conference*, volume 5 of *International Cosmic Ray Conference*, pages 215–+, 2005. 42

[R+05b] P. W. A. Roming et al. The Swift Ultra-Violet/Optical Telescope. *Space Science Reviews*, 120:95–142, October 2005, arXiv:astro-ph/0507413. 29

[R+09a] E. Resconi et al. The classification of flaring states of blazars. *Astronomy & Astrophysics*, 502:499–504, August 2009, 0904.1371. 63

[R+09b] C. Rödig et al. Multiwavelength periodicity study of Markarian 501. *Astronomy & Astrophysics*, 501:925–932, July 2009, 0904.4392. 21

[R+09c] C. Rodriguez et al. H I Observations of the Supermassive Binary Black Hole System in 0402+379. *Astrophysical Journal*, 697:37–44, May 2009, 0902.4444. 20

[R+10] A. A. Radu et al. A Site Evaluation Campaign for a Ground Based Atmospheric Cherenkov Telescope in Romania. *ArXiv e-prints*, November 2010, 1011.2741. 113

[R+11a] A. A. Radu et al. An astroclimatological study of candidate sites to host an imaging atmospheric Cherenkov telescope in Romania. *ArXiv e-prints*, October 2011, 1110.2304. 113

[R+11b] C. Ramos Almeida et al. Are luminous radio-loud active galactic nuclei triggered by galaxy interactions? *ArXiv e-prints*, August 2011, 1109.0021. accepted for publication in MNRAS. 21

[R+11c] A. Rappoldi et al. Preliminary results on TeV sources search with AGILE. *Nuclear Instruments and Methods in Physics Research A*, 630:202–205, February 2011. 76

[R+11d] J. L. Richards et al. Blazars in the Fermi Era: The OVRO 40 m Telescope Monitoring Program. *Astrophysical Journal Supplements*, 194:29–+, June 2011, 1011.3111. 26

[Rad08] A. A. Radu. Towards gamma ray astronomy at the institute for space science, October 2008. Presented at *12th ASPERA National Day*, Bucharest, Romania http://www.aspera-eu.org/index.php?option=com_content&task=view&id=300&Itemid=141. 113

[RBP05] A. Reimer, M. Böttcher, and S. Postnikov. Neutrino Emission in the Hadronic Synchrotron Mirror Model: The "Orphan" TeV Flare from 1ES 1959+650. *Astrophysical Journal*, 630:186–190, September 2005, arXiv:astro-ph/0505233. 19, 78

[Ree67] M. J. Rees. Studies in radio structure-II. The relaxation of relativistic electron spectra in self-absorbed radio sources. *Monthly Notices of the Royal Astronomical Society*, 136:279–+, 1967. 15

[Ree07] P. Reegen. SigSpec. I. Frequency- and phase-resolved significance in Fourier space. *Astronomy & Astrophysics*, 467:1353–1371, June 2007, arXiv:physics/0703160. 80

[Rej98] A. Rej. Gamma-ray Bursts, Supernovae and Interacting Galaxies. In J. Paul, T. Montmerle, and E. Aubourg, editors, *Abstracts of the* 19*th* *Texas Symposium on Relativistic Astrophysics and Cosmology, Paris, France*, page 14, December 1998. 8

[RGS03] T. A. Rector, D. C. Gabuzda, and J. T. Stocke. The Radio Structure of High-Energy-Peaked BL Lacertae Objects. *Astronomical Journal*, 125:1060–1072, March 2003, arXiv:astro-ph/0302397. 69, 71

[Rie05a] Benjamin Riegel. Systematische Untersuchung der Bildparameter zur Entwicklung einer Standardanalyse für das MAGIC-Teleskop. Diplomarbeit, Julius-Maximilians-Universität Würzburg, July 2005. 42

[Rie05b] F. M. Rieger. Periodic variability and binary black hole systems in blazars. In F. A. Aharonian, H. J. Völk, & D. Horns, editor, *High Energy Gamma-Ray Astronomy*, volume 745 of *American Institute of Physics Conference Series*, pages 487–492, February 2005, arXiv:astro-ph/0506720. 18

[Rie07] F. M. Rieger. Supermassive binary black holes among cosmic gamma-ray sources. *Astrophysics and Space Science*, 309:271, June 2007. arXiv:astro-ph/0611.224. 21

[Rie08] F. M. Rieger. Possible variability signatures of Supermassive Binary Black Holes in Blazars. In *Blazar Variability across the Electromagnetic Spectrum*, volume BLAZARS2008 of *Proceedings of Science*, 2008. 21

[Rit04] S. Ritt. The DRS2 Chip: a 4.5 GHz Waveform Digitizing Chip for the MEG Experiment. In *Proc. IEEE Nat. Science Symp.*, 2004. 46

[Rit08] S. Ritt. Design and Performance of the 6 GHz Waveform Digitizing Chip DRS4. In *Proc. IEEE Nat. Science Symp.*, 2008. 48

[RL85] George B. Rybicki and Alan P. Lightman. *Radiative Processes in Astrophysics*. John Wiley & Sons, 1985. 13

[RL09] D. Renker and E. Lorenz. Advances in solid state photon detectors. *Journal of Instrumentation*, 4:4004, April 2009. 46

[RM00] F. M. Rieger and K. Mannheim. Implications of a possible 23 day periodicity for binary black hole models in Mkn 501. *Astronomy & Astrophysics*, 359:948–952, July 2000, arXiv:astro-ph/0005478. 21

[RM01] F. M. Rieger and K. Mannheim. A Possible Black Hole Binary in Mkn 501. In F. A. Aharonian and H. J. Völk, editors, *American Institute of Physics Conference Series*, volume 558 of *American Institute of Physics Conference Series*, page 716, 2001. 21, 22

[RMR11] E. Rivers, A. Markowitz, and R. Rothschild. Spectral Survey of X-ray Bright Active Galactic Nuclei from the Rossi X-ray Timing Explorer. *Astrophysical Journal Supplements*, 193:3, March 2011, 1101.1545. 74

[Rol09] Sebastian Rollke. Untersuchung von Charakteristika von SiPM für ihren Einsatz als Photomultiplier in Teleskopen und Vermessung von Ganz-Aluminium-Spiegeln für das DWARF-Teleskop. Diplomarbeit, Technische Universität Dortmund, November 2009. 51, 53

[S^+88] A. Sillanpää et al. OJ 287 - Binary pair of supermassive black holes. *Astrophysical Journal*, 325:628–634, February 1988. 19, 21

[S^+93a] J. F. Schachter et al. Ten new BL Lacertae objects discovered by an efficient X-ray/radio/optical technique. *Astrophysical Journal*, 412:541–549, August 1993. 67, 73

[S^+93b] V. Schoenfelder et al. Instrument description and performance of the Imaging Gamma-Ray Telescope COMPTEL aboard the Compton Gamma-Ray Observatory. *Astrophysical Journal Supplements*, 86:657–692, June 1993. 31

[S^+99] R. Scarpa et al. The Hubble Space Telescope Survey of BL Lacertae Objects: Gravitational Lens Candidates and Other Unusual Sources. *Astrophysical Journal*, 521:134–144, August 1999, arXiv:astro-ph/9902333. 67, 69

[S+00] V. Schönfelder et al. The first COMPTEL source catalogue. *Astronomy and Astrophysics Supplement*, 143:145–179, April 2000, arXiv:astro-ph/0002366. 31, 75

[S+01] L. Strüder et al. The European Photon Imaging Camera on XMM-Newton: The pn-CCD camera. *Astronomy & Astrophysics*, 365:L18–L26, January 2001. 30

[S+06] M. F. Skrutskie et al. The Two Micron All Sky Survey (2MASS). *Astronomical Journal*, 131:1163–1183, February 2006. 27, 177

[S+08a] J. R. Sacahui et al. A High Altitude Mexican ACT Project, OMEGA. In F. A. Aharonian, W. Hofmann, and F. Rieger, editors, *American Institute of Physics Conference Series*, volume 1085 of *American Institute of Physics Conference Series*, pages 858–861, December 2008. 113

[S+08b] J. G. Stacy et al. Limits on MeV Gamma-Ray Emission from Active Galaxies and Other Unidentified High-Latitude Gamma-Ray Sources Observed with COMPTEL. In *International Cosmic Ray Conference*, volume 3 of *International Cosmic Ray Conference*, pages 1085–1088, 2008. 31, 75

[S+08c] D. Steele et al. Results from the Blazar Monitoring Campaign at the Whipple 10m Gamma-ray Telescope. In *30th International Cosmic Ray Conference, Mérida, Mexico*, volume 3 of *International Cosmic Ray Conference*, pages 989–992, 2008, 0709.3869. 66, 110

[S+09a] T. Sakamoto et al. Goddard Robotic Telescope. In C. Meegan, C. Kouveliotou, & N. Gehrels, editor, *American Institute of Physics Conference Series*, volume 1133 of *American Institute of Physics Conference Series*, pages 244–246, May 2009. 28

[S+09b] K. Satalecka et al. Monitoring of Bright Blazars with MAGIC in the 2007/2008 Season. In D. Bastieri and R. Rando, editors, *American Institute of Physics Conference Series*, volume 1112 of *American Institute of Physics Conference Series*, pages 223–232, April 2009, 0902.4594. 78

[S+10] K. V. Sokolovsky et al. Constraints on the gamma-ray emitting region in blazars from multi-frequency VLBI measurements. In T. Savolainen, E. Ros, R. W. Porcas, and J. A. Zensus, editors, *Fermi meets Jansky - AGN in Radio and Gamma-Rays*, pages 167–170, June 2010, 1006.3084. 105

[S+11] G. D. Senturk et al. GeV-TeV Blazar Population Studies. *ArXiv e-prints*, November 2011, 1111.0378. 103

[Sat10] Konstancja Satalecka. *Multimessenger studies of point-sources using the IceCube neutrino telescope and the MAGIC gamma-ray telescope*. PhD thesis, Humbold-Universität zu Berlin, May 2010. 78, 83, 85, 86

[SBAe08] K. Satalecka, E. Bernardini, M. Ackermann, and et al. Cluster Search for neutrino flares from pre-defined directions. In *30th International Cosmic Ray Conference, Mérida, Mexico*, volume 5 of *International Cosmic Ray Conference*, pages 1353–1356, 2008. 63, 78

[Sca93] L. Scarsi. SAX overview. *Astronomy and Astrophysics Supplement*, 97:371–383, January 1993. 30

[Sch63] M. Schmidt. 3C 273 : A Star-Like Object with Large Red-Shift. *Nature*, 197:1040, March 1963. 17

[Sch06a] R. Schmitt. Beobachtung von 1ES1959+650 mit dem MAGIC-Teleskop. Diplomarbeit, Julius-Maximilians-Universität Würzburg, June 2006. 78, 85, 86

[Sch06b] Peter Schneider. *Einführung in die Extragalaktische Astronomie und Kosmologie*. Springer-Verlag Berlin Heidelberg, 2006. 16, 20

[Sch07a] F. Schmidt. Corsika shower images, November 2007. `http://www.ast.leeds.ac.uk/~fs/showerimages.html`. 36

[Sch07b] M. Scholz. *Scalable and Accurate Knowledge Discovery in Real-World Databases*. PhD thesis, Universität Dortmund, 2007. 42

[Sch09] Cornelia Schulz. Novel All-Aluminium Mirrors of the MAGIC Telescope Project and Low Light Level Silicon Photo-Multiplier Sensors for Future Telescopes. Diplomarbeit, Fachhochschule München, October 2009. 50, 52, 54

[SK07] Ł. Stawarz and J. G. Kirk. Automatic Quenching of High-Energy γ-Ray Sources by Synchrotron Photons. *Astrophysical Journal Letters*, 661:L17–L20, May 2007, arXiv:astro-ph/0701633. 102

[SNO02] SNO Collaboration. Direct Evidence for Neutrino Flavor Transformation from Neutral-Current Interactions in the Sudbury Neutrino Observatory. *Physical Review Letters*, 89:11301, 2002. 12

[Sta10] Todor Stanev. *High Energy Cosmic Rays*. Springer-Verlag Berlin Heidelberg, second edition, 2010. 3, 4

[Sup98] SuperKamiokande Collaboration. Evidence for Oscillation of Atmospheric Neutrinos. *Physical Review Letters*, 81:1562, 1998. 12

[SVA74] W. C. Saslaw, M. J. Valtonen, and S. J. Aarseth. The Gravitational Slingshot and the Structure of Extragalactic Radio Sources. *Astrophysical Journal*, 190:253–270, June 1974. 20

[T$^+$80] A. R. Thompson et al. The Very Large Array. *Astrophysical Journal Supplements*, 44:151–167, October 1980. 27

[T$^+$01] M. J. L. Turner et al. The European Photon Imaging Camera on XMM-Newton: The MOS cameras : The MOS cameras. *Astronomy & Astrophysics*, 365:L27–L35, January 2001, arXiv:astro-ph/0011498. 30

[T$^+$02] S. Tremaine et al. The Slope of the Black Hole Mass versus Velocity Dispersion Correlation. *Astrophysical Journal*, 574:740–753, August 2002, arXiv:astro-ph/0203468. 68

[T+03] G. Tagliaferri et al. Wide band X-ray and optical observations of the BL Lac object 1ES 1959+650 in high state. *Astronomy & Astrophysics*, 412:711–720, December 2003, arXiv:astro-ph/0309568. 180, 181

[T+05] N. Tonello et al. Observation of gamma-ray emission above 200 GeV from the AGN 1ES1959+650 during low x-ray and optical activity. In *International Cosmic Ray Conference*, volume 4 of *International Cosmic Ray Conference*, page 339, 2005. 78

[T+07a] L. O. Takalo et al. Optical Monitoring of Candidate TeV Blazars. In L. C. Ho & J.-W. Wang, editor, *The Central Engine of Active Galactic Nuclei*, volume 373 of *Astronomical Society of the Pacific Conference Series*, page 249, October 2007. 71

[T+07b] A. Tramacere et al. SWIFT observations of TeV BL Lacertae objects. *Astronomy & Astrophysics*, 467:501–508, May 2007, arXiv:astro-ph/0611276. 73, 98, 178, 182

[T+08a] G. Tagliaferri et al. Simultaneous Multiwavelength Observations of the Blazar 1ES 1959+650 at a Low TeV Flux. *Astrophysical Journal*, 679:1029–1039, June 2008, 0801.4029. 71, 72, 73, 75, 78, 86, 101, 102, 105, 106, 115, 139, 144, 156, 178, 182, 183, 184, 185, 186, 191

[T+08b] M. Tavani et al. The AGILE space mission. *Nuclear Instruments and Methods in Physics Research A*, 588:52–62, April 2008. 31

[T+08c] M. Teshima et al. SiPM development for Astroparticle Physics applications. In *30th International Cosmic Ray Conference, Mérida, Mexico*, volume 5 of *International Cosmic Ray Conference*, pages 985–988, 2008, 0709.1808. 46

[T+08d] J. Tueller et al. Swift BAT Survey of AGNs. *Astrophysical Journal*, 681:113–127, July 2008, 0711.4130. 74

[T+10a] F. Tavecchio et al. TeV BL Lac objects at the dawn of the Fermi era. *Monthly Notices of the Royal Astronomical Society*, 401:1570–1586, January 2010, 0909.0651. 105

[T+10b] G. B. Thomson et al. Results from the Telescope Array Experiment. In *35th International Conference of High Energy Physics*, volume ICHEP 2010 of *Proceedings of Science*, October 2010, 1010.5528. 5, 6

[T+10c] M. Tluczykont et al. Long-term lightcurves from combined unified very high energy γ-ray data. *Astronomy & Astrophysics*, 524:A48+, December 2010, 1010.5659. 64, 80

[T+10d] D. B. Tridon et al. The MAGIC-II gamma-ray stereoscopic telescope system. *Nuclear Instruments and Methods in Physics Research A*, 623:437–439, November 2010. 39

[T$^+$10e] J. Tueller et al. The 22 Month Swift-BAT All-Sky Hard X-ray Survey. *Astrophysical Journal Supplements*, 186:378–405, February 2010, 0903.3037. 74, 187

[T$^+$11] M. Tsujimoto et al. Cross-calibration of the X-ray instruments onboard the Chandra, INTEGRAL, RXTE, Suzaku, Swift, and XMM-Newton observatories using G21.5-0.9. *Astronomy & Astrophysics*, 525:A25+, January 2011, 1009.2812. 29

[TDDH11] P. Tsalmantza, R. Decarli, M. Dotti, and D. W. Hogg. A Systematic Search for Massive Black Hole Binaries in the Sloan Digital Sky Survey Spectroscopic Sample. *Astrophysical Journal*, 738:20–+, September 2011, 1106.1180. 20

[Tes09] D. Tescaro. Private communication, August 2009. 85, 86

[The05] The High Resolution Fly's Eye Collaboration. Monocular Measurement of the Spectrum of UHE Cosmic Rays by the FADC Detector of the HiRes Experiment. *Astroparticle Physics*, 23:157, 2005. arXiv:astro-ph/0208.301. 9

[The10] The CTA Consortium. Design Concepts for the Cherenkov Telescope Array. *ArXiv e-prints*, page 1008.3703, August 2010, 1008.3703. 45

[The11a] The Fermi-LAT Collaboration. Fermi Large Area Telescope Second Source Catalog. *Astrophysical Journal Supplement Series*, August 2011, 1108.1435. Submitted for publication. 77, 189

[The11b] The Pierre Auger Collaboration. The Pierre Auger Observatory I: The Cosmic Ray Energy Spectrum and Related Measurements. In *32nd International Cosmic Ray Conference, Beijing, China*, International Cosmic Ray Conference, July 2011, 1107.4809. 9, 10

[The11c] The Pierre Auger Collaboration. The Pierre Auger Observatory II: Studies of Cosmic Ray Composition and Hadronic Interaction models. In *32nd International Cosmic Ray Conference, Beijing, China*, International Cosmic Ray Conference, July 2011, 1107.4804. 5, 6

[Thi12] Anita M. Thieler. *Period Search for Unevenly Sampled Datasets with Red Noise*. PhD thesis, Technische Universität Dortmund, 2012. in preparation. 82

[Tho04] G. Thomson. New Results from the HiRes Experiment. *Nuclear Physics B Proceedings Supplements*, 136:28–33, November 2004. 5

[TK03] N. Tonello and D. Kranich. Study of the VHE Gamma Ray Emission from the AGN 1ES1959+650 with the HEGRA Cherenkov Telescope CT1. In *International Cosmic Ray Conference*, volume 5 of *International Cosmic Ray Conference*, page 2615, July 2003. 78, 83

[TMG98a] F. Tavecchio, L. Maraschi, and G. Ghisellini. Constraints on the Physical Parameters of TeV Blazars. *Astrophysical Journal*, 509:608–619, December 1998, arXiv:astro-ph/9809051. 19

[TMG98b] F. Tavecchio, L. Maraschi, and G. Ghisellini. Constraints on the Physical Parameters of TeV Blazars. *Astrophysical Journal*, 509:608–619, December 1998, arXiv:astro-ph/9809051. 101

[Ton06] Nadia Tonello. *Study of the VHE gamma-ray emission from the Active Galactic Nucleus 1ES1959+650*. PhD thesis, Technische Universität München, February 2006. 78, 83, 85, 86, 191, 192

[Tru82] J. Truemper. The ROSAT mission. *Advances in Space Research*, 2:241–249, 1982. 73

[TSKB07] M. Tluczykont, M. Shayduk, O. Kalekin, and E. Bernardini. Long-term gamma-ray lightcurves and high state probabilities of Active Galactic Nuclei. *Journal of Physics Conference Series*, 60:318–320, March 2007. 64

[Tt06] N. Tonello and the MAGIC collaboration. Observation of the AGN 1ES1959 + 650 with the MAGIC telescope. *Journal of Physics Conference Series*, 39:457–459, May 2006. 78

[Tt09] Y. Tameda and the Telescope Array Experiment. Telescope Array Experiment. *Nuclear Physics B Proceedings Supplements*, 196:74–79, December 2009. 5

[UB07] A. Unsöld and B. Baschek. *Der neue Kosmos*. Springer, 7th edition, November 2007. 12

[Uel09] Malwina Uellenbeck (geb. Thom). Anaylse der Quelle 1ES 1959+650 mit MAGIC und die Implementierung eines Webinterfaces für die automatische Monte-Carlo-Produktion. Diplomarbeit, Technische Universität Dortmund, July 2009. 78, 85, 86, 156, 192

[Uel12] Malwina Uellenbeck (geb. Thom). *Analyse von Aktiven Galaktischen Kernen mit MAGIC (Arbeitstitel)*. PhD thesis, Technische Universität Dortmund, 2012. in preparation. 78, 85, 86, 156, 192

[UP95] C. M. Urry and P. Padovani. Unified Schemes for Radio-Loud Active Galactic Nuclei. *The Publications of the Astronomical Society of the Pacific*, 107:803–+, September 1995, arXiv:astro-ph/9506063. 17

[Urr04] C. Urry. AGN Unification: An Update. In G. T. Richards & P. B. Hall, editor, *AGN Physics with the Sloan Digital Sky Survey*, volume 311 of *Astronomical Society of the Pacific Conference Series*, pages 49–+, June 2004, arXiv:astro-ph/0312545. 17

[V$^+$96] G. E. Villa et al. EPIC system onboard the ESA XMM. In O. H. Siegmund & M. A. Gummin, editor, *Society of Photo-Optical Instrumentation Engineers (SPIE) Conference Series*, volume 2808 of *Society of Photo-Optical Instrumentation Engineers (SPIE) Conference Series*, pages 402–413, October 1996. 29

[V$^+$99a] W. Voges et al. The ROSAT all-sky survey bright source catalogue. *Astronomy & Astrophysics*, 349:389–405, September 1999, arXiv:astro-ph/9909315. 73

[V$^+$99b] H.-H. Voigt et al. *Landolt-Börnstein: Numerical Data and Functional Relationships in Science and Technology.* Springer, 1999. 5

[V$^+$03] S. Vaughan et al. On characterizing the variability properties of X-ray light curves from active galaxies. *Monthly Notices of the Royal Astronomical Society*, 345:1271–1284, November 2003, arXiv:astro-ph/0307420. 79

[V$^+$07] F. Verrecchia et al. The BeppoSAX WFC X-ray source catalogue. *Astronomy & Astrophysics*, 472:705–713, September 2007. 73, 75

[V$^+$08] M. J. Valtonen et al. A massive binary black-hole system in OJ287 and a test of general relativity. *Nature*, 452:851–853, April 2008, 0809.1280. 21

[Vas99] V. V. Vassiliev. VERITAS: Performance characteristics (baseline design). In 26th *International Cosmic Ray Conference ICRC, Salt Lake City, USA*, volume 5 of *International Cosmic Ray Conference*, page 299, 1999. 115

[Vie95] M. Vietri. The Acceleration of Ultra–High-Energy Cosmic Rays in Gamma-Ray Bursts. *Astrophysical Journal*, 453:883–+, November 1995, arXiv:astro-ph/9506081. 10

[VMD09] M. Volonteri, J. M. Miller, and M. Dotti. Sub-Parsec Supermassive Binary Quasars: Expectations at $z < 1$. *Astrophysical Journal Letters*, 703:L86–L89, September 2009, 0903.3947. 21

[VV06] M.-P. Véron-Cetty and P. Véron. A catalogue of quasars and active nuclei: 12th edition. *Astronomy & Astrophysics*, 455:773–777, August 2006. 10

[W$^+$89] T. C. Weekes et al. Observation of TeV gamma rays from the Crab nebula using the atmospheric Cerenkov imaging technique. *Astrophysical Journal*, 342:379–395, July 1989. 36, 110

[W$^+$03] C. Winkler et al. The INTEGRAL mission. *Astronomy & Astrophysics*, 411:L1–L6, November 2003. 28

[W$^+$04] M. W. Werner et al. The Spitzer Space Telescope Mission. *Astrophysical Journal Supplements*, 154:1–9, September 2004, arXiv:astro-ph/0406223. 27

[W$^+$05] J.-H. Woo et al. Black Hole Masses and Host Galaxy Evolution of Radio-Loud Active Galactic Nuclei. *Astrophysical Journal*, 631:762–772, October 2005, arXiv:astro-ph/0506316. 68

[W$^+$07] Z. Wu et al. VLBI observations of seven BL Lacertae objects from RGB sample. *Astronomy & Astrophysics*, 466:63–73, April 2007, 0706.0191. 71

[W$^+$09a] R. G. Wagner et al. The Next Generation of Photo-Detectors for Particle Astrophysics. In *Astro2010: Technology Development Papers*, volume 2010 of *The Astronomy and Astrophysics Decadal Survey*, pages 59–+, 2009, 0904.3565. 46

[W+09b] Q. Weitzel et al. A Novel Camera Type for Very High Energy Gamma-Astronomy. In *31st International Cosmic Ray Conference, Łódź, Poland*, International Cosmic Ray Conference, page 1074, July 2009. Published online: http://icrc2009.uni.lodz.pl/proc/html. 46

[W+10] R. Walter et al. INTEGRAL in HEAVENS. In *8th INTEGRAL Workshop "The Restless Gamma-ray Universe"*, volume INTEGRAL 2010 of *Proceedings of Science*, 2010. 72

[W+11a] R. Wagner et al. Long-term monitoring of blazars. In *32nd International Cosmic Ray Conference, Beijing, China*, International Cosmic Ray Conference, page 1030, August 2011. accepted for publication. 78

[W+11b] R. Walter et al. HEAVENS official website, November 2011. http://www.isdc.unige.ch/heavens. 144, 188

[Wag04] Wolfgang Wagner. *Design and Realisation of a new AMANDA Data Acquisition System with Transient Waveform Recordes*. PhD thesis, Universität Dortmund, October 2004. DissDo 2004-169. 4

[Wax95] E. Waxman. Cosmological Gamma-Ray Bursts and the Highest Energy Cosmic Rays. *Physical Review Letters*, 75:386–389, July 1995, arXiv:astro-ph/9505082. 10

[WB92] R. L. White and R. H. Becker. A new catalog of 30,239 1.4 GHz sources. *Astrophysical Journal Supplements*, 79:331–467, April 1992. 25

[WB95] R. L. White and R. H. Becker. The North 20cm Survey (White+ 1992). *VizieR Online Data Catalog*, 8017:0, August 1995. 25

[WBM98] B. Wiebel-Sooth, P. L. Biermann, and H. Meyer. Cosmic rays. VII. Individual element spectra: prediction and data. *Astronomy & Astrophysics*, 330:389, February 1998. arXiv:astro-ph/9709.253. 5

[Wee03] Trevor C. Weekes. *Very High Energy Gamma-Ray Astronomy*. Institute of Physics Publishing, 2003. 13, 33

[Wil05] D. A. Williams. Studies of Nearby Blazars with Milagro. In F. A. Aharonian, H. J. Völk, & D. Horns, editor, *High Energy Gamma-Ray Astronomy*, volume 745 of *American Institute of Physics Conference Series*, pages 499–504, February 2005. 84

[WLZ02] X.-B. Wu, F. K. Liu, and T. Z. Zhang. Supermassive black hole masses of AGNs with elliptical hosts. *Astronomy & Astrophysics*, 389:742–751, July 2002, arXiv:astro-ph/0203158. 68

[Wo02] T. Weekes and others. 1ES 1959+650. *INTERNATIONAL ASTRONOMICAL UNION - Central Bureau for Astronomical Telegrams*, Circular No. 7903:1, May 2002. ISSN 0081-0304, http://cfa-www.harvard.edu/iau/cbat.html. 78

[WS10] M. Weidinger and F. Spanier. Modelling the variability of 1ES1218+30.4. *Astronomy & Astrophysics*, 515:A18, June 2010, 1005.3747. 101, 103, 105

[WU02] J.-H. Woo and C. M. Urry. Active Galactic Nucleus Black Hole Masses and Bolometric Luminosities. *Astrophysical Journal*, 579:530–544, November 2002, arXiv:astro-ph/0207249. 68

[X+02] G. Z. Xie et al. Supermassive Black Holes in BL Lacertae Objects: Estimated Masses and Their Relation to Nuclear Luminosity. *Astronomical Journal*, 123:2352–2357, May 2002. 68

[Y+95] S. Yoshida et al. The cosmic ray energy spectrum above 3x10ˆ18 eV measured by the Akeno Giant Air Shower Array. *Astroparticle Physics*, 3:105, March 1995. 9

[Y+99] T. Yamamoto et al. The Utah Seven Telescope Array. In *International Cosmic Ray Conference*, volume 5 of *International Cosmic Ray Conference*, page 275, 1999. 77

[Y+08a] T. Yamamoto et al. The UHECR spectrum measured at the Pierre Auger Observatory and its astrophysical implications. In 30^{th} *International Cosmic Ray Conference ICRC, Mérida, Mexico*, volume 4 of *International Cosmic Ray Conference*, pages 335–338, 2008, 0707.2638. 9

[Y+08b] J.-H. Yang et al. Long-term Variability Properties of Mkn501. *Chinese Astronomy and Astrophysics*, 32:129–139, April 2008. 21

[Z+10] A. C. Zoglauer et al. Reanalysis of COMPTEL Measurements with the Latest Compton Event and Image Reconstruction Techniques. In *AAS/High Energy Astrophysics Division #11*, volume 42 of *Bulletin of the American Astronomical Society*, pages 668–+, February 2010. 31

[Z+11] J. Zhang et al. Radiation Mechanisms and Physical Properties of GeV-TeV BL Lac Objects. *Astrophysical Journal*, July 2011, 1108.0146. Submitted for publication. 19

[Zan06] Roberta Zanin. Observation an Analysis of VHE Gamma Emission from the AGN 1ES1959+650 with the MAGIC Telescope. Tesi di laurea, Università Degli Studi di Padova, September 2006. 78, 85, 86

[ZK66] G.T. Zatsepin and V.A. Kuzmin. Upper limit of the spectrum of cosmic rays. *Pisma Zhurnal Eksp. Teor. Fiziki*, 4:114, 1966. 9

Author’s Publications

In the following, publications this thesis is partially based on or that are associated with this thesis with myself being (among) the main author(s) are listed in their order of publication.

[1] T. Bretz, M. Backes, et al. Long term VHE gamma-ray monitoring of bright blazars with a dedicated Cherenkov telescope. In *Blazar Variability across the Electromagnetic Spectrum*, volume BLAZARS2008 of *Proceedings of Science*, 2008.

[2] M. Backes et al. Long-Term Monitoring of Bright Blazars with a Dedicated Cherenkov Telescope. *International Journal of Modern Physics D*, 18:1645–1649, 2009.

[3] T. Bretz, M. Backes, et al. Long-term monitoring of bright blazars with a dedicated Cherenkov telescope. In F. A. Aharonian, W. Hofmann, and F. Rieger, editors, *American Institute of Physics Conference Series*, volume 1085 of *American Institute of Physics Conference Series*, pages 850–853, December 2008.

[4] I. Braun, M. Backes, et al. First Avalanche-photodiode camera test (FACT): A novel camera using G-APDs for the observation of very high-energy γ-rays with Cherenkov telescopes. *Nuclear Instruments and Methods in Physics Research A*, 610:400–403, October 2009.

[5] M. Backes et al. Long-term monitoring of blazars - the DWARF network. In *31st International Cosmic Ray Conference, Łódź, Poland*, International Cosmic Ray Conference, page 1452, July 2009. Published online: http://icrc2009.uni.lodz.pl/proc/html.

[6] A.M. Thieler, R. Backes, M. Fried, and W. Rhode. Period search in unevenly sampled data. Forschungsbericht 2010/1, TU Dortmund, Fakultät Statistik, 2010. 82

[7] H. Anderhub, M. Backes, et al. FACT – The first Cherenkov telescope using a G-APD camera for TeV gamma-ray astronomy. *Nuclear Instruments and Methods in Physics Research A*, 639:58–61, May 2011, 1010.2397.

[8] R. Wagner, M. Backes, et al. Monitoring of bright, nearby Active Galactic Nuclei with the MAGIC telescopes. In *32nd International Cosmic Ray Conference, Beijing, China*, volume 8 of *International Cosmic Ray Conference*, pages 143–146, August 2011, 1109.6774. Accepted for publication.

[9] A.M. Thieler, M. Backes, R. Fried, and W. Rhode. Robustified methods to detect periods in irregularly sampled time series. *Statistical Analysis and Data Mining*, Special Issue on Astrostatistics, 2011. Submitted for publication. 82

[10] T. Voigt, R. Fried, M. Backes, and W. Rhode. Threshold Optimization for Classification in Imbalanced Data with Unknown Misclassification Costs. *Advances in Data Analysis and Classification*, 2011. Submitted for publication. 42, 44

[11] M. Helf, K. Morik, M. Backes, and W. Rhode. Data Mining on the Rocks – Improving the *Ada*^{2}*Boost* algorithm through Fuzzification and Sampling Techniques for Very Large Datasets in Gamma-Ray Astronomy. 2012. In preparation. 42, 44

[12] J. Aleksić et al. Monitoring of bright, nearby Active Galactic Nuclei with the MAGIC telescope. 2012. In preparation. 65, 70

Acknowledgments / Danksagung

- First of all, I would like to thank Prof. Dr. Dr. Wolfgang Rhode, for the possibility to conduct this interesting research project in his group and for all the opportunities to attend conferences and schools.
- I would also like to thank Jun.-Prof. Dr. Julia K. Becker for her efforts in being the second referee of this thesis.
- Special thanks go to all members of the astroparticle physics working group at TU Dortmund University, especially to
  - Jan-Hendrik Köhne and Dominik Neise with whom the characterization of the FACT mirrors has been conducted and to
  - Malwina Uellenbeck who has been the leading MAGIC data analyst for 1ES 1959+650.
- For his great and unreserved support for several funding applications and enlightening discussions, I am grateful to Trevor C. Weekes.
- For his always brilliant advices and his tireless pushing forward of FACT, I thank Eckart Lorenz.
- Theoretical modeling of the spectral energy distribution has been conducted with great support of Matthias Weidinger, whom I thank a lot for this.
- For collaborative work on the periodicity analysis of irregularly sampled time series, I thank Anita M. Thieler, Katy Holman, and Bhavika Haria.
- Developments in data-mining and statistical analysis have been conducted together with Tobias Voigt and Marius Helf, whom I thank for this.
- I thank a lot all those people who supplied me with (partially unpublished) data from the different experiments (in order of rising frequency):
  - Lars Fuhrmann and Ioannis Nestoras from the F-GAMMA project for data from the Effelsberg 100 m and IRAM telescopes,
  - David Paneque and the according telescope teams for data from OVRO, GRT, NMS, and Tenagra-II as well as for the high energy analysis of Fermi–LAT data,
  - Anne Lähteenmäki, Merja Tornikoski, and Elina Nieppola for data from Metsähovi,
  - Elina Lindfors and Kari Nilsson for data from KVA,

- Francesco Massaro for data from Swift–XRT and *Beppo*SAX,
- Liz Rivers and Alex Markovitz for data from RXTE–PCA and RXTE–HEXTE,
- Eugenio Bottacini for data from Palomar60, Swift–UVOT, Swift–XRT, and INTEGRAL–IBIS-ISGRI,
- Francesco Longo, Francesco Verrecchia, and Carlotta Pittori (on behalf of the AGILE collaboration) for data from AGILE–GRID,
- Benoit Lott for data from Fermi–LAT, and
- Masaaki Hayashida for data from the MAGIC telescope.

- For their help related to ROOT, I thank Thomas Bretz and Nicole Fields.
- For proof-reading this document, special thanks attain to Miriam Hutterer, Misty Barth, Marlene Doert, Nikola Strah, Malwina Uellenbeck, Björn Eichmann, and Matthias Weidinger.
- This work has been supported by the Physics Faculty, TU Dortmund University, the Collaborative Research Center SFB 876, the German Academic Exchange Service (DAAD) through the PPP programs USA, Spain, and Croatia, the Wilhelm und Else Heraeus-Stiftung, and the German Academic Exchange Service (DAAD) through personal funding and through funding RISE interns.

The possibility to use astronomical databases is gratefully acknowledged:

- This research has made use of NASA's Astrophysics Data System (ADS).
- This research has made use of the NASA/IPAC Extragalactic Database (NED), which is operated by the Jet Propulsion Laboratory, California Institute of Technology, under contract with the National Aeronautics and Space Administration.
- Part of this work is based on archival data, software or on-line services provided by the ASI Science Data Center (ASDC).
- This research has made use of the SIMBAD database, operated at CDS, Strasbourg, France.
- This research has made use of the VizieR catalogue access tool, CDS, Strasbourg, France.
- This research has made use of the NASA/IPAC Infrared Science Archive (IRSA), which is operated by the Jet Propulsion Laboratory, California Institute of Technology, under contract with the National Aeronautics and Space Administration.
- This research has made use of data obtained from the High Energy Astrophysics Science Archive Research Center (HEASARC), provided by NASA's Goddard Space Flight Center.
- This research has made use of ISDC's High-Energy Astrophysics Virtually ENlightened Sky (HEAVENS).

- This research has made use of data from the MOJAVE database that is maintained by the MOJAVE team [L+09e].

- Some of the data presented in this paper were obtained from the Multimission Archive at the Space Telescope Science Institute (MAST). STScI is operated by the Association of Universities for Research in Astronomy, Inc., under NASA contract NAS5-26555. Support for MAST for non-HST data is provided by the NASA Office of Space Science via grant NNX09AF08G and by other grants and contracts.

Being member of the MAGIC and FACT collaborations, I also include the collaborative acknowledgments:

- **MAGIC:** We would like to thank the Instituto de Astrofísica de Canarias for the excellent working conditions at the Observatorio del Roque de los Muchachos in La Palma. The support of the German BMBF and MPG, the Italian INFN, the Swiss National Fund SNF, and the Spanish MICINN is gratefully acknowledged. This work was also supported by the Marie Curie program, by the CPAN CSD2007-00042 and MultiDark CSD2009-00064 projects of the Spanish Consolider-Ingenio 2010 programme, by grant DO02-353 of the Bulgarian NSF, by grant 127740 of the Academy of Finland, by the YIP of the Helmholtz Gemeinschaft, by the DFG Cluster of Excellence "Origin and Structure of the Universe", by the DFG Collaborative Research Centers SFB823/C4 and SFB876/C3, and by the Polish MNiSzW grant 745/N-HESS-MAGIC/2010/0.

- **FACT:** The important contributions from ETH Zurich grant ETH-10.08-2 as well as the funding of novel photo-sensor research by the German BMBF Verbundforschung are gratefully acknowledged. We also thank the Instituto de Astroísica de Canarias allowing us to operate the telescope at the Observatorio del Roque de los Muchachos in La Palma, and the Max-Planck-Institut für Physik for providing us with the mount of the former HEGRA CT3 telescope. We thank the MAGIC collaboration for their hospitality and support.

Unter all diesen Danksagungen möchte ich ganz besonders meine Eltern Jürgen und Karin Backes, sowie meine Großmutter Florentine Backes und meine Freundin Miriam Hutterer hervorheben, die durch ihren Beistand, ihre Unterstützung und ihren Antrieb diese Arbeit erst ermöglicht haben – ich danke Euch!